

FEDERAL UNIVERSITY OF MINAS GERAIS
School of Engineering
Graduate Program in Structural Engineering

Larissa Novelli

**ADAPTIVE FEM-SPIM COUPLING FOR PHASE-FIELD
MODELLING OF FRACTURE**

Belo Horizonte
2023

Larissa Novelli

**ADAPTIVE FEM-SPIM COUPLING FOR PHASE-FIELD MODELLING
OF FRACTURE**

Thesis submitted to the Graduate Program in Structural Engineering of the School of Engineering at the Federal University of Minas Gerais, in partial fulfillment of the requirements for the degree of “Doctor in Structural Engineering”.

Supervisor: Prof. Dr. Roque Luiz da Silva Pitangueira

Co-Supervisor: Prof. Dr. Lapo Gori

Belo Horizonte
2023

N938a

Novelli, Larissa.

Adaptive fem-spim coupling for phase-field modelling of fracture
[recurso eletrônico] / Larissa Novelli. - 2023
1 recurso online (181 f. : il., color.) : pdf.

Orientador: Roque Luiz da Silva Pitangueira.

Coorientador: Lapo Gori.

Tese (doutorado) Universidade Federal de Minas Gerais,
Escola de Engenharia.

Anexos: f. 158-181.

Bibliografia: f.147-157.

1. Engenharia de estruturas - Teses. 2. Mecânica da fratura - Teses.
I. Pitangueira, Roque Luiz da Silva. II. Gori, Lapo. III. Universidade Federal
de Minas Gerais. Escola de Engenharia. IV. Título.

CDU: 624(043)



UNIVERSIDADE FEDERAL DE MINAS GERAIS



PROGRAMA DE PÓS-GRADUAÇÃO EM ENGENHARIA DE ESTRUTURAS



ATA DA DEFESA DE TESE DE DOUTORADO EM ENGENHARIA DE ESTRUTURAS Nº: 94 DA ALUNA LARISSA NOVELLI

Às **8:00** horas do dia **14** do mês de **setembro** de **2023**, reuniu-se em ambiente virtual, na Escola de Engenharia da Universidade Federal de Minas Gerais - UFMG, a Comissão Examinadora indicada pelo Colegiado do Programa em **07 de julho de 2023**, para julgar a defesa da Tese de Doutorado intitulada "**ADAPTIVE FEM-SPIM COUPLING FOR PHASE-FIELD MODELLING OF FRACTURE**", cuja aprovação é um dos requisitos para a obtenção do Grau de DOUTOR EM ENGENHARIA DE ESTRUTURAS na área de ESTRUTURAS.

Abrindo a sessão, o Presidente da Comissão, **Prof. Dr. Roque Luiz da Silva Pitangueira**, após dar a conhecer aos presentes o teor das Normas Regulamentares passou a palavra à candidata para apresentação de seu trabalho. Seguiu-se a arguição pelos examinadores, com a respectiva defesa da candidata. Logo após, a Comissão se reuniu, sem a presença da candidata e do público, para julgamento e expedição do resultado final.

Prof. Dr. Roque Luiz da Silva Pitangueira - DEES - UFMG (Orientador)

Prof. Dr. Lapo Gori - DEES - UFMG (Coorientador)

Prof. Dr. Samuel Silva Penna - DEES - UFMG

Prof. Dr. Renato Cardoso Mesquita - DEE - UFMG

Prof. Dr. José Antônio Fontes Santiago - UFRJ

Prof. Dr. Roberto Dalledone Machado - UFPR

Após reunião, a Comissão considerou a candidata **APROVADA**, conforme pareceres em anexo.

O resultado final foi comunicado publicamente à candidata pelo Presidente da Comissão. Nada mais havendo a tratar, o Presidente encerrou a reunião e lavrou a presente ATA, que será assinada por todos os membros participantes da Comissão Examinadora.

Belo Horizonte, 14 de setembro de 2023

Observações:

1. A aprovação da candidata na defesa da Tese de Doutorado não significa que o mesmo tenha cumprido todos os requisitos necessários para obtenção do Grau de Doutor em Engenharia de Estruturas;

2. Este documento não terá validade sem a assinatura do Coordenador do Programa de Pós-Graduação.



Documento assinado eletronicamente por **Lapo Gori, Professor do Magistério Superior**, em 14/09/2023, às 11:55, conforme horário oficial de Brasília, com fundamento no art. 5º do [Decreto nº 10.543, de 13 de novembro de 2020](#).



Documento assinado eletronicamente por **Renato Cardoso Mesquita, Professor do Magistério Superior**, em 14/09/2023, às 11:55, conforme horário oficial de Brasília, com fundamento no art. 5º do [Decreto nº 10.543, de 13 de novembro de 2020](#).



Documento assinado eletronicamente por **Samuel Silva Penna, Professor do Magistério Superior**, em 14/09/2023, às 11:57, conforme horário oficial de Brasília, com fundamento no art. 5º do [Decreto nº 10.543, de 13 de novembro de 2020](#).



Documento assinado eletronicamente por **Roque Luiz da Silva Pitangueira, Professor do Magistério Superior**, em 14/09/2023, às 12:56, conforme horário oficial de Brasília, com fundamento no art. 5º do [Decreto nº 10.543, de 13 de novembro de 2020](#).



Documento assinado eletronicamente por **Roberto Dalledone Machado, Usuário Externo**, em 14/09/2023, às 15:52, conforme horário oficial de Brasília, com fundamento no art. 5º do [Decreto nº 10.543, de 13 de novembro de 2020](#).



Documento assinado eletronicamente por **José Antonio Fontes Santiago, Usuário Externo**, em 14/09/2023, às 18:15, conforme horário oficial de Brasília, com fundamento no art. 5º do [Decreto nº 10.543, de 13 de novembro de 2020](#).



Documento assinado eletronicamente por **Felicio Bruzzi Barros, Coordenador(a) de curso de pós-graduação**, em 02/10/2023, às 16:35, conforme horário oficial de Brasília, com fundamento no art. 5º do [Decreto nº 10.543, de 13 de novembro de 2020](#).



A autenticidade deste documento pode ser conferida no site https://sei.ufmg.br/sei/controlador_externo.php?acao=documento_conferir&id_orgao_acesso_externo=0, informando o código verificador **2598026** e o código CRC **6D797673**.

Agradecimentos

Agradeço primeiramente à Deus, pelo dom da sabedoria e persistência.

À minha família, por todo apoio e confiança durante esta jornada.

Ao Jardel, por todo amor, suporte e incentivo.

Ao professor orientador Roque Pitangueira, por todo conhecimento compartilhado e incentivo na orientação deste trabalho.

Ao professor co-orientador Lapo Gori, por toda dedicação e pela disponibilidade durante todo o desenvolvimento deste trabalho.

Aos meus amigos do PROPEEs, Samir, Hugo, Matheus, Livia e Eduarda, por estarem sempre dispostos a ajudar e sempre presentes mesmo que de forma virtual.

À CAPES e ao CNPq, pelo apoio financeiro.

Resumo

Esta tese propõe um acoplamento adaptativo entre o Método dos Elementos Finitos (MEF) e as diferentes versões do método sem malha *Smoothed Point Interpolation Method* (SPIM), para a discretização de modelos de *phase-field* aplicados ao problema de propagação de trincas. Para essas aplicações, a formulação fraca-enfraquecida, adotada para o problema de deslocamentos no SPIM, foi estendida para o problema de *phase-field* e a suavização do gradiente, adotada para o cálculo da derivada das funções de forma, foi aplicada à variável *phase-field*. A estratégia tem como objetivo diminuir o custo computacional mantendo as vantagens inerentes de cada um dos métodos. O estudo teve início com o uso de modelos nos quais a malha é previamente refinada na região da trinca. Nestes estudos iniciais, duas alternativas distintas foram adotadas, a saber: todo o domínio com o método sem malha SPIM e acoplamento prévio FEM-SPIM, com o SPIM na região de propagação da trinca. Na estratégia adaptativa, o domínio é inicialmente discretizado com uma malha de FEM grosseira, a partir da qual a região de propagação da trinca é detectada, sendo esta região substituída pelo SPIM e refinada se necessário. Todo o processo é realizado de forma automática e o usuário deve informar apenas alguns parâmetros da estratégia adaptativa. A implementação é geral de forma que podem ser adotados diferentes formatos para os domínios de suavização do SPIM e diferentes modelos constitutivos de *phase-field*. Simulações numéricas foram realizadas buscando demonstrar a acurácia e estabilidade da estratégia proposta. Os resultados obtidos foram capazes de simular corretamente a propagação das trincas em modelos de fratura frágil e parcialmente frágil e as curvas carga-deslocamento apresentaram boa concordância com os resultados experimentais e numéricos de referência.

Palavras-chave: Phase-Field; Métodos Sem Malha; Smoothed Point Interpolation Method; Modelos acoplados; Adaptatividade.

Abstract

This thesis proposes an adaptive coupling between the Finite Element Method (FEM) and the different versions of the meshfree method Smoothed Point Interpolation Method (SPIM), for the discretisation of phase-field models applied to the crack propagation problem. For these applications, the weak-weakened form, adopted for the displacement problem in SPIM, was extended to the phase-field problem and the gradient smoothing, adopted for the calculation of the derivative of the shape functions, was applied to the phase-field variable. The strategy aims to reduce the computational cost while maintaining the inherent advantages of each method. The study began with the use of models in which the mesh is previously refined in the crack region. In these initial studies, two distinct alternatives were adopted, namely: the entire domain with the SPIM meshfree method and prior FEM-SPIM coupling, with SPIM in the crack propagation region. In the adaptive strategy, the domain is initially discretised with a coarse FEM mesh, from which the crack propagation region is detected, and this region is replaced by SPIM and refined if necessary. The entire process is carried out automatically and the user must inform only a few parameters of the adaptive strategy. The implementation is general so that different formats can be adopted for SPIM smoothing domains and different constitutive models of phase-field. Numerical simulations were performed seeking to demonstrate the accuracy and stability of the proposed strategy. The results obtained were able to correctly simulate crack propagation in brittle and quasi-brittle fracture models and the load-displacement curves showed good agreement with the experimental and numerical reference results.

Key-words: Phase-Field; Meshfree Methods; Smoothed Point Interpolation Method; Coupled models; Adaptivity.

List of figures

2.1	Elastic body with crack.	26
2.2	Geometric representation of the crack for the phase-field modelling.	28
2.3	Energetic degradation function.	32
2.4	First derivatives of the energetic degradation function.	33
2.5	Staggered solver (Adapted of Wu et al. (2020)).	42
3.1	Influence domains for nodes selection (Adapted of Liu (2009)).	46
3.2	T-schemes for nodes selection.	46
3.3	Smoothing domains.	51
4.1	Trigonometric function.	64
4.2	Trigonometric shape function in 1D space for the node $x = 0$	64
5.1	Refinement strategies: a) Original mesh, b) Refinement h, c) Refinement p e d) Refinement r. Adapted from Sousa (2007).	66
5.2	Adaptive refinement of Heister et al. (2015).	68
5.3	Division of the elements: a) 1 edge b) 2 edges e c) 3 edges of Areias et al. (2016).	69
5.4	Refinement meshes of Kastner et al. (2016).	69
5.5	Initial coarse mesh (a) and final mesh to the limit of 0.8 (b) and 0.2 (c) (Badnava et al., 2017).	70
5.6	Adaptive refinement of Tian et al. (2019).	71
5.7	Adaptive refinement of Shao et al. (2019).	72
5.8	Adaptive refinement of Nagarajara et al. (2019) with <i>quadtree</i> division.	73
5.9	Adaptive refinement of Shao et al. (2020).	75
5.10	Coupled model.	77
5.11	Adaptive strategy.	80
5.12	Flowchart of the incremental-iterative process.	81
5.13	Flowchart of the modification of the model.	82
5.14	Flowchart of the coupling FEM-SPIM.	83
5.15	Flowchart of building of the SPIM model.	86
5.16	Flowchart of the refinement of the SPIM region.	87

5.17	Flowchart of building the refined SPIM model.	89
6.1	Bending test: Geometry, loading and boundary conditions.	92
6.2	Bending test: Nodal distribution.	92
6.3	Smoothing domains and FEM mesh of the bending test.	92
6.4	Load-displacement paths of the bending test.	93
6.5	Phase-field contour plots for the bending test with ES-RPIMp T3. Dis- placements of (a) 4.02×10^{-2} mm, (b) 4.17×10^{-2} mm, (c) 9.94×10^{-2} mm and (d) Reference Miehe, Hofacker and Welschinger (2010).	93
6.6	Total number of iterations of the bending test.	94
6.7	L-shaped Panel: (a) Geometry, loading and boundary conditions, and (b) Nodal distribution.	95
6.8	Smoothing domains and FEM mesh of the L-shaped panel.	95
6.9	Load-displacement paths of the L-shaped panel test.	96
6.10	Analysis of the parameter c for the panel-L with ES-RPIMp-T3.	97
6.11	Load-displacement paths of the L-shaped panel for the convergence test.	97
6.12	Critical loads for the panel L plotted with different degrees of mesh refine- ment represented by l_0/h	98
6.13	Load-displacement paths of the L-shaped panel for the convergence test using trigonometric radial function.	98
6.14	Critical loads for the panel L comparing trigonometric and exponential radial function.	99
6.15	Geometry, loading and boundary conditions of the bending test.	99
6.16	Mesh of the bending test.	100
6.17	Coupled FEM-SPIM mesh of the bending test.	100
6.18	Magnified view in the notch region of the bending test.	100
6.19	Load-displacement curve of the bending test.	101
6.20	Phase-field contour plots for the bending test with coupled FEM-CS-RPIMp T4. Displacements of (a) 0.175 mm, (b) 0.35 mm, (c) 0.70 mm and (d) Reference (Wu, 2018b).	101
7.1	Geometry, loading and boundary conditions of the shear test.	103
7.2	Initial mesh of the shear test.	103
7.3	Load-displacement curve: Substitution criteria.	104
7.4	Phase-field contour plots: Substitution criteria.	105
7.5	Load-displacement curve: Critical factor.	106
7.6	Phase-field contour plots: Critical factor.	106
7.7	Load-displacement curve: Scale of substitution.	107
7.8	Phase-field contour plots: Scale of substitution.	107
7.9	Load-displacement curve: Refinement criteria.	108

7.10	Phase-field contour plots: Refinement criteria.	109
7.11	Load-displacement curve: Critical factor for refinement.	109
7.12	Phase-field contour plots: Critical factor for refinement.	110
7.13	Load-displacement curve: Level of refinement.	110
7.14	Phase-field contour plots: Level of refinement.	111
7.15	Load-displacement curve: Smoothing domain.	112
7.16	Phase-field contour plots: Smoothing domain.	112
7.17	Load-displacement curve: Comparison radial basis function.	113
7.18	Phase-field contour plots: Comparison radial function.	113
7.19	Previously refined mesh of the model.	114
7.20	Load-displacement curve: Comparison mesh.	114
7.21	Phase-field contour plots: Comparison mesh.	115
7.22	Total number of iterations.	116
7.23	Geometry, loading and boundary conditions of the tension test.	117
7.24	Initial mesh of the tension test.	117
7.25	Load-displacement curve of the tension test.	118
7.26	Final mesh and phase-field contour plot for the tension test.	118
7.27	Geometry, loading and boundary conditions of the L-shaped panel.	119
7.28	Initial mesh of the L-shaped panel.	120
7.29	Load-displacement curve of the L-shaped panel.	120
7.30	Final mesh and phase-field contour plot of the L-shaped panel.	121
7.31	Strain energy substitution method for the L-shaped panel.	121
7.32	Geometry, loading and boundary conditions of the four-point shear test.	122
7.33	Calibration of the l_0 of the four-point shear test.	122
7.34	Initial mesh of the four-point shear test.	123
7.35	Equilibrium paths of the four-point shear test.	123
7.36	Contour plot of the phase-field and final mesh of the four-point shear test.	124
7.37	Magnified view of the crack region of the four-point shear test.	125
7.38	Geometry, loading and boundary conditions of the bending test.	126
7.39	Initial mesh of the bending test.	126
7.40	Load-displacement curves of the bending test.	127
7.41	Contour plot of the phase-field and final mesh of the bending test.	127
7.42	Magnified view of the crack region of the bending test with edge-based T6/3.	128
7.43	Geometry, loading and boundary conditions of the mixed-mode failure test.	129
7.44	Initial mesh of the mixed-mode failure test.	129
7.45	Load-CMOD curves of the mixed model failure test.	130
7.46	Substitution regions of the mixed-mode failure test with strain energy criterion.	130

7.47	Contour plot of phase-field and final mesh of the mixed-mode failure test with Shao criterion.	131
7.48	Contour plot of phase-field and final mesh of the mixed-mode failure test with phase-field criterion.	131
7.49	Geometry, loading and boundary conditions of the 3 point bending test. . .	132
7.50	Initial mesh of the 3 point bending test.	132
7.51	Mesh of the 3 point bending test by Fortes (2022).	132
7.52	Load-displacement curves of the 3 point bending test.	133
7.53	Contour plot of the phase-field and final mesh of the 3 point bending test.	133
7.54	Geometry, loading and boundary conditions of the Gracia bending.	134
7.55	Calibration of the l_0 parameter of the Gracia bending.	135
7.56	Initial mesh of the Gracia bending.	135
7.57	Load factor versus CMOD of the Gracia bending.	136
7.58	Crack and final mesh of the Gracia bending for cell-based.	137
7.59	Crack and final mesh of the Gracia bending for edge-based.	137
7.60	Geometry, loading and boundary conditions of the notched test.	138
7.61	Initial mesh of the notched test.	138
7.62	Load-displacement curve of the notched test.	139
7.63	Crack propagation in different steps of the notched test.	140
7.64	Final mesh of the Shao et al. (2019) for the notched test.	140
7.65	Geometry, loading and boundary conditions of the asymmetric tensile test.	141
7.66	Initial mesh of the asymmetric tensile test.	141
7.67	Load-displacement curve of the asymmetric tensile test.	142
7.68	Comparison of the crack profile with the reference.	142
7.69	Crack propagation in different steps of the asymmetric tensile test.	143
A.1	Square panel with a hole subjected to a tensile load in the horizontal direction.	159
A.2	Meshes of the square panel with a hole.	160
A.3	Convergence of σ_{xx} at $(x, y) = (0, 1)$	161
A.4	Comparison between the exact solution, FEM and SPIM for σ_{xx}	161
B.1	Classes representation in UML diagram.	163
B.2	Numerical core of the Insane.	163
B.3	Model class.	165
B.4	DataManager class.	166
B.5	DataModel class.	166
B.6	ProblemDriver class.	167
B.7	ConstitutiveModel class.	168
B.8	AnalysisModel class.	169
B.9	Assembler class.	170

B.10 Assembler phase-field class.	171
B.11 Assembler coupled class.	171
B.12 Solution class.	172
B.13 Step class.	173
B.14 Persistence class.	174
B.15 Radial function class.	174
C.1 Input file of the full SPIM model.	176
C.2 Input file of the geometric model.	177
C.3 Input file of the phase-field material.	177
C.4 Input file of the degeneration.	177
C.5 Input file of the nodes.	177
C.6 Input file of the integration domains.	178
C.7 Input file of the coupled model.	179
C.8 Input file of the discrete model parameters.	180
C.9 Input file of the adaptive model.	181

List of tables

2.1	Generic geometric crack function.	31
2.2	Energetic degradation functions $g(\phi)$	32
4.1	Phase-field models with meshfree methods.	58
6.1	Computational time (in ms) of the bending test.	94
7.1	Computational time (in ms) of the shear test.	115
7.2	Average length of the background cells of the four-point shear test.	125
7.3	Total number of nodes in the bending test.	128
7.4	Total number of nodes in the 3 point bending test.	134

List of abbreviations and acronyms

SPIM	Smoothed Point Interpolation Method
FEM	Finite Element Method
PF	Phase-field
PIM	Point Interpolation Method
RPIM	Radial Point Interpolation Method
INSANE	INteractive Structural ANalysis Environment
EFG	Element-free Galerkin
MLS	Moving Least-Square
NS-PIM	Node-Based Smoothed Point Interpolation Method
ES-PIM	Edge-Based Smoothed Point Interpolation Method
CS-PIM	Cell-Based Smoothed Point Interpolation Method
SPH	Smoothed Particle Hydrodynamics
SFEM	Smoothed Finite Element Method
CMOD	Crack Mouth Opening Displacement
CMSD	Crack Mouth Sliding Displacement

List of symbols

Chapter 2: Phase-Field modelling of fracture

Ω	body domain
$\partial\Omega$	body boundary
$\partial\Omega_u$	body boundary with prescribed displacements
$\partial\Omega_t$	body boundary with prescribed forces
E_t	energy functional
ψ_s	strain energy
Ψ_c	crack surface energy
P_{ext}	external load potential
ε	strain tensor
\mathbf{u}	displacement vector
$\nabla\mathbf{u}$	gradient of displacements
$\boldsymbol{\sigma}$	stress tensor
ψ	energy density
λ_0	first Lamé constant
μ_0	second Lamé constant
G_c	critical energy release rate
Γ	crack surface
\mathbf{b}	body forces
\mathbf{t}	surface forces
$\dot{\gamma}$	crack surface density rate
t	time
\dot{E}_t	energy rate functional
δE_t	first variation of energy functional
\mathbf{n}	surface normal vector
$\dot{\mathbf{u}}$	displacements rate vector
$\dot{\mathbf{b}}$	body forces rate vector
$\dot{\mathbf{t}}$	surface forces rate vector
$\delta\mathbf{u}$	first variation displacements vector
\underline{I}	second order identity tensor

\mathcal{G}	variation of strain energy functional with respect to the crack surface
ϕ	phase-field
l_0	length scale parameter
γ	crack surface density function
ϵ	perturbation
∇	nabla operator
\mathcal{B}	damage part of the body
$\partial\mathcal{B}$	damaged surface of the body
Y	crack driving force
\bar{Y}	effective crack driving force
g	energetic degradation function
α	geometrical crack function
ξ	parameter of the geometric crack function
f_t	strength tensile
k_0	initial slope of the softening law
w_c	ultimate crack opening
ψ_0^+	active strain energy density
ψ_0^-	inactive strain energy density
ϵ_D	deviatoric part of the strain tensor
ϵ_V	volumetric part of the strain tensor
ϵ^-	inactive strain tensor
ϵ^+	active strain tensor
H	Heaviside function
\mathbf{I}	fourth order identity tensor
\mathbf{P}^+	positive \mathbf{P} tensor (used in Miehe, Hofacker and Welschinger (2010) constitutive model)
\mathbf{P}^-	negative \mathbf{P} tensor (used in Miehe, Hofacker and Welschinger (2010) constitutive model)
E_0	linear elastic isotropic constitutive tensor
H	historical variable
\mathbf{d}	nodal displacements
\mathbf{N}	interpolation matrix
\mathbf{B}	strain matrix
\mathbf{r}^u	residual of displacements
\mathbf{r}^ϕ	residual of phase-field
\mathbf{K}	stiffness matrix

Chapter 3: Smoothed Point Interpolation Methods for linear elasticity

$\mathbf{P}(\mathbf{x})$	vector of monomials of the polynomial basis
\mathbf{a}	vector of coefficients a_i
\mathbf{P}_Q	moment matrix

\mathbf{d}_s	vector of the nodal parameters
$N(\mathbf{x})$	shape function in a point \mathbf{x} of the domain
$\mathbf{R}(\mathbf{x})$	vector of radial basis
\mathbf{R}_Q	moment matrix of the radial basis
\mathbf{P}_m	moment matrix of the polynomial function
\mathbf{b}	vector of coefficients b_j
r_i	distance
r_i^*	scaled distance
c	shape parameter of the exponential function
C	shape parameter of the multiquadric function
q	shape parameter of the multiquadric function
\mathbf{D}_k^S	smoothing domain
p_k	centre of the smoothing domain
\widetilde{W}	<i>smoothing function</i>
$n_j^{(k)}$	unitary outward normal vector field
$\partial\mathbf{D}_k^S$	boundary of the smoothing domain
A_k	area of the smoothing domain
$\widetilde{\boldsymbol{\varepsilon}}$	smoothed strain tensor
$\boldsymbol{\varepsilon}$	displacement gradient
$\widetilde{\mathbf{B}}_I$	smoothed strain gradient matrix
$\widetilde{N}_{I,l}$	derivative of the shape function
$\mathbf{K}(p_k)$	smoothed stiffness matrix

Chapter 4: Smoothed Point Interpolation Methods for phase-field modelling of fracture

$\nabla\phi$	phase-field gradient
$\widetilde{\nabla\phi}$	smoothing phase-field gradient
$\widetilde{N}_{I,l}^u$	derivative of the displacement shape function
$\widetilde{N}_{I,l}^\phi$	derivative of the phase-field shape function
$\widetilde{\mathbf{B}}_I^u$	smoothed gradient tensor of displacement
$\widetilde{\mathbf{B}}_I^\phi$	smoothed gradient tensor of phase field
\mathbf{K}^u	displacement stiffness matrix
\mathbf{F}^u	vector of forces
\mathbf{C}^u	constitutive matrix of displacement
\mathbf{K}^ϕ	phase-field stiffness matrix
\mathbf{F}^ϕ	vector of phase-field residual
\mathbf{C}^ϕ	constitutive matrix of phase-field

Chapter 5: Adaptive FEM-SPIM coupling for phase-field modelling

$u_i^{(1)}$	nodal displacement in the region 1
$f_i^{(1)}$	forces in the region 1
K_{ij}^{PIM}	stiffness matrix of the PIM region
K_{ij}^{FEM}	stiffness matrix of the FEM region
A_{total}	total area of the domain
n_{elem}	number of FEM elements
n_{id}	number of integration domains
A_k	area of the element or integration domain
ε_k	strain vector
σ_k	stress vector
ε_i	eigenvalue of the strain tensor
H	strain energy history
d	phase-field
H_c	critical factor of the shao criterion
d_c	critical phase-field
$A_{meshfree}$	total area of the meshfree region
A_i^{cell}	area of the face
p_i^{cell}	average value of the parameter in the face
$Factor_{critical}$	factor of the refinement of the meshfree region
$Factor_{DecayRate}$	factor the modify the $Factor_{critical}$

Table of contents

1	Introduction	22
1.1	Motivations	22
1.2	Objective	24
1.3	Outline	24
2	Phase-Field modelling of fracture	26
2.1	Variational approach to fracture	26
2.2	The phase-field modelling for diffuse cracks	28
2.3	Geometric crack function	31
2.4	Energetic degradation function	31
2.4.1	General softening laws	33
2.5	Strain energy models	34
2.5.1	Anisotropic model of Lancioni and Royer-Carfagni (2009)	35
2.5.2	Anisotropic model of Amor et al. (2009)	36
2.5.3	Anisotropic model of Miehe, Welschinger and Hofacker (2010)	36
2.5.4	Hybrid formulations	37
2.6	Phase-field equations in the weak form	38
2.7	FEM discretisation	39
2.8	Solvers	40
2.8.1	Monolithic solver	40
2.8.2	Staggered solver	41
3	Smoothed Point Interpolation Methods for linear elasticity	44
3.1	The main concepts of the meshfree methods	44
3.2	Point Interpolation Method (PIM)	47
3.3	Radial Point Interpolation Method with Polynomial Reproduction (RPIMp)	48
3.4	Smoothing domains	50
4	Smoothed Point Interpolation Methods for phase-field modelling of fracture	54
4.1	State of the art	54

4.2	SPIM for phase-field modelling	58
4.2.1	Smoothing operation for phase-field models	59
4.2.2	SPIM discretisation of the phase-field models	60
4.2.3	Trigonometric radial basis function	63
5	Adaptive FEM-SPIM coupling for phase-field modelling	65
5.1	State of the art	65
5.1.1	Adaptive refinement for phase-field modelling	65
5.1.2	Coupled FEM-meshfree models	76
5.2	Adaptive FEM-SPIM coupling strategy	78
5.2.1	Adaptive strategy	79
5.2.2	Modification of the model	82
5.2.3	Coupling FEM-SPIM	83
5.2.4	Refinement SPIM	87
5.2.5	Resize the vectors of the incremental process	90
6	Fixed mesh simulations	91
6.1	Full SPIM discretisations	91
6.1.1	Three point bending test	91
6.1.2	L-shaped panel	95
6.2	Fixed SPIM-FEM coupling	99
7	Adaptive SPIM-FEM coupling simulations	102
7.1	A parametric study on the shear test	102
7.1.1	Substitution criterion	104
7.1.2	Critical factor for substitution	105
7.1.3	Scale of substitution	106
7.1.4	Refinement criterion	108
7.1.5	Critical factor for refinement	109
7.1.6	Level of refinement	110
7.1.7	Smoothing domain and T-schemes	111
7.1.8	Comparison radial basis function	112
7.1.9	Comparison mesh	113
7.1.10	Computational time	115
7.2	Brittle and quasi-brittle constitutive models	116
7.2.1	Brittle model	116
7.2.2	Quasi-brittle model	119
7.3	Level of refinement	121
7.4	Type of smoothing domain	125
7.5	Substitution criterion	128

7.6	Refinement criterion	131
7.7	Comparison with adaptive damage models	134
7.8	Notched rectangular specimen with a hole	138
7.9	Two regions of substitution and refinement	140
8	Conclusions	144
8.1	Full SPIM	145
8.2	Previously coupled FEM-SPIM	145
8.3	Adaptive SPIM-FEM coupling	145
8.4	Future research topics	146
	Appendices	158
A	Trigonometric radial function for linear elastic problem	159
B	INSANE: INteractive Structural ANalysis Environment	162
B.1	Numerical core	163
B.2	Model	164
B.2.1	Problem Driver	166
B.2.2	Constitutive Model	167
B.2.3	Analysis Model	168
B.3	Assembler	169
B.4	Solution	172
B.5	Persistence	173
B.6	Radial Function	174
C	Input file model	175

Chapter 1

Introduction

1.1 Motivations

The modelling of fracture is an important tool to predict the failure in engineering applications such as structures, pressure vessels, aircraft fuselages and automobile components. Problems due to fracture in these structures can occur quickly and lead to catastrophic failure. These fracture processes are associated to many materials such as concrete, rock, ceramic and metals. Therefore, the ability to prevent material failure are of great interest to engineering. The first studies on brittle fractures began with Griffith's Theory. This theory is based on an energy principle, through a balance between the elastic strain energy of the body and the energy necessary to the formation of the crack. Griffith's model, despite being widely used, it is not able to determine the crack initiation and the merging between different cracks.

Phase-field modelling of fracture has been shown to be a promising strategy for the simulation of complex cracks evolution, since it is able to simulate the nucleation, propagation, branching and merging of cracks. This strategy is a variational formulation of Griffith's theory, where crack initiation and propagation is based on the minimisation of an energy functional. A scalar field variable, called phase-field, indicates the degradation of the material and introduce a transition region between the intact material and the completely broken material. When combined with the Finite Element Method (FEM), phase-field modelling has the advantage of not needing an exact representation of the crack geometry and it does not require the use of stress intensity indicators. Given these advantages, the phase-field method has been widely used recently. Among the applications of the model there are: brittle fracture, quasi-brittle fracture, ductile fracture, anisotropic materials and dynamic analysis.

In phase-field models, a length scale parameter (l_0) is adopted as an indicator of the width of the degraded region. When this parameter is close to zero the crack approaches a discrete crack. To guarantee the accuracy of the solution, the size of the FEM mesh ele-

ments must be smaller than the parameter l_0 . When a uniformly refined mesh is adopted, this leads to a high computational cost. Therefore, many studies use locally refined meshes when the crack path is previously known. However, for complex problems, where the crack evolution region is unknown, this strategy cannot be adopted. In these cases, adaptive refinement strategies are adopted. In these strategies, a criterion detects the region that needs refinement and automatically the mesh is refined in these regions. In FEM models, adaptive refinement can be complex, as it is necessary to ensure a conforming mesh or to provide a special treatment for hanging nodes. Meshfree methods, on other hand, have the advantage of not needing a mesh of elements to build the approximation functions. The process of obtaining these functions is performed using the support nodes of a given point, obtained from a cloud of nodes. In this case, refinement takes place by inserting nodes in the region of interest in the model, without the need to ensure a conforming mesh. Another advantage of this methods is that the approximation is not necessarily performed using polynomials but other functions can also be used, such as exponential functions. Many works in the literature have adopted such methods for discretisation of the phase-field models.

There are different meshfree methods in the literature, each one with its properties and particularities. Examples of these methods are the Smoothed Point Interpolation Methods (SPIM). In these methods, the shape functions can be obtained by the Point Interpolation Method (PIM) and Radial Point Interpolation Method (RPIM). These functions possess the Kronecker delta property, allowing for an easier application of essential boundary conditions, when compared to other meshfree strategies. But they may present discontinuity in the shape functions, when moving from one set of support nodes to another. Seeking to overcome this problem, the strain smoothing technique is adopted, making the formulation independent on the derivatives of the shape functions. The domain is divided into regions called smoothing domains, that, in plane models, can be based on cells (cell-based), edges (edge-based) or nodes (node-based). In each domain, the integrals of the strain measures are recasted in boundary integrals, using the Green's theorem, reducing the order of continuity required for the shape functions. When the smoothed gradient is adopted, the standard weak form for a boundary value problem in classic media can be recasted as a weakened-weak form where the domain integral is a summation over each smoothing. Despite the advantages of meshfree methods, they can lead to a high computational cost due to the calculations for the construction of the shape functions.

Knowing the advantages and disadvantages of the FEM and meshfree methods, many studies adopted a coupling between the methods. The meshfree methods is considered only in the interest region and in the rest of the domain the FEM is used. This strategy decreases the computational cost and keeps the advantages of the shape functions of the meshfree methods. In these coupled models, special attention should be given to the

interface between the two methods because the compatibility of displacement must be satisfied. In methods that possess the Kronecker delta property, the coupling is performed directly.

1.2 Objective

In view of what has been presented, this thesis proposes to develop an efficient and accurate adaptive FEM-SPIM coupling for the discretisation of phase-field models. This strategy is applied to two-dimensional problems under quasi-static loadings. In the adaptive analysis, a criterion automatically detects the regions of the FEM domain that need further refinement. These regions must be replaced by meshfree method and a correct refinement level is applied. The coupling between FEM and SPIM methods can be performed directly due to the Kronecker delta property that the shape functions of SPIM possess.

In this work, SPIM meshfree method is proposed, for the first time, for the discretisation of phase-field models. For this application, the smoothing operation, which is used to calculate the derivative of the shape functions, is applied to the phase-field variable and the weakened-weak form is extended to the phase-field problem. The different phase field models, proposed in the literature, could be analysed. In SPIM, cell-, edge-, and node-based approaches for the domain tessellation are considered, together with different strategies for the selection of the support nodes at each integration point.

With this strategy we intend to reduce the computational cost of the analysis compared with a full SPIM model and keep the advantages of using the SPIM shape functions.

The computational system INSANE (*INteractive Structural ANalysis Environment*) (Fonseca and Pitangueira, 2007), a free software developed by the Department of Structural Engineering of the Federal University of Minas Gerais ¹, was used for the development of the thesis. This system has the implementation of the meshfree methods of the SPIM family. Furthermore, the system contains the implementation of phase-field models.

1.3 Outline

This thesis is divided in 8 chapters and 3 appendices.

Chapters 2 and 3 cover the theoretical background. Chapter 2 presents the theoretical foundation about the phase-field modelling and the Chapter 3 presents the formulation of the SPIM methods.

¹More information on the project can be found at <https://www.insane.dees.ufmg.br/>; the development code is freely available at the Git repository <http://git.insane.dees.ufmg.br/insane/insane.git>.

Chapters 4 and 5 present the review of the literature and new contributions. Chapter 4 presents the use of meshfree methods for the discretisation of phase-field models. A review of the literature is shown and the formulation of the SPIM for phase-field modelling is present for the first time. In Chapter 5, adaptive mesh refinement strategies and coupled models are discussed. Here, the novel strategy for adaptive coupled FEM-SPIM for phase-field modelling is presented.

In chapters 6 and 7, the new contributions are analysed through numerical simulations. In Chapter 6, the numerical simulations using SPIM for discretisation of the phase-field models are shown. The meshes are refined in the known region of crack propagation. Domains considering fully SPIM and fixed SPIM-FEM coupling are analysed. Chapter 7 presents the numerical simulations considering the adaptive strategy proposed in this work. The influence of each parameter of the adaptive strategy is investigated separately.

In Chapter 8, the text of the thesis is concluded, analysing the main contributions of the work and presenting suggestions for the continuation of the research.

In the first Appendix A, a linear elastic problem is presented for the analysis of the proposed trigonometric radial function. In the Appendix B, the modifications realized in the software INSANE are presented. Finally, the Appendix C illustrates an example of input file for adaptive analysis.

Chapter 2

Phase-Field modelling of fracture

This chapter presents the theoretical foundation about the phase-field modelling. It starts with the variational approach for models with cracks, followed by the presentation of the phase-field modelling for cracks with the strong and weak formulations of the problem. The discretisation of the model using finite elements is shown, and finally the solvers of the problem are discussed.

2.1 Variational approach to fracture

Studies of phase-field models by the mechanics community began with Francfort and Marigo (1998), where the variational formulation for the Griffith's model was developed. Let's consider an isotropic elastic solid with small deformations and a internal crack set as shown in Fig. 2.1. The elastic body occupies a domain $\Omega \subset \mathbb{R}^n$ with external boundary $\partial\Omega = \partial\Omega_t \cup \partial\Omega_u$, where $\partial\Omega_t$ is the region where the loadings are applied, while $\partial\Omega_u$ is the region of prescribed displacements. The crack is represented by the set $\Gamma \subset \mathbb{R}^{n-1}$.

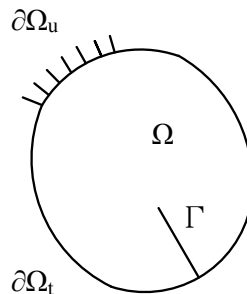


Figure 2.1: Elastic body with crack.

The total energy functional of the body is expressed by:

$$E_t = \Psi_s + \Psi_c - P_{ext} \quad (2.1)$$

where Ψ_s is the strain energy, Ψ_c is the crack surface energy and P_{ext} is the work of the external loads.

The strain energy of the body is given by

$$\Psi_s(\boldsymbol{\varepsilon}(\mathbf{u})) = \int_{\Omega \setminus \Gamma} \psi(\boldsymbol{\varepsilon}(\mathbf{u}), \Gamma) dV \quad (2.2)$$

where ψ is the energy density, $\boldsymbol{\varepsilon}$ is the strain tensor and \mathbf{u} is the displacement vector. The variation of the strain energy is

$$\frac{\partial \Psi_s}{\partial \boldsymbol{\varepsilon}} : \delta \boldsymbol{\varepsilon} = \int_{\Omega \setminus \Gamma} \frac{\partial \psi}{\partial \boldsymbol{\varepsilon}} : \delta \boldsymbol{\varepsilon} dV = \int_{\Omega \setminus \Gamma} \boldsymbol{\sigma} : \boldsymbol{\varepsilon}(\delta \mathbf{u}) dV \quad (2.3)$$

where $\boldsymbol{\sigma}$ is the stress tensor and it is, by definition, obtained by taking the strain energy derivative with respect to the strain tensor.

For isotropic materials, the elastic energy density is given by Hooke's law as

$$\psi_s(\boldsymbol{\varepsilon}(\mathbf{u})) = \frac{\lambda}{2} (\text{tr}(\boldsymbol{\varepsilon}))^2 + \mu \text{tr}(\boldsymbol{\varepsilon}^2) \quad (2.4)$$

where λ and μ are the Lamé's constants.

The crack surface energy is given by

$$\Psi_c = \int_{\Gamma} G_c dA \quad (2.5)$$

where G_c is the Griffith's critical energy release rate, a material parameter.

The potential of the external loads of the body is expressed by

$$P_{ext} = \int_{\Omega} \mathbf{b} \cdot \mathbf{u} dV + \int_{\partial \Omega} \mathbf{t} \cdot \mathbf{u} dA \quad (2.6)$$

where \mathbf{b} are the body forces and \mathbf{t} are the surface forces.

The variational problem of crack propagation is based on the three following conditions:

- Irreversibility condition: The crack only grows as time goes on

$$\dot{\Gamma}(t) \geq 0 \quad (2.7)$$

- Unilateral stationary condition: The pair $(\mathbf{u}(t), \Gamma(t))$ is the stationary point of the energy functional $(E_t(\mathbf{u}, \Gamma))$. This condition indicates that there will always be an energy consumption

$$\delta E_t(\mathbf{u}, \Gamma) \geq 0 \quad (2.8)$$

- Energy conservation condition: The energy functional E_t has to satisfy the energy balance when the cracks grows in time

$$\dot{E}_t = \int_{\partial\Omega_u} (\boldsymbol{\sigma} \cdot \mathbf{n}) \cdot \dot{\mathbf{u}} dA - \int_{\Omega} \dot{\mathbf{b}} \cdot \mathbf{u} dV - \int_{\partial\Omega_t} \dot{\mathbf{t}} \cdot \mathbf{u} dA \quad (2.9)$$

Applying the unilateral stationary condition to the total energy functional Eq. 2.1, results in the equilibrium equation 2.10, in the boundary conditions 2.11 and 2.12, and the propagation of a crack is ruled by conditions 2.13:

$$\nabla \cdot \boldsymbol{\sigma} + \mathbf{b} = 0 \quad \text{in } \Omega \setminus \Gamma \quad (2.10)$$

$$\boldsymbol{\sigma} \cdot \mathbf{n} = \mathbf{t} \quad \text{in } \partial\Omega_t \quad (2.11)$$

$$\boldsymbol{\sigma} \cdot \mathbf{n} = 0 \quad \text{in } \Gamma \quad (2.12)$$

$$\dot{\Gamma} \geq 0, \quad \mathcal{G} - G_c \leq 0, \quad (\mathcal{G} - G_c) \dot{\Gamma} = 0 \quad (2.13)$$

where \mathcal{G} is defined as $\mathcal{G} = -\frac{\partial \Psi_s}{\partial \Gamma}$.

2.2 The phase-field modelling for diffuse cracks

Bourdin et al. (2000) proposed the use of a scalar parameter to regularize the geometry of the discrete crack in a diffuse form. The crack is represented by a discontinuous function $\phi(x) \in [0, 1]$ with $\phi = 1$ in Γ and $\phi = 0$ in the region of intact material, as shown in Fig. 2.2 for 1D problem.

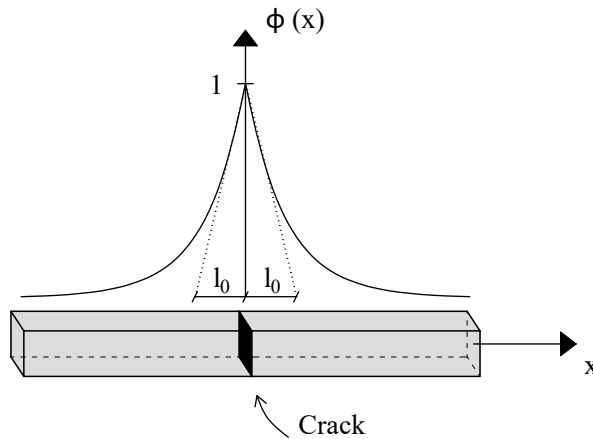


Figure 2.2: Geometric representation of the crack for the phase-field modelling.

Can be observed, a parameter l_0 governs the width of the diffuse region. Thus, the discontinuity problem becomes a continuous problem and when the parameter l_0 tends to zero, the crack approximate of a discrete crack.

For the application of phase-field functions it is assumed that the damage region is part of the domain $\mathcal{B} \subseteq \Omega$ with boundary $\partial\mathcal{B}$. This region \mathcal{B} is called localisation band. The crack surface energy can be expressed in terms of the phase-field variable, as

$$\Psi_c := \int_{\Gamma} G_c dA \approx \int_{\mathcal{B}} G_c \gamma(\phi, \nabla\phi) dV \quad (2.14)$$

where γ is called crack surface density.

The previously defined strain energy now depends on the strain tensor and on the value of the phase-field:

$$\Psi_s(\mathbf{u}, \phi) = \int_{\Omega} \psi(\boldsymbol{\varepsilon}(\mathbf{u}), \phi) dV. \quad (2.15)$$

Applying the new formulation of strain energy and crack surface energy, the total energy functional becomes:

$$E_t = \int_{\Omega} \psi(\boldsymbol{\varepsilon}(\mathbf{u}), \phi) dV + \int_{\mathcal{B}} G_c \gamma(\phi, \nabla\phi) dV - \int_{\Omega} \mathbf{b} \cdot \mathbf{u} dV - \int_{\partial\Omega} \mathbf{t} \cdot \mathbf{u} dA. \quad (2.16)$$

The values of displacements and phase-field are found minimising the 2.16. Considering the first variation of the energy functional, we have:

$$\delta E_t = \int_{\Omega} \boldsymbol{\sigma} \delta \boldsymbol{\varepsilon} dV + \int_{\mathcal{B}} \frac{\partial \psi}{\partial \phi} \delta \phi dV + \int_{\mathcal{B}} G_c \left(\frac{\partial \gamma}{\partial \phi} \delta \phi + \frac{\partial \gamma}{\partial \nabla \phi} \cdot \delta \nabla \phi \right) dV - \int_{\Omega} \mathbf{b} \cdot \delta \mathbf{u} dV - \int_{\partial\Omega_t} \mathbf{t} \cdot \delta \mathbf{u} dA. \quad (2.17)$$

The application of the divergence theorem yields

$$\delta E_t = \int_{\Omega} (\nabla \cdot \boldsymbol{\sigma} + \mathbf{b}) \cdot \delta \mathbf{u} dV + \int_{\partial\Omega_t} (\boldsymbol{\sigma} \cdot \mathbf{n} - \mathbf{t}) \cdot \delta \mathbf{u} dA + \int_{\mathcal{B}} \left(\frac{\partial \psi}{\partial \phi} + G_c \delta_{\phi} \gamma \right) \delta \phi dV + \int_{\partial\mathcal{B}} G_c \left(\frac{\partial \gamma}{\partial \nabla \phi} \cdot \mathbf{n}_{\mathcal{B}} \right) dA \quad (2.18)$$

where $\delta_{\phi} \gamma := \frac{\partial \gamma}{\partial \phi} - \nabla \cdot \left(\frac{\partial \gamma}{\partial \nabla \phi} \right)$ and $\mathbf{n}_{\mathcal{B}}$ is the outward unit normal vector of the boundary $\partial\mathcal{B}$ of the localisation band.

Due to the unilateral stationary condition, $\delta E_t = 0$ for $\delta \phi > 0$ and $\delta E_t > 0$ for $\delta \phi = 0$. The boundary conditions are

$$\nabla \cdot \boldsymbol{\sigma} + \mathbf{b} = 0 \quad \text{in } \Omega \quad (2.19a)$$

$$\boldsymbol{\sigma} \cdot \mathbf{n} = \mathbf{t} \quad \text{in } \partial\Omega_t \quad (2.19b)$$

thus, Eq. 2.18 become:

$$Y - G_c \delta_\phi \gamma = 0, \quad \text{for } \dot{\phi} > 0 \quad (2.20a)$$

$$Y - G_c \delta_\phi \gamma < 0, \quad \text{for } \dot{\phi} = 0 \quad (2.20b)$$

defining the crack driving force $Y = -\frac{\partial \psi}{\partial \phi}$ and $\frac{\partial \gamma}{\partial \nabla \phi} \cdot \mathbf{n} = 0$ in the boundary $\partial \mathcal{B}$.

The strain energy is related to the value of phase-field through an energy degradation function, defined as $g(\phi)$. The characteristics of this function will be presented in section 2.4. Thus, performing the chain rule in the crack driving force equation, we obtain:

$$Y = -\frac{\partial \psi}{\partial \phi} = -\frac{\partial \psi}{\partial g} \cdot \frac{\partial g}{\partial \phi} \quad (2.21)$$

$\bar{Y} = \frac{\partial \psi}{\partial g}$ is defined as the effective crack driving force

$$Y = -g'(\phi) \bar{Y}. \quad (2.22)$$

As it has already been discussed, the irreversibility of the crack must be guaranteed. This condition is defined as:

$$\dot{\Gamma}_l := \frac{d}{dt} \Gamma_l(\phi) \geq 0 \quad (2.23)$$

as the crack surface is defined from the crack density function:

$$\dot{\Gamma}_l = \int_{\mathcal{B}} \dot{\gamma} dV = \int_{\mathcal{B}} \dot{\phi} \delta_\phi \gamma dV. \quad (2.24)$$

This condition is defined as the global irreversibility of the crack, and it is met provided that:

$$\delta_\phi \gamma \geq 0 \quad (2.25)$$

$$\dot{\phi} \geq 0. \quad (2.26)$$

The phase-field equations can be rewritten as Karush-Kuhn-Tucker conditions

$$\dot{\phi} \geq 0, \quad f(Y, \phi) \leq 0, \quad \dot{\phi} f(Y, \phi) \equiv 0 \quad (2.27)$$

where $f(Y, \phi)$ is defined as:

$$f(Y, \phi) := Y - G_c \delta_\phi \gamma \leq 0. \quad (2.28)$$

The crack phase-field is zero for $Y/G_c = 0$. Wu et al. (2020) indicate that high value to G_c can be used to avoid cracks near of the supports or point loads. Furthermore, the

strategy of applying $\phi(x) = 0$ to the selected nodes can be used.

2.3 Geometric crack function

The crack surface density function $\gamma(\phi, \nabla\phi)$, that define the topology of the crack, can be represented by different functions for brittle and quasi-brittle fracture. Wu (2017) proposed a generalization to the crack surface density function as:

$$\gamma(\phi, \nabla\phi) = \frac{1}{c_0} \left[\frac{1}{l_0} \alpha(\phi) + l_0 |\nabla\phi|^2 \right] \quad (2.29)$$

$$\delta_\phi \gamma = \frac{1}{c_0} \left[\frac{1}{l_0} \alpha'(\phi) - 2l_0 \Delta\phi \right] \quad (2.30)$$

where $\alpha(\phi)$ is called geometric crack function and $c_0 := 4 \int_0^1 \alpha^{\frac{1}{2}}(\hat{\phi}) d\hat{\phi}$.

The geometric crack function must take on values between zero and one and satisfy property of $\alpha(0) = 0$ and $\alpha(1) = 1$ (Wu et al., 2020). Wu (2017) proposed a general formulation for this function

$$\alpha(\phi) = \xi\phi + (1 - \xi)\phi^2 \in [0, 1] \quad \forall \phi \in [0, 1] \quad (2.31)$$

where the parameter $\xi \in [0, 2]$.

Table 2.1: Generic geometric crack function.

$\alpha(\phi)$	ξ	c_0	$\phi(x)$
ϕ^2	0	2	$\exp\left(-\frac{ x }{l_0}\right)$
ϕ	1	8/3	$\left(-\frac{ x }{2l_0}\right)^2$
$2\phi - \phi^2$	2	ϕ	$1 - \sin\left(\frac{ x }{l_0}\right)$

By adopting $\xi = 0$, the geometric crack function results in the classical formulation for brittle fracture $\alpha = \phi^2$. For quasi-brittle fracture the geometric crack function $\alpha = 2\phi - \phi^2$ with $\xi = 2$ is usually adopted (Wu, 2017).

2.4 Energetic degradation function

The strain energy is related to the value of the phase-field variable through the energy degradation function. This function guarantees a smooth transition between the intact material and the broken material and it must satisfy some conditions:

- $g(\phi) : [0, 1] \rightarrow [1, 0]$;

- $g(0) = 1$ (intact material) and $g(1) = 0$ (broken material);
- $g'(\phi) = dg/d\phi < 0$, $g(\phi)$ is a monotonically decreasing function;
- $g'(1) = 0$.

A collection of functions presented by different authors is shown in Table 2.2. All functions have polynomial character to guarantee the properties shown above. Furthermore, it is usual to add a very small numerical parameter k to guarantee the good conditioning of the system of equations when the value of phase-field approaches 1.

Table 2.2: Energetic degradation functions $g(\phi)$.

$g(\phi)$	Authors
$(1 - \phi)^2$	Bourdin et al. (2000)
$3(1 - \phi)^2 - 2(1 - \phi)^3$	Karma et al. (2001)
$4(1 - \phi)^3 - 3(1 - \phi)^4$	Kuhn et al. (2015)
$\frac{(1 - \phi)^p}{(1 - \phi)^p + Q(\phi)}$, $Q(\phi) = a_1\phi + a_1a_2\phi^2 + a_1a_2a_3\phi^3$	Wu (2017)

Figures 2.3 and 2.4 illustrate the curves for the functions and their first derivatives, respectively.

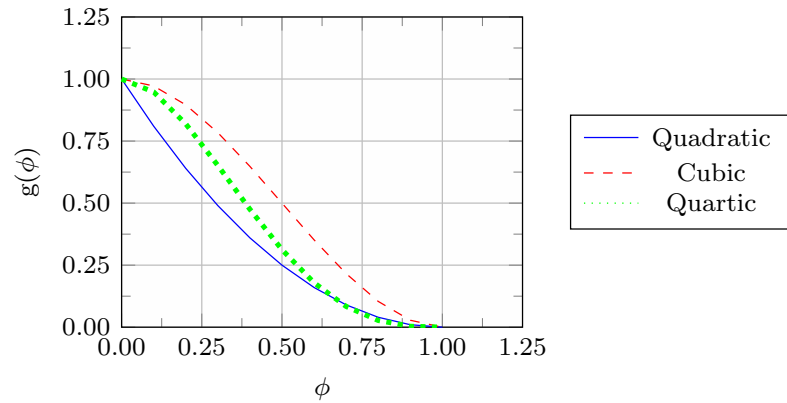


Figure 2.3: Energetic degradation function.

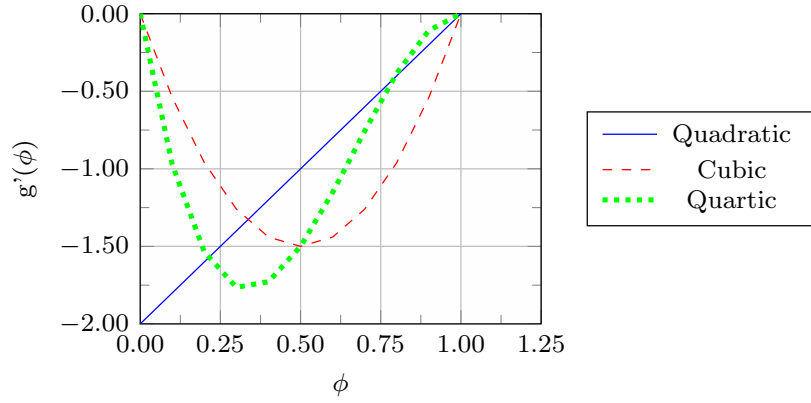


Figure 2.4: First derivatives of the energetic degradation function.

Wu (2017) proposed the calibration of the coefficients a_i from standard material properties. In addition to Young's modulus and fracture energy properties, these coefficients consider the strength tensile (f_t). The coefficients are determined from Eq. 2.32:

$$a_1 = \frac{2E_0G_f}{f_t^2} \cdot \frac{\xi}{C_0l_0} \quad (2.32a)$$

$$a_2 = \frac{1}{\xi} \left[\left(-\frac{4\pi\xi G_f}{C_0f_t} k_0 \right)^{\frac{2}{3}} + 1 \right] - (p+1) \quad (2.32b)$$

$$a_3 = \begin{cases} 0 & p > 2 \\ \frac{1}{2} \left[\frac{1}{\xi} \left(\frac{c_0w_c f_t}{2\pi G_f} \right)^2 - (1 + a_2) \right] & p = 2 \end{cases} \quad (2.32c)$$

where ξ is the same parameter adopted in the geometric crack function, k_0 is the initial slope of the softening law and w_c is the ultimate crack opening.

2.4.1 General softening laws

Softening laws are used to determine the k_0 and w_c parameters. Wu (2017) presented different softening laws adopted for quasi-brittle fracture. These laws described the behavior of the stress-strain curve in the fracture process. Thus, the parameters a_i are calibrated for each law.

- Linear softening:

$$\sigma(w) = f_t \max \left(1 - \frac{f_t}{2G_c} w, 0 \right), \quad k_0 = -\frac{f_t^2}{2G_f}, \quad w_c = \frac{2G_f}{f_t} \quad (2.33)$$

For $\xi = 2$ and $p = 2$:

$$a_2 = -\frac{1}{2}, \quad a_3 = 0 \quad (2.34)$$

- Exponential softening:

$$\sigma(w) = f_t \exp\left(-\frac{f_t}{G_c} w\right), \quad k_0 = -\frac{f_t^2}{G_f}, \quad w_c = +\infty \quad (2.35)$$

For $\xi = 2$ and $p = 5/2$:

$$a_2 = 2^{\frac{5}{3}} - 3, \quad a_3 = 0 \quad (2.36)$$

- Hyperbolic softening:

$$\sigma(w) = f_t \left(1 + \frac{f_t}{G_c} w\right)^{-2}, \quad k_0 = -\frac{2f_t^2}{G_f}, \quad w_c = +\infty \quad (2.37)$$

For $\xi = 2$ and $p = 4$:

$$a_2 = 2^{\frac{7}{3}} - \frac{9}{2}, \quad a_3 = 0 \quad (2.38)$$

- Cornelissen's softening:

$$\begin{aligned} \sigma(w) &= f_t \left[(1 + \eta_1^3 r^3) \exp(-\eta_2 r) - r(1 + \eta_1^3) \exp(-\eta_2) \right], \\ k_0 &= -1.3546 \frac{f_t^2}{G_f}, \quad w_c = 5.1361 \frac{G_f}{f_t} \end{aligned} \quad (2.39a)$$

For $\xi = 2$ and $p = 2$:

$$a_2 = 1.3868, \quad a_3 = 0.6567 \quad (2.40)$$

2.5 Strain energy models

Regarding the strain energy, phase-field models can be divided into two distinct categories, isotropic model and anisotropic models. In the isotropic model the energy degradation function is applied at all strain energy. Thus, the energy density function can be expressed as:

$$\psi(\varepsilon, \phi) = g(\phi) \psi_0(\varepsilon) \quad (2.41)$$

The stress field is given by:

$$\boldsymbol{\sigma} = \frac{\partial \psi}{\partial \boldsymbol{\varepsilon}} = g(\phi) \bar{\boldsymbol{\sigma}} \quad (2.42)$$

where

$$\bar{\sigma} = \frac{\partial \psi_0}{\partial \boldsymbol{\varepsilon}} = E_0 : \boldsymbol{\varepsilon} \quad (2.43)$$

and the phase-field evolution law

$$G_c \delta_\phi \gamma = -g'(\phi) \bar{Y} \quad (2.44)$$

$$\bar{Y} = \frac{\partial \psi}{\partial g} = \psi_0(\boldsymbol{\varepsilon}). \quad (2.45)$$

In order to predict cracks in the compression region of the model, the strain energy must be divided into tensile regions and compression regions. Models that make this division are called anisotropic models. For such models, the energy degradation function is applied only to the positive portion associated with traction.

$$\psi_0(\boldsymbol{\varepsilon}) = \psi_0^+(\boldsymbol{\varepsilon}) + \psi_0^-(\boldsymbol{\varepsilon}) \quad (2.46)$$

$$\psi_0(\boldsymbol{\varepsilon}, \phi) = g(\phi) \psi_0^+(\boldsymbol{\varepsilon}) + \psi_0^-(\boldsymbol{\varepsilon}) \quad (2.47)$$

Using such a decomposition, the stress field becomes

$$\boldsymbol{\sigma} := \frac{\partial \psi}{\partial \boldsymbol{\varepsilon}} = g(\phi) \frac{\partial \psi_0^+}{\partial \boldsymbol{\varepsilon}} + \frac{\partial \psi_0^-}{\partial \boldsymbol{\varepsilon}} \quad (2.48)$$

and the evolution phase-field law becomes:

$$Y = G_c \delta_\phi \gamma = -g'(\phi) \bar{Y} \quad (2.49)$$

$$\bar{Y} = \frac{\partial \psi}{\partial g} = \psi_0^+(\boldsymbol{\varepsilon}). \quad (2.50)$$

Following are presented different anisotropic energetic models and their equations.

2.5.1 Anisotropic model of Lancioni and Royer-Carfagni (2009)

In this model, the authors propose a division of energy based on the deviatoric ($\boldsymbol{\varepsilon}_D$) and spherical ($\boldsymbol{\varepsilon}_V$) parts of the strain tensor. Thus, the strain tensor is decomposed into:

$$\boldsymbol{\varepsilon} = \boldsymbol{\varepsilon}_D + \boldsymbol{\varepsilon}_V \quad (2.51)$$

where

$$\boldsymbol{\varepsilon}_V = \frac{1}{3} \text{tr}(\boldsymbol{\varepsilon}) \mathbf{I} \quad (2.52)$$

$$\boldsymbol{\varepsilon}_D = \boldsymbol{\varepsilon} - \frac{1}{3}tr(\boldsymbol{\varepsilon})\mathbf{I}. \quad (2.53)$$

The degradation affects only the deviatoric part. The positive and negative parts of the energy are written as:

$$\psi_0^+(\boldsymbol{\varepsilon}) = \mu_0 \boldsymbol{\varepsilon}_D : \boldsymbol{\varepsilon}_D \quad (2.54)$$

$$\psi_0^-(\boldsymbol{\varepsilon}) = \frac{1}{2}K_0 tr^2(\boldsymbol{\varepsilon}) \quad (2.55)$$

where $K_0 = \lambda_0 + 2\mu_0/3$. The stress field becomes:

$$\boldsymbol{\sigma} = g(\phi)2\mu_0\boldsymbol{\varepsilon}_D + K_0tr(\boldsymbol{\varepsilon})\mathbf{I}. \quad (2.56)$$

2.5.2 Anisotropic model of Amor et al. (2009)

In this model, the authors proposed a new division of the energy and the stress field:

$$\psi_0^+(\boldsymbol{\varepsilon}) = \frac{1}{2}K_0\langle tr(\boldsymbol{\varepsilon}) \rangle^2 + \mu_0\boldsymbol{\varepsilon}_D : \boldsymbol{\varepsilon}_D \quad (2.57)$$

$$\psi_0^-(\boldsymbol{\varepsilon}) = \frac{1}{2}K_0\langle -tr(\boldsymbol{\varepsilon}) \rangle^2 \quad (2.58)$$

$$\boldsymbol{\sigma} = g(\phi)[K_0\langle tr(\boldsymbol{\varepsilon}) \rangle\mathbf{I} + 2\mu_0\boldsymbol{\varepsilon}_D] - K_0\langle -tr(\boldsymbol{\varepsilon}) \rangle\mathbf{I} \quad (2.59)$$

where $\langle a \rangle := \max\{a, 0\}$.

According to Wu et al. (2020), this model is able to limit partially the creation of cracks in compressed regions.

2.5.3 Anisotropic model of Miehe, Welschinger and Hofacker (2010)

Unlike the previous models, the spectral decomposition of the strain tensor is considered

$$\boldsymbol{\varepsilon} = \sum_{n=1}^3 \varepsilon_n \mathbf{p}_n \otimes \mathbf{p}_n = \boldsymbol{\varepsilon}^+ + \boldsymbol{\varepsilon}^- \quad (2.60)$$

where:

$$\boldsymbol{\varepsilon}^+ := \sum_{n=1}^3 \langle \varepsilon_n \rangle_+ \mathbf{p}_n \otimes \mathbf{p}_n \quad (2.61)$$

$$\boldsymbol{\varepsilon}^- := \sum_{n=1}^3 \langle \varepsilon_n \rangle_- \mathbf{p}_n \otimes \mathbf{p}_n \quad (2.62)$$

and where ε_n and \mathbf{p}_n are the principal strains and principal strain directions of $\boldsymbol{\varepsilon}$. The positive and negative parts of the initial strain energy are given by:

$$\psi_0^\pm(\boldsymbol{\varepsilon}) := \frac{1}{2} \lambda_0 [\langle \text{tr}(\boldsymbol{\varepsilon}) \rangle_\pm]^2 + \mu_0 \boldsymbol{\varepsilon}^\pm : \boldsymbol{\varepsilon}^\pm. \quad (2.63)$$

The stress field is given by:

$$\boldsymbol{\sigma} = g(\phi) [\lambda_0 \langle \text{tr}(\boldsymbol{\varepsilon}) \rangle_+ \mathbf{I} + 2\mu_0 \boldsymbol{\varepsilon}^+] + \lambda_0 \langle \text{tr}(\boldsymbol{\varepsilon}) \rangle_- \mathbf{I} + 2\mu_0 \boldsymbol{\varepsilon}^-. \quad (2.64)$$

The constitutive tensor can be obtained by expressing the positive and negative parts of the strains in terms of the strain tensor:

$$\boldsymbol{\varepsilon}^+ := \mathbf{P}^+ : \boldsymbol{\varepsilon}, \quad \boldsymbol{\varepsilon}^- := \mathbf{P}^- : \boldsymbol{\varepsilon} \quad (2.65)$$

using the fourth-order projection tensors \mathbf{P}^+ and \mathbf{P}^- , expressed by

$$\mathbf{P}^+ = \sum_{n=1}^3 \frac{1}{2} (\text{sign}(\varepsilon_n) + 1) \mathbf{p}_n \otimes \mathbf{p}_n \otimes \mathbf{p}_n \otimes \mathbf{p}_n, \quad \mathbf{P}^- = \mathbf{I} - \mathbf{P}^+ \quad (2.66)$$

Similarly, $\langle \text{tr}(\boldsymbol{\varepsilon}) \rangle_\pm$ can be recasted as

$$\langle \text{tr}(\boldsymbol{\varepsilon}) \rangle_+ = R_n^+ \text{tr}(\boldsymbol{\varepsilon}), \quad \langle \text{tr}(\boldsymbol{\varepsilon}) \rangle_- = R_n^- \text{tr}(\boldsymbol{\varepsilon}) \quad (2.67)$$

where:

$$R_n^+ = \frac{1}{2} (\text{sign}(\text{tr}(\boldsymbol{\varepsilon})) + 1), \quad R_n^- = \frac{1}{2} (\text{sign}(-\text{tr}(\boldsymbol{\varepsilon})) + 1) \quad (2.68)$$

Replacing Eqs. 2.65 and 2.67 into Eq. 2.64, results in the following expression of the stress tensor:

$$\boldsymbol{\sigma} = g(\phi) [\lambda_0 R_n^+ \text{tr}(\boldsymbol{\varepsilon}) \mathbf{I} + 2\mu_0 \mathbf{P}^+ : \boldsymbol{\varepsilon}] + \lambda_0 R_n^- \text{tr}(\boldsymbol{\varepsilon}) \mathbf{I} + 2\mu_0 \mathbf{P}^- : \boldsymbol{\varepsilon} \quad (2.69)$$

Results presented in the literature indicate that this model completely limits the creation of cracks in the compression region.

2.5.4 Hybrid formulations

In all anisotropic models presented, the stress field $\boldsymbol{\sigma}$ and the evolution law of the phase-field are obtained from a single energy functional. In this case, the sub-problem of displacement is nonlinear due to the split of the strain tensor in tension/compression parts. This nonlinear equation increases the computational cost. An alternative for this issue is

the use of hybrid models. In such models, the stress field and the phase-field correspond to distinct energy functions. The sub-problem of displacements is now a linear problem.

$$\boldsymbol{\sigma} := \frac{\partial \psi}{\partial \boldsymbol{\varepsilon}} = g(\phi) \bar{\boldsymbol{\sigma}} \quad \text{with} \quad \bar{\boldsymbol{\sigma}} = \frac{\partial \psi_0}{\partial \boldsymbol{\varepsilon}} = E_0 : \boldsymbol{\varepsilon} \quad (2.70)$$

$$Y := -\frac{\partial \bar{\psi}}{\partial \phi} = -g'(\phi) \bar{Y} \quad \text{with} \quad \bar{Y} = \frac{\partial \bar{\psi}}{\partial g} = \bar{\psi}_0(\boldsymbol{\varepsilon}) \quad (2.71)$$

In Wu (2017), the authors proposed:

$$\bar{\psi}_0(\boldsymbol{\varepsilon}) = \frac{1}{2E_0} \bar{\sigma}_{eq}^2 \quad (2.72)$$

where $\bar{\sigma}_{eq}$ is the equivalent effective stress defined as

$$\bar{\sigma}_{eq} = \frac{1}{1 + \beta_c} \left(\beta_c \langle \bar{\sigma}_1 \rangle + \sqrt{3\bar{J}_2} \right) \quad (2.73)$$

where $\beta_c := \frac{f_c}{f_t} - 1$ related to the ratio of the uniaxial compressive strength f_c and the uniaxial tensile strength f_t , $\bar{\sigma}_1$ denotes the largest principal value of the effective stress and \bar{J}_2 is the second invariant of the deviatoric effective stress tensor.

In Wu (2018b), the authors proposed:

$$\bar{\psi}_0(\boldsymbol{\varepsilon}) = \frac{1}{2E_0} \langle \bar{\sigma}_1 \rangle^2 \quad (2.74)$$

where $\bar{\sigma}_1$ is the first major principle value of the effective stress. This formulation differ of the Wu (2017) because the deviatoric effective stress tensor are neglected.

2.6 Phase-field equations in the weak form

Eqs. 2.19 and 2.20 obtained for the phase-field problem in the strong form can be rewritten in the weak form as

$$\begin{cases} \int_{\Omega} \boldsymbol{\sigma} : \delta \boldsymbol{\varepsilon} dV = \delta P_{ext} \\ \int_{\mathcal{B}} [g'(\phi) \bar{Y} \delta \phi + G_c \delta \gamma] dV \geq 0 \end{cases} \quad (2.75)$$

where variation of the generic crack surface density function is expressed as:

$$\delta \gamma = \frac{1}{C_0} \left[\frac{1}{l_0} \alpha'(\phi) \delta \phi + 2l_0 \nabla \phi \cdot \nabla \delta \phi \right]. \quad (2.76)$$

In the equations system 2.75, the second equation refers to the variational inequality on the damage field and boundary condition $\phi(x) \in [0, 1]$ and irreversibility condition $\dot{\phi}(x) \geq 0$ have to be dealt with carefully. To guarantee the condition of irreversibility some strategies can be used.

In Miehe, Welschinger and Hofacker (2010), the authors adopted the effective driving force \bar{Y} as a historical variable $H(\mathbf{x}, t)$:

$$\bar{Y} = H(\mathbf{x}, t) = \max \psi_0^+(\boldsymbol{\varepsilon}(\mathbf{x}, t')) \quad (2.77)$$

Although this strategy is widely used, it does not guarantee that the boundary condition $\phi(\mathbf{x}) \in [0, 1]$ is met everywhere. To guarantee this condition, the geometric function of the crack must be $\alpha(\phi) = \phi^2$.

Another strategy to ensure irreversibility was presented by Amor et al. (2009), where the condition is applied directly to a bound-constrained optimisation problem. To solve this problem, the so-called primal-dual active set strategy presented in Heister et al. (2015) is used. More details about these two strategies will be presented in Section 2.8.

2.7 FEM discretisation

Considering a bi-dimensional problem, each node of the model has the displacements x and y , and the phase-field variable.

As previously presented, there is a length l_0 that defines the width of the degraded region. For the case of the finite element model, to guarantee the accuracy of the solution, it is necessary that the size of the elements h be smaller than l_0 . Several works present a relationship between these two lengths. For the case of the brittle fracture model, Miehe, Welschinger and Hofacker (2010) indicates the following relationship $h \leq l_0/2$. As for the quasi brittle fracture model, Wu (2017) indicates $h \leq l_0/5$.

The displacement field \mathbf{u} and the strain field $\boldsymbol{\varepsilon}$ in a point of the domain (\mathbf{x}) can be approximated by the nodal displacements \mathbf{d}_I .

$$\mathbf{u}(\mathbf{x}) = \sum_I \mathbf{N}_I^u(\mathbf{x}) \mathbf{d}_I \quad (2.78)$$

$$\boldsymbol{\varepsilon}(\mathbf{x}) = \sum_I \mathbf{B}_I^u(\mathbf{x}) \mathbf{d}_I \quad (2.79)$$

where the interpolation matrix \mathbf{N}^u and the strain-displacement matrix \mathbf{B}^u are given by:

$$\mathbf{N}_I^u(\mathbf{x}) = \begin{bmatrix} N_I^u(\mathbf{x}) & 0 \\ 0 & N_I^u(\mathbf{x}) \end{bmatrix} \quad (2.80)$$

$$\mathbf{B}_I^u(\mathbf{x}) = \begin{bmatrix} N_{I,x}^u & 0 \\ 0 & N_{I,y}^u \\ N_{I,y}^u & N_{I,x}^u \end{bmatrix}. \quad (2.81)$$

Similar to the displacements, the value of phase-field and its derivative in a point of

the domain (\mathbf{x}) are interpolated by the phase-field values a_I in the nodes.

$$\phi(\mathbf{x}) = \sum_I \mathbf{N}_I^\phi(\mathbf{x}) a_I \quad (2.82)$$

$$\nabla\phi(\mathbf{x}) = \sum_I \mathbf{B}_I^\phi(\mathbf{x}) a_I \quad (2.83)$$

where the interpolation matrix \mathbf{N}^ϕ and \mathbf{B}^ϕ are given by:

$$\mathbf{N}^\phi(\mathbf{x}) = N_I^\phi(\mathbf{x}) \quad (2.84)$$

$$\mathbf{B}^\phi(\mathbf{x}) = \begin{bmatrix} N_I^\phi, x \\ N_I^\phi, y \end{bmatrix}. \quad (2.85)$$

Based on these definitions, the weak form equations 2.75 can be written as:

$$\int_{\Omega} (\mathbf{B}^u)^T \boldsymbol{\sigma} dV = f_{ext} \quad (2.86)$$

$$\int_{\mathcal{B}} g' \bar{Y} (\mathbf{N}^\phi)^T dV + \int_{\mathcal{B}} \frac{G_c}{C_0} \left(\frac{1}{l_0} \alpha' (\mathbf{N}^\phi)^T + 2l_0 (\mathbf{B}^\phi)^T \nabla\phi \right) dV \geq 0. \quad (2.87)$$

The residual form of the equation is:

$$\mathbf{r}^u := \int_{\Omega} (\mathbf{B}^u)^T \boldsymbol{\sigma} dV - f_{ext} = 0 \quad (2.88)$$

$$\mathbf{r}^\phi := - \int_{\mathcal{B}} (\mathbf{N}^\phi)^T (g' \bar{Y} + \frac{1}{C_0 l_0} \alpha' G_c) dV - \int_{\mathcal{B}} \frac{2l_0}{C_0} G_c (\mathbf{B}^\phi)^T \nabla\phi dV \leq 0. \quad (2.89)$$

2.8 Solvers

The phase-field problem is given by a system composed of two equations, one referring to the displacements and the other to the phase-field. The nodal displacements are obtained from the displacement equation and the values of phase-field at nodes are obtained from the phase-field equation. The solvers of this system of equations are divided into two main categories: monolithic solver and staggered solver.

2.8.1 Monolithic solver

In the monolithic solver, the two equations of the system are solved together using the Newton Raphson method. Thus, at each iteration both displacements and phase-field at nodes are obtained.

The tangent stiffness matrix necessary for the solution of the problem can be divided into four parts that will be presented below:

$$\mathbf{K} = \begin{bmatrix} \mathbf{K}^{uu} & \mathbf{K}^{u\phi} \\ \mathbf{K}^{\phi u} & \mathbf{K}^{\phi\phi} \end{bmatrix} \quad (2.90)$$

where:

$$\mathbf{K}^{uu} = \int_{\Omega} (\mathbf{B}^u)^T \frac{\partial \boldsymbol{\sigma}}{\partial \boldsymbol{\varepsilon}} \mathbf{B}^u dV \quad (2.91)$$

$$\mathbf{K}^{u\phi} = \int_{\Omega} (\mathbf{B}^u)^T \frac{\partial \boldsymbol{\sigma}}{\partial \phi} \mathbf{N}^{\phi} dV \quad (2.92)$$

$$\mathbf{K}^{\phi u} = \int_{\mathcal{B}} (\mathbf{N}^{\phi})^T g' \frac{\partial \bar{Y}}{\partial \boldsymbol{\varepsilon}} \mathbf{B}^u dV \quad (2.93)$$

$$\mathbf{K}^{\phi\phi} = \int_{\mathcal{B}} (\mathbf{N}^{\phi})^T (g'' \bar{Y} + \frac{1}{C_0 l_0} \alpha'' G_c) \mathbf{N}^{\phi} dV + \int_{\mathcal{B}} \frac{2l_0}{C_0} G_c (\mathbf{B}^{\phi})^T \mathbf{B}^{\phi} dV. \quad (2.94)$$

For anisotropic models $\frac{\partial \boldsymbol{\sigma}}{\partial \boldsymbol{\varepsilon}}$ e $\frac{\partial \boldsymbol{\sigma}}{\partial \phi}$ are given by:

$$\frac{\partial \boldsymbol{\sigma}}{\partial \boldsymbol{\varepsilon}} = g(\phi) \frac{\partial^2 \psi_0^+}{\partial \boldsymbol{\varepsilon}^2} + \frac{\partial^2 \psi_0^-}{\partial \boldsymbol{\varepsilon}^2} \quad (2.95)$$

$$\frac{\partial \boldsymbol{\sigma}}{\partial \phi} = g'(\phi) \frac{\partial \psi_0^+}{\partial \boldsymbol{\varepsilon}} \quad (2.96)$$

Wu et al. (2020) indicate that the monolithic solver may present robustness problems since the energy functional may not be convex for both displacements and phase-field, and it is not possible to obtain a point of convergence.

2.8.2 Staggered solver

In this solver, first the displacement equation is solved, then the phase-field equation, or vice versa. This solution is carried out alternately until a point of convergence is reached for both equations.

The following is the staggered solver algorithm proposed in Wu et al. (2020). The first step of this algorithm is the solution of the displacement equation keeping the phase-field variable constant. The second step is the calculation of the phase-field, considering the already calculated nodal displacements constant. This process is carried out until the general convergence of the model is found. After that, the values of nodal displacement and nodal phase-field of the converged step are updated.

```

Data:  $d_n, a_n$ 
Result:  $d_{n+1}, a_{n+1}$ 
1 for Step  $n + 1$  do
2   Initialisation of the variables:  $(d_{n+1}^{(0)}, a_{n+1}^{(0)}) = (d_n, a_n), k = 1;$ 
3   while not converged do
4     1 - Compute de nodal displacements  $(d_{n+1}^{(k)})$  with fixed nodal crack
        phase-field of the previous iteration  $(a_{n+1}^{(k-1)})$ ;
5     2 - Compute phase-field variables  $a_{n+1}^{(k)}$  using the nodal displacements  $d_{n+1}^{(k)}$ 
        that have already been calculated ;
6     3 - Set iteration  $k = k + 1;$ 
7   end
8   Update the displacements and phase-field variables:  $(d_{n+1}, a_{n+1}) = (d_{n+1}^{(k)},$ 
         $a_{n+1}^{(k)});$ 
9 end

```

Figure 2.5: Staggered solver (Adapted of Wu et al. (2020)).

The anisotropic phase-field models, which decompose the strain energy into parts associated with positive and negative strains, lead to a system of nonlinear equations for the displacement problem. For the solution of this system it is necessary an iterative process like the Newton-Raphson.

Despite the great robustness of the alternate solver, it leads to a high computational cost, since it has a slow convergence rate, as indicated in Wu (2018b).

In relation to the phase-field equation, for the quasi brittle fracture the sub-problem of phase-field is nonlinear and it is necessary an iterative process for the solution. For the brittle fracture, with the energy degradation function $g(\phi) = (1 - \phi)^2$ and the geometric crack function $\alpha(\phi) = \phi^2$, the tangential stiffness matrix for the phase-field problem (Eq. 2.94) is linear in relation to phase-field variable.

As previously presented in the Section 2.6, for the solution of the phase-field problem is necessary to enforce the damage boundedness $\phi(\mathbf{x}) \in [0, 1]$ and the irreversibility condition $\dot{\phi} \geq 0$.

The first process is the use of the historical variable together with the crack geometric function $\alpha(\phi) = \phi^2$. In this case, the boundary condition $\phi(x) \in [0, 1]$ is guaranteed directly by α . This strategy is used for brittle fracture, where the functions $\alpha(\phi) = \phi^2$ and $g(\phi) = (1 - \phi)^2$ are adopted. For quasi-brittle fracture, where other degradation functions are adopted, it is not possible to use this strategy.

The second process is the use of a constrained optimization problem, where the constraints are the boundary conditions that must be met. By Farrell and Maurini (2017), the boundary conditions are:

$$\begin{cases} \bar{a}_{I,n} < \bar{a}_{I,n+1} < 1 & r_I^\phi = 0 \\ \bar{a}_{I,n+1} = \bar{a}_{I,n} & r_I^\phi \leq 0 \\ \bar{a}_{I,n} = 1 & r_I^\phi \geq 0 \end{cases} \quad (2.97)$$

To solve this problem, an appropriated solver is needed. In Wu et al. (2020), the authors use the reduced-space active set Newton method proposed by Benson and Munsun (2006). According to this method, nodes are divided into two sets: active and inactive nodes. Active nodes are the nodes that meet the boundary conditions and are not calculated in the current iteration, while inactive nodes are the nodes that will be calculated. By Wu et al. (2020), in each iteration

- The first step is determine the active nodes from the conditions ($\bar{a}_{I,n+1} = \bar{a}_{I,n}, r_I^\phi < 0$) or ($\bar{a}_{I,n+1} = 1, r_I^\phi > 0$).
- The Newton scheme is solved considering the inactive nodes.
- The solution is updated and projected onto the bounds (if ($\bar{a}_I > 1$ set ($\bar{a}_I = 1$)).
- The truncated residuals is computed to check for convergence, and the above process is repeated.

Chapter 3

Smoothed Point Interpolation Methods for linear elasticity

In this chapter, the formulation of the SPIM method is presented. First, the motivations that led to the proposition of meshfree methods and their general characteristics are introduced. Next, the construction of approximation functions of the type PIM and RPIMp is presented. Finally, the concept of smoothing domains and the gradient smoothing technique are presented.

3.1 The main concepts of the meshfree methods

Meshfree methods are a set of methods in which no predefined meshes of elements are needed for the solution of the system of differential equations. Unlike the finite element method, where shape functions are built based on elements, in meshfree methods, the shape functions, at a given point in the domain, are built from a cloud of nodes called *support nodes*. These functions can be diverse depending on the method, different from the FEM that adopts mainly polynomial functions.

As pointed out by Liu (2009), the standard FEM presents the following limitations:

- The need for a “quality” mesh, which makes it difficult to automate the mesh generation process;
- The need for mesh compatibility which results in a loss of freedom of construction of shape functions;
- Loss of accuracy of the solution in large deformations;
- Difficulty in simulating the growth of cracks or breaking the material into numerous fragments;
- Produces only a “lower bound” for the exact solution.

As most of the limitations presented are associated with rigidity in the use of elements, the use of meshfree methods guarantees the necessary flexibility by not using elements.

While in FEM the numerical integration process is normally based on Gaussian Quadrature, in meshfree methods, the integration can be based on cells. As such, meshfree methods cannot be said to be completely without the need for a mesh, however these base cells are considered more flexible than elements. According to Liu (2009), these cells can have different geometries depending on the method:

- Triangular and quadrilateral cells for Element-free Galerkin (EFG) (Belytscho et al., 1994);
- Node-based smoothed domains for the Node-Based Smoothed Point Interpolation Method (NS-PIM) (Liu et al., 2005);
- Edge-based smoothed domains for the Edge-Based Smoothed Point Interpolation Method (ES-PIM) (Liu and Zhang, 2008);
- Triangular cells or triangular subcells for the Cell-Based Smoothed Point Interpolation Method (CS-PIM) (Liu and Zhang, 2009).

As presented, in the meshfree methods the model is formed by a set of distributed nodes, this distribution being normally non-uniform. The set of support nodes, necessary for calculating the approximation functions, can be obtained from influence domains or T-schemes. An influence domain is defined as a domain over which the node exerts influence, being calculated from predefined functions, as shown in Fig. 3.1. These domains are normally obtained from a defined shape and size. For a given point of the domain, its set of support nodes is obtained by the nodes in which the influence domain contains the referred point. T-schemes are based on background cells, as illustrated in Fig. 3.2. For points located inside the cells, the T3 or T6/3 schemes can be adopted. In T3 schemes, 3 nodes of the triangular cell are selected. In T6/3 schemes, for points located in the boundary cells, the 3 nodes of the cell are selected and for points in the interior cells, 3 nodes of the cells and 3 nodes located in the boundary cells are selected. For points located in the boundary of the cell, the T4 scheme should be adopted. For edges of the interior, 4 nodes referring to the two cells of a common boundary are selected, and for edges of the boundary of the problem, 3 nodes are selected.

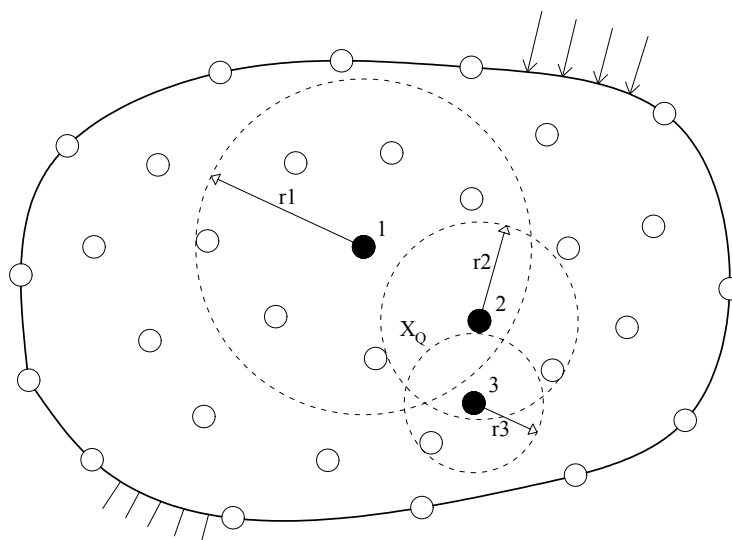


Figure 3.1: Influence domains for nodes selection (Adapted of Liu (2009)).

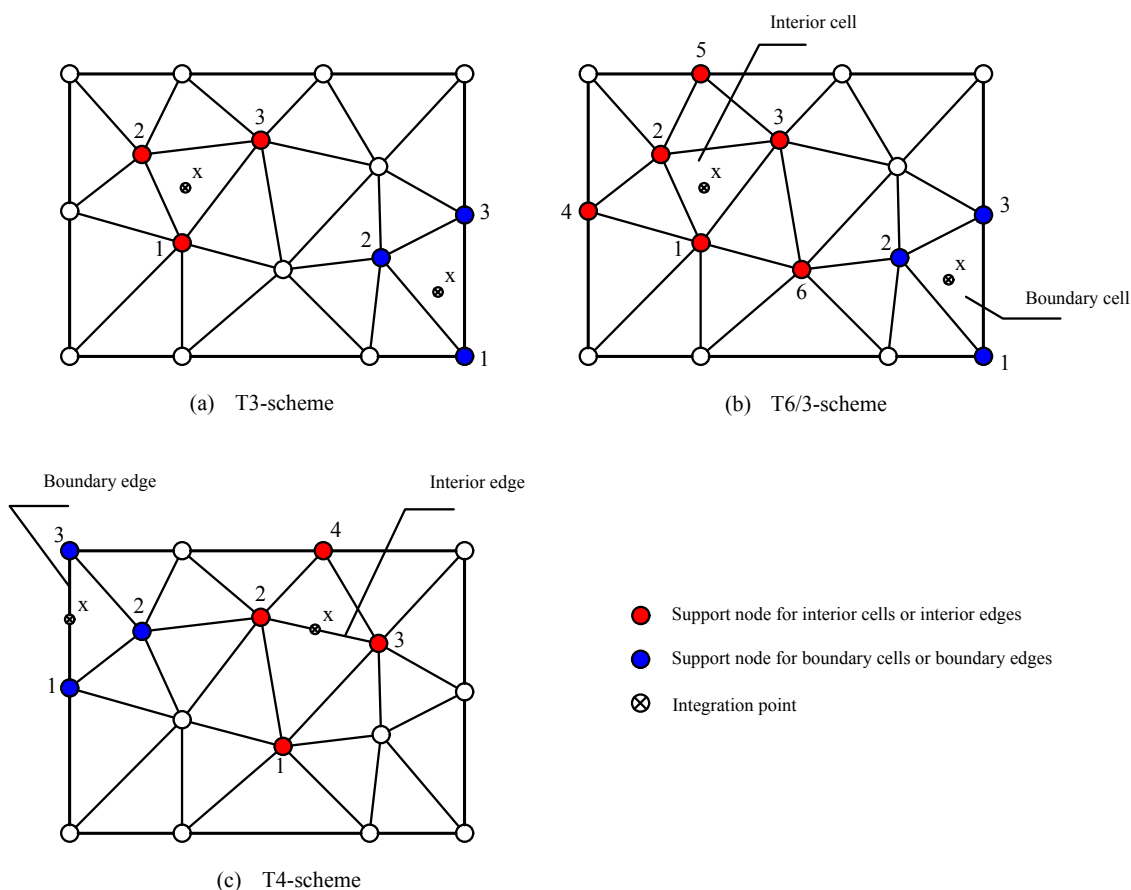


Figure 3.2: T-schemes for nodes selection.

According to Liu (2009), from the shape functions and using the weak or weakened-weak form, it is possible to formulate the discrete equations of the problem. These equations are usually assembled for the complete domain of the problem on a similar

way to FEM, the solution of these equations is performed for the nodal values and from them the internal variables are calculated.

3.2 Point Interpolation Method (PIM)

The PIM was originally proposed by Liu and Gu (2001). In this method, the approximation functions are obtained by a polynomial interpolation, where the field variables, such as the displacements, are interpolated by the nodal values of the support domain.

The approximation function in a point of the domain \mathbf{x} is given by:

$$u^h(\mathbf{x}) = \sum_{j=1}^n p_j(\mathbf{x})a_j \equiv \mathbf{p}^T(\mathbf{x})\mathbf{a} \quad (3.1)$$

where n is the number of support nodes, $p_j(\mathbf{x})$ are the monomials of the polynomial basis and a_j are the coefficients corresponding to the monomials.

The vector \mathbf{a} of the coefficients is:

$$\mathbf{a} = \{a_1, a_2, \dots, a_n\}^T \quad (3.2)$$

The vector \mathbf{p} contains the monomials of the polynomial basis. For 1D problems, this vector is given by

$$\mathbf{p}^T(x) = \{1, x, x^2, \dots, x^n\} \quad (3.3)$$

for 2D problems, this vector is given by

$$\mathbf{p}^T(x, y) = \{1, x, y, xy, x^2, y^2, \dots, x^n, y^n\}. \quad (3.4)$$

Imposing that the approximation functions must meet the nodal value at each node of the support domain, it is possible to find the value of the coefficients a_j . Thus, for each node j of the support domain we have:

$$u_j = \mathbf{p}^T(\mathbf{x}_j)\mathbf{a} \quad (3.5)$$

Rewriting in the compact form for all nodes:

$$\mathbf{d}_s = \mathbf{P}_Q\mathbf{a}. \quad (3.6)$$

\mathbf{d}_s is the vector of the nodal parameters of the field variable.

$$\mathbf{d}_s = \{u_1, u_2, \dots, u_n\} \quad (3.7)$$

The matrix \mathbf{P}_Q is defined as the *moment matrix* and it is composed by the monomials

evaluated at a support nodes:

$$\mathbf{P}_Q^T = \{\mathbf{p}(\mathbf{x}_1), \mathbf{p}(\mathbf{x}_2), \dots, \mathbf{p}(\mathbf{x}_n)\}. \quad (3.8)$$

Assuming that the moment matrix \mathbf{P}_Q is invertible, it is possible to obtain the matrix of coefficients \mathbf{a} as:

$$\mathbf{a} = \mathbf{P}_Q^{-1} \mathbf{d}_s \quad (3.9)$$

Replacing Eq. 3.9 in Eq. 3.1, lead to:

$$u^h(\mathbf{x}) = \mathbf{p}^T(\mathbf{x}) \mathbf{P}_Q^{-1} \mathbf{d}_s \quad (3.10)$$

Using Eq. 3.10 is possible to define the PIM shape function as:

$$N(\mathbf{x}) = \mathbf{p}^T(\mathbf{x}) \mathbf{P}_Q^{-1} \quad (3.11)$$

The derivative of the PIM shape functions are obtained directly, since polynomial functions are used.

As the formulation imposed that the approximation values in the nodes are equal to the values of the nodal field variable, the approximation functions of the PIM posses the Kronecker delta property. Thus, the boundary conditions can be applied directly. PIM shape functions do not use weight functions to build the approximation, so they are not compatible functions, in general. Thus, the value of functions can be discontinuous when passing from a support domain to another. During the formulation it was assumed that the moment matrix is invertible, however this matrix may be singular. To avoid the singularity of the matrix, some strategies can be adopted, as listed by Liu (2009).

- Random distribution of support domain nodes;
- Rotation of nodal coordinates;
- Use of radial basis functions;
- Moment matrix triangularization;
- Use of a triangular background mesh and T-schemes for support nodes selection.

3.3 Radial Point Interpolation Method with Polynomial Reproduction (RPIMp)

As previously mentioned, the use of a radial basis functions is an alternative to guarantee the inversibility of the moment matrix. The study of this functions was presented in Wang and Liu (2000). However, as indicated by Liu (2009), the adoption of only radial functions may not pass the standard *patch test*, that is, it does not reproduce the linear field. Thus,

Wang and Liu (2002) suggest the addition of polynomials in the basis functions to restore the consistency of the shape functions.

The RPIM shape functions at a point \mathbf{x} is given by:

$$u^h(\mathbf{x}) = \sum_{i=1}^n R_i(\mathbf{x})a_i + \sum_{j=1}^m p_j(\mathbf{x})b_j \equiv \mathbf{R}^T(\mathbf{x})\mathbf{a} + \mathbf{p}^T(\mathbf{x})\mathbf{b} \quad (3.12)$$

where n is the number of nodes of the support domain, m is the number of monomials composing the polynomial basis, a_i are the unknown coefficients of radial basis and b_j are the unknown coefficients of the polynomial basis.

The coefficients a_i and b_j , at a specific point \mathbf{x} , can be obtained by imposing the interpolation condition at all the nodes of the support domain of \mathbf{x} :

$$u_k = \sum_{i=1}^n R_i(\mathbf{x}_k)a_i + \sum_{j=1}^m p_j(\mathbf{x}_k)b_j, \quad k = 1, \dots, n \quad (3.13)$$

To determine the $n + m$ coefficients, it is necessary to impose the following additional conditions:

$$\sum_{i=1}^n p_j(q_i)a_i = 0 \quad j = 1, \dots, m \quad (3.14)$$

The Eqs. 3.13 and 3.14 can be written in a matricial form as:

$$\begin{bmatrix} \mathbf{R}_Q & \mathbf{P}_m \\ \mathbf{P}_m^T & \mathbf{0} \end{bmatrix} \begin{Bmatrix} \mathbf{a} \\ \mathbf{b} \end{Bmatrix} = \begin{Bmatrix} \mathbf{d}_s \\ \mathbf{0} \end{Bmatrix} \quad (3.15)$$

where \mathbf{R}_Q is the moment matrix of the radial basis, \mathbf{P}_m is the moment matrix of the polynomial function and \mathbf{d}_s is the vector with the nodal variables of the support domain, \mathbf{a} is the vector of coefficients a_i and \mathbf{b} is the vector of coefficients b_j .

Inverting the matrix that contains the moment matrices it is possible to obtain the vectors \mathbf{a} e \mathbf{b} .

$$\mathbf{b} = \mathbf{S}_b \mathbf{d}_s \quad \mathbf{a} = \mathbf{S}_a \mathbf{d}_s \quad (3.16)$$

where

$$\mathbf{S}_b = [\mathbf{P}_m^T \mathbf{R}_Q^{-1} \mathbf{P}_m]^{-1} \mathbf{P}_m^T \mathbf{R}_Q^{-1} \quad (3.17)$$

$$\mathbf{S}_a = \mathbf{R}_Q^{-1} [\mathbf{I} - \mathbf{P}_m \mathbf{S}_b] = \mathbf{R}_Q^{-1} - \mathbf{R}_Q^{-1} \mathbf{P}_m \mathbf{S}_b. \quad (3.18)$$

The Eq. 3.13 can be recasted as:

$$u(\mathbf{x}) = [\mathbf{R}^T(\mathbf{x})\mathbf{S}_a + \mathbf{p}^T(\mathbf{x})\mathbf{S}_b] \mathbf{d}_s = N(\mathbf{x})\mathbf{d}_s \quad (3.19)$$

Thus, the shape function for a node k is given by:

$$N_k(\mathbf{x}) = \sum_{i=1}^n R_i(\mathbf{x})S_{ik}^a + \sum_{j=1}^m p_j(\mathbf{x})S_{jk}^b. \quad (3.20)$$

The radial basis functions $R_i(\mathbf{x})$ can be of different types, where they only depend on the distance between the point \mathbf{x} and the support node. For 2D problems, this distance is defined by

$$r_i = \sqrt{(x - x_i)^2 + (y - y_i)^2}. \quad (3.21)$$

In order to obtain a function less dependent on the nodal spacing, an alternative is to adopt a scaled radial distance, given for example by

$$r_i^* = \frac{r_i}{\max(r)} \quad (3.22)$$

where r_i is the distance (Eq. 3.21) and $\max(r)$ is the maximum distance r_i of the support domain.

- Exponential function:

$$R_i(r_i^*) = \exp(-cr_i^{*2}) \quad (3.23)$$

where c is a shape parameter.

- Multiquadric function:

$$R_i(r_i^*) = (r_i^{*2} + C^2)^q \quad (3.24)$$

where C and q are the shape parameters.

3.4 Smoothing domains

As pointed out in the previous section, the shape functions of the type PIM present the Kronecker delta propriety, which facilitates the imposition of boundary conditions. However, they are incompatible, since they may exhibit discontinuities when moving from one support domain to another. This issue led Liu and his co-authors (Liu, 2010) to propose a new formulation where the continuity is not required for convergence of the weak form of the problem. This formulation establishes new concepts such as smoothing domains, *G-space theory* and *weakened-weak form*, which can be found in Liu (2009).

Smoothing domains are defined as parts of the domain where constant strains are adopted and it is not necessary to guarantee the continuity of the shape functions. The calculation of strains is carried out from an integral on the boundary of the domain. Thus, it is necessary that at the boundary of the smoothing domains the approximation functions

to be continuous. Numerical integration is performed from these domains, adopting one integration point by smoothing domain, located in the center of the domain.

These domains can be of the type *Cell-Based*, *Edge-Based* or *Node-Based*, and the creation of these domains is performed from generally triangular background cells, as illustrated in Fig. 3.3. In the type *Cell-Based*, smoothing domains are equivalent to background cells. In the *Edge-Based* type, the smoothing domains are formed from the edges of the background cells. And in the *Node-Based* type, the number of smoothing domains is equal to the number of nodes of the model.

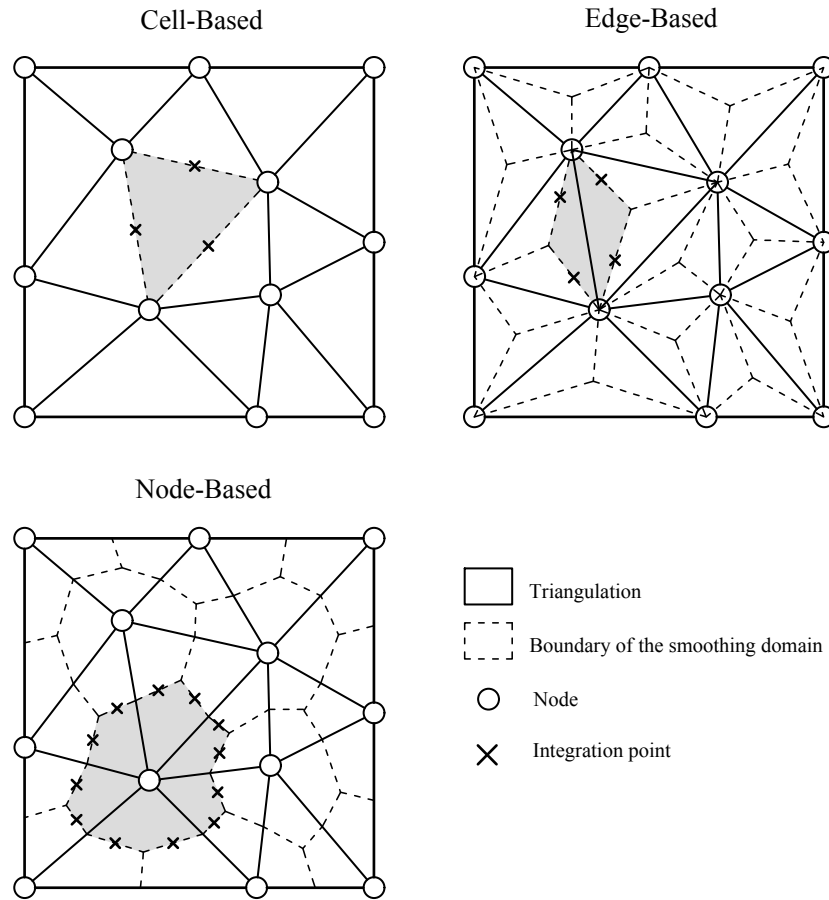


Figure 3.3: Smoothing domains.

In the smoothing operation, it is not necessary to calculate the derivative of the shape functions directly. The calculation of the strains is based on Green's divergence theorem, where the integral of the shape functions is performed on the boundary of the domain.

In each smoothing domain, the derivative of the displacement field at a point p_k can be rewritten as a *smoothed derivative*:

$$u_{i,j}(p) = \widetilde{u}_{i,j}(p_k) := \int_{\mathbf{D}_k^S} u_{i,j}(\xi) \widetilde{W}(p_k - \xi) d\mathcal{V}, \quad p \in \mathbf{D}_k^S \quad (3.25)$$

where p_k is the centre of the smoothing domain and \widetilde{W} is a *smoothing function*. If the

field variable u is continuous, the Green's divergence theorem can be applied, resulting in

$$\widetilde{u}_{i,j}(p_k) = \int_{\partial \mathbf{D}_k^S} (u_i(\xi) \otimes n_j^{(k)}(\xi)) \widetilde{W}(p_k - \xi) dS - \int_{\mathbf{D}_k^S} u_i(\xi) \otimes \widetilde{W}_{,j}(p_k - \xi) dV \quad (3.26)$$

where $n_j^{(k)}$ is the unitary outward normal vector field on the boundary $\partial \mathbf{D}_k^S$.

The smoothing function constant is applied.

$$\widetilde{W}(p_k - \xi) := \begin{cases} 1/A_k & se \quad \xi \in \mathbf{D}_k^S \\ 0 & se \quad \xi \notin \mathbf{D}_k^S \end{cases} \quad (3.27)$$

where $A_k = \int_{\mathbf{D}_k^S} dV$ is the area of each smoothing domain, and the term $\widetilde{W}_{,j}$ disappear.

Replacing the Eq.3.27 in Eq.3.26, has

$$\widetilde{u}_{i,j}(p_k) = \frac{1}{A_k} \int_{\partial \mathbf{D}_k^S} u_i(\xi) \otimes n_j^{(k)}(\xi) dS. \quad (3.28)$$

The smoothed strain tensor $\widetilde{\boldsymbol{\varepsilon}}$ is obtained considering the smoothed derivatives

$$\widetilde{\varepsilon}_{ij} = \frac{1}{2} (\widetilde{u}_{i,j} + \widetilde{u}_{j,i}). \quad (3.29)$$

Thus, it is written as

$$\widetilde{\boldsymbol{\varepsilon}}(p_k) = \sum_{I \in S_d} [\widetilde{\mathbf{B}}_I(p_k)] \mathbf{d}_I \quad (3.30)$$

where $\widetilde{\mathbf{B}}_I$ is the smoothed strain gradient matrix, given by:

$$\widetilde{\mathbf{B}}_I = \begin{bmatrix} \widetilde{N}_{I,x}(p_k) & 0 \\ 0 & \widetilde{N}_{I,y}(p_k) \\ \widetilde{N}_{I,y}(p_k) & \widetilde{N}_{I,x}(p_k) \end{bmatrix} \quad (3.31)$$

where

$$\widetilde{N}_{I,l}(p_k) := \frac{1}{A_k} \int_{\partial \mathbf{D}_k^S} n_l^{(k)}(\xi) N_I(\xi) dS, \quad l = x, y \quad (3.32)$$

Gauss points are adopted to integrate on the boundary of the smoothing domains, in this case Eq. 3.32 results in

$$\widetilde{N}_{I,l}(p_k) := \frac{1}{A_k} \sum_{m=1}^{n_{seg}} L_m \left(\sum_{n=1}^{n_{pg}} W_n^{pg} N_I(p_{m,n}) n_{l,m}^{(k)} \right), \quad l = x, y \quad (3.33)$$

where n_{seg} is the number of segments in the boundary of the domain, L_m is the length of the segment, n_{pg} is the number Gauss points in the segment, W_n is the weight associated with the integration point n_{pg} , $p_{m,n}$ is the integration point n of the segment m of the

boundary and $n_{l,m}^{(k)}$ is the outward unit normal in the direction l to the segment m of the smoothing domain k .

When the smoothing technique is adopted, the weak form for the boundary value problem is replaced by the weakened-weak form. In each smoothing domain, the strain tensor is constant and the constitutive operator is adopted as constant. In this way, the domain integral has been transformed in a summation over the smoothing domain. The smoothed stiffness matrix of each smoothing domain is given by

$$\mathbf{K}(p_k) = A_k \widetilde{\mathbf{B}}(p_k)^T \mathbf{C} \widetilde{\mathbf{B}}(p_k). \quad (3.34)$$

Chapter 4

Smoothed Point Interpolation

Methods for phase-field modelling of fracture

This chapter discusses the extension of SPIMs and their weakened-weak form to phase-field modelling of fracture, one of the main contributions of this work. To give some context, the chapter opens with a bibliographic review on the more general topic of meshfree methods combined with phase-field modelling of fracture.

4.1 State of the art

Due to the presented advantages of using the phase-field for crack modelling, the study and expansion of this model is a topic of great interest. Its application to the finite element method is already quite consolidated and widely investigated. Recently, several works involving meshfree methods have emerged with the aim to extend the advantages of meshfree methods discussed in Chapter 3 to phase-field models.

Studies with meshfree methods began with the work of Amiri et al. (2014), where the authors adopted the classic phase-field model for brittle fracture in Kirchoff-Love plates. The meshfree method called *Local Maximum Entropy* (Arroyo and Ortiz, 2006) was adopted; its use was justified by its high smoothness and robustness of the shape functions.

Li et al. (2015) proposed a phase-field model for brittle materials with highly anisotropic fracture. This work was applied to polymers, crystals and organic materials due to the high anisotropy of these materials. The *Local Maximum Entropy* meshfree method was adopted. Tension test with initial cracks in different angles was performed, but only the contour plots of phase-field were presented. The load-displacement curves are not shown.

Amiri et al. (2016) applied the phase-field model with *Local Maximum Entropy* ap-

proximation to crack propagation problems. The isotropic model of phase-field was considered. The staggered solver was used for the solution. In the numerical simulations, two-dimensional cantilever beam, three-dimensional tension test and three-dimensional notched beam with initial crack are performed.

Moutsanids et al. (2018) used brittle fracture phase-field modelling in dynamic fracture problems. The formulation proposed a coupled isogeometric-meshfree discretisation (Cottrell et al., 2009), where the *Reproducing-Kernel Particle Method* (Chen et al., 1996) was used. The model was applied to explosion-structure interaction problems and the fact that this formulation not use a mesh ensured flexibility in the representation of structural fragmentation. The adopted phase-field model was presented in Kamensky et al. (2018). In it, a hyperbolic partial differential equation was introduced for the phase-field modelling.

Following his work, Amiri (2019) proposed the use of the phase-field model with approximations of *Local Maximum Entropy* and *Maximum Second-Order Entropy* (Rosolen et al., 2013). In this work, it is indicated that the *Maximum Second-Order Entropy* presents more stable results compared to the local maximum entropy. In the numerical examples, only 1D model was considered.

Shao et al. (2019) applied the meshfree method of *Element-Free Galerkin* (EFG) (Beletschko et al., 1994, Krysl and Beletschko, 1997) to the phase-field brittle fracture model. *Moving Least-Square* (MLS) was adopted to calculate the approximations, where it is possible obtain high-order approximation functions. The integration domain adopted is the 3-point integration scheme. The authors employed the classic phase-field formulation for brittle fracture and the split energy of Miehe, Welschinger and Hofacker (2010). The staggered solver was adopted. Unlike other works, which presented a fixed discretisation, in this work adaptivity was applied. Different examples were performed: shear test, L-shaped panel, notched rectangular with a hole and wing crack problem. However, only the shear test presented the load-displacement curve to compare with the literature.

Wu et al. (2019) presented a gradient smoothing meshfree formulation for phase-field modelling of brittle fracture. The *Reproducing Kernel Gradient Smoothing* (Wang and Wu, 2019) was adopted as the meshfree method. The numerical integration was based on triangular cells with 3 integration points. The authors used the division of energy by spectral decomposition of the strain tensor (Miehe, Welschinger and Hofacker, 2010) and the staggered solver. Similar to Shao et al. (2019), many examples were illustrated. The tension, shear and bending tests proposed by Miehe, Welschinger and Hofacker (2010) were analysed, but only bending test presented the load-displacement curve.

Nguyen et al. (2019) applied the *Kringing Meshfree Method* (Cressie, 1990) to discretise the phase-field model. This model was used only for brittle fracture of one-dimensional problems and the staggered solver was adopted.

Kasirajan et al. (2020) modelled the quasi-brittle fracture phase-field using *Natural*

Neighbor Galerkin Method (Balachandran et al., 2008). In this method, the approximations are based on a division of areas with a grid integration with 3 points per Delaunay triangle. The method uses smooth non-polynomial type Sibson interpolants. For the phase-field model they used the decomposition energy of Miehe, Welschinger and Hofacker (2010), and as this division leads to a non-linear problem they adopt a hybrid model. This model uses the linear momentum equilibrium equation but ensures that the tensile part of the problem is driven by the phase-field. Thus, the computational cost is compared to the isotropic model and the phase-field evolution occurs only in the tensioned part of the problem. The staggered solver is used. The load-displacement curves were shown for all the examples and the results confirmed the accuracy of the method.

Shao et al. (2020) presented an evolution of the work Shao et al. (2019) now for three-dimensional models. The authors used the phase-field model of brittle fracture with the energy division proposed by Miehe, Welschinger and Hofacker (2010). The meshfree method adopted is *Consistent Element-Free Galerkin* (CEFG) with approximation functions built by *Moving Least Square*. For the integration process, tetrahedral cells with 4 integration points are considered. The tension test, shear test, bending test and L-shaped panel are performed, but again only one example present the curve for comparison with the literature.

In the work of Ghoneim (2020), the author applied the meshfree method *Smoothed Particle Hydrodynamics* (SPH) (Lucy, 1977, Gingold and Monaghan, 1977) for the phase-field simulation of dendritic solidification. The approximations are built from Kernel approximation functions with radial basis functions and *Moving Least Square*. The application of this work was for the area of metallurgy in the growth of dendrites.

Sun et al. (2020) adopted a *Hybrid Finite Element-Meshfree Method* (FEMM) to discretise three-dimensional hydraulic fracture propagation problems using phase-field. The shape functions of the meshfree method are used in the nodal approximation, and the classical shape functions of isoparametric elements are used in the construction of the partition of unity. The authors used the classical brittle fracture formulation for the phase-field with the spectral decomposition of the strain tensor (Miehe, Welschinger and Hofacker, 2010). It was adopted the staggered solver.

Nguyen-Thanh et al. (2020) presented an adaptive refinement process using a isogeometric-meshfree method to simulate 2D and 3D cracks in polycrystalline materials. The meshfree method is the *Kernel Reproduction Method*. The phase-field models are adopted for anisotropic brittle fracture. The anisotropy is added to the model by a parameter that depends on the orientation. The anisotropic model of Amor et al. (2009) is used for decomposition of the strain tensor and the maximum energy associated with positive strains is adopted as a historical variable to ensure irreversibility. The alternate solution scheme is adopted as a solution process. The authors presented the tension and shear tests to demonstrate the robustness of the proposed method and examples with 2D and

3D polycrystalline structures.

In addition to meshfree methods, another way to discretise the phase-field problem is through the finite element method with gradient smoothing (*Smoothed Finite Element Method*). In this method, the calculation of the derivatives of the shape functions is not performed directly, but domains of constant derivatives are adopted. To calculate these derivatives, boundary integrals are performed based on the divergence theorem. These smoothed domains can be cell (*cell-based*) (Liu et al., 2007), node (*node-based*) (Liu, Nguyen, Nguyen and Lam, 2009), edge (*edge-based*) (Liu, Nguyen and Lam, 2009) or the face (*face-based*) (Nguyen et al., 2009). This method has as main advantages an excellent performance for highly distorted meshes, since there is no need to calculate the inverse of the Jacobian.

Next, some works that use the smoothed FEM to discretise the phase-field are presented.

Bhowmick and Liu (2018) modelled the phase-field for brittle fracture with cell-based smoothed finite element method. The authors adopted the classic phase-field formulation and the isotropic model, where the degradation function is applied throughout the model. Gradient smoothing was considered only for the displacement gradient. Quadrilateral elements were used, where each element was divided into 4 cells. The staggered solver was used to solve the problem. Only tensile and bending tests were performed.

Li et al. (2019) also used the cell-based SFEM to model the phase-field for brittle fracture with the isotropic model. The smoothing is applied to both the displacement gradient and the phase-field gradient. Quadrilateral elements are modelled for 2D and hexahedral for 3D. Only tensile tests were presented.

Peng, Huang, Ma, Zhang and Zhang (2020) adopted the cell-based smoothed FEM to model the phase-field for brittle fracture considering the spectral decomposition of deformations. The smoothing strategy is used for both the displacement gradient and the phase-field gradient. The hybrid formulation of phase-field proposed in Ambati et al. (2015) was used. In addition to the tensile tests, in this article the shear test and the L panel are performed.

Tian et al. (2020) proposed an adaptive edge-based SFEM for phase-field modelling of fractures at large deformations. The phase-field model for large deformations presents the classical formulation adding a term referring to extra energy dissipation. Furthermore, the spectral decomposition of the strain tensor is considered according to Miehe, Welschinger and Hofacker (2010). Smoothed domains are constructed by edge-based from triangular elements and smoothing is adopted for the displacement gradient and phase-field gradient.

Peng, Huang, Zhang, Guo and Ma (2020) adopted the edge-based smoothed FEM to discretise the phase-field model of large deformations. The energy degradation function is applied to the whole model and the smoothing technique is applied to the displacement gradient and phase-field gradient. Examples with distorted meshes were used and shown

that the model was insensitive to mesh distortion.

The Table 4.1 summarises the different meshfree and SFEM methods used for discretisation of phase-field models.

Table 4.1: Phase-field models with meshfree methods.

Discretisation Method	Papers
Local Maximum Entropy	(Amiri et al., 2014), (Li et al., 2015), (Amiri et al., 2016) Amiri (2019)
Reproducing Kernel Particle Method	(Moutsanids et al., 2018)
Element Free Galerkin	(Shao et al., 2019), (Shao et al., 2020)
Reproducing Kernel Gradient Smoothing	(Wu et al., 2019)
Natural Neighbor Galerkin Method	(Kasirajan et al., 2020)
Smoothed Particle Hydrodynamics	(Ghoneim, 2020)
Isogeometric-Reproducing Kernel	(Nguyen et al., 2019)
SFEM Cell-based	(Bhowmick and Liu, 2018), (Li et al., 2019), (Peng, Huang, Ma, Zhang and Zhang, 2020)
SFEM Edge-based	(Tian et al., 2020), (Peng, Huang, Zhang, Guo and Ma, 2020)

4.2 SPIM for phase-field modelling

As it can be seen from the state of the art show above, *Point Interpolation Methods* have never been used for the discretisation of phase-field models despite the advantages of these methods. These advantages, already discussed in Chapter 3, are summarised below:

- Posses the Kronecker delta property, that compared to other meshfree methods, allowing for an easier application of essential boundary conditions.
- It is possible to use different shape functions as radial functions.
- In the SPIM methods, similar to SFEM, the derivatives of the shape functions are calculated using a smoothing technique. There is no need to calculate the inverse of the Jacobian.

Such advantages motivated the use of these methods by the research group where the work presented here has been developed. In the sequence, the works that mark the beginning of this research are presented.

The PIM was adopted for the first time in Novelli et al. (2021) for phase-field modelling of brittle fracture. The PIM and RPIMp shape functions were used with T3 and T6/3 schemes for node selection. In the phase-field model, the geometric crack function and degradation function of Bourdin et al. (2000) were used, and the strategy of Miehe, Welschinger and Hofacker (2010) was adopted to decompose the strain energy. The results presented that the use of PIM meshfree method was able to simulate crack nucleation, propagation and branching similar to FEM.

The second investigation was the use of SPIM for the discretisation of phase-field models. This study was presented in Novelli, Gori and Pitangueira (2022). The phase-field modelling of brittle fracture was adopted for simulation of crack propagation, similar to the Novelli et al. (2021). Node-based, cell-based and edge-based were used as smoothing domains with T-schemes for nodes selection of the support domain. This required the extension of the SPIMs smoothing operation (Section 3.4) to the phase-field equations,

in order to take into account the additional field variable. These studies are shown in Section 4.2.1 and 4.2.2, respectively. In the paper, five different examples were analysed: tension test, shear test, bending test, L shaped panel and asymmetric tension test. The results presented that all different SPIM strategies were capable to correctly reproduce the contour plots of phase-field. For load-displacement paths, however, the cell and edge-based strategies presented better results when compared with the node-based one.

4.2.1 Smoothing operation for phase-field models

The smoothing operation is the strategy used to calculate the derivatives of the shape functions. As illustrated in Chapter 2, the strain measures of the phase-field problem are represented by the displacements gradient, the phase-field gradient, and the phase-field itself. When the SPIM is adopted to discretise the problem, all these terms should be smoothed, in order to make them constant within each smoothing domain and in order to reduce the continuity requirement on the interpolation functions.

The same smoothing technique illustrated in Chapter 3 for the displacement gradient in classic elasticity, is applied here to both the displacements and phase-field gradients. For each point p in \mathbf{D}_k^S , these gradients are expressed by

$$\boldsymbol{\varepsilon}(p) \simeq \widetilde{\boldsymbol{\varepsilon}}(p_k) := \int_{\mathbf{D}_k^S} \boldsymbol{\varepsilon}(\xi) \widetilde{W}(p_k - \xi) d\mathcal{V}, \quad p \in \mathbf{D}_k^S \quad (4.1)$$

$$\nabla\phi(p) \simeq \widetilde{\nabla}\phi(p_k) := \int_{\mathbf{D}_k^S} \nabla\phi(\xi) \widetilde{W}(p_k - \xi) d\mathcal{V}, \quad p \in \mathbf{D}_k^S \quad (4.2)$$

where \widetilde{W} is a smoothing function. Applying the divergence theorem, and considering the smoothing function of the Eq. 3.27, the expressions above can be recasted as

$$\widetilde{\boldsymbol{\varepsilon}}(p_k) = \frac{1}{A_k} \int_{\partial\mathbf{D}_k^S} \mathbf{u}(\xi) \otimes \mathbf{n}^{(k)}(\xi) dS. \quad (4.3)$$

$$\widetilde{\nabla}\phi(p_k) = \frac{1}{A_k} \int_{\partial\mathbf{D}_k^S} \phi(\xi) \mathbf{n}^{(k)}(\xi) dS. \quad (4.4)$$

where $\mathbf{n}^{(k)}$ is the unitary outward normal vector on the boundary $\partial\mathbf{D}_k^S$.

When the same shape functions are used for the displacement field and the phase-field, the smoothing derivatives of the shape functions, used to construct both the displacements and phase-field gradients, are defined by

$$\widetilde{N}_{I,l}^u(p_k) = \widetilde{N}_{I,l}^\phi(p_k) := \frac{1}{A_k} \int_{\partial\mathbf{D}_k^S} n_l^{(k)}(\xi) N_I(\xi) dS, \quad l = x, y \quad (4.5)$$

In the paper by Novelli, Gori and Pitangueira (2022) and in this work, one Gauss point is adopted in the midpoint of each edge of the boundary of the smoothing domain.

In this case, Eq. 4.5 results in

$$\widetilde{N}_{I,l}^u(p_k) = \widetilde{N}_{I,l}^\phi(p_k) := \frac{1}{A_k} \sum_{J=1}^{N_{seg}} N_I(p_J) n_{l,J}^{(k)} L_J, \quad l = x, y \quad (4.6)$$

where N_{seg} is the number of segments, p_J is the midpoint of the boundary segment, $n_{l,J}^{(k)}$ is the outward unit normal in the direction l to the segment J of the smoothing domain k and L_J is the length of the segment.

The application of SPIM techniques to problems where a field variable also appears among the strain measures has already been discussed in the literature, resulting in two possible approaches. Tootoonchi and Khosghalb (2016) investigated the application of the cell-based smoothed point interpolation method to axisymmetric problems. The field variable appearing in the strain measure was treated considering a numerical integration in the domain integral, adopting integral points inside each smoothing domain. This approach results in the following expression for the smoothed phase-field:

$$\widetilde{\phi}(p_k) := \frac{1}{A_k} \int_{\mathbf{D}_k^S} \phi(\xi) d\mathcal{V}. \quad (4.7)$$

Chen et al. (2002) proposed a nodal integration strategy for Galerkin meshfree methods applied to geometrical non-linearities and elasto-plasticity. For the axisymmetric problem, the authors indicated that the field variable should be evaluated nodally. An analogous approach was followed by Gori et al. (2019), where the authors applied the SPIM formulation to micropolar media. There, the smoothed value of the microrotation field variable appearing in the strain measures was assumed to be equal to the value of the microrotation at the centre of the smoothing domain. Within this second approach, the smoothed phase-field should be considered equal to the value at the centre p_k of the smoothing domain \mathbf{D}_k :

$$\widetilde{\phi}(p_k) := \phi(p_k) \quad (4.8)$$

In the paper Novelli, Gori and Pitangueira (2022) and in this work, the same approach followed by Chen et al. (2002) and by Gori et al. (2019) is adopted, thus using the expression given in Eq. 4.8. The value of the phase-field at p_k is the interpolation of its nodal values at the support nodes of the k -smoothing domain, interpolated using the RPIMp shape functions.

4.2.2 SPIM discretisation of the phase-field models

The discretisation of the phase-field problem in meshfree methods is similar to that presented for the finite element method. The main difference is the fact that the calculation of the shape functions is not based on the finite element nodes, but on the support nodes

of a given point. For SPIM meshfree methods, another important difference is the tessellation of the model. For these methods, the domain is divided in smoothing domains and the derivatives of the shape functions are calculated using the smoothing strategy, as shown in Chapter 3.

As presented in the FEM discretisation, in Miehe, Welschinger and Hofacker (2010) and Wu (2017) relationship between the length scale l_0 and the size of the elements h were proposed. These relationship are based on accuracy tests. For meshfree methods, as they do not have elements, a strategy is to compare the size of the triangular background cells. Wu et al. (2019) used the relationship indicated by Miehe, Welschinger and Hofacker (2010) ($l_0/h = 2$) for brittle fracture. In Novelli, Gori and Pitangueira (2022), the same ratio was used.

The approximation of both the displacements field \mathbf{u} and phase-field ϕ at a point \mathbf{x} of the domain are expressed in terms of the same shape functions, as an interpolation of their nodal values at the support nodes, \mathbf{d}_I and a_I , respectively:

Wu et al. (2020) note that identical interpolation functions $N_I(\mathbf{x})$ are generally used in the approximation of the displacement and phase-field.

$$\mathbf{u}(\mathbf{x}) = \sum_{I=1}^{SN} \mathbf{N}_I(\mathbf{x}) \mathbf{d}_I \quad \phi(\mathbf{x}) = \sum_{I=1}^{SN} N_I(\mathbf{x}) a_I \quad (4.9)$$

where SN are the support nodes.

These approximations result in the following expressions of the smoothed strain tensor and smoothed gradient of the phase-field:

$$\boldsymbol{\varepsilon}(\mathbf{x}) = \sum_{I=1}^{SN} \widetilde{\mathbf{B}}_I^u(\mathbf{x}) \mathbf{d}_I \quad \nabla \phi(\mathbf{x}) = \sum_{I=1}^{SN} \widetilde{\mathbf{B}}_I^\phi(\mathbf{x}) a_I \quad (4.10)$$

where

$$\widetilde{\mathbf{B}}_I^u(\mathbf{x}) = \begin{bmatrix} \widetilde{N}_{I,x}^u & 0 \\ 0 & \widetilde{N}_{I,y}^u \\ \widetilde{N}_{I,y}^u & \widetilde{N}_{I,x}^u \end{bmatrix} \quad (4.11)$$

$$\widetilde{\mathbf{B}}_I^\phi(\mathbf{x}) = \begin{bmatrix} \widetilde{N}_{I,x}^\phi \\ \widetilde{N}_{I,y}^\phi \end{bmatrix} \quad (4.12)$$

where $\widetilde{N}_{I,x}$ and $\widetilde{N}_{I,y}$ are the smoothed derivatives of the shape functions, illustrated in Eq. 4.6.

Replacing the expressions above into Eq. 2.75 results in the following weakened-weak form

$$\int_{\Omega} (\widetilde{\mathbf{B}}^u)^T \boldsymbol{\sigma} dV = f_{ext} \quad (4.13)$$

$$\int_{\Omega} g' \bar{Y} (\mathbf{N}^{\phi})^T dV + \int_{\Omega} \frac{G_c}{C_0} \left(\frac{1}{l_0} \alpha' (\mathbf{N}^{\phi})^T + 2l_0 (\tilde{\mathbf{B}}^{\phi})^T \nabla \phi \right) dV \geq 0. \quad (4.14)$$

The first expression is the displacement problem, that can be recasted as

$$\mathbf{K}^u \mathbf{d} = \mathbf{F}^u \quad (4.15)$$

where

$$\mathbf{K}^u = \int_{\Omega} (\tilde{\mathbf{B}}^u)^T \mathbf{C}^u \tilde{\mathbf{B}}^u dV = \sum_{k=1}^{N_S} (\tilde{\mathbf{B}}_k^u)^T \mathbf{C}_k^u \tilde{\mathbf{B}}_k^u A_k \quad (4.16)$$

$$\mathbf{F}^u = \int_{\Omega} (\mathbf{N}^u)^T \mathbf{b} dV + \int_{\partial\Omega_{\sigma}} (\mathbf{N}^u)^T \mathbf{t} dA. \quad (4.17)$$

It's worth it to note that in the expression of the stiffness matrix (Eq. 4.16), the domain integral has been transformed in a summation over the N_S smoothing domains, due to the fact that both the constitutive matrix \mathbf{C} and the matrix $\tilde{\mathbf{B}}^u$ are constant within each smoothing domain. A_k is the area of each smoothing domain.

The second equation is the phase-field problem that, like the displacements problem, can be recasted in the following matricial form.

$$\mathbf{K}^{\phi} \mathbf{a} = \mathbf{F}^{\phi} \quad (4.18)$$

where

$$\mathbf{K}^{\phi} = \int_{\Omega} (\tilde{\mathbf{B}}^{\phi})^T \mathbf{C}^{\phi} \tilde{\mathbf{B}}^{\phi} dV = \sum_{k=1}^{N_S} (\tilde{\mathbf{B}}_k^{\phi})^T \mathbf{C}_k^{\phi} \tilde{\mathbf{B}}_k^{\phi} A_k \quad (4.19)$$

$$\tilde{\mathbf{B}}_I^{\phi}(\mathbf{x}) = \begin{bmatrix} N_I^{\phi} \\ \tilde{N}_{I,x}^{\phi} \\ \tilde{N}_{I,y}^{\phi} \end{bmatrix} \quad (4.20)$$

The phase-field problem is a linear problem for the phase-field model with brittle fracture. In this case, \mathbf{C}^{ϕ} and \mathbf{F}^{ϕ} can be written as:

$$\mathbf{C}^{\phi} = \begin{bmatrix} (2\bar{Y} + \frac{G_c}{l_0}) & 0 & 0 \\ 0 & G_c l_0 & 0 \\ 0 & 0 & G_c l_0 \end{bmatrix} \quad (4.21)$$

$$\mathbf{F}^{\phi} = \int_{\Omega} 2\bar{Y} (\mathbf{N}^{\phi})^T dV. \quad (4.22)$$

For problems of quasi-brittle fracture, the phase-field problem is non-linear and the values of \mathbf{C}^{ϕ} and \mathbf{F}^{ϕ} are given by:

$$\mathbf{C}^\phi = \begin{bmatrix} (g''\bar{Y} + \frac{G_c}{l_0}\alpha''G_c) & 0 & 0 \\ 0 & \frac{2l_0}{C_0}G_c & 0 \\ 0 & 0 & \frac{2l_0}{C_0}G_c \end{bmatrix} \quad (4.23)$$

$$\mathbf{F}^\phi = - \int_{\Omega} (\mathbf{N}^\phi)^T (g'\bar{Y} + \frac{1}{C_0 l_0} \alpha' G_c) dV - \int_{\Omega} \frac{2l_0}{C_0} G_c (\mathbf{B}^\phi)^T \nabla \phi dV \leq 0. \quad (4.24)$$

4.2.3 Trigonometric radial basis function

Section 2.3 presented different geometric crack functions used in phase-field models. For brittle fracture, the geometric crack function is $\alpha = \phi^2$ and it determines the exponential distribution of the phase-field $\phi(x) = \exp(\frac{|x|}{l_0})$. For this case, the use of exponential shape functions can approximate better the phase-field, for example, the exponential function used in the radial basis function. For quasi-brittle fracture, the geometric crack function $\alpha = 2\phi - \phi^2$ is adopted. This function determines the distribution of the crack phase-field $\phi(x) = 1 - \sin(\frac{|x|}{l_0})$.

Looking for a better representation of this trigonometric phase-field distribution, this section propose, for the first time, a new radial basis function based on a trigonometric function.

$$R_i(r_i^*) = 1 - \sin(\frac{\pi}{2} \cdot r_i^*) \quad (4.25)$$

where r_i^* is the scaled radial distance, given by

$$r_i^* = \frac{r_i}{\max(r)} \quad (4.26)$$

and where r_i is the distance between the point \mathbf{x} and the support node and $\max(r)$ is the maximum distance r_i of the support domain.

The graphic representation of this function is illustrated in Fig. 4.1.

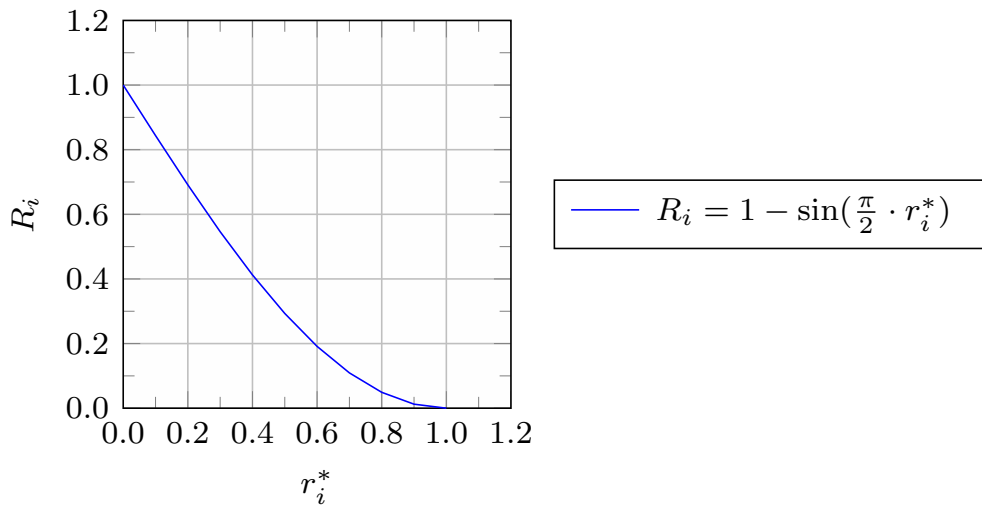


Figure 4.1: Trigonometric function.

For the construction of the RPIMp shape functions, this function is used as a radial basis function, similar to exponential function and multiquadric function. This shape function possesses the Kronecker delta property.

Fig. 4.2 shows the trigonometric radial basis function in 1D space. Five nodes evenly distributed in the support domain of $[-1, 1]$ are used for computing the shape function for the node at $x = 0$.

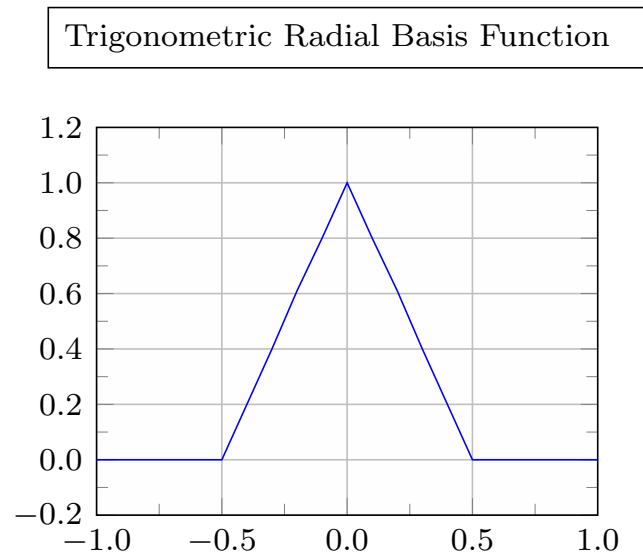


Figure 4.2: Trigonometric shape function in 1D space for the node $x = 0$.

The influence of the application of this new radial function in a linear elastic problem is presented in Appendix A.

Chapter 5

Adaptive FEM-SPIM coupling for phase-field modelling

This chapter presents the major contribution of this work, that is the development of an adaptive FEM-SPIM strategy for phase-field modelling of fracture. First, in Section 5.1, a bibliographic review is presented, that illustrates previous works on adaptive analyses for phase-field models and works that use coupling between Finite Elements and meshfree methods. In Section 5.2, the novel adaptive coupling strategy for FEM and SPIM applied to phase-field modelling of fracture is illustrated.

5.1 State of the art

5.1.1 Adaptive refinement for phase-field modelling

As previously presented, in phase-field models, for the degraded region of the material to approach the representation of a discrete crack, the parameter l_0 must approach zero. To ensure the accuracy of the problem, the variable h , that represents the size of the mesh elements, must be less than l_0 . This fact results in extremely refined meshes in the phase-field growth region.

When the problem has complex cracks, where the crack growth path is not previously known, it is necessary either to use a refined mesh in the whole domain or to adopt an adaptive refinement. The first case leads to a high computational cost, which can make the analysis infeasible. When using an adaptive strategy, an initially coarse mesh is used to discretise the whole domain; that mesh is then refined in the regions of interest during the analysis. In this way, discretisation problems do not interfere in the results, since an adequate and automatic refinement is always adopted.

The regions that need further refinement are obtained by refinement criteria. In the case of damage models, such regions are obtained through error estimators. In the case of

phase-field models, normally the value of phase-field is adopted as a threshold parameter.

There are different strategies for mesh refinement, which are presented below:

- **h-refinement** (Fig. 5.1b): Consists of decreasing the size of the elements, introducing new nodes to the model and increasing the degrees of freedom. In this strategy, the order of approximation functions remains constant. In the splitting process, the original elements can be split into other elements or a new mesh can be generated across the region of interest.

The h-adaptive version is suitable for cases where the solution is not smooth throughout the domain, such as interfaces between different materials, boundary layers, border of a plastic front, etc. (Novotny and Fancello, 1998).

- **p-refinement** (Fig. 5.1c): There is an increase in the degree of approximation functions in each element, keeping the mesh fixed.

The p-adaptive version is suitable for problems where the analytic solution does not have singularity points (Novotny and Fancello, 1998).

- **r-refinement** (Fig. 5.1d): According to Sousa (2007), in this strategy the existing nodes are repositioned so that they are closer to the regions of interest. There are no new nodes or degrees of freedom added. Normally, the Laplacian method of weights is used for repositioning.

- **hp-refinement**: In this strategy there is a combination of strategies h and p. According to Novotny and Fancello (1998), a way to apply the hp process is to first apply refinement h until obtaining the singularities and then perform a refinement p until finding the desired level of refinement.

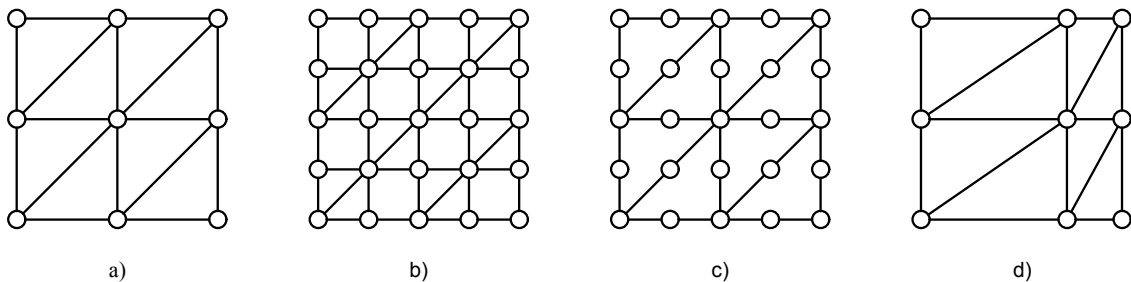


Figure 5.1: Refinement strategies: a) Original mesh, b) Refinement h, c) Refinement p e d) Refinement r. Adapted from Sousa (2007).

The advantages of adopting an adaptive refinement instead of an initially refined mesh are:

- Lower computational cost;
- Greater economy of data storage;
- No prior knowledge of stress concentration or crack growth regions is required.

Several works propose adaptive meshes for the phase-field model. Most of these works present the value of phase-field as an indicator parameter of mesh refinement, and if the

value of phase-field in the element is greater than a certain threshold value, the element passes through a refinement.

Burke et al. (2010) presented two adaptive finite element algorithms for solving phase-field brittle fracture models. Both algorithms adopt a residual estimation technique as an indicator of refinement. The difference between the two algorithms is the stage at which the refinement takes place. In the first algorithm, the refinement occurs after convergence of the alternating minimization process. In the second algorithm, the refinement occurs at each step of the alternate process, that is, after the displacements have converged and after the phase-field has converged. In the numerical simulations, only one example is analysed and it considers a previously refined initial mesh. Both the algorithm presented similar contour plots for phase-field, but the second algorithm require more refinement iterations.

Artina et al. (2015) presented a modification of the phase-field functional that includes additional constraints to ensure irreversibility of the crack through penalty parameters. Furthermore, an error estimator for the mesh adaptation process is shown. The meshes are automatically generated and have the characteristic of being highly anisotropic along the crack and presenting an isotropic behaviour at the crack tip. For the adaptive process a metric tensor is generated from the error estimator. In the numerical experiments, the initial mesh have a high refinement in the tip crack.

In the work by Heister et al. (2015) the authors developed a predictor-corrector scheme for mesh adaptivity. This scheme guarantees that the mesh size h is always smaller than the length scale parameter l_0 . It is used the *primal-dual active* method as the solution scheme, which is based on the minimization of the functional and used the division of the deformation tensor into positive and negative parts based on Miehe, Welschinger and Hofacker (2010).

Among the properties of the predictor-corrector algorithm there are: (i) The length l_0 is kept constant during the solution, (ii) the mesh size h must be sufficiently smaller than l_0 , and (iii) no prior knowledge of the location of the crack is required. Finally, it is indicated that adapting the mesh considering only the current location of the crack does not guarantee that the crack is resolved in a region of adequate refinement. The adaptive strategy proposed in Heister et al. (2015) is summarised below:

Prior to the solution, first define the parameter l_0 . Then we find the refinement level r based on the mesh size h . The mesh must be refined so that the r level is in the crack region. Figure 5.2 presents the scheme for mesh adaptivity. First, the solution for time t^n is presented. From this mesh, the complete problem is solved for the time t^{n+1} . If the crack exceeds the refined mesh region, the so-called predictor-corrector cycle is applied. The first step is to refine the mesh and transfer data from the old mesh to the new mesh. This refinement occurs for all cells that have a value of phase-field greater than the critical one. After refinement of the mesh, the solution is solved again for time t^{n+1} and this cycle

is repeated until no more changes occur in the mesh. These cycles are required when the crack grows rapidly from one step to the next. The authors indicate that there is a price to pay for executing such cycles, but it is guaranteed that the crack grows together with the mesh. The tension, shear and bending tests of Miehe, Welschinger and Hofacker (2010) are performed.

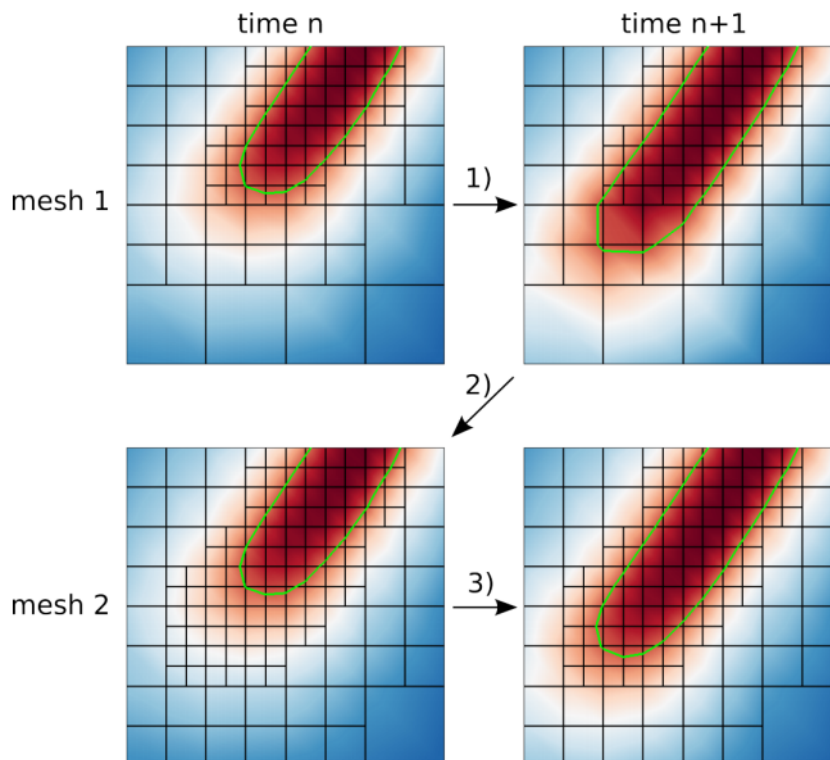


Figure 5.2: Adaptive refinement of Heister et al. (2015).

In the work by Areias et al. (2016) the authors developed an adaptive phase-field model for plates and shells. In this model two phase-field values are assumed, one for the top and one for the bottom of the plate. The adaptive scheme is composed by the division of elements and nodal repositioning, when necessary. The phase-field value of each element is taken as the average between the maximum value of the element nodes for the top and bottom of the plate. From this, each side is classified separately and the value is given as the maximum between the two adjacent elements. During the refinement process, each side of the element is analysed, and according to the need for refinement, the element is divided into two, three or four elements (Fig. 5.3). For the repositioning of nodes, the Laplacian method of weights is adopted. After the refinement step, a process of mapping constitutive variables and nodal variables is carried out.

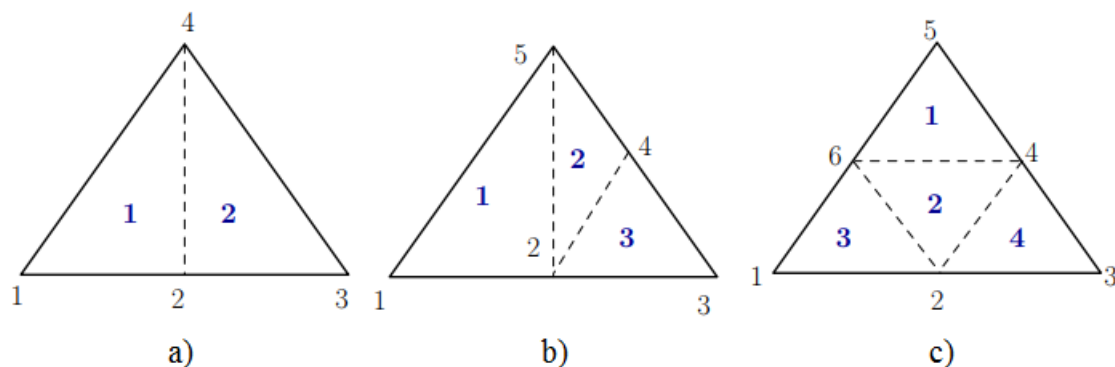


Figure 5.3: Division of the elements: a) 1 edge b) 2 edges c) 3 edges of Areias et al. (2016).

In Kastner et al. (2016) the authors proposed an adaptive phase-field model for brittle fracture. Two mesh refinement strategies are presented T-splines and B-splines (Fig. 5.4). The authors indicate that the refinement based on T-spline is not a local refinement like the B-spline, so the B-spline approximations are adopted to discretise the phase-field model.

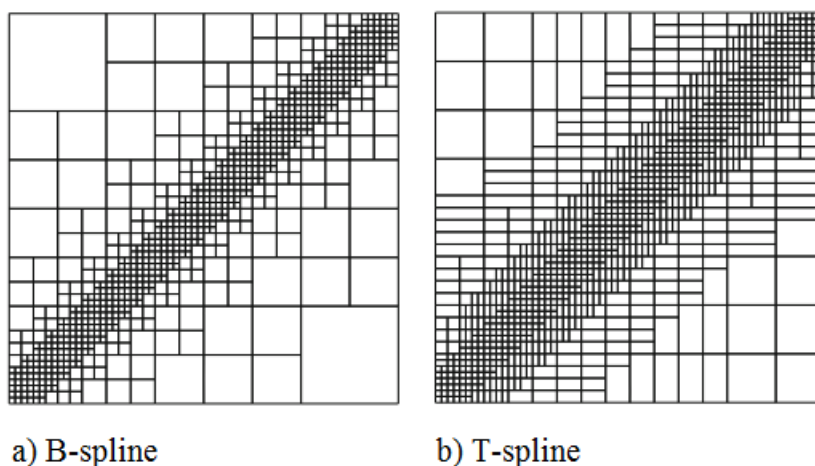


Figure 5.4: Refinement meshes of Kastner et al. (2016).

The authors adopted a critical phase-field value of 0.5 as the refinement criterion. The elements that present the value of phase-field, for the quadrature points, greater than the critical value are refined. Only the shear test is illustrated. Similar to previously papers presented, the initial mesh has a high refinement in the tip crack.

Badnava et al. (2017) present the brittle fracture phase-field model for thermomechanical cracking. For mesh refinement, the predictor-corrector strategy proposed by Heister et al. (2015) was used, where an element is refined when the value of phase-field reaches a threshold. After mesh refinement, the entire system is resolved again to the increment of the previous step. This process repeats until the mesh no longer changes within the same increment. Different threshold values for phase-field are presented in the analyses. In the proposed strategy the length scale l_0 is computed for every change of the elements size,

this fact differ of the standard phase-field where the length scale is a material parameter and it is considered fixed. Fig. 5.5 compares the value of 0.2 and 0.8 for the shear test.

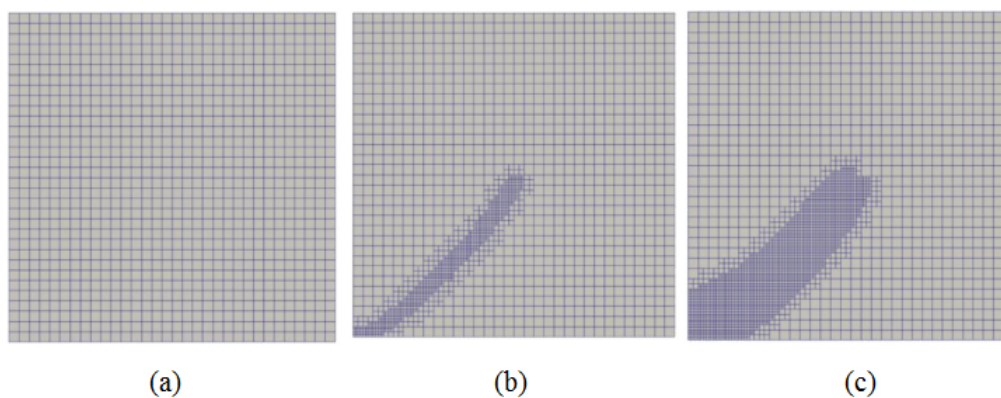


Figure 5.5: Initial coarse mesh (a) and final mesh to the limit of 0.8 (b) and 0.2 (c) (Badnava et al., 2017).

Patil et al. (2017) proposed an adaptive multiscale finite element method coupled to the hybrid phase-field model Ambati et al. (2015) to simulate brittle fracture problems. In this strategy, the model is divided into two regions, one with a coarse mesh and one with a fine mesh, and these two regions are individually modelled and coupled through the use of multiscale basis functions. For the adaptive process, the value of nodal phase-field and the distance between the elements and the crack are analysed. If the value of phase-field exceeds 0.1, the element is refined or if the distance between the element and the crack is smaller than a certain threshold, the element is refined. At work, this limit distance is 1.5 the size of the coarse mesh. The extended finite element method is adopted to model pre-existing discontinuities and voids. Different examples are performed and for all examples the load-displacement curve are shown.

In Zhang, Huang, Li and Zhang (2018), the authors proposes the *Moving Mesh Finite Element Method* (MMPDE) for solving brittle fracture problems using the phase-field. In addition, they use methods for smoothing the strain tensor and calculating the Jacobian matrix using finite differences. The objective of the MMPDE is to generate a uniform adaptive mesh on the metric M by minimizing the functional. In this process the mesh is reorganized and no new nodes or elements are added, this leads to a highly distorted mesh close to the crack. The initial meshes are extremely refined.

In Zhou and Zhuang (2018) an adaptive phase-field method for modelling cracks in rocks is proposed. The strain tensor decomposition by Miehe, Welschinger and Hofacker (2010) is used. For mesh adaptivity, a predictor-corrector scheme similar to Badnava et al. (2017) is adopted. In the first step, the system of equations to predict the crack path is solved. Then, each element of the mesh is analysed to determine which ones will be refined or not. Finally, the system is solved again with the refined mesh. The value of phase-field limit of 0.85 is adopted as a refinement criterion. The brazilian splitting test

is performed for the first time using phase-field models.

In the work by Tian et al. (2019) the so-called *hybrid adaptive finite element phase-field method* (ha-PFM) is used to solve brittle fracture problems. The hybrid phase-field formulation used was proposed by Ambati et al. (2015) and aims to reduce the complexity of deformation tensor division algorithms. It was introduced an adaptive strategy that does not require knowledge of the crack tip. The critical value of phase-field is adopted equal to 0.25 for the refinement criterion. All nodes that have a phase-field value greater than the critical one are marked for refinement. For the refinement process, the set of nodes marked at time t and the set of nodes marked for time $t + 1$ are separated. The nodes that belong to the time set $t + 1$ and do not belong to the time t are considered crack tip nodes. For each of these nodes a rectangular region of refinement is defined and the sum of all these regions indicates the total range of refinement. After finding the refinement region, the division of elements is performed. This division passes through levels as indicated in Fig. 5.6. The zero level refers to the initial quadrilateral elements. Level one is equivalent to dividing the quadrilateral elements into two triangular elements. Level two is the division of each triangular element into two triangular elements. This last step is repeated until finding the expected refinement for the ready crack. The authors indicate that when the expected level of refinement is obtained, two triangular elements are united to form a quadrilateral element again. In addition to the refinement steps, mesh thickening steps also occur in regions where the phase-field value is less than the critical one and the element's refinement level is greater than or equal to 1.

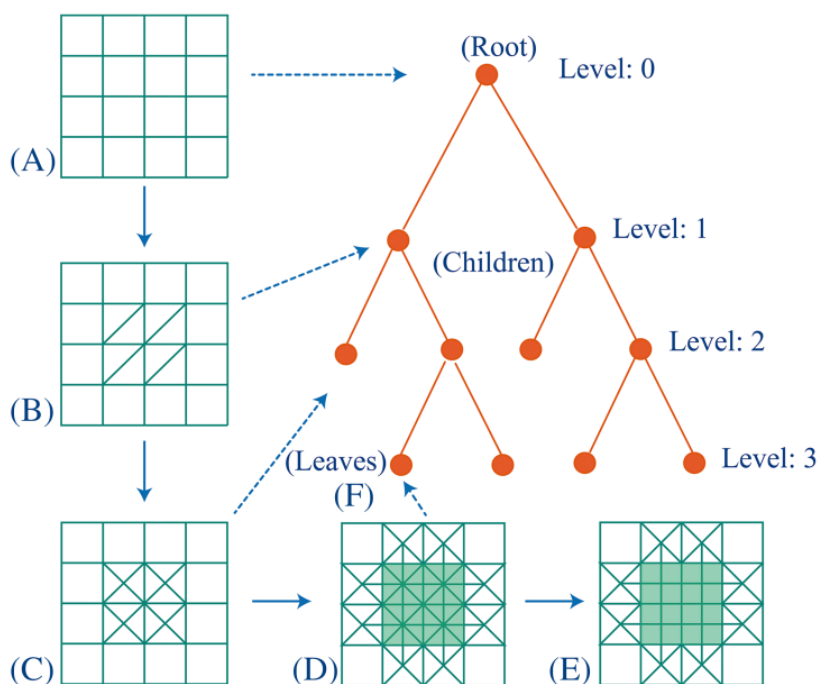


Figure 5.6: Adaptive refinement of Tian et al. (2019).

In Shao et al. (2019) an adaptive refinement for the EFG meshfree method is proposed.

The authors propose as refinement criterion a combination of the value of phase-field and the strain energy. The value of phase-field is high in crack region and zero away from the crack, so this value is usually not adequate for crack initiation. On the other hand, the strain energy has high values for initiation, at the tip crack and crack region. Thus, a combination of the two values proves to be an interesting refinement criterion. The following equation is proposed:

$$(1 - d)^2 H > H_c \quad \text{ou} \quad d > d_c \quad (5.1)$$

where $H_c = 0.6 \max(1 - d_k)^2 H_k, k = 1, 2, \dots, n_{qp}$ being n_{qp} the maximum number of integration points and d_c is the critical phase-field taken equal to 0.4 and 0.5 in the examples. Thus, $(1 - d)^2 H$ has minimum values along the crack and maximum values at the crack tip.

For refinement, it is analysed if the integration points of the integration cells meet the refinement criteria. If the cell needs to be refined, additional nodes are inserted at the midpoint of each side of the cell contour, as shown in Fig. 5.7. With this each cell is divided into four new cells. It is observed that the cells do not have the necessary guarantee of conformity for the MEF. The stopping criterion for the refinement is that the size h of the cells is smaller than a previously informed critical size h_c . Different simulations for brittle fracture problems are illustrated. The initial mesh is coarse compared to previous works.

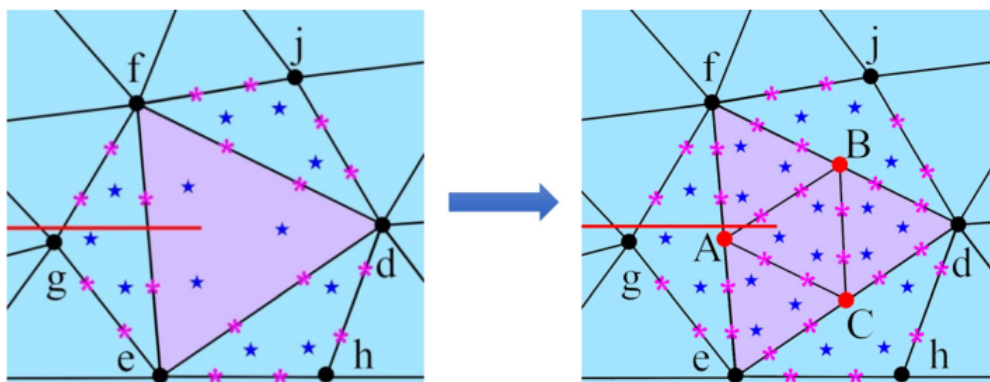


Figure 5.7: Adaptive refinement of Shao et al. (2019).

Hirshikesh et al. (2019) proposed an adaptive brittle fracture phase-field method based on an error indicator and quadtree decomposition. The authors adopted the classic formulation of phase-field with spectral decomposition of the strain tensor and the hybrid model proposed by Ambati et al. (2015). To identify the elements to be refined, they used the recovery-based error indicator proposed by Bordas et al. (2008). In this method, an improved strain field is computed from standard nodal displacements and Moving Least Square type functions. At each point of the domain, the nodes of the support domain are

found, and the nodal values of these nodes are used to calculate the deformations. To calculate the MLS shape functions, the polynomial $P(x) = [1 \ x \ y]$ and the fourth order weight function are adopted.

The error considered is the error between the enhanced deformation field and the standard deformation field. For a certain element i this error is given by:

$$\|e\|_{\Omega_i} = \sqrt{\int_{\Omega_i} \|\epsilon(x) - \epsilon_s(x)\|^2 dx} \quad (5.2)$$

When the error in an element is greater than a certain tolerance, this element undergoes a refinement. This refinement is performed by a quadtree decomposition, where each element splits into 4. The adaptive process is carried out until the element size is $h \leq \frac{h_0}{2}$. The standard tests shear, tension and L-shaped panel are illustrated.

Nagarajara et al. (2019) proposed an adaptive refinement technique using dynamic brittle fracture phase-field and the finite cell method. In the mesh refinement, the multi-level technique hp -FEM presented in (Zander et al., 2015) is adopted. In the hp -FEM technique, smaller and lower polynomial order elements are used in the crack region, larger elements are used in the regions outside the crack, and larger elements with high polynomial order are adopted in the interface region. The implementation of this technique can be complex due to the presence of hanging nodes. This justifies the adoption of the multi-level strategy. In it, the coarse base mesh is superimposed with a finer mesh in the crack regions, not requiring mesh compliance. As a refinement criterion, a phase-field value of 0.25 was considered. The finite cell method is adopted for the mesh generation process through the quadtree subdivision method (Fig. 5.8).

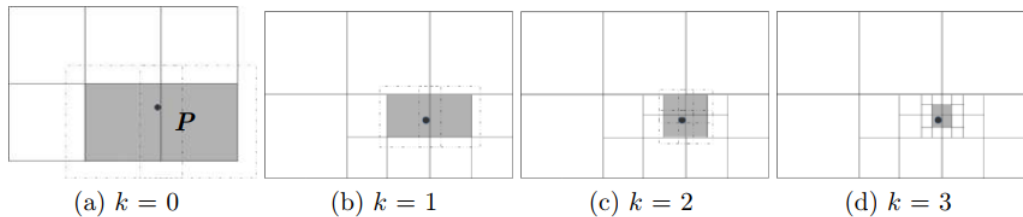


Figure 5.8: Adaptive refinement of Nagarajara et al. (2019) with *quadtree* division.

In the work by Goswami et al. (2020) an adaptive analysis is presented for the fourth-order phase-field proposed in Bourden et al. (2014). The isogeometric analysis is used as a solution tool to guarantee continuity C^1 for the functions, a necessary condition for the fourth-order phase-field. Furthermore, a cubic degradation function is employed instead of a quadratic function. Hybrid alternation is applied as a solution algorithm and a critical value of phase-field is used as a refinement criterion. Prior to the solution, an algorithm runs through all elements of the mesh and verify whether the phase-field value for the integration points is greater than the critical value. If it is higher, a boolean variable is applied to this element that will indicate the need for refinement. In the same

algorithm, the neighborhood elements that must also be refined are analysed. Each level of refinement is obtained by dividing an element into four new elements. After refinement, data from the old mesh must be transferred to the new mesh, among these data are the field variables computed at the nodes and the constitutive variables computed at the integration points. The numerical simulations present that the initial crack region must have a high refinement at the beginning of the analysis.

The work by Nguyen-Thanh et al. (2020), previously presented for meshfree and phase-field methods, shows an adaptive process that uses the phase-field variable together with its gradient as an error estimator. As it is known, the phase-field is a good estimator for regions around the crack, but it is not efficient to indicate crack tip regions. Thus, the gradient is used to indicate these crack initiation regions.

The mean intensity of the error estimator is given by:

$$r_e = g_e \frac{a_e}{n_e}, \quad (5.3)$$

where a_e is the area of the element e and n_e is the number of integration points. The gradient of phase-field is given by:

$$g_e = \frac{\sum_{i=1}^{n_e-1} \sum_{j=i+1}^{n_e} |\phi_i - \phi_j| / l_{ij}}{n_e!}, \quad (5.4)$$

where l_{ij} is the distance between two nodes.

The refinement criterion used by the authors is given by:

$$\text{If } \phi > \phi_c \text{ or } r_e > R_{thre} \quad \text{refine} \quad (5.5)$$

where ϕ_c is the critical value of phase-field and R_{thre} is $0.8R_{max}$.

As shown earlier for works involving meshless methods, Shao et al. (2020) present an evolution of Shao et al. (2019) for three-dimensional problems. The refinement criterion adopted is the same, involving the phase-field value and the historical strain energy. For refinement in the three-dimensional case, a node is inserted on each side of the tetrahedral cell, thus dividing it into eight new tetrahedral cells (Fig. 5.9). After refinement, the old mesh is mapped to the new mesh and the deformations are calculated at the new integration points. From this it is possible to obtain the tensile part of the strain tensor and calculate the historical strain energy.

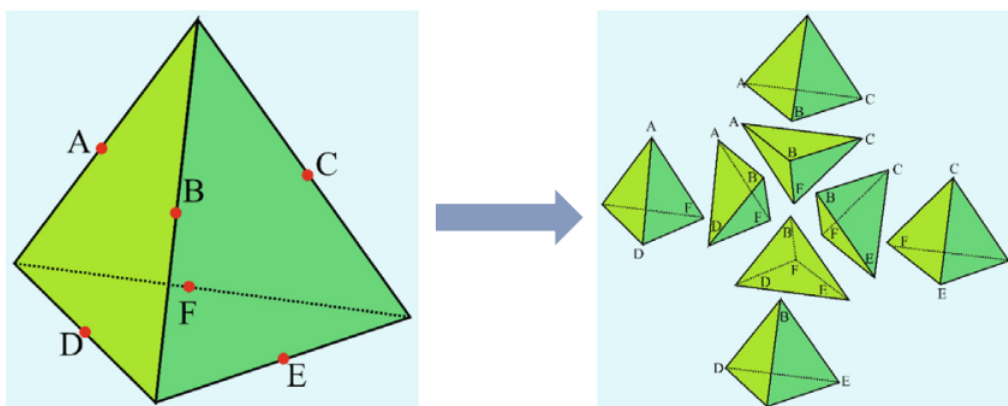


Figure 5.9: Adaptive refinement of Shao et al. (2020).

In Li et al. (2020), the authors proposed the phase-field modelling of brittle fracture in 3D polycrystalline material using an adaptive isogeometric-meshfree method. The gradient of phase-field variable is used as the error estimator for identify the elements for refinement.

In Hirshikesh et al. (2021) is illustrated a adaptive refinement that is based on the stability analysis and quadtree decomposition. The refinement criterion is a stability criteria applied to general degradation function, that in the paper was used the quadratic function. The quadtree decomposition for refinement is similar to other papers.

Qiu et al. (2022) presented a adaptive FEM for hybrid phase-field modelling of 3D cracks. The refinement criterion used was similar to Shao et al. (2019, 2020). For the refinement of the tetrahedral element are inserted new nodes in middle points of edge, centers of surfaces and volume. The displacements and phase-field variables are generated by linear interpolation from parent nodes. Each element have a “refinement level” that indicate the number of refinements that was realized. The hanging nodes have a treatment that consist in three steps:

- The hanging nodes are excluded from being imposed boundary conditions;
- In construction of stiffness matrix and load vector the hanging node is not to be associated to integration points.
- After the solution of the equations, the value of displacement and phase-field of the hanging nodes are obtained by interpolation from parent nodes.

Several examples were presented to validate the strategy proposed and the results indicated a reduction of 80% CPU time.

Similar to other papers, Li et al. (2022) presented an adaptive isogeometric-meshfree approach. The strategy is applied to interfacial debonding in multi-phase materials. The phase-field and its gradient are used as refinement criteria. The critical phase-field variable adopted was 0.6. The implementation of the refinement strategy is similar to Li et al. (2020).

The last article is Yue et al. (2022). The authors using an adaptive bilinear elements

for tensile-compressive-shear fracture. For the discretisation of the problem is used a multi-node element, where it can be inserted nodes on the element boundary arbitrarily and does not raise the orders of quadrature and shape functions. The refinement criterion is based on the phase-field and size of the element. Yue et al. (2022) shown the following analyse:

Suppose that \tilde{d} is the threshold element size for refinement, an element will be divided if $d > \tilde{d}$. \tilde{d} can be computed by

$$\tilde{d} = \begin{cases} d_0 & \text{if } s_{ele} \leq s_{min} \\ l_0/c & \text{if } s_{ele} \geq s_{max} \\ \frac{(s_{max} - s_{ele}) \times (d_0 - l_0/c)}{s_{max} - s_{min}} & \text{if } s_{min} < s_{ele} < s_{max} \end{cases} \quad (5.6)$$

where d_0 is the original mesh size of an element. $s_{min} \leq s_{ele} \leq s_{max}$ is the range for linear interpolation. s_{ele} is the maximum phase-field of all nodes in an element. c is adopted to represent the ratio of the element size for regularized l_0 . $s_{min} = 0.01$, $s_{max} = 0.1$ and $c = 4$ are recommended.

5.1.2 Coupled FEM-meshfree models

Coupled models are models where the domain of the problem is discretised with two different methods, such as FEM and meshfree. As presented, the meshfree methods have many advantages, but they can lead to a high computational cost due to the operations for the shape functions construction. Thus, the coupled models emerge as an alternative and the meshfree methods are applied only in the regions of interest.

Most works in the literature adopt Element Free Galerkin (EFG) as a meshfree method. The main work that studies the FEM-EFG coupling is Belytschko and Organ (1995). In this work, the authors proposed that the elements and the nodes of meshfree have influence in the interface. The coupling satisfies the displacement continuity because a ramp function is used and some nodes of the finite elements are replaced by meshfree nodes. But the derivatives are not continuous at the interface.

The other work that uses the coupling is Duarte et al. (2005) where the authors use the meshfree method based on the partition of unity. The advantage is that these shape functions have the unity partition property which makes the procedure simple.

In Ullah et al. (2013), the authors proposed the used of EFG with maximum entropy shape functions. This functions facilitates the coupling between the models.

Wu et al. (2013) adopted the Reproducing Kernel Particle Method (RKPM) as meshfree method. They used a nodal integration scheme known as *stabilized conforming nodal integration* (SCNI), which is responsible for integrating the entire domain, and capable of storing the state variables directly at the nodal points, making the transition of variable values unnecessary.

Yuan et al. (2014) adopted for the first time the RPIM as meshfree method. In this case, the coupling is directly. In this strategy the domain is initially FEM and it is automatically replaced by nodes of RPIM.

Liu et al. (2016) used the coupling between the *Meshless Local Petrov-Galerkin* (MLPG) and FEM, where the shape functions are RPIMp.

Saliba et al. (2021) proposed, for the first time, the coupling between FEM and SPIM to problems with scalar damage. In the strategy, the user inform the region for substitution and the FEM is replaced by SPIM. Numerical simulations were presented and the results compared with full FEM and full SPIM. The coupled model shown to be capable to preserve the good convergence qualities of a full SPIM.

In relation to phase-field modelling, the only work that presents a coupled between two different discretisation methods is Sargado et al. (2021). In this paper, the authors propose to combine a finite element approximation of the displacement equation using P1 shape functions with a finite volume scheme for the phase-field equation. The phase-field model for brittle fracture is adopted. In the finite volume structure, the way in which the phase field is calculated in the cells allows for the implicit occurrence of a cusp within the control volume and can thus capture the irregularity in the phase field profile more efficiently. Numerical examples are shown and studies about the ratio l_o/h are performed. The results presented that FE–FV yields a lower critical load for a relatively coarse discretisation with $l_o/h = 1$ than FE–FE on a mesh with $l_o/h = 2$. Compared to a pure FE formulation utilizing linear elements, the proposed framework results in looser restrictions on mesh refinement with respect to the phase-field length scale.

5.1.2.1 Coupled FEM-SPIM models

In the coupled models, the domain (Ω) is divided in two or more regions (Ω_1 and Ω_2), and the interface (Γ_i) as illustrated in Fig. 5.10.

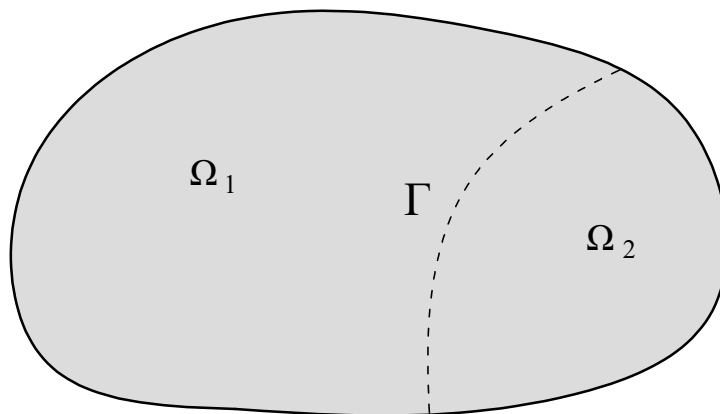


Figure 5.10: Coupled model.

For the coupling between the two models, the compatibility of displacement and the load equilibrium conditions must be satisfied:

- the nodal displacement $u_i^{(1)}$ and $u_i^{(2)}$ in Γ_i for Ω_1 and Ω_2 must be equal:

$$u_i^{(1)} = u_i^{(2)} = u_i \quad (5.7)$$

- the forces $f_i^{(1)}$ and $f_i^{(2)}$ in Γ_i for Ω_1 and Ω_2 must be zero:

$$f_i^{(1)} - f_i^{(2)} = 0 \quad (5.8)$$

The compatibility of displacement is the main requirement for the coupling. As the SPIM methods possess the Kronecker delta property, the coupling is performed directly and any additional technique is unnecessary.

To calculate the stiffness matrix of the complete domain, the sums of the FEM region and the SPIM region are performed. For the nodes in the transition zone the stiffness is given by:

$$K_{ij} = K_{ij}^{SPIM} + K_{ij}^{FEM} \quad (5.9)$$

5.2 Adaptive FEM-SPIM coupling strategy

As presented in the literature, several works have implemented adaptive refinement strategies for phase-field models. In this work is presented, for the first time, an adaptive FEM-SPIM coupling strategy for phase-field modelling of fracture.

In Novelli, Gori and Pitangueira (2022), the authors indicated that the SPIM meshfree methods were able to correctly reproduce the contour plots of crack and load-displacement curves. On the other hand, due to the high refinement of the mesh of the phase-field this methods presented a high pre-processing cost. This pre-processing refers to the preparation of the model, that consists in loading the smoothing domains data and in searching for the support nodes at each integration point on the boundary of the smoothing domains.

In Saliba et al. (2021), the authors illustrated the advantages of using coupled FEM-SPIM for damage models. The first advantage is that the coupling between SPIM and FEM does not require the use of additional techniques, as presented in Section 5.1.2.1. This occurs because SPIM has the Kronecker delta property. The second advantage is that the model start with only FEM and in the regions of interest the model is replaced by SPIM. This strategy reduces the computational cost.

In Saliba (2022), the author proposes an adaptive FEM-SPIM coupling for elastic degradation constitutive models. In the strategy presented, the model is initially discretised only by finite elements and throughout the analysis a criterion detects the regions that will be replaced by SPIM. During the adaptive strategy, if necessary, the integration

point of the T3 elements can be converted in a new node and one level of refinement additional can be performed in the meshfree region. The edge-, cell- and node-based can be adopted as smoothing domains. The numerical results presented a good agreement with the experimental results as well as the damage configuration at the end of the simulation.

Combining the advantages presented for SPIM with phase-field models and coupled FEM-SPIM models, the use of an adaptive FEM-SPIM coupling for the discretisation of phase-field problem can present interesting results. It is also important to emphasize that although phase field models require more refined meshes compared to damage models, they are capable of simulating more complex cracks.

In this new strategy, similar to Saliba (2022), the SPIM is adopted in the crack regions while the FEM is adopted in the rest of the domain. The coupling can be performed of two ways: a fixed coupling and an adaptive coupling.

When the crack path is known and the mesh has the adequate refinement, the coupling is performed in preprocessing time. In this case, the user informs the region of substitution and the FEM model is substitute by SPIM method before of the solution. There are two ways of indicate this region: informing the identifier of the elements or the polygon region. As in phase-field mesh the number of elements is too high becomes impracticable inform all elements for substitution. In the polygon region, the user must inform the vertices of the polygon and all the elements that are contained in the region are replaced. During the solution process all matrices and vectors are assembler together for FEM model and meshfree model.

This previous coupling was studied in Novelli, Saliba, Gori and Pitangueira (2022). In this article, the authors knew the crack path and then was informed the polygon region for substitution. The edge and cell based were used for the smoothing domains. Two numerical simulations were shown to study this strategy, the tension test and the bending test. The results were compared with the literature and with complete domain with FEM. The load-displacement curves obtained in both tests presented a good agreement with the results of the literature and FEM. The contour plots for the phase-field were analysed too and the results were similar to those of the literature.

When the crack path is not know or the mesh does not have the adequate refinement is performed the adaptive coupled process. This process is presented next in Section 5.2.1.

5.2.1 Adaptive strategy

In this strategy, the coupling and adaptivity are performed during the solution of the problem. The adaptive strategy is illustrated in Fig. 5.11, and is composed by the following steps.

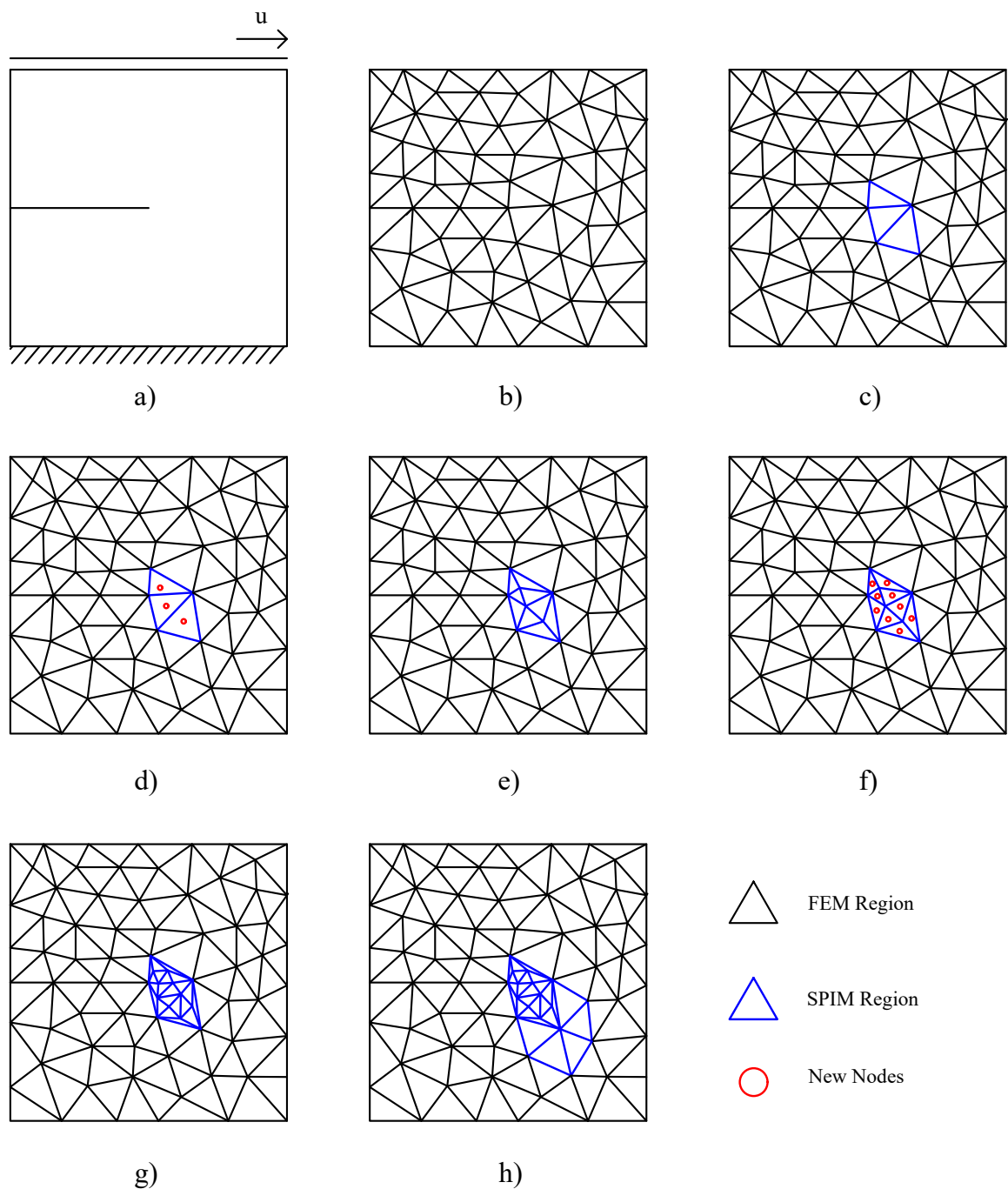


Figure 5.11: Adaptive strategy.

- (a) The model adopted to exemplify the strategy is the shear test.
- (b) Initially the model is discretised only by finite elements in a coarse mesh.
- (c) A criterion identify the region that must be substitute by meshfree method. In the case of shear test, this region is the tip crack and the blue elements are replaced. There are many parameters that are used in the process of modification of the model and that treated throughout the text.
- (d) In the processing of substitution, the integration points of the elements can be converted in new nodes (red points).

- (e) If new nodes are inserted, the meshfree region is refined.
- (f) During the analysis, if a higher level of refinement is required, new nodes are inserted in the center of the cell of the meshfree region.
- (g) A new triangulation is generated and new smoothed domains are created.
- (h) With the propagation of the crack, new regions of FEM elements are replaced by SPIM regions.

The phase-field solution is composed by three steps: solution of the displacement equation, solution of phase-field equation and global convergence check. In the adaptive strategy, the verification of the modification of the model is realized after the “global convergence”, that refers to converged of both displacement and phase-field. The new incremental-iterative process for phase-field models is presented in Fig. 5.12.

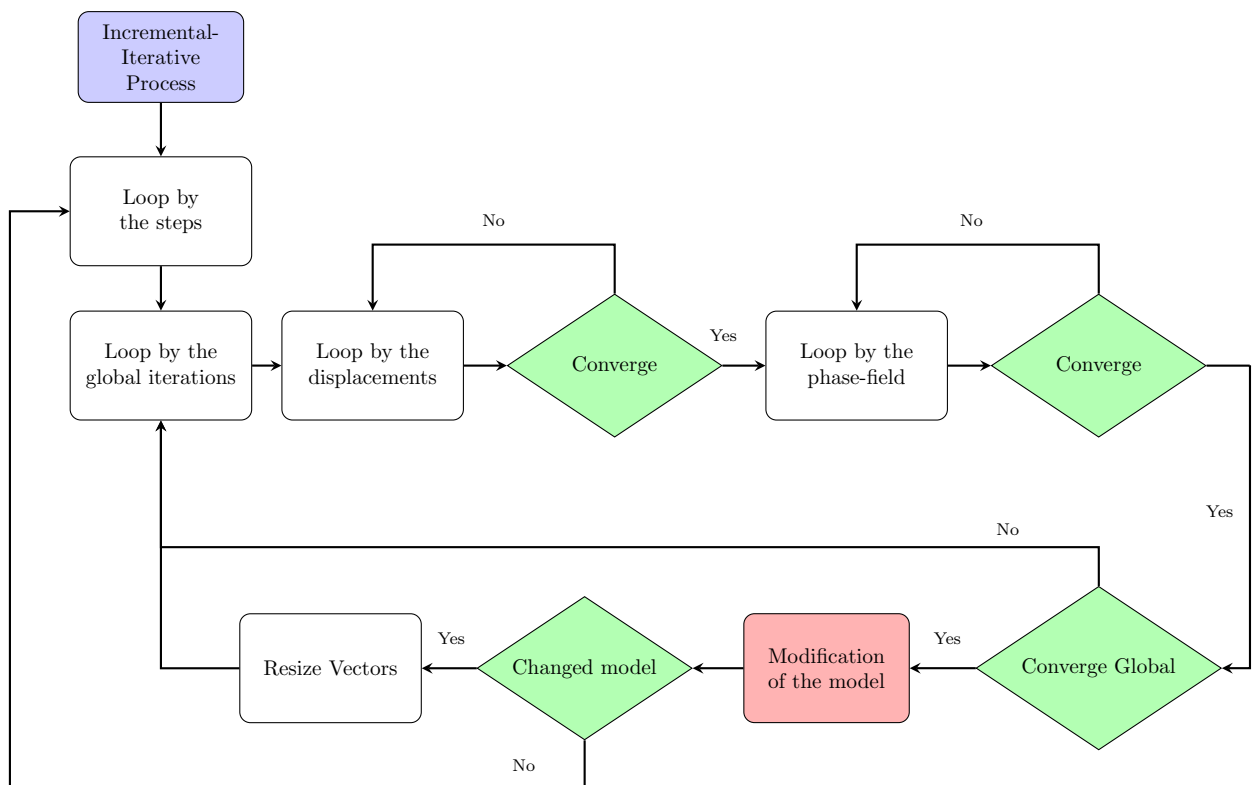


Figure 5.12: Flowchart of the incremental-iterative process.

This process of the phase-field solution is composed by the loop by the steps and loop by the global iterations. The loop by the steps corresponds to increment of load or displacements and the step converges when the global convergence is achieved. Each global iteration refers to the solution of the displacement problem and the phase-field problem. After the global convergence is activated, the verification of the model is performed. If the model has not been modified, the analysis proceeds to the next step. If the model has any modification, the vectors are resized and a new global iteration is performed. The resizing of the vectors is better explained in Section 5.2.5. The new global iteration is important for verifying the convergence of both displacement and phase-field variables after the

modification of the model.

With this strategy is possible to performer many substitutions and level refinements in a single step. It is important emphasize that after each modification, substitution or refinement, the correction iterations are performed. In each modification, the model is substituted or refined, the two operations are not performed simultaneously. The control of this operations is realized external to iterative process and this will be dealt with later in Section 5.2.2.

The strategy of can be realized many modifications in a single step is very important in the phase-field models. In this models, the crack can be propagated quickly and it is necessary that the level of refinement in the crack region be adequate. The criteria that detected the crack region search the crack tip but is not possible indicated a large region ahead of the crack. That way, the substitutions are realized slowly and many refinements in the same step ensure that the crack grows together with the mesh. In the numerical simulations is possible to verify this strategy.

5.2.2 Modification of the model

According it was presented, the modification of the model is external to incremental-iterative process. In this stage, it is analysed whether a substitution or refinement is necessary. Each modification is performed independently. The Fig. 5.13 present this process.

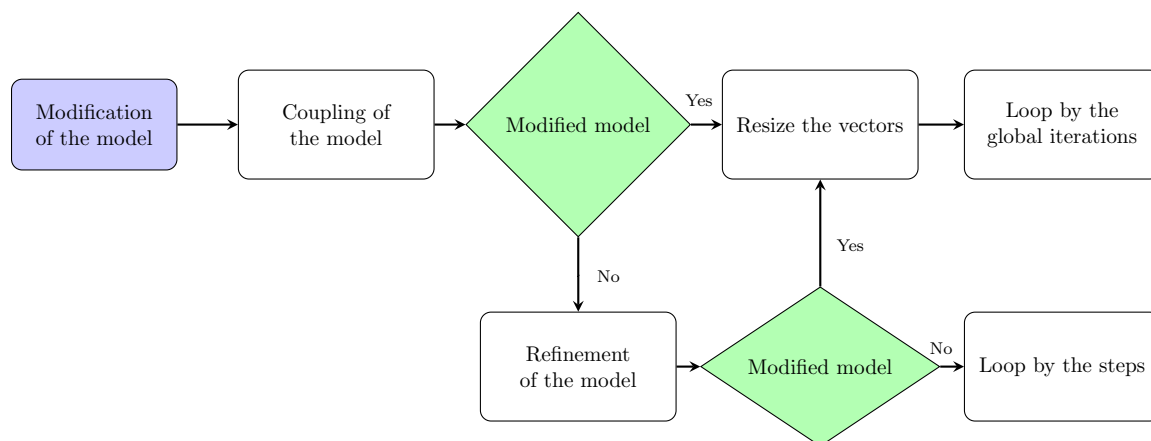


Figure 5.13: Flowchart of the modification of the model.

The first step is verify the substitution. A criterion identify the elements that need to be replaced by SPIM method. This substitution can be in more than one region of the model. If any replaced was performed, the process return to incremental process for resize of the vectors. The substitution of the elements in a coupled meshfree is shown in Section 5.2.3.

The second step is verify the refinement. This verification is activated if no replacement was realized in the current global iteration and if the user indicated that the model need

of refinement. If any refinement was performed, the process return to incremental process for resize of the vectors. The strategy of refinement of the meshfree region is presented in Section 5.2.4.

If no replacement or refinement has been performed the process return to incremental process for a new step of load and no resize of the vectors is necessary.

5.2.3 Coupling FEM-SPIM

In the coupling between the methods SPIM and FEM, some elements of the FEM are substitute by a meshfree region. As the shape functions of the SPIM posses the Kronecker delta property, no treatment is needed on the contour between the models. The stages of this process are illustrated in Fig. 5.14.

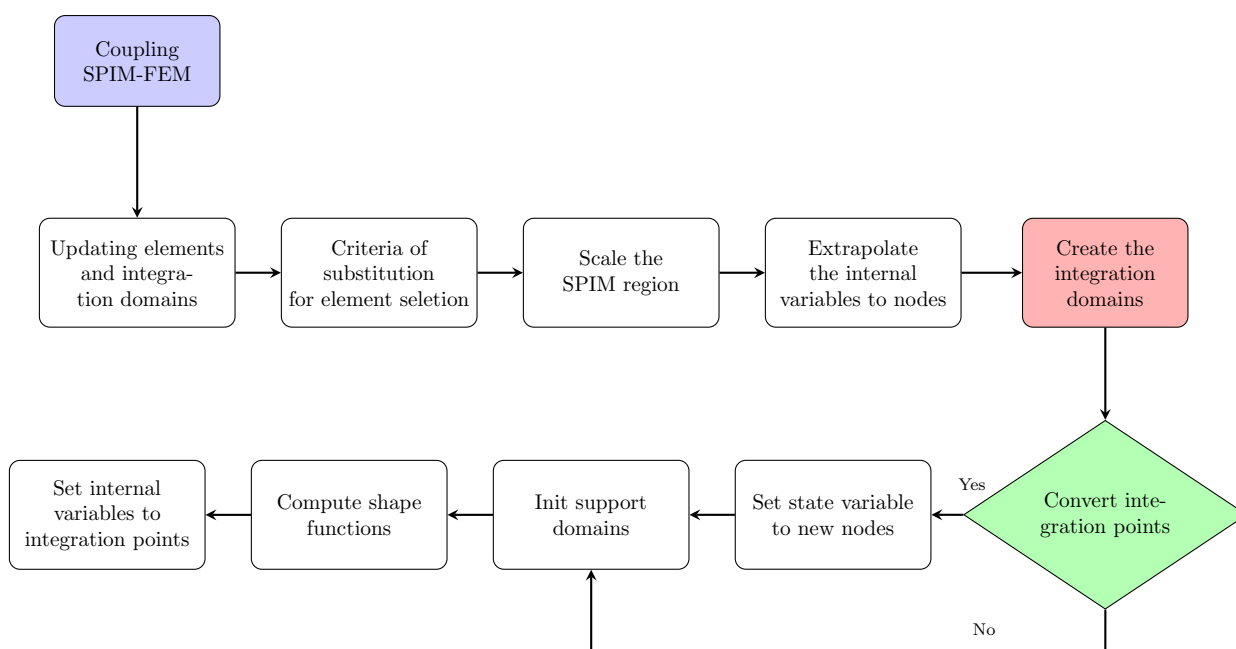


Figure 5.14: Flowchart of the coupling FEM-SPIM.

The first stage is detected the elements for the substitution. There are different criteria for this and they are presented in Section 5.2.3.1. This criterion is the first parameter of the adaptive strategy.

After detecting the elements, the region for the substitution can be increased. This stage is important for three reasons: first is that entire region of the crack is in the meshfree region, second is that the transition between the two models is smooth and third that does not present distorted cells. This importance is better observed when is need a high level of refinement in the meshfree region. This increase of the region is given by the following strategy. For each detected element is generated a region around of the integration point. All the elements of the mesh that have your integration points include in this region are adding to substitution region. There are two parameters that control

this window of selection: the shape and the scale. The shape can be circle or square and the scale modify the length of this window. For the circle, the scale modify the diameter and for the square modify the edge. The shape and scale are parameters that given be informed by the user for the adaptive strategy.

In the process, all the elements selected for the substitution are excluded of the FEM mesh, but these elements contains in their integration points the constitutive variables. These variables give be transferred to the integration points of the meshfree model. In this case, as smoothing domains are used, the variables are transferred to the integration point of each domain. The strategy used to not lose the constitutive variables is to transfer these variables to nodes and then recover them to the integration points. For the phase-field models, this transfer is performed using simple average. A loop is performed through all nodes in the meshfree region. For each node, the elements and the smoothing domains that have this node as a vertex are found. The integration points of these elements and smoothing domains are used for the average.

The next step is to build the meshfree model. In this stage, integration domains are created and the process is presented in Section 5.2.3.2.

From these integration domains, the shape functions are calculated for the central integration point of the smoothing domain and for the integration points of the boundary that are used for compute the derived shape function.

If the integration point of the elements was converted into a new node, this node needs to have the state variable. These state variables are displacements and the phase-field variable. These variables are interpolated using the shape functions of the elements. Next, the element is excluded from the FEM model.

The last process is to set the constitutive variables for integration points. If the coordinates of the integration point are the same of the old integration point, the constitutive variables are cloned, otherwise the variables are obtained from the values stored in the nodes. In this case, the calculation varies according to the smoothing domain type. For cell-based, the values are obtained by averaging the three nodes. For edge-based, the values are obtained by averaging the two nodes.

5.2.3.1 Substitution criteria

In this strategy, the substitution criterion is responsible for obtaining the set of FEM elements that should be replaced by the SPIM region. In the phase-field models, it is interesting that the region found for substitution is the crack region. The most used parameter in the literature is the phase-field value, but there are other parameters can be used.

The criteria implemented in this work are shown below.

- Phase-field value:

All the elements that have the phase-field value at the integration point greater than

the reference are marked for substitution. As the phase-field presents values between zero and one, this parameter can be easily indicated by the user. The smaller the adopted value, the larger the replacement area. The disadvantage of this parameter is that the FEM model will be replaced by the meshfree model only when the analysis is already advanced, that is, when the phase-field presents high values in the model. In other hand, this parameter works very well when the model has a crack with a prescribed phase-field.

- Strain energy:

In this criterion, the elements that present the strain energy greater than the average strain energy of the model multiplied by a factor are selected to replacement. This factor is the parameter that can be informed by the user in the adaptive strategy. The average strain energy is calculated as:

$$U_{average} = \frac{1}{A_{total}} \left(\sum_{i=1}^{n_{elem}} \frac{A_i}{2} \varepsilon_i \sigma_i + \sum_{j=1}^{n_{id}} \frac{A_j}{2} \varepsilon_j \sigma_j \right) \quad (5.10)$$

where A_{total} is the total area of the domain, n_{elem} is the number of FEM elements, n_{id} is the number of integration domains, A_k is the area of the element or integration domain, ε_k is the strain vector and σ_k is the stress vector.

The advantage of this criterion in relation to the phase-field is that the strain energy is able to detect regions for replacement from the beginning of the analysis. The disadvantage of this criterion is that it detects tension and compression regions for replacement and in the phase-field model it is interesting that only tension regions are detected.

- Equivalent strain:

In this criterion, all the elements that present equivalent strain greater than the limit value are marked for replacement. This limit value is informed by the user. The equivalent strain adopted is proposed by Mazars (1984) as:

$$\sqrt{\sum_{i=1}^3 \langle \varepsilon_i \rangle_+^2} \quad (5.11)$$

where ε_i are the eigenvalue of the strain tensor and $\langle \varepsilon_i \rangle_+ = (\varepsilon_i + |\varepsilon_i|)/2$ its positive part.

In this criterion, the user must inform the limit value and this value does not have a range of values like the phase-field.

- Shao criterion:

This criterion was proposed by Shao et al. (2019) and it was shown in 5.2. It adopts the phase-field value and the strain energy history. The strain energy history consider the energy associated with the traction part of the problem. Remembering that the value of phase-field is considered high throughout the crack and zero outside it, so this value alone cannot be used to indicate crack initiation and crack tipping. On the other hand, the strain energy presents high values for initiation, at the crack tip and throughout the crack. Thus, a combination of the two parameters proves to be an interesting refinement

criterion.

The criterion is given by:

$$(1 - d)^2 H > H_c \quad \text{ou} \quad d > d_c \quad (5.12)$$

$$H_c = factor * max(1 - d_k)^2 H_k \quad (5.13)$$

where k is the number of FEM elements and integration domains, $factor$ is factor that limit the criterion and d_c is the critical phase-field.

Thus, the user must inform two parameters $factor$ and d_c . The parameter d_c is similar to phase-field criterion because detect the regions with phase-field greater that the limit. The parameter $factor$ control the H_c that detected the region of crack initiation and crack tip.

As already mentioned, this criterion is able to detecting elements for substitution at the beginning of the analysis and only the traction regions.

5.2.3.2 Building of the SPIM model

From the elements that will be replaced and of the old meshfree region, a new meshfree region is created. The process of building a new meshfree model is illustrated in Fig. 5.15.

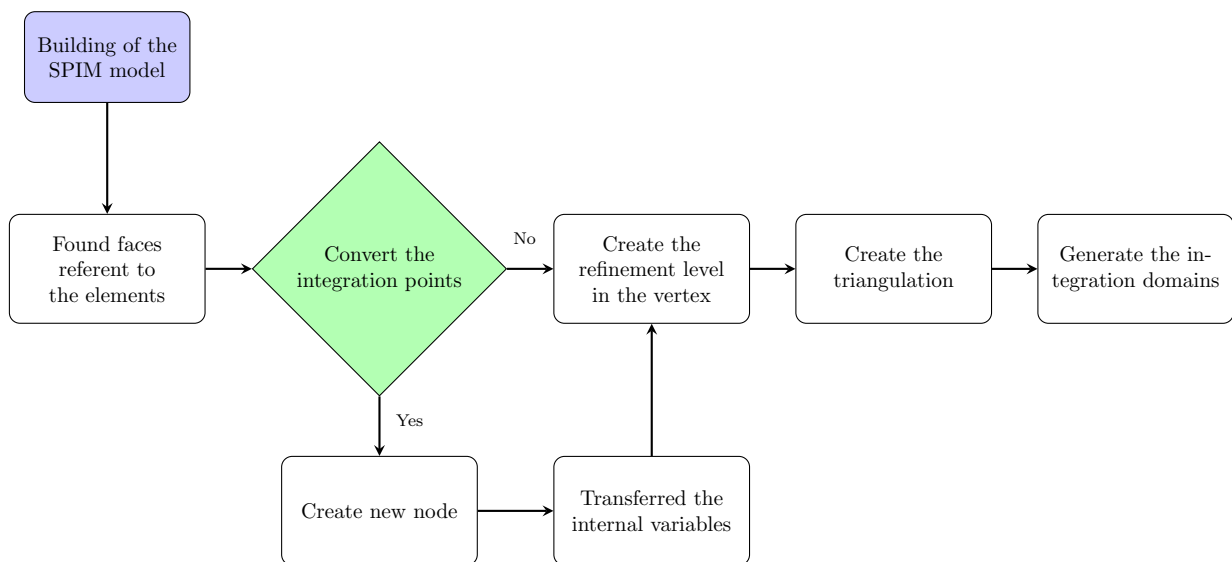


Figure 5.15: Flowchart of building of the SPIM model.

In the process of creating of the new model, it is necessary to create the new halfedge data structure and from it create the integration domains.

The first stage is to store the old face list of the meshfree model. The second stage is to find the faces referring to the elements and organize in the correct region. At is time, adjacent faces are found the regions are joined when necessary.

The next stage is to check the third important parameter of the adaptive strategy: the convert of the integration point. The user can choose to convert the integration point. In this case, the integration point of the element is converted to a new node. The constitutive variables are transferred directly to node and this node is added to model. The adoption of this strategy increases the refinement of the meshfree region.

With all faces, the boundary of the region is found by checking the edges of the faces. If the edge belongs to more than one face, this edge is internal.

The next stage is exclusive of the adaptive strategy for phase-field models. Add the vertex refinement level. The level is added at the vertex because the faces are replaced every time that the model is refined and this information would be lost during the analysis. At the time of substitution, the vertex has not undergone any refinement, so it is set the level zero.

With all the vertices and the boundary of region the new halfedge data structure is created. In this process, Delaunay is adopted to create the triangulation.

The last stage of building of the model is generate the integration domains. As presented, in SPIM the integration domains are the smoothing domains. They can be based on cell, edge or node. In this study, the cell and edge-based are adopted and the triangular background mesh is used for the construction.

5.2.4 Refinement SPIM

The adaptive refinement is applied when a region of the model has already been replaced by a SPIM model and further refinement is required. The refinement strategy is divided into the steps presented in Fig. 5.16.

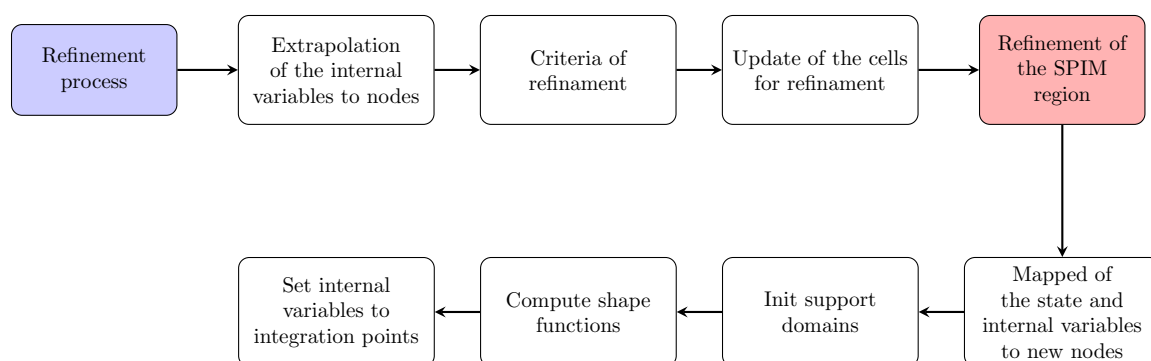


Figure 5.16: Flowchart of the refinement of the SPIM region.

Different of the substitution, the refinement is applied in the regions with meshfree methods. In the SPIM methods, the integration domains are based on cells or edge and these domains are generated from the triangular background mesh. In the adopted strategy, the integration domains are not refined, but the background cells and the new integration domains are generated. In this case, it is necessary to find the triangular cells

that need refinement. These cells do not have the constitutive variables stored. Thus, the first step is extrapolate the constitutive variables of the integration points to the nodes. This stage is similar to the one performed in the substitution. For each node of the meshfree region, the integration points of the elements and smoothing domains that have this node as a vertex are found. For the set of integration points, the average value is calculate and stored in the node.

The next step is to detect the cells that needs of refinement. There are many criteria and they are shown in Section 5.2.4.1.

After selecting the cells that need refinement, these cells are updated. In this stage, it is checked if the cell can be refined or not. There are two cases where the cell cannot be refined: the cell belongs to the boundary or the cell has the refinement level limit. The boundary cells are not refined so as not to generate distorted cells. Regarding the refinement level limit, this is a parameter entered by the user and stored in the vertices. In this refinement strategy, at each refinement new nodes are added and a new triangulation is generated. Thus, the informations of the faces are lost therefore it was chosen decided to store this parameter in the vertex. This level of refinement is related to the initial mesh and the length scale (l_0). As previously presented, there are relationships between these two parameters that must be adopted according to constitutive model. A face is marked for refinement when the refinement level of all its vertices is less than the limit refinement level.

With a set of faces in need of refinement, the next step is to perform the refinement of the faces and creation of the integration domains. This process is presented in Section 5.2.4.2.

In the refinement, new nodes were added in the SPIM model. For these new nodes is necessary mapped the state and internal variables. For the mapping of the state variables, each face is considered as a T3 element and these variables are computed from the shape functions. Displacements and phase-field are these variables. For the mapping of the internal variables, the values for the new nodes are obtained from average of the vertices that belong to face.

From the support nodes scheme, the support domains are generated for all nodes of the meshfree region and the shape function are computed.

The last step is mapped the internal variables for the integration points of the integration domains. This variables are stored in the nodes and they are mapped to the integration points similar to presented in the coupling.

5.2.4.1 Refinement criteria

There are different criteria can be used to detected the region of the meshfree domain that need to refinement. They are: phase-field, strain energy and equivalent strain. All these parameters use the same strategy.

The objective is detected the face that need a refinement, for this is measured the parameters stored in the vertices of the face.

The first step is to calculate the average value of the face. This calculation is performed by a simple average between the value of the three vertices.

The second step is to calculate the average value of the all meshfree region $p_{meshfree}$. This value is given by the Eq. 5.14:

$$p_{meshfree} = \frac{1}{A_{meshfree}} \sum_{i=1}^{n_{cell}} p_i^{cell} A_i^{cell} \quad (5.14)$$

where $A_{meshfree}$ is the total area of the meshfree region, A_i^{cell} is the area of the face and p_i^{cell} is the average value of the parameter in the face.

The third step is to compare the parameter of the face with the average parameter of the meshfree region. All the faces that have a value greater than the average value are refined.

$$p^{cell} \geq Factor_f * p_{meshfree} \quad (5.15)$$

where $Factor_f$ is the combination of two other parameters informed by the user.

These parameters are $Factor_{critical}$ and $Factor_{DecayRate}$. $Factor_{critical}$ has as objective modify the average value of the meshfree region and $Factor_{DecayRate}$ modify the $Factor_{critical}$ for that the refinement is realized gradually in the region.

If the number of refinement (n_{ref}) is smaller that the limit refinement level (n_{lim}):

$$Factor_f = Factor_{critical} - (n_{lim} - n_{ref}) * Factor_{DecayRate}.$$

If the number of refinement is greater that the the limit refinement level:

$$Factor_f = Factor_{critical}.$$

5.2.4.2 Building the refined SPIM model

The refinement process is illustrated in Fig. 5.17.

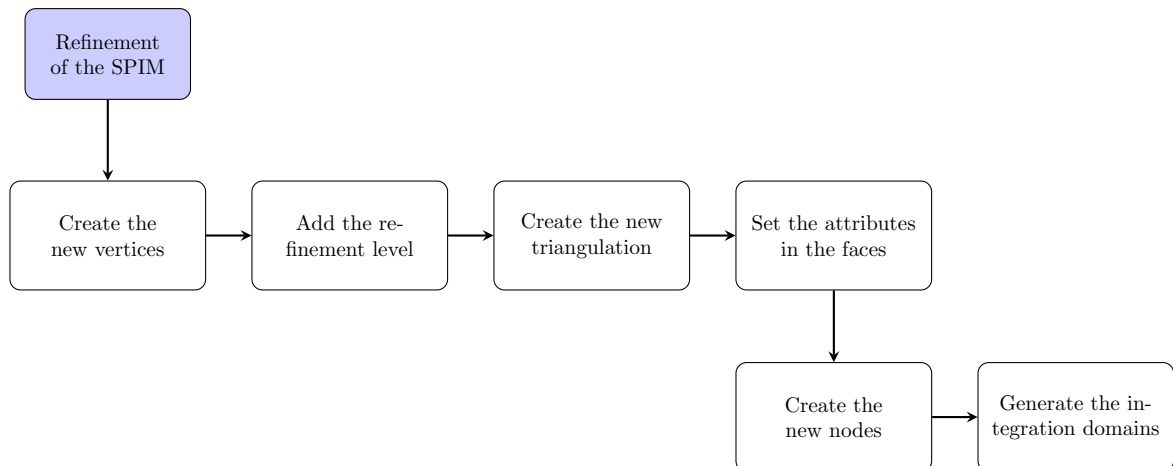


Figure 5.17: Flowchart of building the refined SPIM model.

The first stage is to create the new vertices. These vertices are created at the centroid of the faces and in the boundary when necessary. In this moment, all the vertices of the refined faces have the “RefinedLevel” added by one and the “RefinedLevel” of the new vertex is the lowest level of the vertices of the face.

With all the vertices and the boundary of the domain, a new triangulation is generated using the Delaunay. For the new faces is added the attributes as type of shape functions, analysis model and support node scheme.

In the sequence, new nodes are created from the new vertices added. These nodes are numbered from the total number of nodes in the model and are added to the model.

From the triangulation, the integration domains are created. This domains can be cell or edge based.

5.2.5 Resize the vectors of the incremental process

After substitution or refinement of the model, the vectors of the incremental-iterative process need to be resize. These vectors are external load, internal load, displacements and phase-field.

In this stage, check how many nodes were added to the model and increase these vectors. The value of the variables for the new nodes is set to zero. This values will be corrected in the next global iterations.

Chapter 6

Fixed mesh simulations

This chapter presents the results of phase-field simulation performed with fixed discretisations, that is without resorting on adaptive strategies. Section 6.1 deals with domains that are fully discretised by an SPIM discretisation, while Section 6.2 considers a fixed SPIM-FEM coupling. Since there is no adaptivity, all the discretisations are refined in the known region of crack propagation.

6.1 Full SPIM discretisations

The objective of this section is to validate the use of SPIM for discretisation of the phase-field models. Two examples are presented: three point bending test and L-shaped panel. Remembering that many verifications are presented in Novelli, Gori and Pitangueira (2022).

6.1.1 Three point bending test

This example refers to the three point bending test investigated by Miehe, Hofacker and Welschinger (2010). The geometry, loading and boundary conditions are shown in Fig. 6.1. The plane-strain state is considered and the following material parameters are adopted: Young's modulus $E = 20.8 \text{ kN/mm}^2$, Poisson's ratio $\nu = 0.3$, critical energy release rate $G_c = 5.0 \times 10^{-4} \text{ kN/mm}$ and length scale parameter $l_0 = 0.06 \text{ mm}$. The exponential radial basis function (Eq. 3.23) is adopted with $c = 1$. The constitutive model of Miehe, Welschinger and Hofacker (2010) is applied with the energetic degradation function of Bourdin et al. (2000) and the geometric crack function with $\xi = 0$.

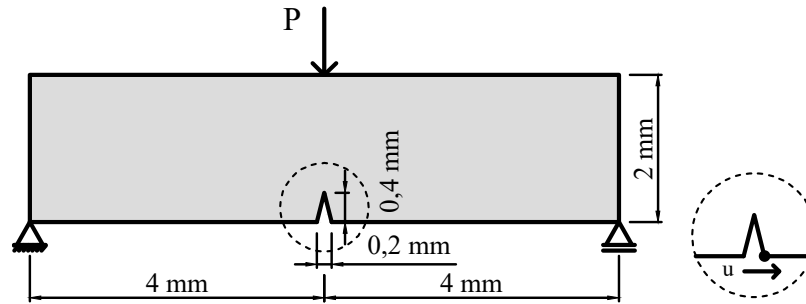


Figure 6.1: Bending test: Geometry, loading and boundary conditions.

The domain was discretised considering a nodal spacing of 0.02 mm in the phase-field propagation region, resulting in the nodal distribution illustrated in Fig. 6.2, and in the FEM mesh and smoothing domains illustrated in Fig. 6.3.

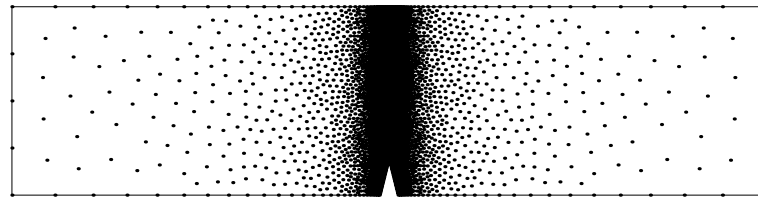


Figure 6.2: Bending test: Nodal distribution.

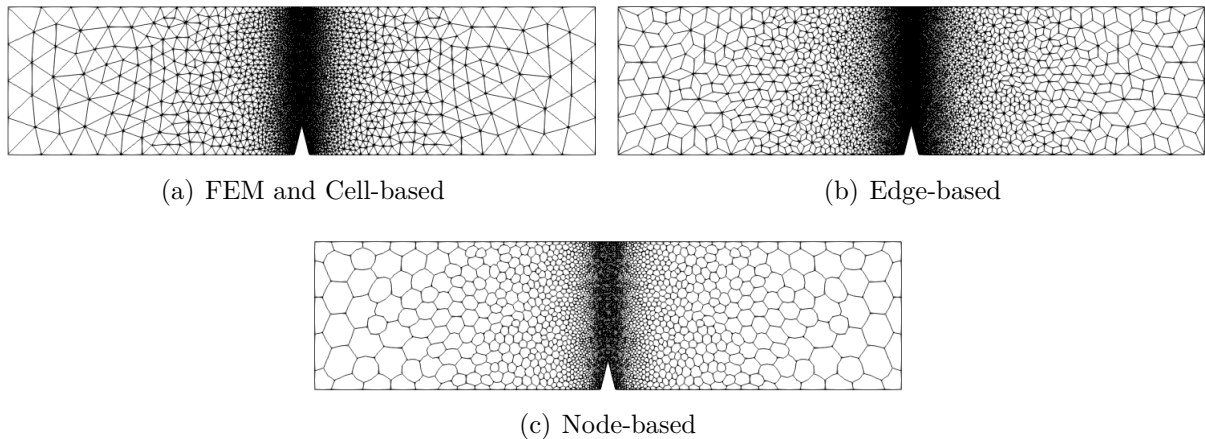


Figure 6.3: Smoothing domains and FEM mesh of the bending test.

The nonlinear process was solved using the direct displacement control method, considering increments $\Delta u = 1 \times 10^{-4}$ mm of the horizontal displacement of the control node depicted in Fig. 6.1.

The results in term of load-displacement paths for the point of application of the load are illustrated in Fig. 6.4 for the different SPIM strategies and FEM. The results obtained with the SPIM strategies, except the NS-RPIMp, presented a good agreement with the reference Miehe, Hofacker and Welschinger (2010), for the peak load and post-critical behaviour. The path obtained with FEM presented a different initial slope compared

with the reference, but the peak load is similar. In the analyses it is possible to observe a “snap-back” in the paths, which has not been shown in the reference. It was possible to describe the snap-back behaviour because the horizontal displacement of the crack opening point was controlled, in a different strategy from the one used by Miehe, Hofacker and Welschinger (2010) that have chosen to control the vertical displacement of the load point.

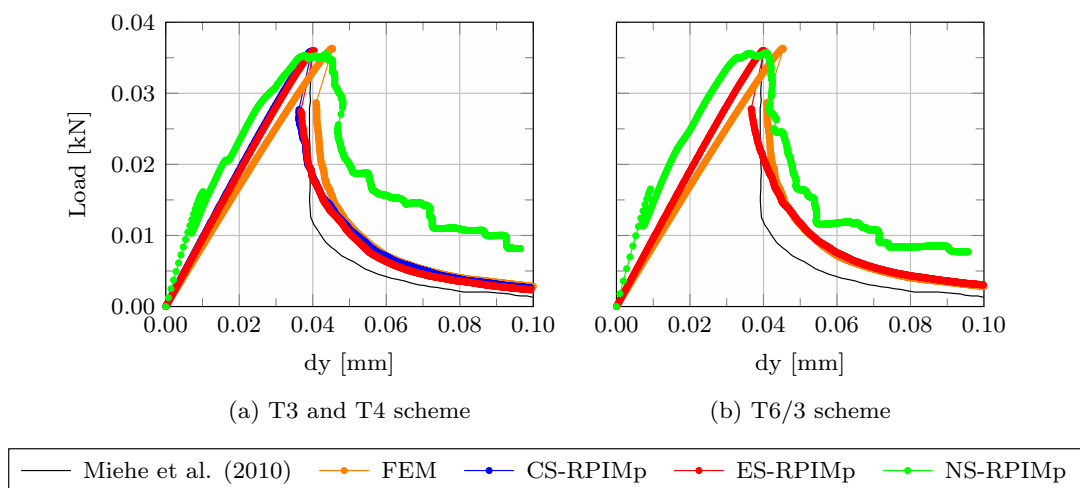


Figure 6.4: Load-displacement paths of the bending test.

The contour plots of the phase-field at three different steps of the analysis, considering for simplicity only the ES-RPIMp with T3 scheme, are depicted in Fig. 6.5. The results are in good agreement with those presented in the literature Miehe, Hofacker and Welschinger (2010), Wu et al. (2019), Kasirajan et al. (2020), Bhowmick and Liu (2018), as can be seen in Fig. 6.5 (d).

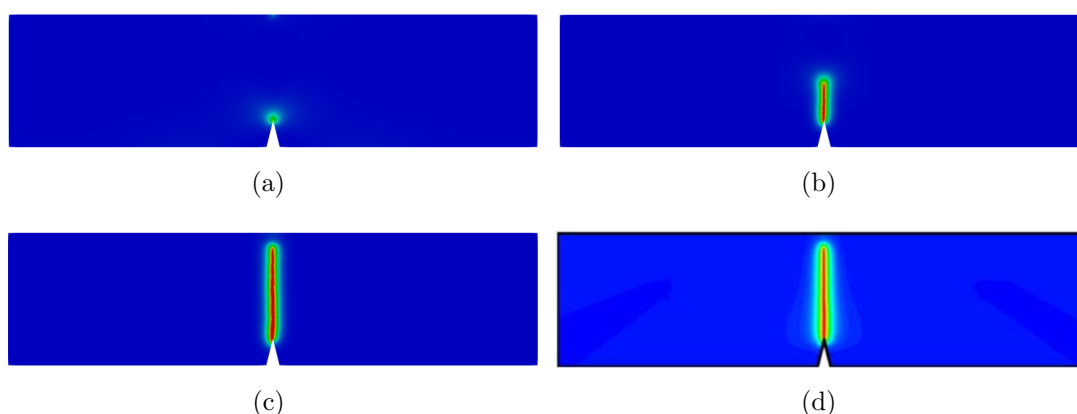


Figure 6.5: Phase-field contour plots for the bending test with ES-RPIMp T3. Displacements of (a) 4.02×10^{-2} mm, (b) 4.17×10^{-2} mm, (c) 9.94×10^{-2} mm and (d) Reference Miehe, Hofacker and Welschinger (2010).

For this example, the efficiency of the different strategies is also verified. The parameters chosen to measure the efficiency are the number of iterations needed to solve each

incremental step of the nonlinear process and the time required to perform different pre-processing and processing tasks. These iterations correspond to the ones named “global iterations” (Section 5.2.1). The analyses performed with the node-based strategy are excluded from these results, since this approach has been shown to be unable to correctly reproduce the load-displacements paths.

Fig. 6.6 presents the total number of iterations of the analyses. As it can be observed, the different strategies exhibited a similar number of iterations, with the meshfree approaches performing slightly better than the FEM.

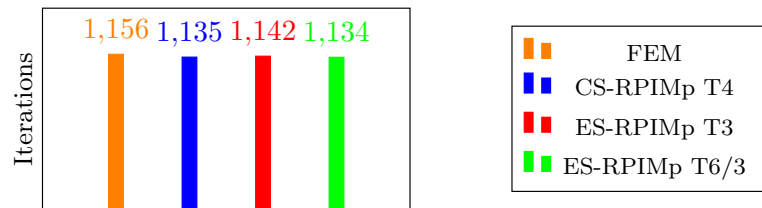


Figure 6.6: Total number of iterations of the bending test.

The computational time required for the simulations is shown in Table 6.1. The computational time is divided between processing time and preprocessing time, the latter further divided into: smoothing domains construction, support nodes selection, and shape functions evaluation.

Table 6.1: Computational time (in ms) of the bending test.

Strategy	Preprocessing			Processing	Total
	Smoothing Domains	Support Nodes	Shape Functions		
FEM	-	-	-	4.3733×10^6	4.3733×10^6
CS-RPIMp-T4	1.7100×10^2	7.4206×10^4	4.0700×10^2	2.1174×10^6	2.1922×10^6
ES-RPIMp-T3	2.8249×10^5	1.1600×10^2	8.4700×10^2	2.4627×10^6	2.7461×10^6
NS-RPIMp-T3	3.7188×10^4	1.4700×10^2	7.1200×10^2	2.9469×10^7	2.9508×10^7
ES-RPIMp-T6/3	2.8249×10^5	6.0926×10^5	9.7900×10^2	4.0871×10^6	4.9798×10^6
NS-RPIMp-T6/3	3.7188×10^4	4.9249×10^5	8.6800×10^2	5.2877×10^6	5.8182×10^6

As it can be observed, the meshfree approaches exhibited a lower time than the FEM, except in the case of the NS-RPIMp and ES-RPIMp with T6/3 support nodes schemes. The table clearly show that the performance of the SPIM strategies is strongly affected by the preprocessing tasks. It’s worth emphasising that in the SPIM analyses the shape functions are evaluated in the preprocessing phase, and their value is stored in the memory for later use, while in the FEM analyses the shape functions are evaluated during the processing time, at each iteration. With this in mind it seems fair to compare the processing time of the FEM with the processing time of the SPIMs combined with the shape functions evaluation time.

6.1.2 L-shaped panel

This section considers the L-shaped panel simulated and experimentally test by Winkler (2001). Despite the availability of experimental results, here the aims is not to try to reproduce these experimental results, but to investigate the stability of the different SPIM strategies on a well-know problem.

The geometry, loading and boundary conditions are depicted in Fig. 6.7(a). The plane-stress state with thickness of 100 mm is considered and the material parameters: Young's modulus $E = 25.85 \text{ kN/mm}^2$, Poisson's ratio $\nu = 0.18$, critical energy release rate $G_c = 9.0 \times 10^{-5} \text{ kN/mm}$, and length scale parameter $l_0 = 24 \text{ mm}$. The constitutive model of Miehe, Welschinger and Hofacker (2010) is applied with the energetic degradation function of Bourdin et al. (2000) and the geometric crack function with $\xi = 0$. The domain was discretised considering a nodal spacing of 4 mm in the region where the phase-field propagation was expected, resulting in the nodal distribution illustrated in Fig. 6.7(b), and in the FEM mesh and smoothing domains illustrated in Fig. 6.8. The exponential radial basis function is adopted with $c = 1$.

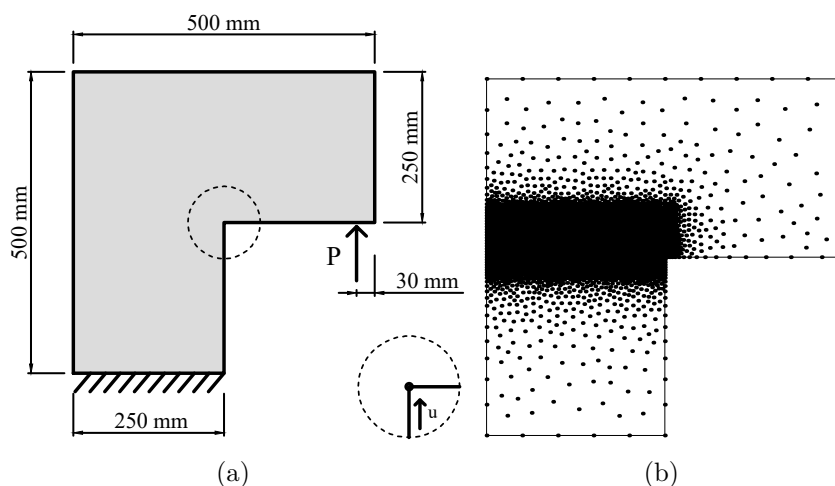


Figure 6.7: L-shaped Panel: (a) Geometry, loading and boundary conditions, and (b) Nodal distribution.

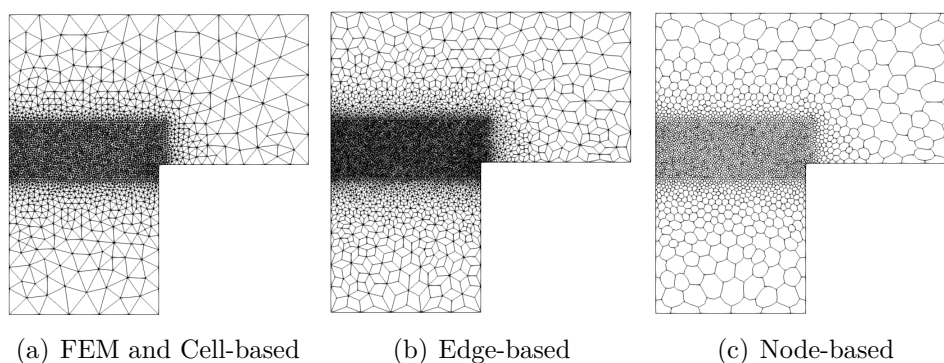


Figure 6.8: Smoothing domains and FEM mesh of the L-shaped panel.

The displacement control method is adopted, considering increments of $\Delta u = 1 \times 10^{-3}$ mm in the reentrant corner node of the panel. The load-displacement curves for the point of load application are illustrated in Fig. 6.9. As observed in the previous example, the node-based smoothing domains do not give good results.

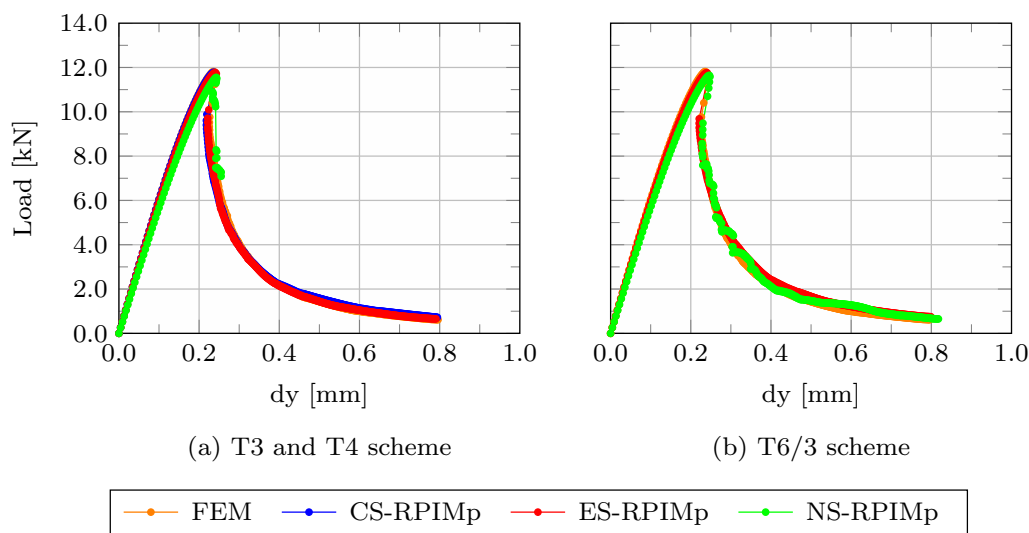


Figure 6.9: Load-displacement paths of the L-shaped panel test.

For this same example, a study of the influence of the parameter c in the analysis is proposed. This parameter is used in the exponential radial basis functions. The L-shaped panel discretised with ES-RPIM-T3 was adopted and five different values of c were considered. Fig. 6.10 shows the analysis. As can be observed, the modification of this parameter did not present a significant influence on the results. This can be justified by the use of the polynomial enrichment in the shape functions and the weakened-weak form. According to Gu et al. (2011), adding polynomial terms reduces the sensitivity of the shape parameters. Liu (2009) indicated that when weakened-weak form is used, tuning shape parameters are much less important, and a very wide range of parameters can be used.

A convergence test was also performed for the L-shaped panel. This test aims to verify whether the same requirements that are valid in finite elements for the l_0/h ratio also apply to SPIM. Different values of the l_0/h ratio are tested, where h is the mean nodal spacing. Four different meshes were considered with h equal to 3, 4, 6, and 12, for a single value of $l_0 = 12$. In all the meshes, the discretisation was refined in the same region shown in Fig. 6.7 (b).

The first analyses are performed considering exponential radial function and $c = 1$. The load-displacement plots obtained with the different FEM and SPIM strategies are illustrated in Fig. 6.11.

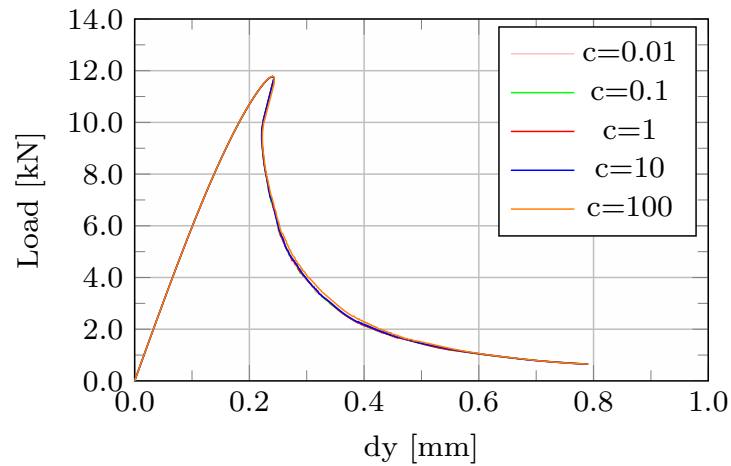


Figure 6.10: Analysis of the parameter c for the panel-L with ES-RPIMp-T3.

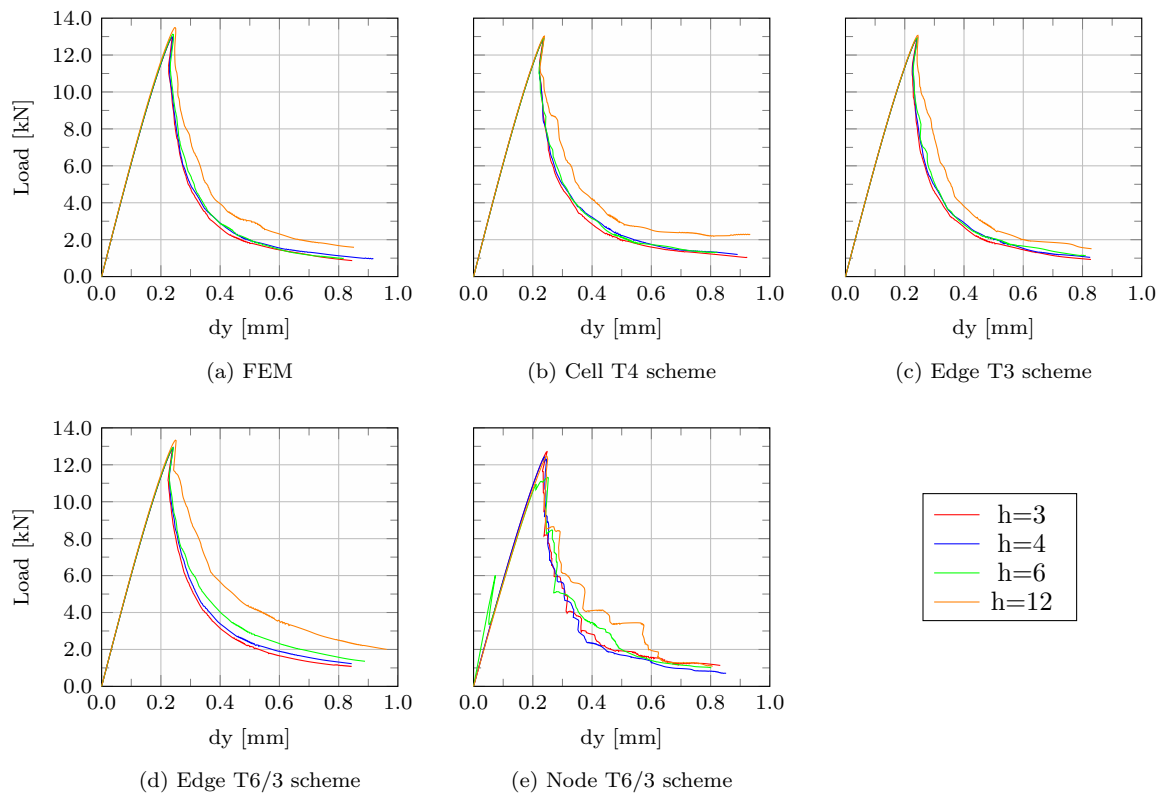


Figure 6.11: Load-displacement paths of the L-shaped panel for the convergence test.

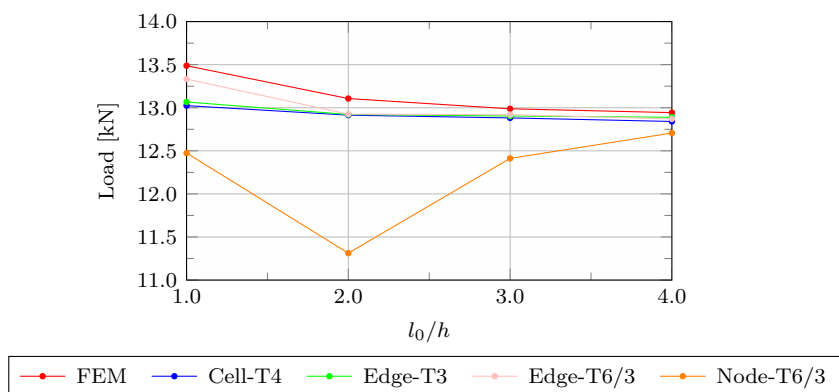


Figure 6.12: Critical loads for the panel L plotted with different degrees of mesh refinement represented by l_0/h .

As it can be observed, the different strategies exhibited a good convergence with the refinement of the discretisation, except the node-based strategy with T6/3 scheme, that presented some instabilities. Convergence results are also depicted in Fig. 6.12, that illustrates the maximum load values obtained with the different strategies and discretisations. It is known from the literature, that FEM discretisations should present ratios $l_0/h > 2$ in order to give accurate results. As it can be observed in Fig. 6.12 the FEM result with $l_0/h = 1$ ($h = 12$) exhibited an overestimation of the maximum load with respect to the finer discretisations. While this overestimation is also exhibited by the edge-based model with the T6/3 scheme, it is sensibly reduced in the cell- and edge-based simulations with the T3 scheme. However, the representation of the post peak trajectory still needs a smaller l_0/h ratio.

This same convergence test was performed for cell-based T4 using the trigonometric radial basis function. The load-displacement paths and the maximum load values are shown in Fig. 6.13 and Fig. 6.14, respectively. It is possible to observe that the curves presented the same convergence as those cell-based with exponential radial basis function.

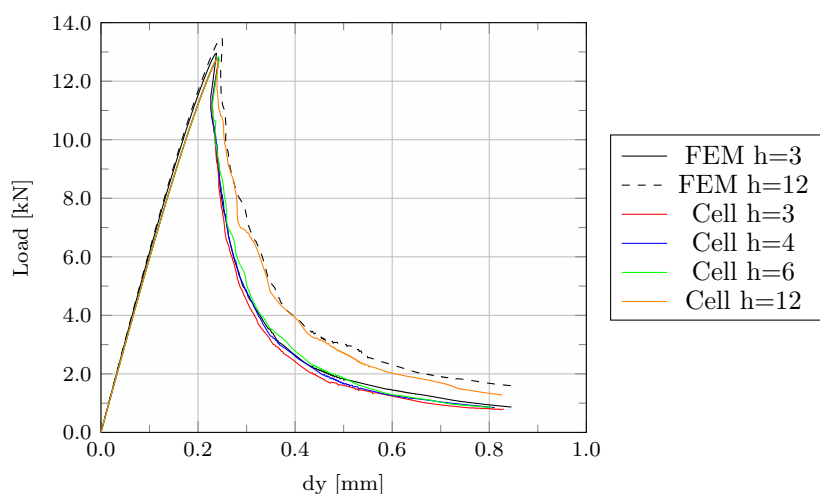


Figure 6.13: Load-displacement paths of the L-shaped panel for the convergence test using trigonometric radial function.

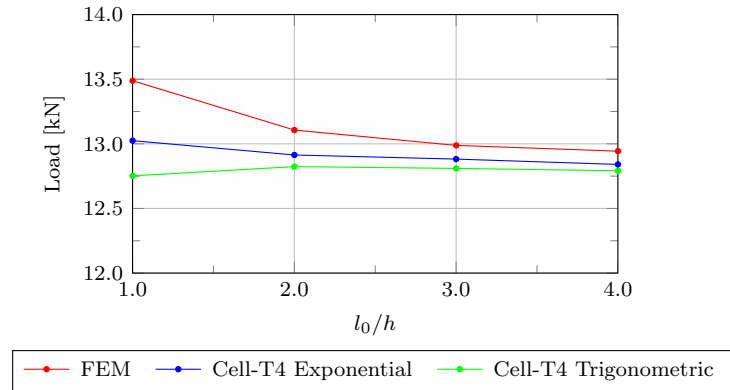


Figure 6.14: Critical loads for the panel L comparing trigonometric and exponential radial function.

6.2 Fixed SPIM-FEM coupling

In this section, results obtained with a fixed SPIM-FEM coupling are presented. The example refers to the test of four-point bending concrete notched beams reported in Hordijk (1991) and illustrated in Fig. 6.15. The vertical force is $P = 0.5$ kN. This problem was simulated by Wu (2018b) using the crack shape function with $\xi = 2$ and the energetic degradation function of Cornelissen with $p = 2$, $a_2 = 1.3868$ and $a_3 = 0.6567$. The material properties are: Young's modulus $E = 38.0$ kN/mm², Poisson's ratio $\nu = 0.2$, critical energy release rate $G_c = 1.25 \times 10^{-4}$ kN/mm, $f_t = 3 \times 10^{-3}$ kN/mm² and length scale parameter $l_0 = 5$ mm. The plane-stress state is adopted.

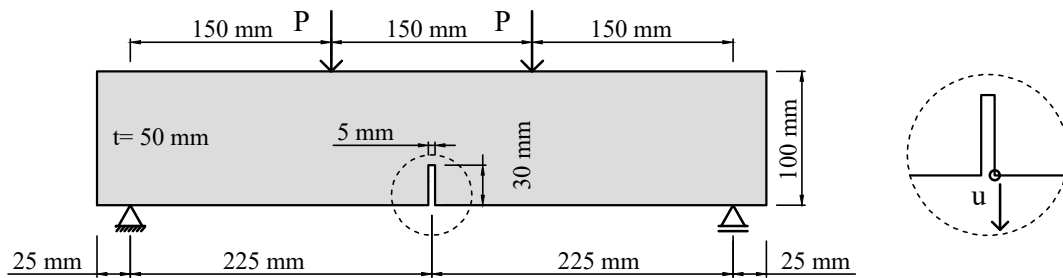


Figure 6.15: Geometry, loading and boundary conditions of the bending test.

The mesh used in the analysis is shown in Fig. 6.16 where the refined region has nodal spacing of 1 mm. A rectangular region was used to create the meshfree region in the coupling models, adopting the two points (245, 30) and (255, 100). The different discretisations for FEM coupled with cell-based and FEM coupled with edge-based are shown in Fig. 6.17, where the color blue represent the FEM domain and the color red represent the meshfree domain. Fig. 6.18 present a magnified view the notch region of the bending test when edge-based is used in the meshfree region.

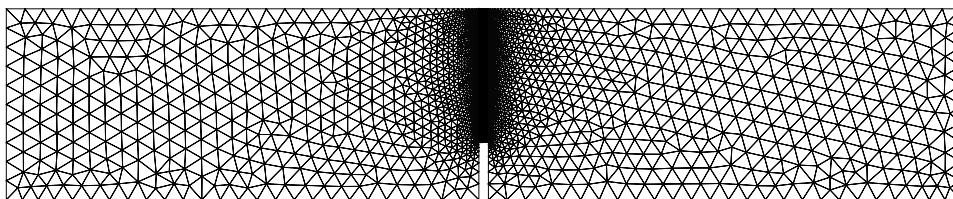
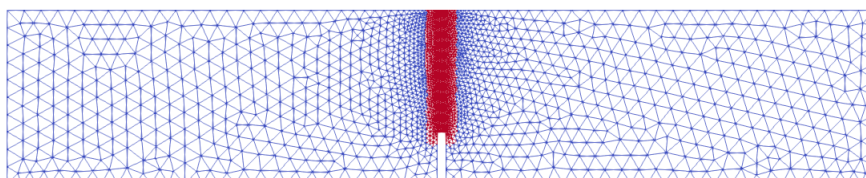
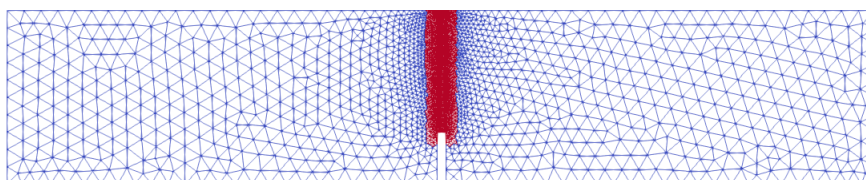


Figure 6.16: Mesh of the bending test.



(a) FEM-Cell based



(b) FEM-Edge based

Figure 6.17: Coupled FEM-SPIM mesh of the bending test.

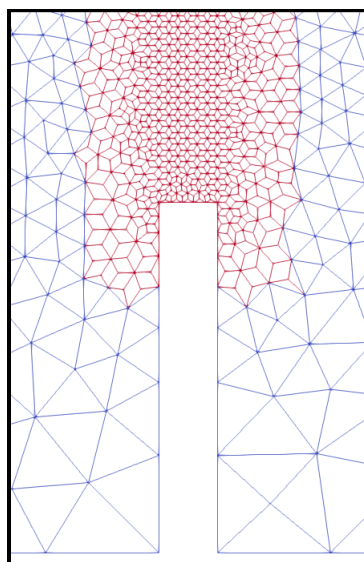


Figure 6.18: Magnified view in the notch region of the bending test.

The nonlinear process was performed by the direct displacement control method, considering increments of $\Delta u = -3.5 \times 10^{-3}$ mm of the vertical direction of the control node depicted in Fig. 6.15 for all the steps. The load-displacement curves are shown in Fig. 6.19 together with the experimental result by Hordijk (1991), the numerical solution performed by Wu (2018b) and the complete domain with FEM. It can be observed that all the curves are in good agreement with the ones obtained by Hordijk (1991) and Wu

(2018b).

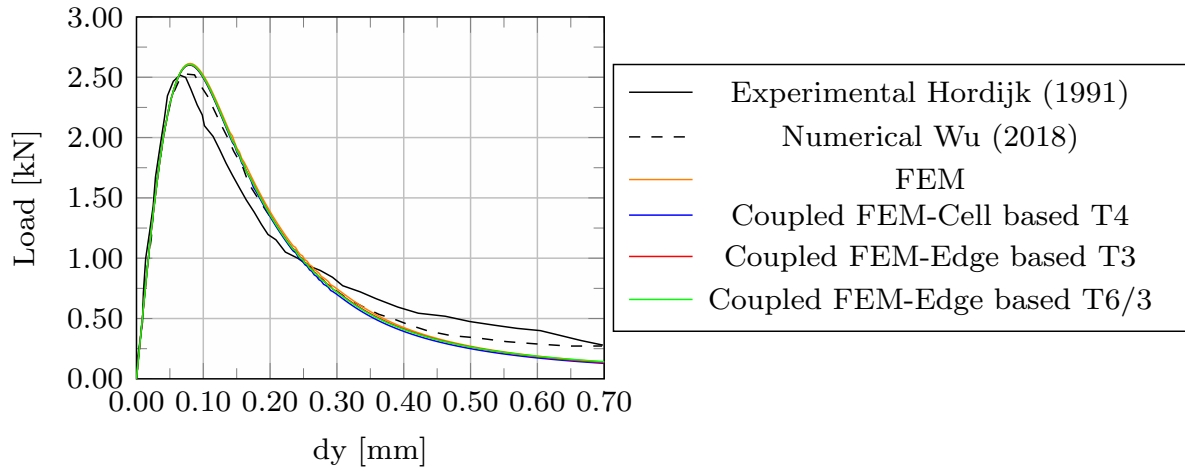


Figure 6.19: Load-displacement curve of the bending test.

The contour plots of the phase-field for the coupled cell-based T4 schemes are illustrated in Fig. 6.20. The phase-field evolution are according with the Wu (2018b).

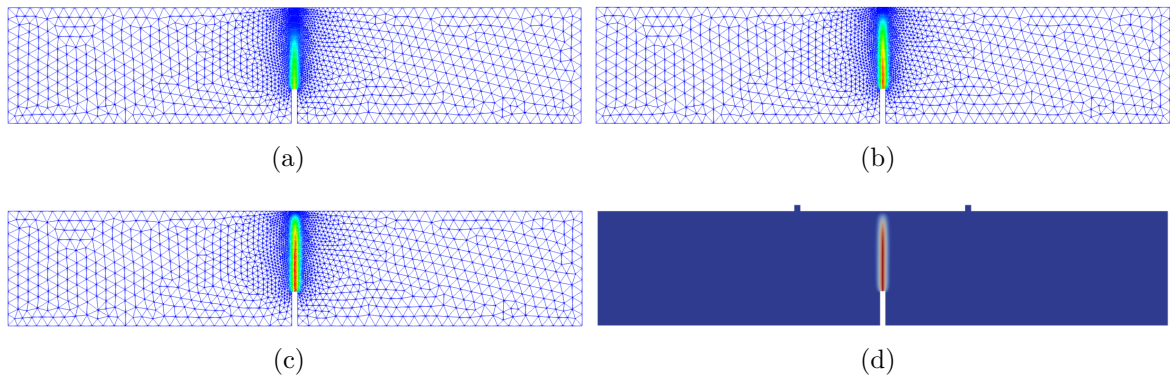


Figure 6.20: Phase-field contour plots for the bending test with coupled FEM-CS-RPIMp T4. Displacements of (a) 0.175 mm, (b) 0.35 mm, (c) 0.70 mm and (d) Reference (Wu, 2018b).

Chapter 7

Adaptive SPIM-FEM coupling simulations

This chapter presents the results of phase-field simulation performed with the adaptive strategy proposed in this work. Section 7.1 illustrates a parametric study on a shear test example, where the influence of all the parameters of the adaptive strategy on the solution is investigated. The remaining sections deal each one with a specific aspect of the adaptive strategy.

7.1 A parametric study on the shear test

The aim of this section is to illustrate a parametric study of the effects of the different parameters of the adaptive strategy, being them:

- Substitution criterion;
- Critical factor for substitution;
- Scale of substitution;
- Refinement criterion;
- Level of refinement;
- Critical factor for refinement;
- Smoothing domain and T-schemes;
- Radial basis function.

The test considered for this parametric study is the shear test illustrated in Fig. 7.1, a well-known example in the phase-field community. The constitutive model of Miehe, Hofacker and Welschinger (2010) and a plane-strain state are considered for all the analyses. The material parameters are: Young's modulus $E = 210 \text{ kN/mm}^2$, Poisson's ratio $\nu = 0.3$, critical energy release rate $G_c = 0.0027 \text{ kN/mm}$ and length scale parameter $l_0 = 0.015 \text{ mm}$. The energetic degradation function of Bourdin et al. (2000) and the geometric crack function with $\xi = 0$ are adopted.

The initial FEM mesh considers a element size of 0.033 mm in the whole domain as illustrated in Fig. 7.2.

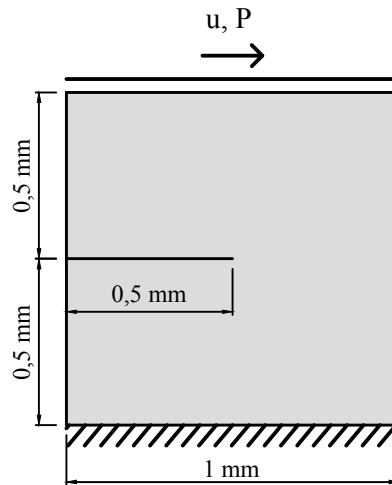


Figure 7.1: Geometry, loading and boundary conditions of the shear test.

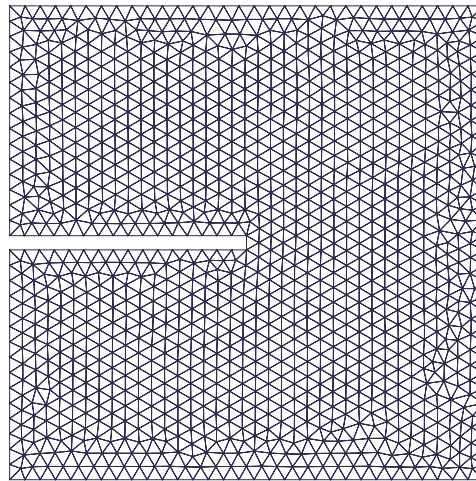


Figure 7.2: Initial mesh of the shear test.

The nonlinear process was controlled by the direct displacement control method, considering increments $\Delta u = 1 \times 10^{-4}$ mm of the top edge in the horizontal direction for all the steps.

The parametric study was performed considering a fixed set of default parameters, and changing them one at the time for each case of the study. The default parameters are:

- Substitution criterion - Shao criterion
- Critical factor for substitution - $factor = 0.3$ and $PF_{critical} = 0.2$
- Scale of substitution - $scale = 2$
- Refinement method - phase-field
- Level of refinement - $ref = 2$

- Critical factor for refinement - $factor = 0.9$
- factor decay rate - $factorDecayRate = 0.1$
- Smoothing domain - Cell-based T4 scheme
- Radial basis function - Exponential $c = 1$

7.1.1 Substitution criterion

The first parameter to be studied is the substitution criterion presented in Section 5.2.3.1. This parameter refers the method used to detect the finite elements that will be replaced by the meshfree region.

As illustrated in Section 5.2.3.1, four different criteria were considered in this work: Shao, phase-field, strain energy and equivalent strain.

The Shao method considers the combination between the phase-field parameter and the strain energy. For this analysis was adopted $Factor = 0.3$ and $d_c = 0.2$

The phase-field method considers a critical value of the phase-field and for this analysis was adopted $d_c = 0.2$

In the strain energy method, the elements are replaced when the strain energy of the element is superior factor multiplied by the average strain energy of the domain. The factor used was $factor = 4$.

The last method is the equivalent strain. This method considers a limit of equivalent strain for replaced, where in this case was $refvalue = 0.01$.

Fig. 7.3 illustrates the load-displacement paths obtained for the all substitution criteria. In general, all the methods presented similar load-displacement curves.

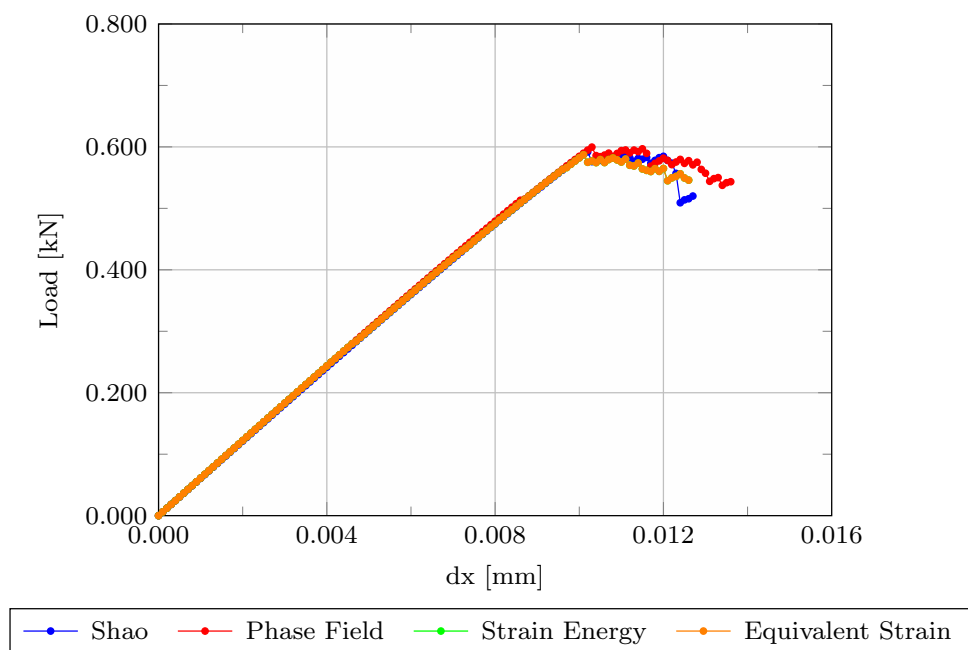


Figure 7.3: Load-displacement curve: Substitution criteria.

The contour plots of the phase-field are depicted in Fig. 7.4. The results are in good agreement with those presented in the literature as can be found in Miehe, Hofacker and Welschinger (2010). It is possible to observe that strain energy and equivalent strain presented a larger substitution area. The shao and phase-field criteria present a better shape for the replacement area because they adopt the phase-field variable in their criteria.

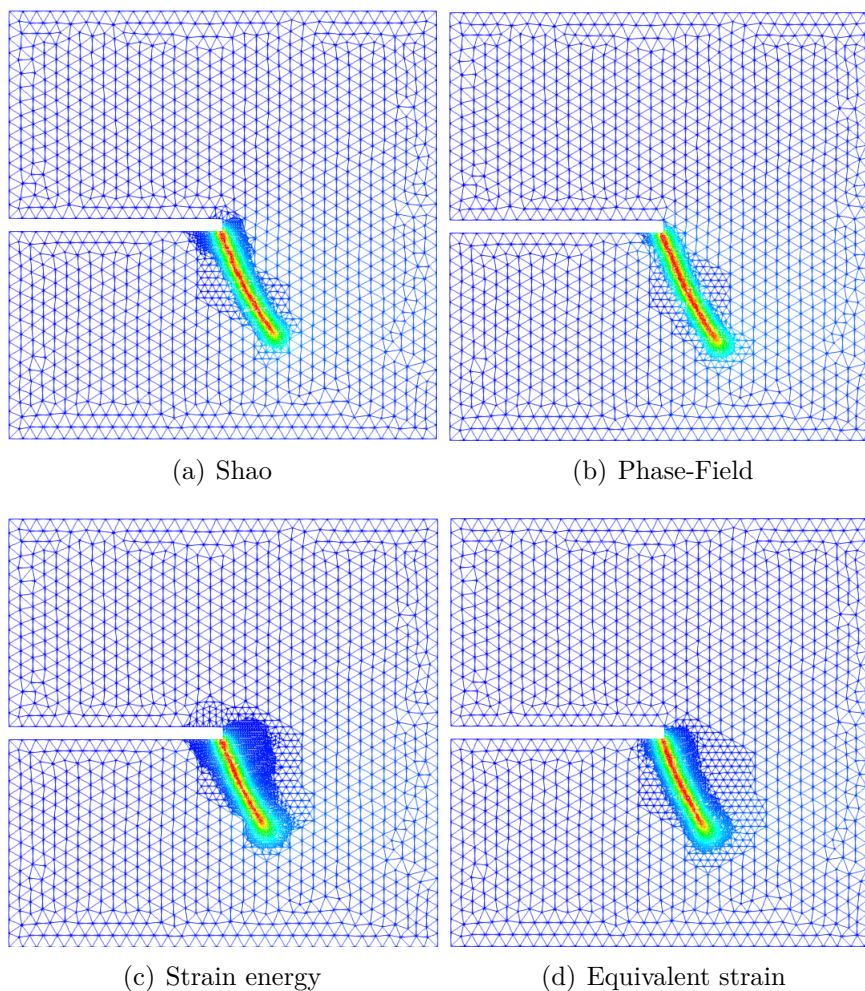


Figure 7.4: Phase-field contour plots: Substitution criteria.

7.1.2 Critical factor for substitution

The second parameter refers to the critical factor for the substitution presented in Section 5.2.3.1. The substitution criterion used is the Shao, the value of the *factor* is modified and the phase-field critical is constant ($PF_{critical} = 0.2$) for all analyses.

Fig. 7.5 show the load-displacement paths obtained for the three factors: 0.2, 0.3 and 0.4. The phase-field contour plots are illustrated in Fig. 7.6. It is possible to observe that the smaller the value of the factor generates the larger replacement region.

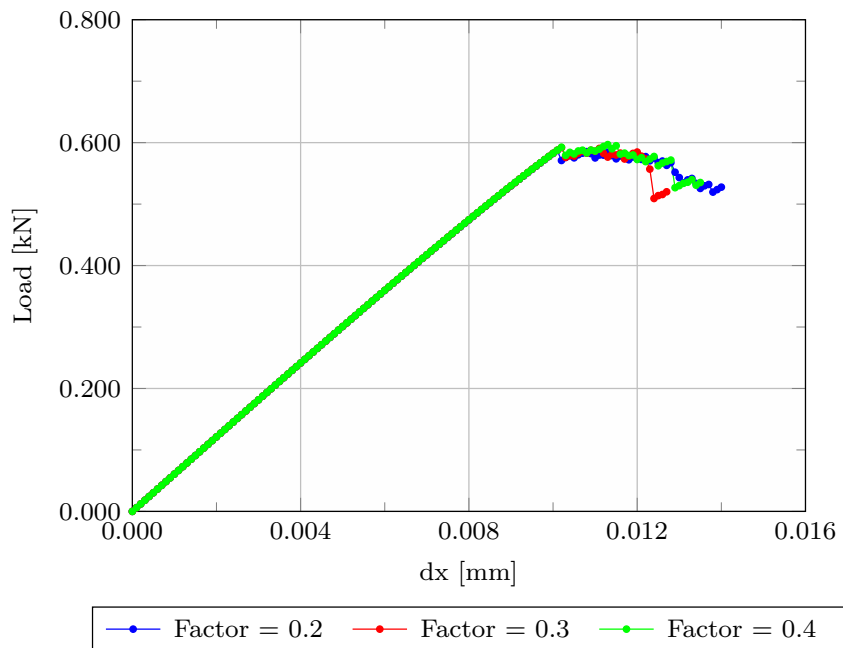


Figure 7.5: Load-displacement curve: Critical factor.

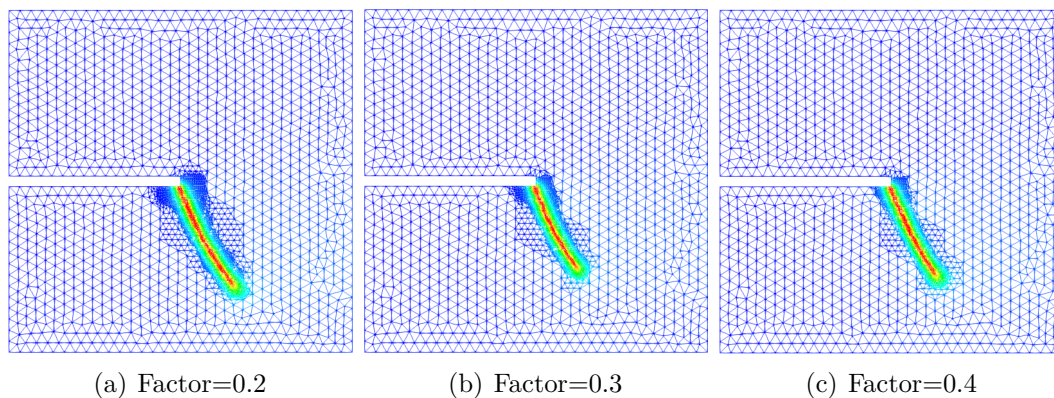


Figure 7.6: Phase-field contour plots: Critical factor.

7.1.3 Scale of substitution

This parameter is responsible for the size of the substitution region shown in Section 5.2.3. After an element has been detected for replacing, that element and the neighbouring elements within the size of the substitution region are replaced by an SPIM discretisation. For the analysis of this parameter, the format of this region is circular and all the elements that are contained in this region are replaced. Three scale parameters were adopted: $scale = 1, 2$ and 3 .

Fig. 7.7 present the load-displacement paths.

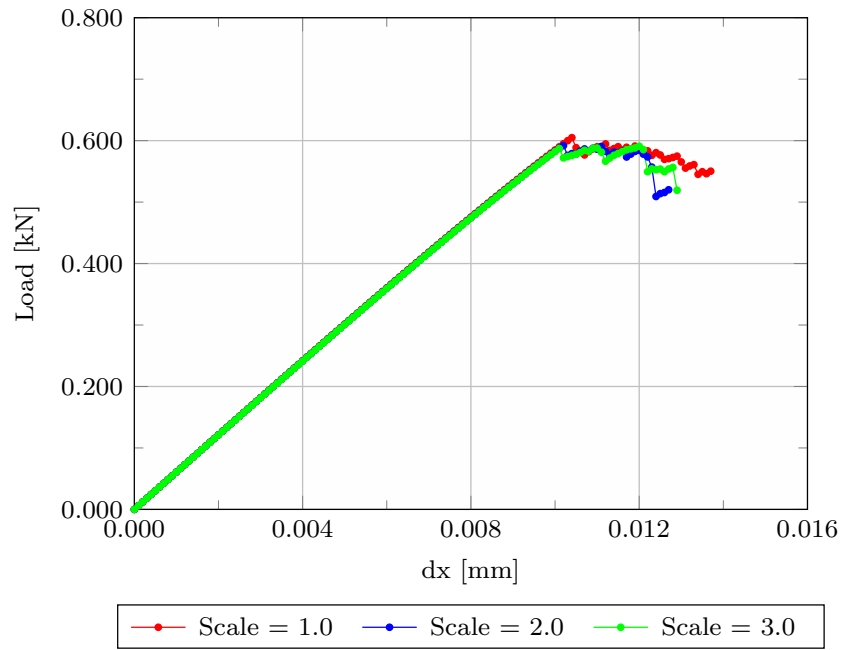


Figure 7.7: Load-displacement curve: Scale of substitution.

The phase-field contour plots are illustrated in Fig. 7.8. It is possible to observe that the substitution region is larger with the increase of the parameter. In $scale = 1$ the region of refinement does not cover smeared crack region. Then it is possible to relate the parameter of scale and the size of the initial elements with the length scale. In this example the initial element size is 0.033 mm and $l_0 = 0.015$ mm. The equation below must be guaranteed:

$$scale * elementsize \geq 2 * l_0 \quad (7.1)$$

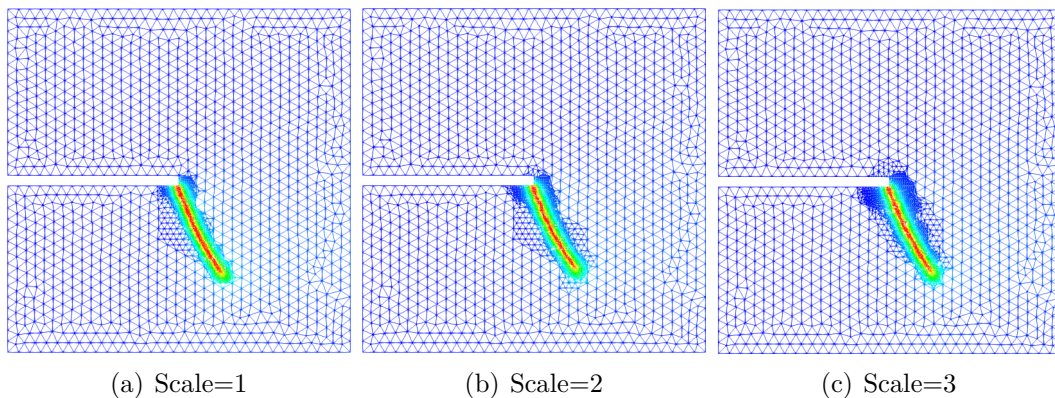


Figure 7.8: Phase-field contour plots: Scale of substitution.

7.1.4 Refinement criterion

After the substitution of the finite elements by the meshfree domain, this region can be refined. Similar to the substitution criteria there are the refinement criteria illustrated in Section 5.2.4.1. These criteria are responsible for detecting the region of the meshfree domain that will be refined. There are three methods: phase-field, strain energy and equivalent strain. In all the methods, the cells of the domain that present the value of the parameter greater than a factor multiplied by the average value of the domain are refined.

Fig. 7.9 show the load-displacement paths for the three different criteria.

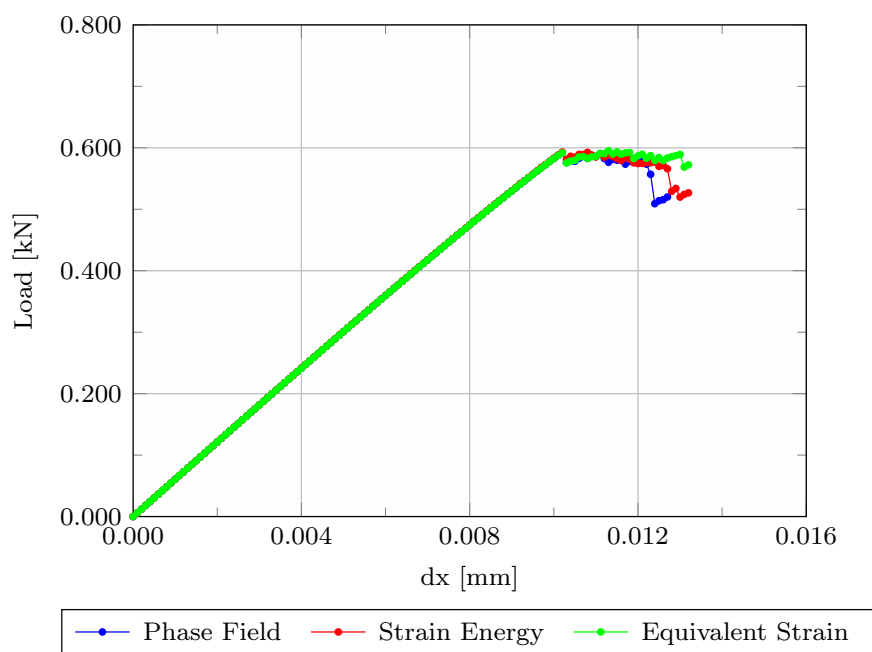


Figure 7.9: Load-displacement curve: Refinement criteria.

The phase-field contour plots are illustrated in Fig. 7.10. Comparing the final mesh for the different criteria, it is possible to observe that in the equivalent strain criterion the refinement becomes concentrated. Unlike the strain energy criterion, where the refinement covers a large region. Therefore, the phase-field criterion proved to be more appropriate.

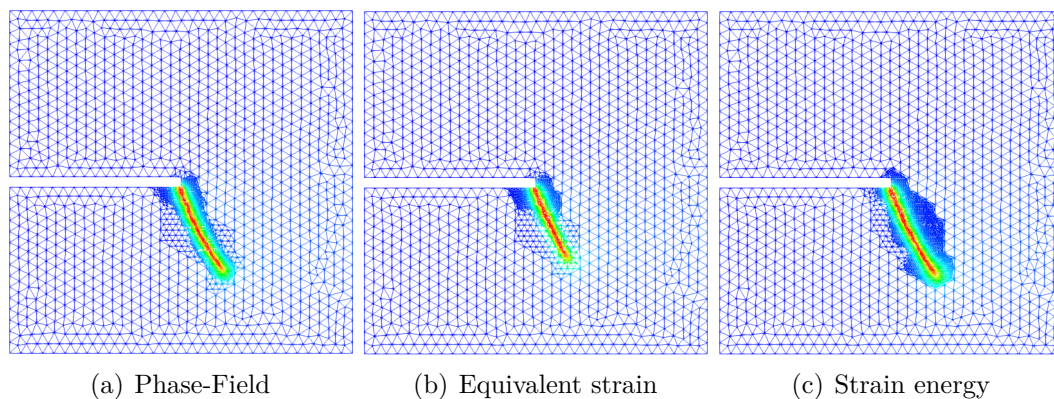


Figure 7.10: Phase-field contour plots: Refinement criteria.

7.1.5 Critical factor for refinement

The critical factor for refinement is a factor that is multiplied by the average value of the domain and is used to indicate if the cell will be refined. This factor is presented in Section 5.2.4.1. Decreasing this factor, the refined region is bigger. Again, three critical factors are analysed.

The load-displacement curves are shown in Fig. 7.11.

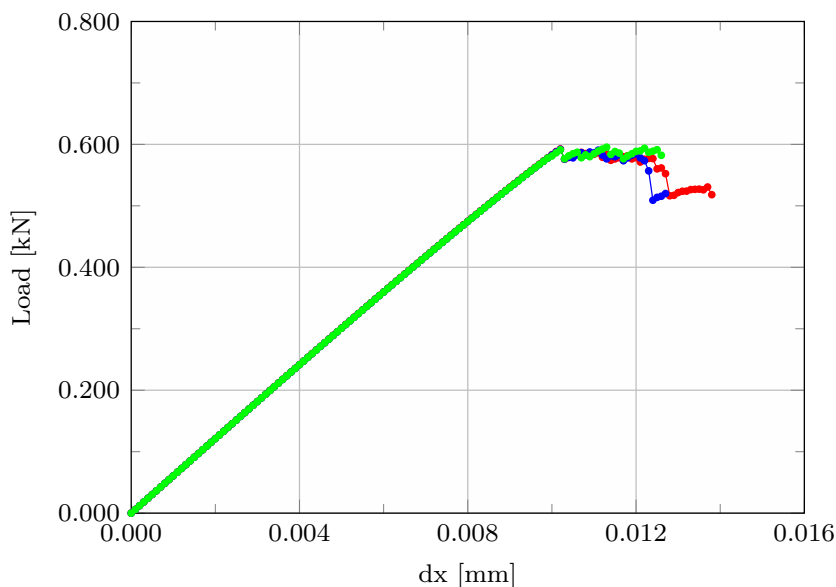


Figure 7.11: Load-displacement curve: Critical factor for refinement.

Fig. 7.12 present the phase-field contour plots for the different values of the factor. It is possible to observe that the refined region is larger for the smallest factor and the crack propagates more compared to the other factors. Therefore, a smaller factor is more suitable for adaptive analysis.

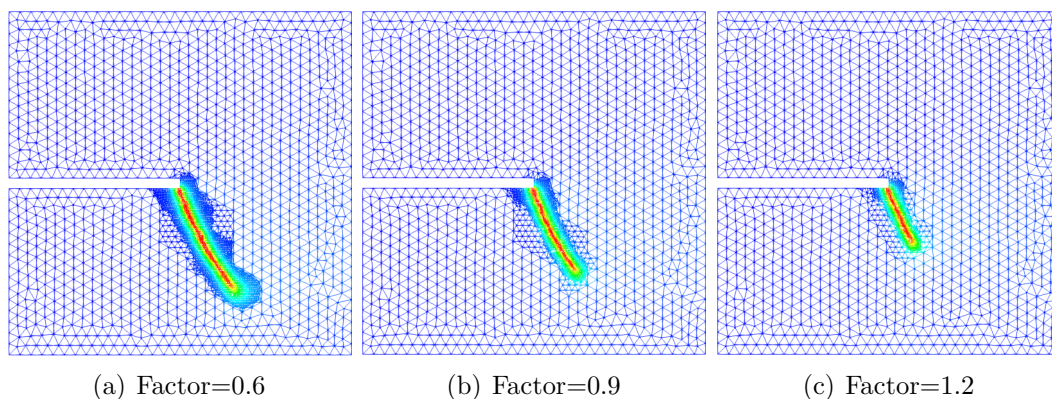


Figure 7.12: Phase-field contour plots: Critical factor for refinement.

7.1.6 Level of refinement

This parameter indicates the final level of refinement of the meshfree region. Same the other parameters, this parameter is indicated by the user and is presented in Section 5.2.4. For this analysis, three level of refinements are performed: $ref = 1$, $ref = 2$ and $ref = 3$. Increasing the level of refinement makes the size of the cells smaller.

The load-displacement paths are plotted in Fig. 7.13. Other three analyses are presented for comparison: FEM with the original mesh, only substitution without refinement and substitution with the convert of the integration point for new node (Section 5.2.3.2). It is possible to observe that the higher the refinement leads to a lower the peak of load. For the same mesh, the substitution without refinement (pink color) presents better results that the FEM (black color). This result is associated to the shape functions and it is explained in Section 7.2.2.

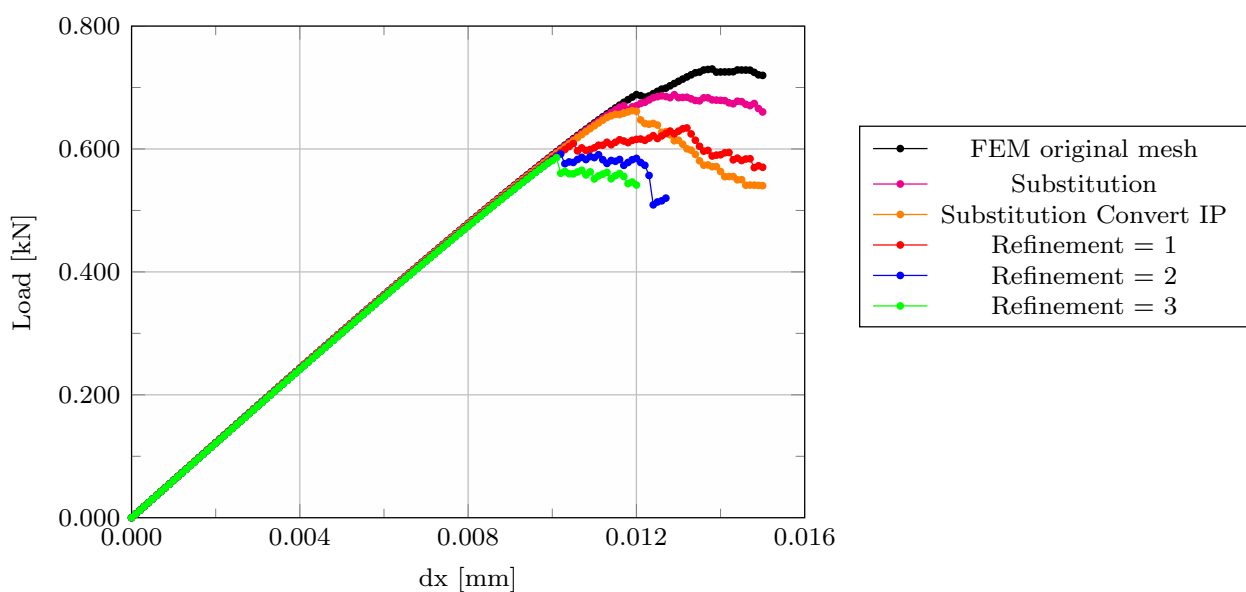


Figure 7.13: Load-displacement curve: Level of refinement.

The phase-field contour plots are shown in Fig. 7.14.

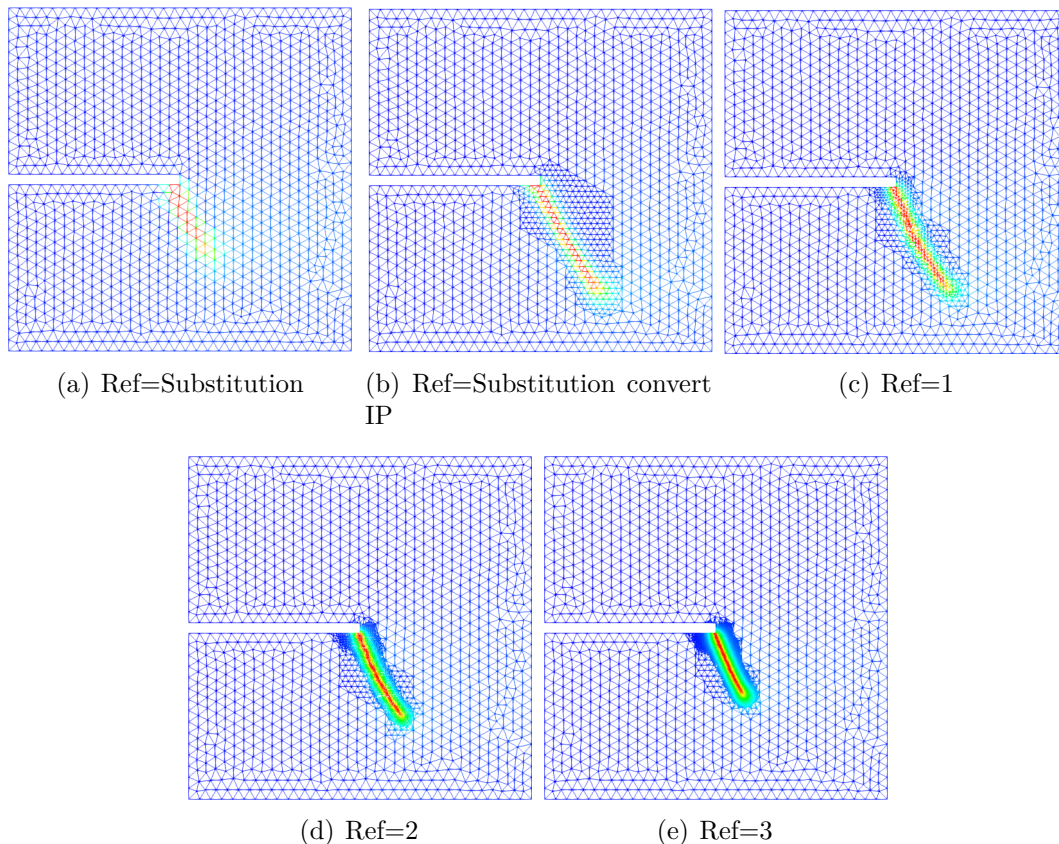


Figure 7.14: Phase-field contour plots: Level of refinement.

7.1.7 Smoothing domain and T-schemes

The last parameter refers to the discretisation of the meshfree domain. For this discretisation can be used the smoothing domain of the type cell-based or edge-based and to selection of the support nodes used the T-schemes. T4 schemes is used for cell-based and T3 or T6/3 is used for edge-based. The load-displacement curves for these smoothing domains are present in Fig. 7.15. The smoothing domain edge-based with T6/3 scheme presented a load-displacement curve with less jumps. This fact can be explained by the greater number of support nodes.

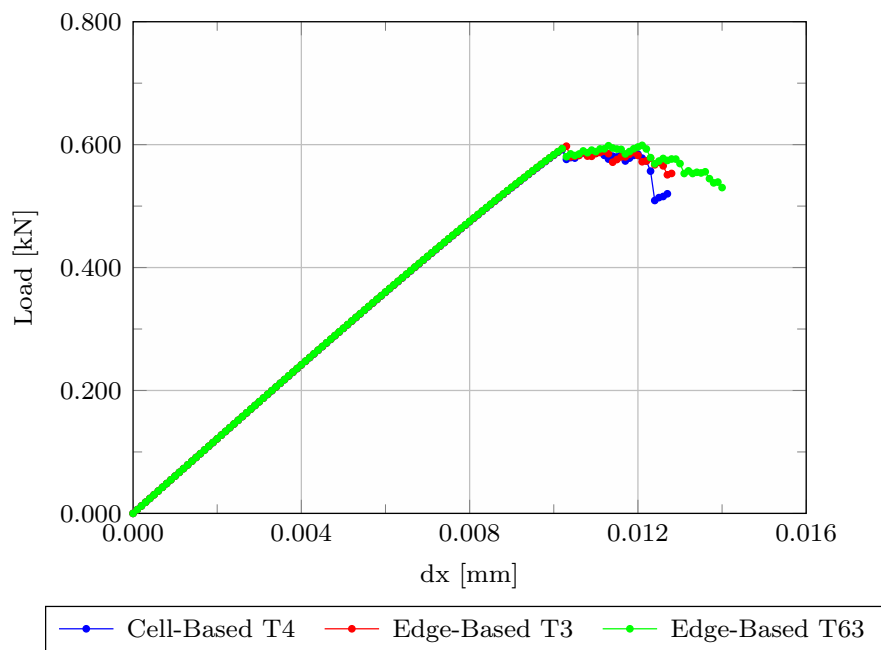


Figure 7.15: Load-displacement curve: Smoothing domain.

The phase-field contour plots are illustrated in Fig. 7.16. In this figure is possible to observe the discretisation of the edge-based smoothing domain. The phase-field contour for the edge-based with T3 is similar to that of the cell-based T4 while for the edge-based with T6/3 the crack propagation is greater.

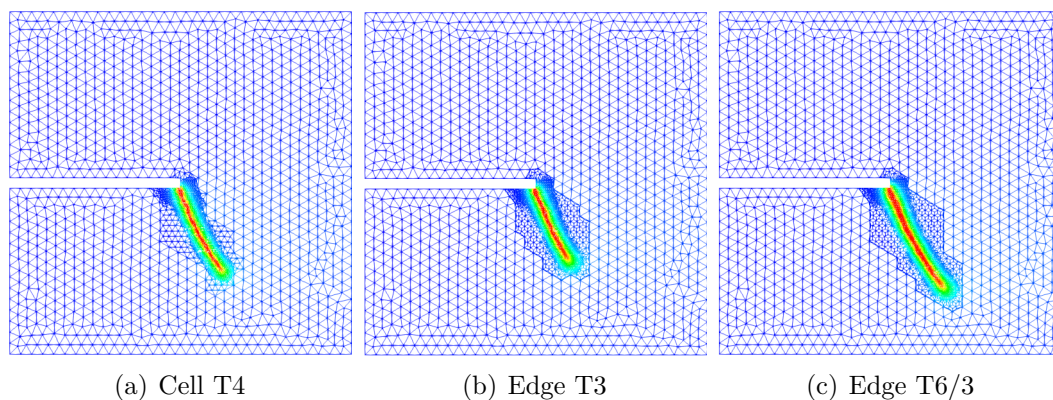


Figure 7.16: Phase-field contour plots: Smoothing domain.

7.1.8 Comparison radial basis function

For this section, it is realized a study of the different radial basis functions. For the adaptive analysis is adopted Cell Based - T4 schemes with the default parameters.

The load-displacement path are shown in Fig. 7.18. It is possible to observe that the trigonometric radial function presented results similar to the exponential radial function. Although the phase-field profile is exponential for the brittle fracture model, the trigonometric function proved to be a good approximation for the analyzed model.

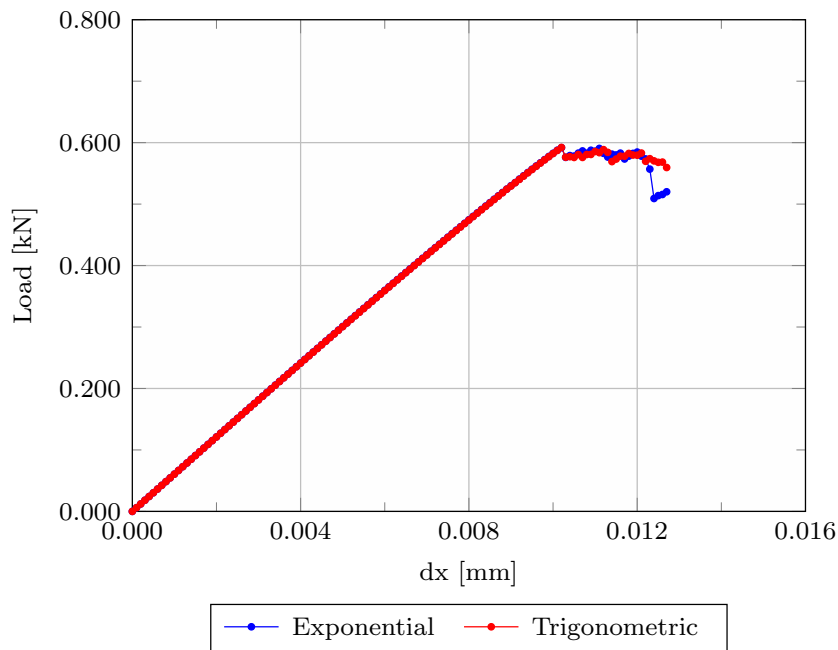


Figure 7.17: Load-displacement curve: Comparison radial basis function.

The phase-field contour plots for the trigonometric and exponential radial function are shown in Fig. 7.18.

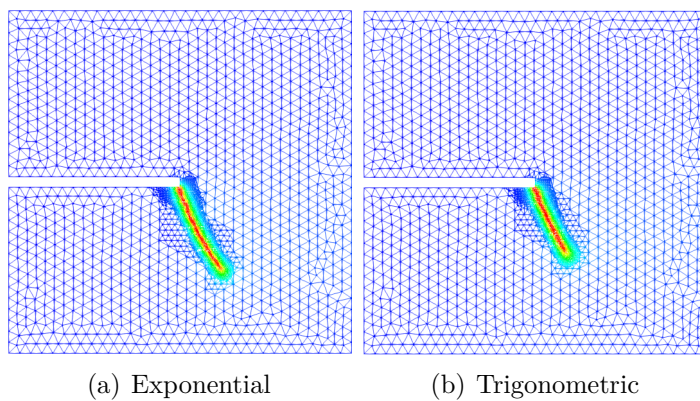


Figure 7.18: Phase-field contour plots: Comparison radial function.

7.1.9 Comparison mesh

This section presents a comparison of the adaptive analysis with a model previously refined as show in Fig 7.19. This model is performed with FEM and with SPIM. The smoothing domains of the type cell-based is analysed. For the adaptive analysis is adopted Cell Based - T4 schemes with the default parameters.

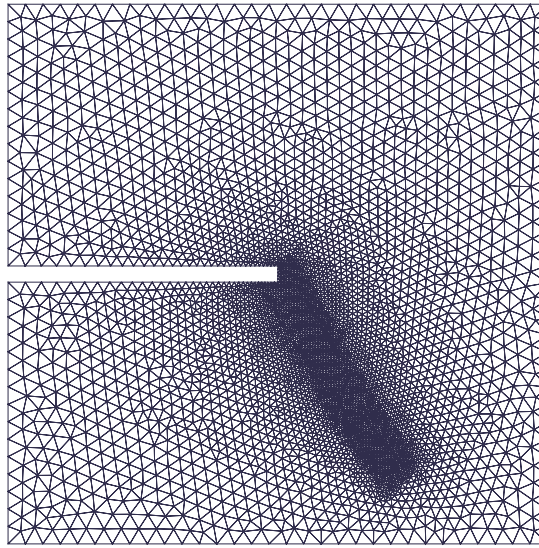


Figure 7.19: Previously refined mesh of the model.

The load-displacement path are shown in Fig. 7.20. It is possible to observe a good agreement between the adaptive analysis and the model previously refined.

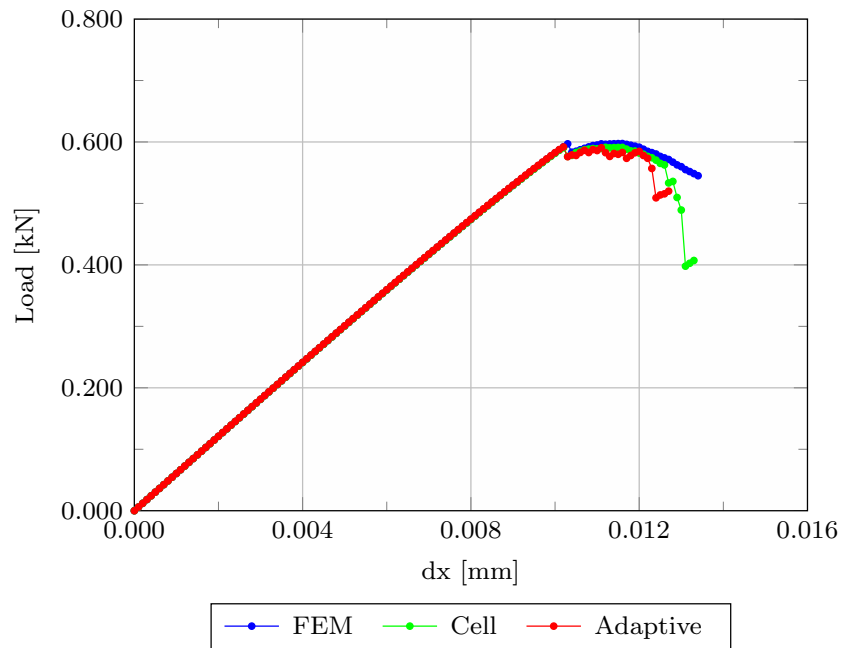


Figure 7.20: Load-displacement curve: Comparison mesh.

The phase-field contour plots for FEM and meshfree method are shown in Fig. 7.21. It is possible to observe that the adaptive strategy is able to correctly represent the crack propagation with a refinement concentrated only in the crack region.

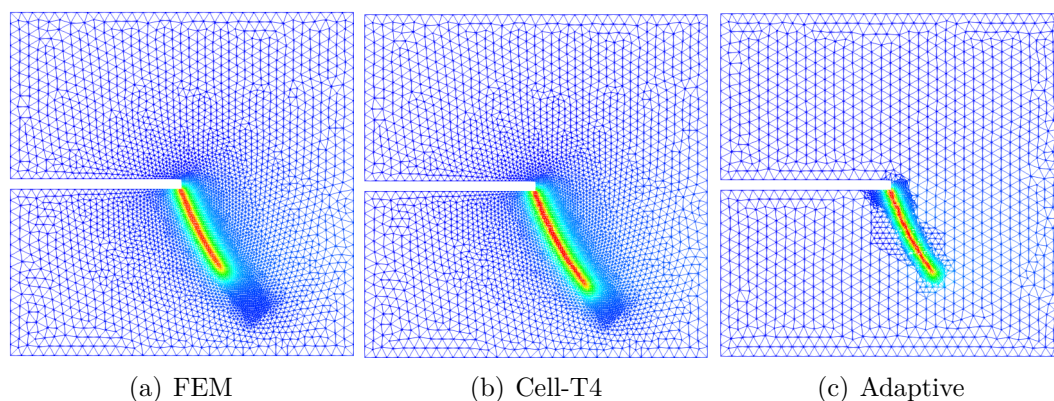


Figure 7.21: Phase-field contour plots: Comparison mesh.

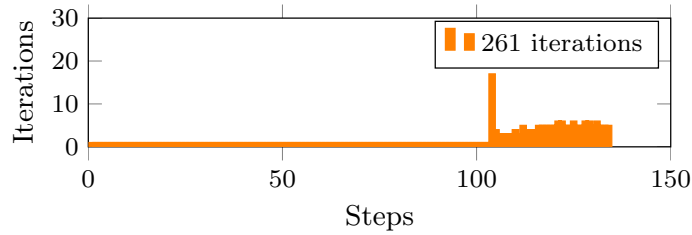
7.1.10 Computational time

The last analysis is the computational time. In the Table 7.1 is presented the computational time for the FEM and Cell-based T4 with the previously refined mesh in comparison with the adaptive cell-based T4. The time obtained with the adaptive strategy is smaller than previously refined and cell-based and it is greater than FEM. But it is important to emphasize that in the fixed refinement mesh the crack propagation path is known. If the entire mesh were refined, the time would be much greater and the advantage of using the adaptive strategy would be highlighted.

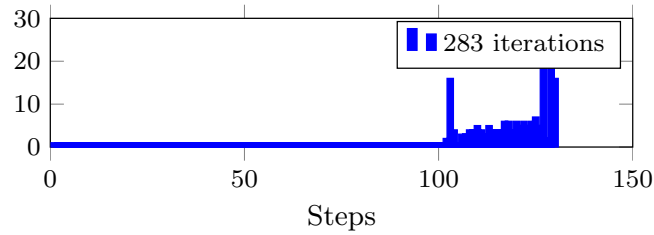
Table 7.1: Computational time (in ms) of the shear test.

Strategy	Preprocessing			Processing	Total
	Smoothing Domains	Support Nodes	Shape Functions		
FEM	-	-	-	1.04×10^6	1.04×10^6
Cell-based T4	1.3×10^3	1.41×10^5	6.30×10^2	1.07×10^6	1.21×10^6
Adaptive Cell-based T4	-	-	-	1.13×10^6	1.13×10^6

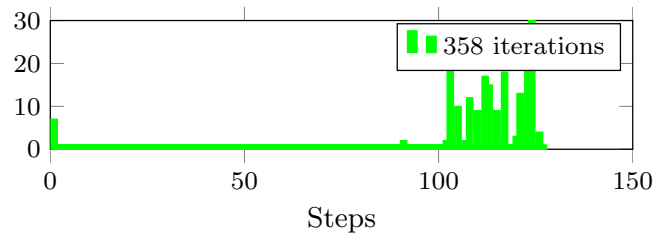
For the same analysis, Fig. 7.22 presents the number of iterations for each step and the total number of iterations. The total number iterations for the adaptive strategy is greater than in the fixed refinement mesh. This result is attributed to the number of necessary correction iterations after mesh refinement.



(a) FEM



(b) CS-RPIMp- T4 scheme



(d) Adaptive Cell-based T4 scheme

Figure 7.22: Total number of iterations.

7.2 Brittle and quasi-brittle constitutive models

This section presents two examples illustrating the results obtained with two common phase-field models: the classic model by Miehe, Welschinger and Hofacker (2010) for brittle fracture, and the model by Wu (2018*b*) for quasi-brittle behaviour. The aim here is to show the capability of the proposed adaptive strategy to work correctly with the two kind of models.

7.2.1 Brittle model

The tension test proposed by Miehe, Welschinger and Hofacker (2010) is adopted for simulate the brittle fracture. The geometry, loading and boundary conditions are presented in Fig. 7.23. The plane-strain state is considered with the material parameters: Young's modulus $E = 210 \text{ kN/mm}^2$, Poisson's ratio $\nu = 0.3$, critical energy release rate $G_c = 0.0027 \text{ kN/mm}$ and length scale parameter $l_0 = 0.015 \text{ mm}$. The energetic degradation function of Bourdin et al. (2000) and the geometric crack function with $\xi = 0$ are adopted.

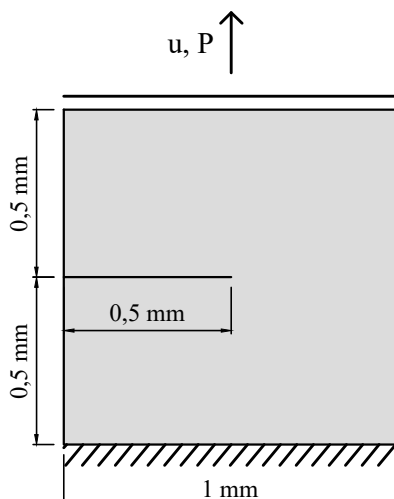


Figure 7.23: Geometry, loading and boundary conditions of the tension test.

The domain was discretised considering the initial mesh illustrated in Fig.7.24. A nodal spacing of 0.033 mm is adopted in the whole domain.

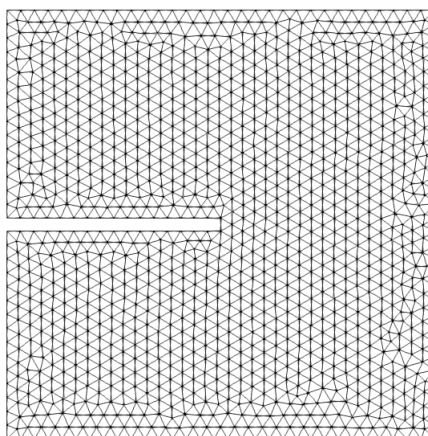


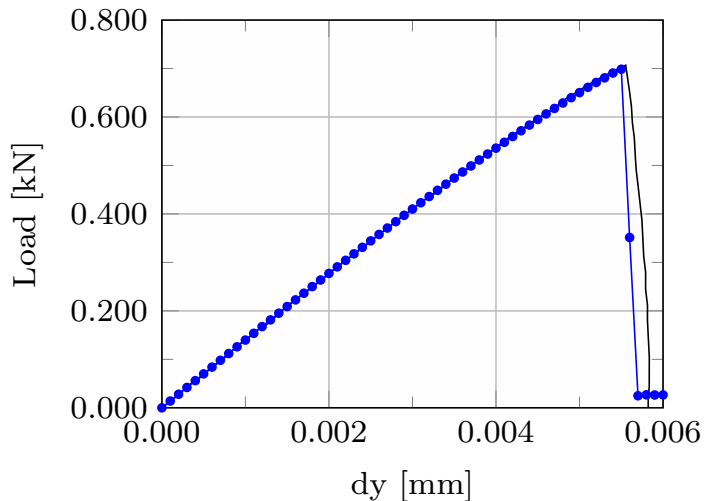
Figure 7.24: Initial mesh of the tension test.

The smoothing domain of the type cell-based with T4 scheme was adopted for the meshfree region with the RPIMp shape functions and scaled exponential radial functions $c = 1$. In the adaptive strategy, the following parameters are used.

- Substitution method - Shao criterion
- Critical factor for substitution - $factor = 0.3$ and $PF_{critical} = 0.2$
- Scale of substitution - $scale = 2.0$
- Refinement method - phase-field method
- Level of refinement - $ref = 2$
- Critical factor for refinement - $factor = 0.9$
- Maximum number of refinements - $n = 15$

The simulations were performed using the direct displacement control method, imposing a uniform vertical displacement of the top edge with increments of $\Delta u = 1 \times 10^{-4}$

mm. The load-displacement curve is illustrated in Fig.7.25. The curve obtained by Miehe, Welschinger and Hofacker (2010) is presented for the comparison. As can be observed, the curve is in good agreement with the obtained by the reference.



— Miehe et al. (2010) ● Cell based - T4 scheme Adaptive

Figure 7.25: Load-displacement curve of the tension test.

The final mesh of the analyse together with the contour plot of the phase-field are shown in Fig. 7.26.

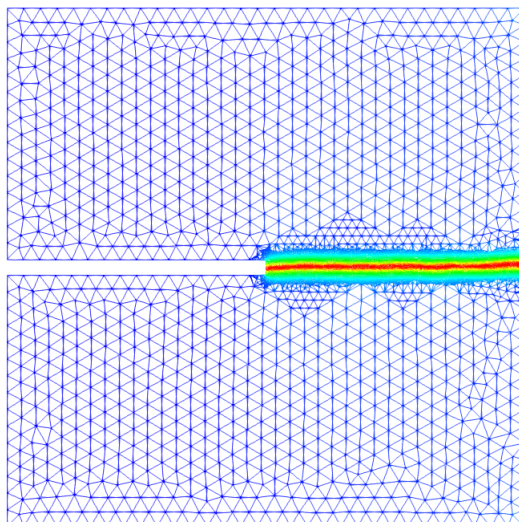


Figure 7.26: Final mesh and phase-field contour plot for the tension test.

7.2.2 Quasi-brittle model

The L-shaped panel by Winkler (2001) is adopted for quasi-brittle fracture. The geometry, loading and boundary conditions is illustrated in Fig. 7.27. The materials parameters are similar to the Wu (2018a): Young's modulus $E = 25.85 \text{ kN/mm}^2$, Poisson's ratio $\nu = 0.18$, critical energy release rate $G_c = 9.0 \times 10^{-5} \text{ kN/mm}$, $f_t = 2.7 \times 10^{-3} \text{ kN/mm}^2$ and length scale parameter $l_0 = 10 \text{ mm}$. This problem was simulated using the crack shape function with $\xi = 2$ and the energetic degradation function of Cornelissen with $p = 2$, $a_2 = 1.3868$ and $a_3 = 0.6567$. The plane-stress state is adopted.

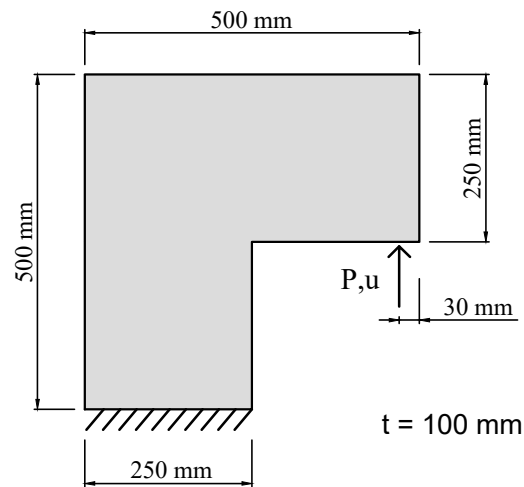


Figure 7.27: Geometry, loading and boundary conditions of the L-shaped panel.

In the adaptive strategy is used the cell-based for the smoothing domains with RPIMp shape functions and exponential function with $c = 1$. The parameters of the strategy are shown below:

- Substitution method - Shao criterion
- Critical factor for substitution - $factor = 0.5$ and $PF_{critical} = 0.05$
- Scale of substitution - $scale = 2.0$
- Refinement method - phase-field method
- Level of refinement - $ref = 3$
- Critical factor for refinement - $factor = 0.4$
- Maximum number of refinements - $n = 100$

The initial mesh of the model is illustrated in Fig. 7.28.

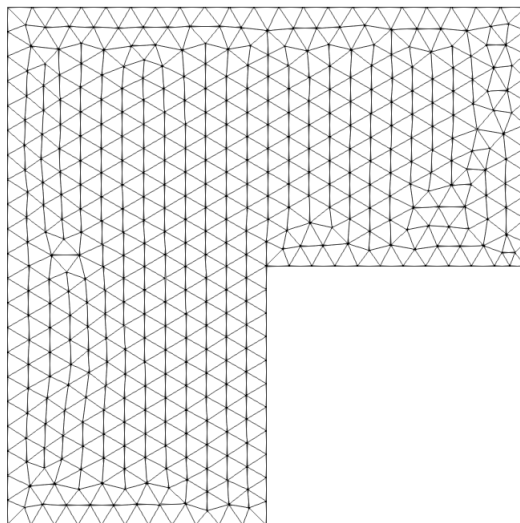


Figure 7.28: Initial mesh of the L-shaped panel.

The non linear analysis is performed adopting the displacement control with increments of $\Delta u = 2.5 \times 10^{-3}$ mm in the load point. The load-displacement curve is shown in Fig. 7.29. The experimental results by Winkler (2001) and numerical results by Wu (2018a) are presented for comparison. It is possible to observe that the curve obtained with the adaptive strategy is similar to the numerical reference.

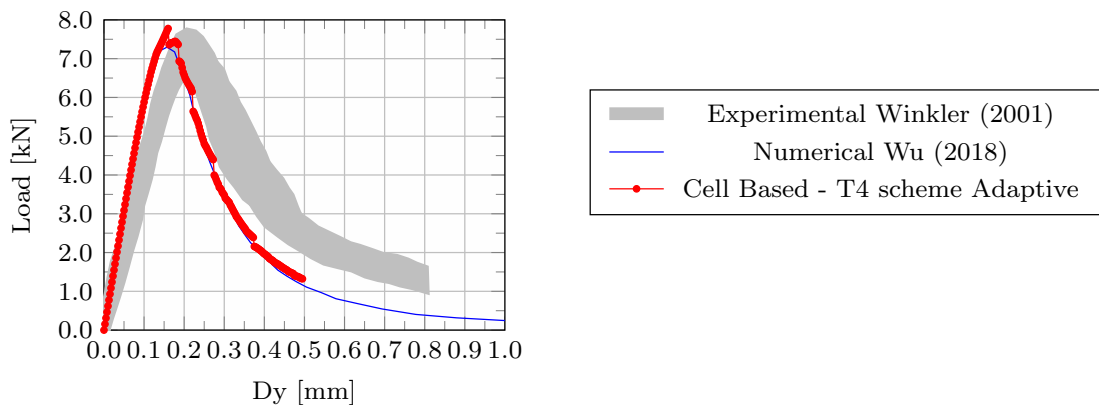


Figure 7.29: Load-displacement curve of the L-shaped panel.

The contour plot of the phase-field and the mesh for the final step of the analysis is illustrated in Fig. 7.30.

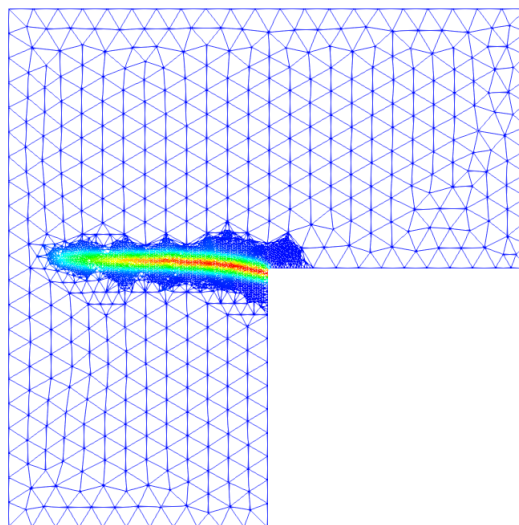


Figure 7.30: Final mesh and phase-field contour plot of the L-shaped panel.

The strain energy substitution method was adopted for this same problem with $factor = 4$. The analysis did not present good results because this method detect the traction and compression regions. The final mesh for the first step is shown in Fig. 7.31. As can be observed, the compression regions of the model were refined.

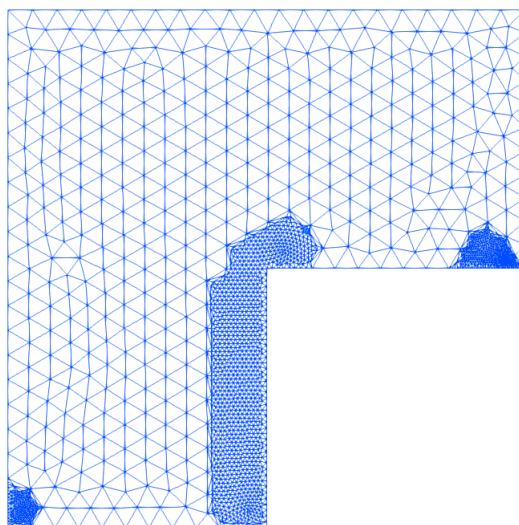


Figure 7.31: Strain energy substitution method for the L-shaped panel.

7.3 Level of refinement

The objective of this section is to verify the influence of the level of refinement of the mesh and the influence of the use of the meshfree model for the analyses. The model adopted was the four-point shear test proposed by Arrea and Ingraffea (1982). The geometry, loading and boundary conditions are depicted in Fig. 7.32.

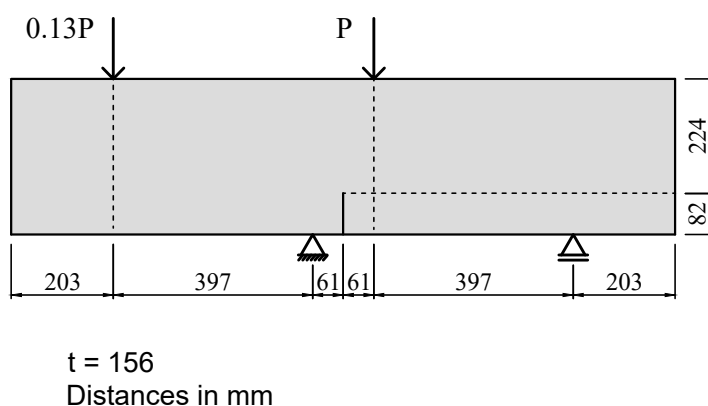


Figure 7.32: Geometry, loading and boundary conditions of the four-point shear test.

The concrete adopted by Arrea and Ingraffea (1982) was characterized by a Young's modulus $E = 24800 \text{ N/mm}^2$, Poisson's ratio $\nu = 0.18$, fracture energy between 0.10 and 0.14 N/mm and tensile uniaxial strength $f_t = 3.4 \text{ N/mm}^2$.

For this example, it is necessary to calibrate the length scale parameter of the phase-field. This calibration is performed using a single Q4 element, subjected to plane stress with thickness of 1 mm. The smeared crack model with Carreira-Ingraffea law was adopted as reference of constitutive model. The other necessary parameters of this constitutive model were based in Penna (2011): $h = 40 \text{ mm}$ and $\epsilon_c = 0.002$. Fig. 7.33 present the curve load-displacement obtained in the calibration. The length scale parameter adopted was $l_0 = 12.5 \text{ mm}$. The simulations was performed using the crack shape function with $\xi = 2$ and the energetic degradation function of Cornelissen with $p = 2$, $a_2 = 1.3868$ and $a_3 = 0.6567$.

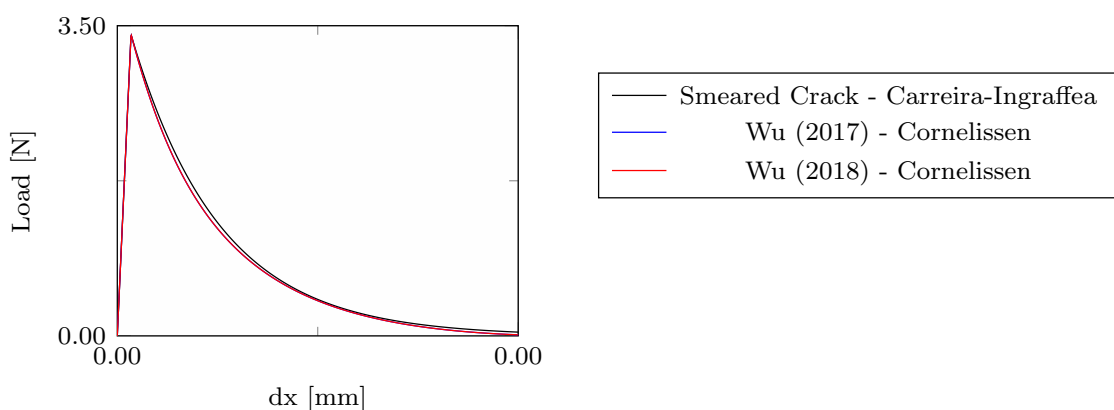


Figure 7.33: Calibration of the l_0 of the four-point shear test.

The initial mesh of the adaptive strategy is shown in Fig. 7.34.

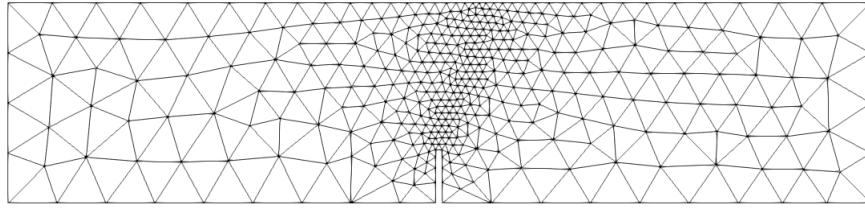


Figure 7.34: Initial mesh of the four-point shear test.

Cell-based smoothing domains with RPIMp shape functions was used. The trigonometric function was adopted as radial function. The adaptive parameters are:

- Substitution method - Shao criterion
- Critical factor for substitution - $factor = 0.5$ and $PF_{critical} = 0.05$
- Scale of substitution - $scale = 3.5$
- Refinement method - phase-field method
- Critical factor for refinement - $factor = 0.6$
- Maximum number of refinements - $n = 50$

The analysis was performed using displacement control method incrementing the horizontal displacement of the right support by steps of $\Delta u = 0.001$ mm. Plane-stress was adopted. Four level of refinement were performed: Substitution with convert integration point (IP) false, substitution with convert IP true, refinement of the meshfree region =1 and refinement of the meshfree region =2. For comparison of the results, the experimental scatter from Arrea and Ingraffea (1982), FEM with the initial coarse mesh and FEM with refined mesh are shown. The FEM refined mesh was adopted by Bayao et al. (2021) and presents $h = 2.5$ mm. The load versus *crack mouth sliding displacement* (CMSD) are illustrated in Fig. 7.35.

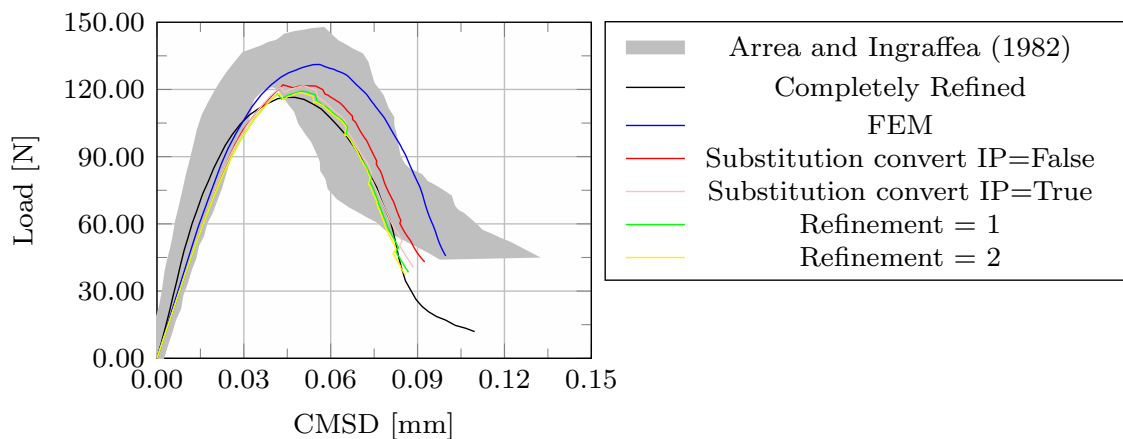
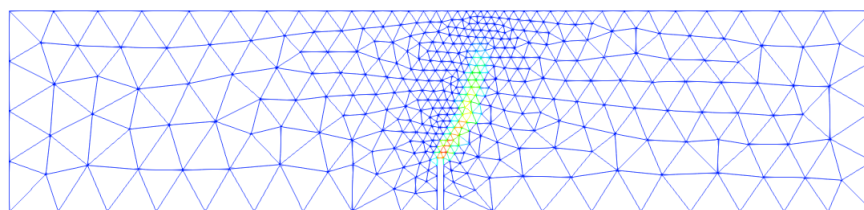


Figure 7.35: Equilibrium paths of the four-point shear test.

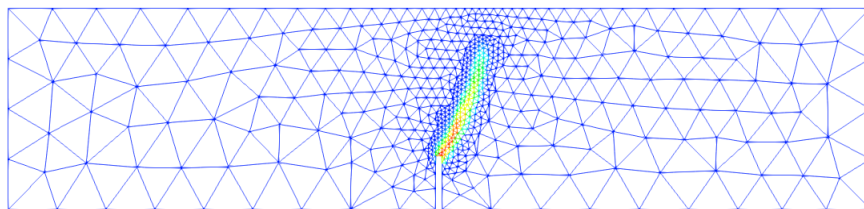
As can be seen, the curve shows a lower peak of load as the model refinement level increase and the curves converge to the completely refinement model. It is important to

emphasize that for the analysis with substitution and `convert IP = false`, the discretisation of the model is the same that the initial mesh, but the analysis with substitution of the region of the crack present a curve more similar to refined model. This fact is justified by the shape function used in the meshfree method. In this case, a trigonometric function was used for the radial function and this function better approximate the phase-field profile compared to linear function used in FEM.

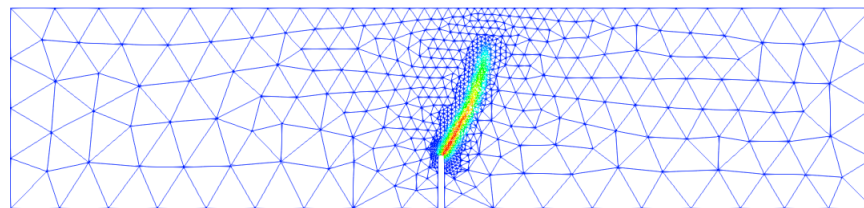
The final mesh and the phase-field contour plot for each level of refinement are illustrated in Fig. 7.36. The magnified view of the crack region for the `refinement=2` is shown in Fig. 7.37. All phase-field contour plot presented correctly the crack profile as observed experimentally.



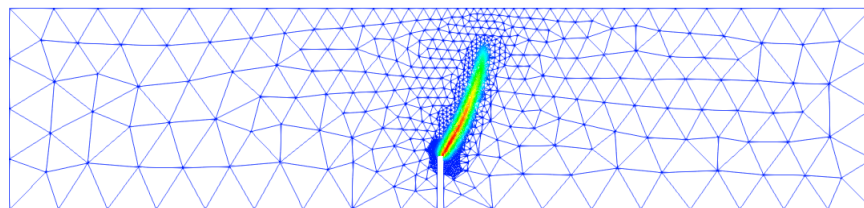
(a) Substitution convert IP=False



(b) Substitution convert IP=True



(c) Refinement = 1



(d) Refinement = 2

Figure 7.36: Contour plot of the phase-field and final mesh of the four-point shear test.

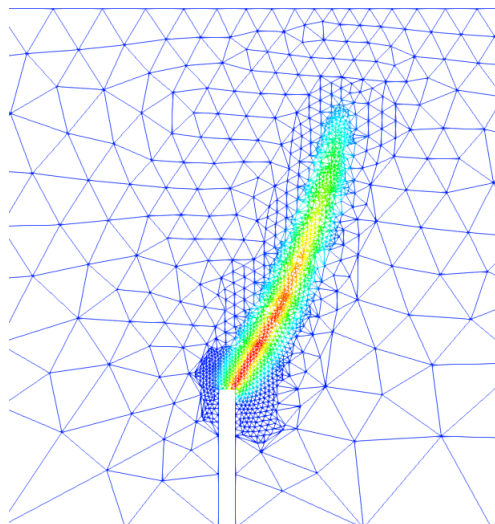


Figure 7.37: Magnified view of the crack region of the four-point shear test..

The average length of the background cells for each level of refinement is presented in Table 7.2.

Table 7.2: Average length of the background cells of the four-point shear test.

Level of refinement	Length of the cells (mm)
Substitution convert IP=False	10
Substitution convert IP=True	6
Refinement=1	3.28
Refinement=2	1.90

7.4 Type of smoothing domain

The influence of the type of smoothing domain and T-scheme for node selection is presented in this section. The three point bending test performed by Miehe, Hofacker and Welschinger (2010) is used. This same model was investigated in Section 6.1 for previously refined mesh and all domain with SPIM. The geometry, loading and boundary conditions are illustrated in Fig. 7.38. The material parameters are: Young's modulus $E = 20.8$ kN/mm², Poisson's ratio $\nu = 0.3$, critical energy release rate $G_c = 5.0 \times 10^{-4}$ kN/mm and length scale parameter $l_0 = 0.06$ mm. Plane-strain state is adopted.

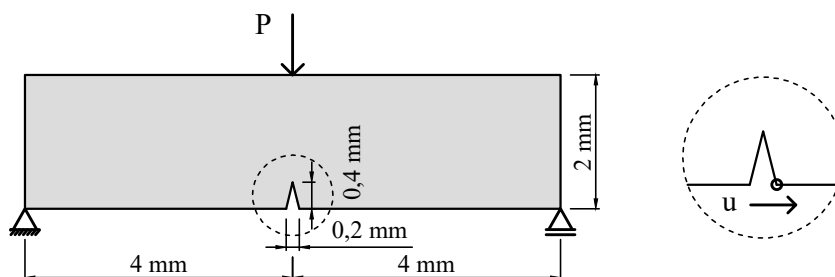


Figure 7.38: Geometry, loading and boundary conditions of the bending test.

The initial mesh of the model is shown in Fig. 7.39.

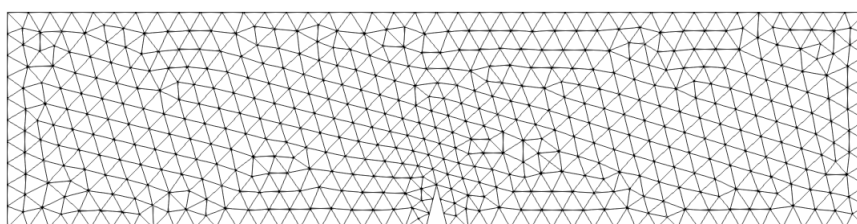


Figure 7.39: Initial mesh of the bending test.

The exponential radial function with $c = 1$ is used and the parameters of the adaptive strategy are indicated below:

- Substitution method - Shao criterion
- Critical factor for substitution - $factor = 0.3$ and $PF_{critical} = 0.01$
- Scale of substitution - $scale = 3.0$
- Refinement method - phase-field method
- Level of refinement - $ref = 2$
- Critical factor for refinement - $factor = 0.8$
- Maximum number of refinements - $n = 50$

The non linear analyses are performed using displacement control method with $\Delta u = 2 \times 10^{-4}$ mm for the point indicated in Fig. 7.38. The simulations are performed adopting cell-based with T4 scheme, edge-based with T3 scheme and edge-based with T6/3 scheme. FEM with the initial coarse mesh and FEM with the pre-refined mesh (Section 6.1.1) are presented for comparison. It is possible to observe that the analyses performed with the adaptive strategy shown a good agreement with the FEM with refined mesh. The peak of load was similar for all smoothing domains and the edge-based with T3 scheme presented a curve more smooth.

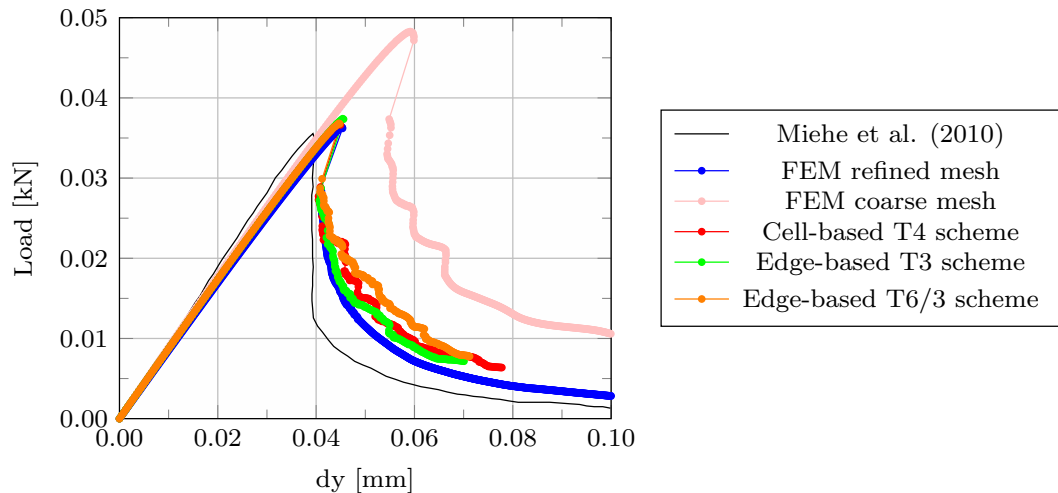
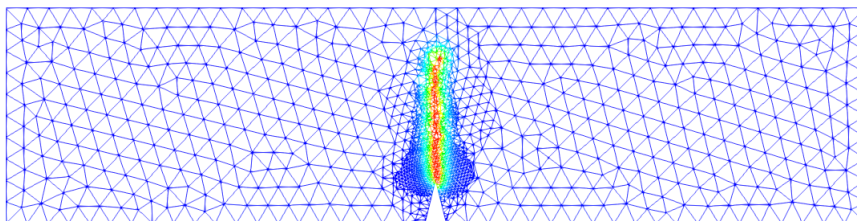
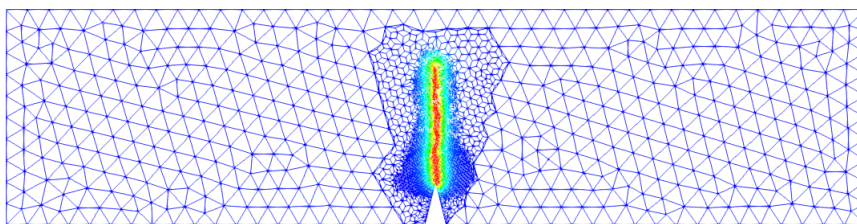


Figure 7.40: Load-displacement curves of the bending test.

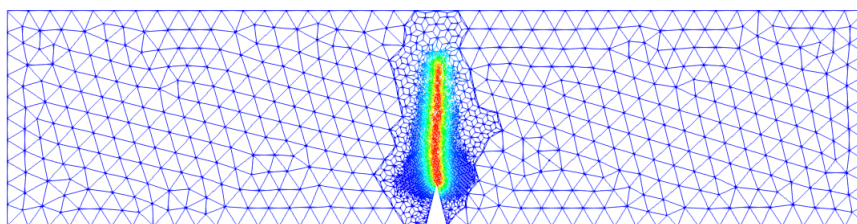
The profile of the phase-field for the final step of the different simulations are illustrated in Fig. 7.41. A magnified view of the crack region for the simulation with edge-based T6/3 scheme is presented in Fig. 7.42. The three different adaptive strategies were able to simulate correctly the crack propagation for this problem.



(a) Cell-based T4



(b) Edge-based T3



(c) Edge-based T6/3

Figure 7.41: Contour plot of the phase-field and final mesh of the bending test.

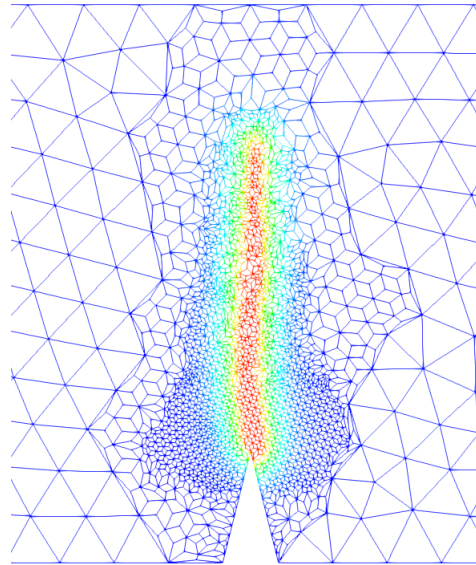


Figure 7.42: Magnified view of the crack region of the bending test with edge-based T6/3.

Table 7.3 compare the total number of nodes of the different analyses: FEM coarse mesh, FEM refined mesh, adaptive cell-based, adaptive edge-based T3 and adaptive edge-based T6/3. It possible to observe that the number of nodes in the adaptive strategies is smaller than the fine mesh.

Table 7.3: Total number of nodes in the bending test.

Type of analysis	Number of nodes
FEM refined mesh	3561
FEM coarse mesh	580
Cell-based T4	1463
Edge-based T3	1496
Edge-based T6/3	1494

7.5 Substitution criterion

This section studies the different substitution criteria. The model adopted is the mixed-mode failure test of Galvez et al. (1998) depicted in Fig. 7.43. The material properties of this test from Galvez et al. (1998) are: Young's modulus $E = 38.0 \text{ kN/mm}^2$, Poisson's ratio $\nu = 0.2$, critical energy release rate $G_c = 6.9 \times 10^{-5} \text{ kN/mm}$ and $f_t = 3.0 \times 10^{-3} \text{ kN/mm}^2$. According to Wu (2018a), the length scale parameter $l_0 = 2.5 \text{ mm}$, the plane-stress is assumed and the Cornelissen softening law is employed with $p = 2$, $a_2 = 1.3868$ and $a_3 = 0.6567$. The constitutive model of Wu (2018b) is adopted and the crack shape function with $\xi = 2$ is used.

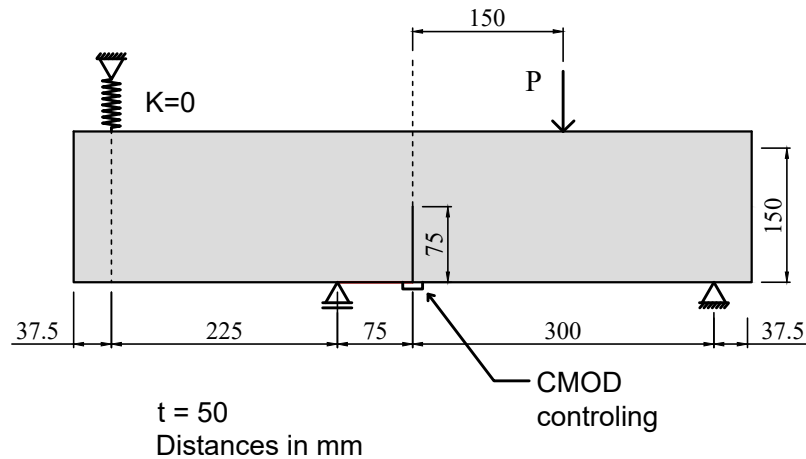


Figure 7.43: Geometry, loading and boundary conditions of the mixed-mode failure test.

The initial mesh adopted is illustrated in Fig. 7.44. Only the region between the supports is considered, as presented in Zhang, Hu, Wang and Yao (2018).

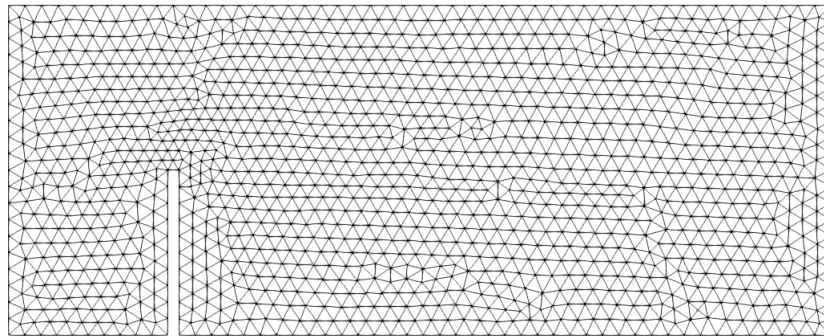


Figure 7.44: Initial mesh of the mixed-mode failure test.

Similar to other examples, the smoothing domain with cell-based and T4 scheme is used for the meshfree region. The RPIMp shape functions and scaled exponential radial functions $c = 1$ are adopted. The parameters of the adaptive strategy are shown below:

- Scale of substitution - $scale = 3.0$
- Refinement method - phase-field method
- Level of refinement - $ref = 2$
- Critical factor for refinement - $factor = 0.7$
- Maximum number of refinements - $n = 100$

Three different substitution criteria are simulated:

- Shao criterion with $factor = 0.5$ and $PF_{critical} = 0.05$
- Phase-field critical criterion with $PF_{critical} = 0.05$
- Strain energy criterion with $factor = 15$

The numerical simulations are performed considering displacement control method incrementing the vertical displacement of the point of load application in $\Delta u = -0.001$

mm. The curves of load versus crack mouth opening displacement (CMOD) are presented in Fig. 7.45. The experimental results by Galvez et al. (1998) and the numerical results by Wu (2018b) are depicted in the same figure. The curve of the strain energy method was not plotted because the analysis stopped in the first step. In models that present traction and compression regions, this method substitute both regions. This fact can be observed in Fig. 7.46. In other hand, the analyses performed with Shao and phase-field criteria presented a good agreement with the numerical curve and the experimental region. The final mesh and phase-field contour plot for these criteria are shown in Fig. 7.47 and Fig. 7.48.

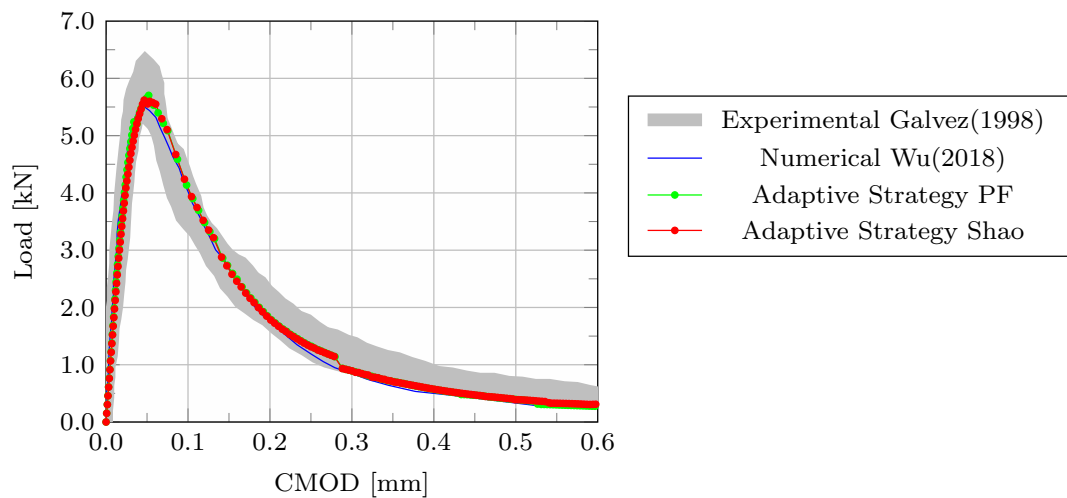


Figure 7.45: Load-CMOD curves of the mixed model failure test.

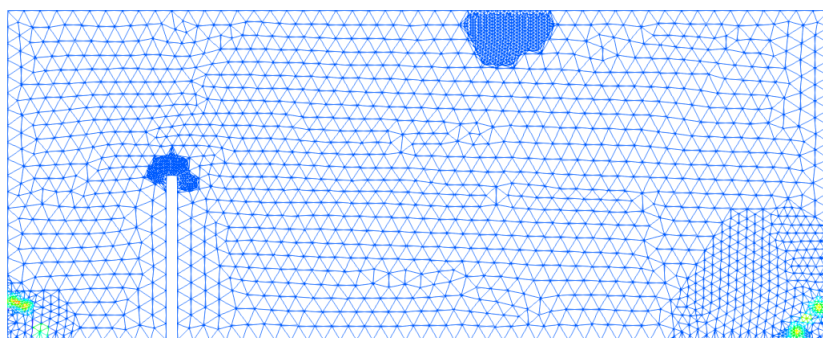


Figure 7.46: Substitution regions of the mixed-mode failure test with strain energy criterion.

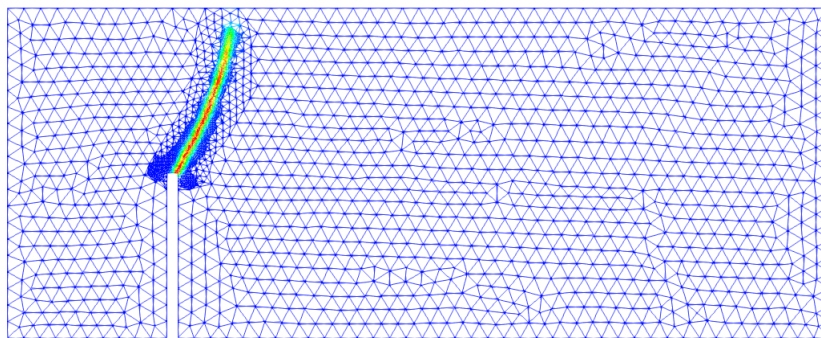


Figure 7.47: Contour plot of phase-field and final mesh of the mixed-mode failure test with Shao criterion.

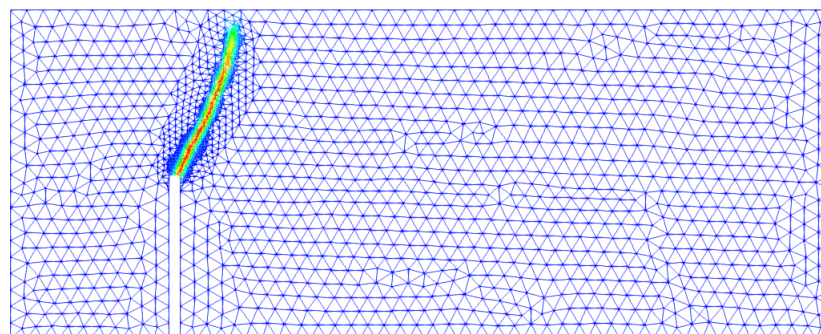


Figure 7.48: Contour plot of phase-field and final mesh of the mixed-mode failure test with phase-field criterion.

7.6 Refinement criterion

This section presents the simulations performed with three different refinement criteria: phase-field (PF), equivalent strain (ES) and strain energy (SE). The 3 point bending test of Petersson (1981) is adopted. The geometry, loading and boundary conditions are depicted in Fig. 7.49. The material parameters used are the same that Bayao et al. (2021) and Fortes (2022). In this works, the authors realized a calibration to obtain the length scale parameter. They adopted the parameters presented in Penna (2011) for smeared crack constitutive model as reference: Young's modulus $E = 30000 \text{ N/mm}^2$, Poisson's ratio $\nu = 0.2$, critical energy release rate $G_c = 0.124 \text{ N/mm}$ and $f_t = 3.3 \text{ N/mm}^2$. The l_0 obtained was 12.5 mm. The constitutive model of Wu (2017) is adopted and plane-stress is assumed. The Cornelissen softening law is employed with $p = 2$, $a_2 = 1.3868$ and $a_3 = 0.6567$. The crack shape function with $\xi = 2$ is used.

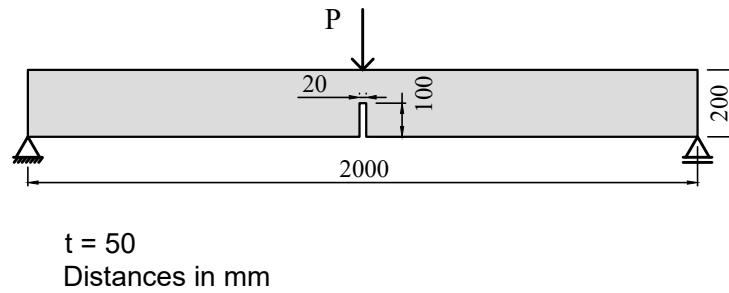


Figure 7.49: Geometry, loading and boundary conditions of the 3 point bending test.

The initial mesh of the adaptive strategy is given in Fig. 7.50 and the mesh adopted by Fortes (2022) is shown in Fig. 7.51.

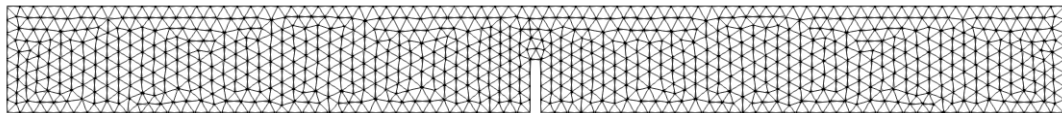


Figure 7.50: Initial mesh of the 3 point bending test.

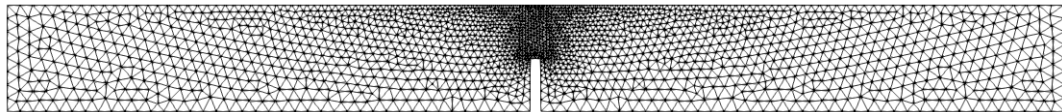


Figure 7.51: Mesh of the 3 point bending test by Fortes (2022).

The RPIMp shape functions and scaled exponential radial functions $c = 1$ are adopted. The parameters of the adaptive strategy are presented below:

- Smoothing domain - Cell-based T4 scheme
- Substitution criterion - Shao criterion
- Critical factor for substitution - $factor = 0.3$ and $PF_{critical} = 0.01$
- Scale of substitution - $scale = 4.0$
- Level of refinement - $ref = 2$
- Critical factor for refinement - $factor = 0.05$
- Decay rate - $factorDecayRate = 0.0$
- Maximum number of refinements - $n = 50$

The numerical simulations are performed using displacement control method incrementing the vertical displacement of the load point in $\Delta u = -0.004$ mm. The load-displacement curves are shown in Fig. 7.52. The curve of FEM with the coarse mesh, the numerical result of Fortes (2022) with refined mesh and the experimental region by Peterson (1981) are presented for comparison. All refinement criteria presented similar curves and results close to the numerical reference. But the curves shown a jump. This jump

occurs because the beam height above notch is small, so when the second substitution is realized, a large mesh modification occurs.

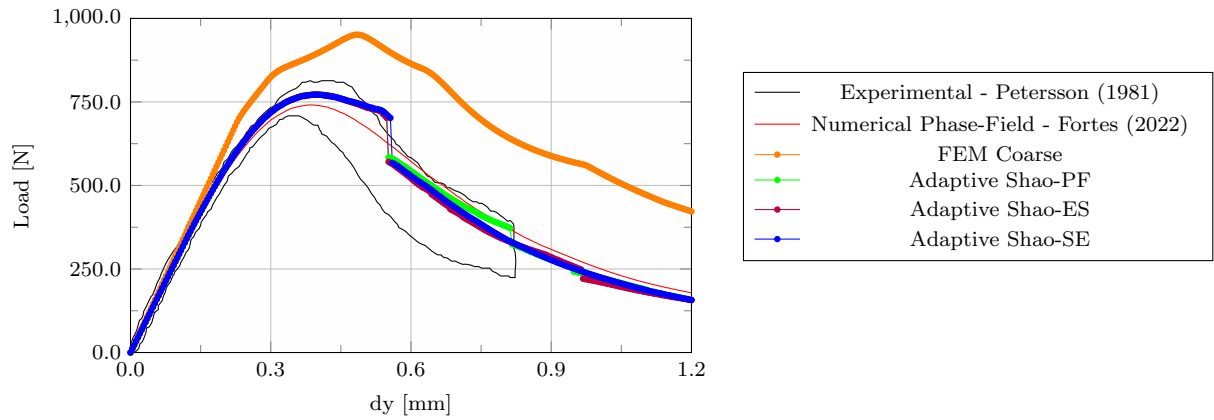
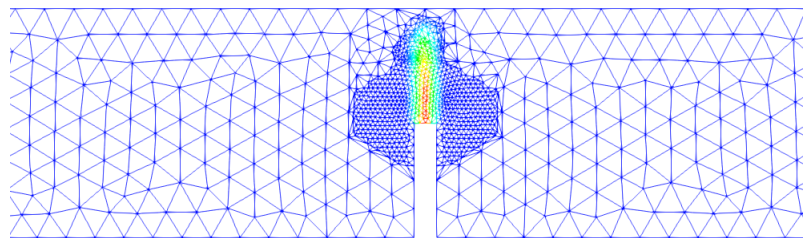
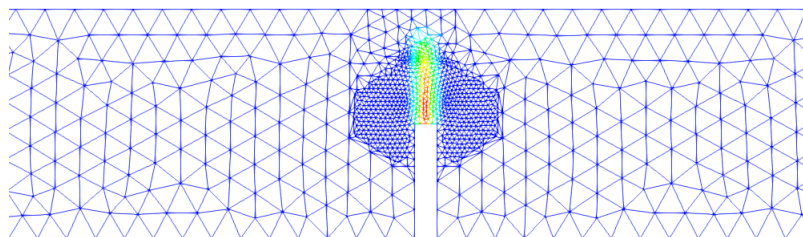


Figure 7.52: Load-displacement curves of the 3 point bending test.

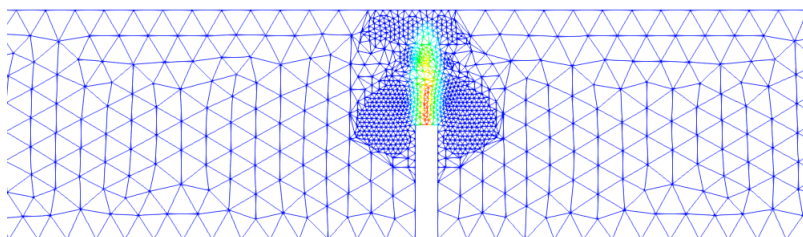
The phase-field profiles are shown in Fig. 7.53. For this example, the phase-field refinement criterion presented the best mesh refinement. The large refined region observed near the notch occurs in the first step. At this stage, the distribution of the phase-field variable is similar throughout the region.



(a) Phase-Field



(b) Equivalent strain



(c) Strain energy

Figure 7.53: Contour plot of the phase-field and final mesh of the 3 point bending test.

Table 7.4 compare the total number of nodes of the different analyses: numerical analysis by Fortes (2022), FEM initial mesh, adaptive Shao-PF, adaptive Shao-ES and adaptive Shao-SE. It is important to emphasize that the nodal spacing adopted in the refined mesh by Fortes (2022) was 6.25 mm and in the adaptive strategy it reaches a nodal spacing of 3.62 mm. Although the adaptive mesh is more refined, the total number of nodes is smaller than in the Fortes (2022).

Table 7.4: Total number of nodes in the 3 point bending test.

Type of analysis	Number of nodes
Fortes (2022)	1979
FEM initial mesh	862
Adaptive Shao-PF	1599
Adaptive Shao-ES	1550
Adaptive Shao-SE	1549

7.7 Comparison with adaptive damage models

This section presents a comparison between the adaptive strategy with the phase-field model and adaptive strategy with smeared crack performed by Saliba (2022). The 3 point bending test with a decentralized notch proposed by Gracia-Álvarez et al. (2012) is used. The geometry, loading and boundary conditions are illustrated in Fig. 7.54. The thickness is 50 mm.

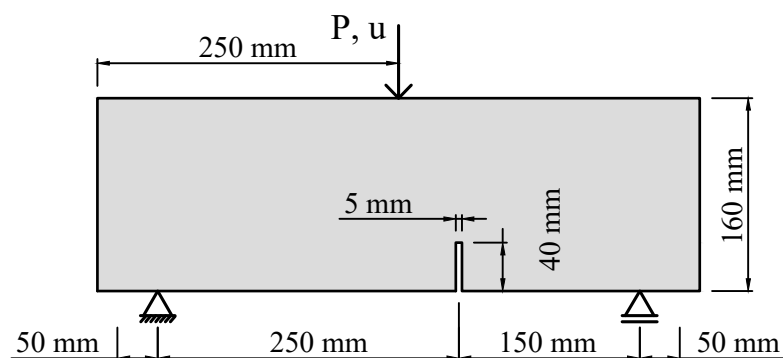


Figure 7.54: Geometry, loading and boundary conditions of the Gracia bending.

The material parameters adopted by Saliba (2022) were the same that indicated by Gracia-Álvarez et al. (2012): Young's modulus $E = 33800 \text{ N/mm}^2$, Poisson's ratio $\nu = 0.2$, critical energy release rate $G_c = 0.08 \text{ N/mm}$ and $f_t = 3.5 \text{ N/mm}^2$. The other parameters necessary to the smeared crack model are: $f_t = 35 \text{ N/mm}^2$, $\epsilon_c = 0.0011$, $h = 12.5 \text{ mm}$ and $\beta_r = 0$.

For the phase-field model is necessary to calibrate the length scale parameter. This calibration was realized using a single Q4 element, subjected to plane stress with thickness

of 1 mm. The simulation were performed using the energetic degradation of Cornelissen and exponential. The crack shape function with $\xi = 2$ is used. The curves are shown in Fig. 7.55. The function of Cornelissen presented a best result and $l_0 = 4$ mm.

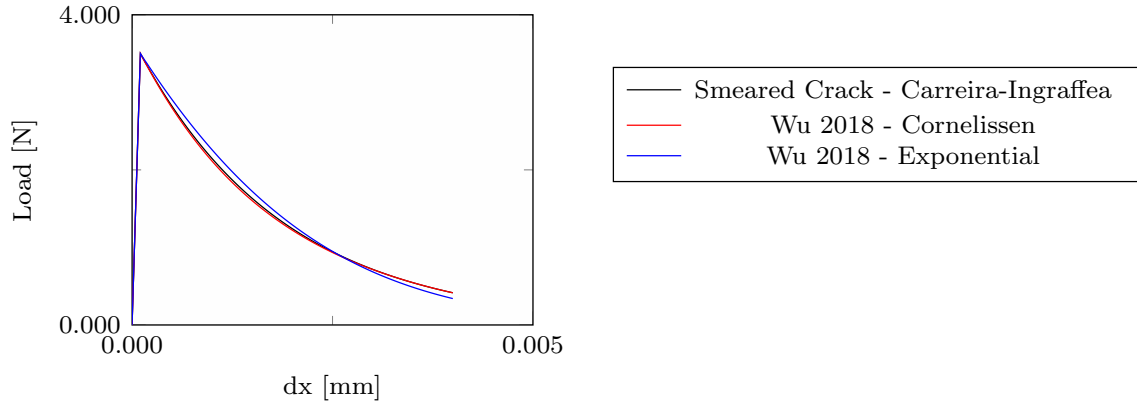


Figure 7.55: Calibration of the l_0 parameter of the Gracia bending.

The RPIMp was used with the exponential function and $c = 1$ for the construction of the shape functions of the meshfree region. For the adaptive strategy, the following parameters are adopted:

- Smoothing domain - Cell-based T4 scheme and Edge-based T3 scheme
- Substitution criterion - Shao criterion
- Critical factor for substitution - $factor = 0.5$ and $PF_{critical} = 0.08$
- Scale of substitution - $scale = 3.0$
- Refinement criterion - phase-field criterion
- Level of refinement - $ref = 2$
- Critical factor for refinement - $factor = 0.6$
- Maximum number of refinements - $n = 5$
- Decay rate - $factorDecayRate = 0.1$

The initial mesh is depicted in Fig. 7.56.

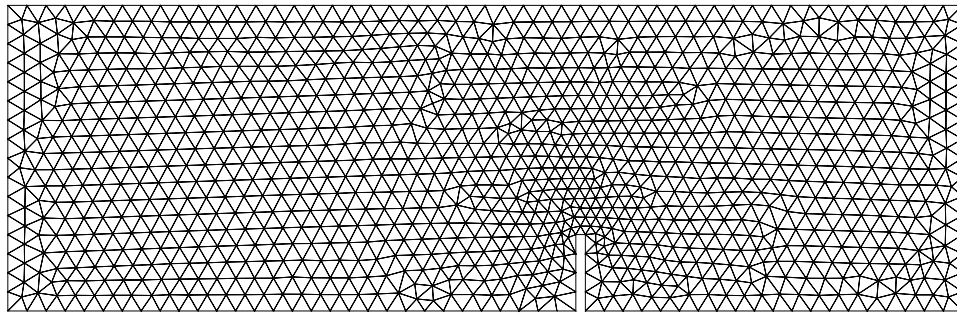


Figure 7.56: Initial mesh of the Gracia bending.

In the non linear analyses, the displacement control method was adopted incrementing vertical displacement of $\Delta u = -0.00005$ mm in the load point. The load applied was

–6200 N. The equilibrium paths presented the load factor versus the *crack mouth opening displacement* (CMOD) in Fig. 7.57. The results with the adaptive strategy and the phase-field model presented good results in relation to experimental region and smooth curves comparing with the smearing crack, that presented jumps.

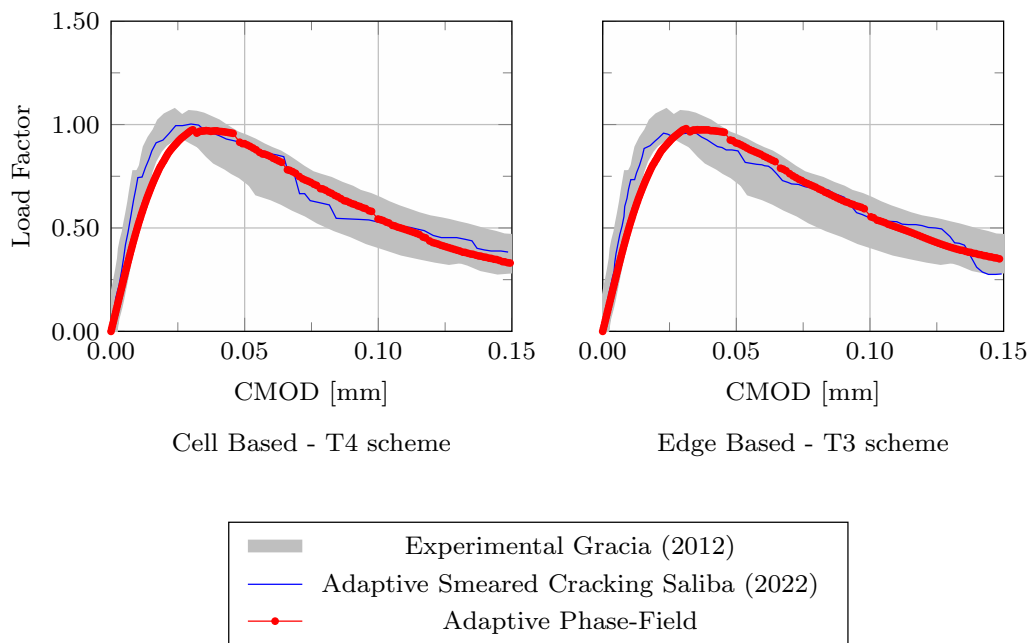
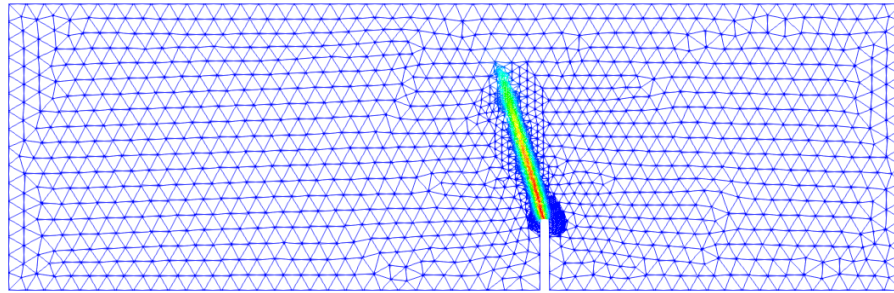
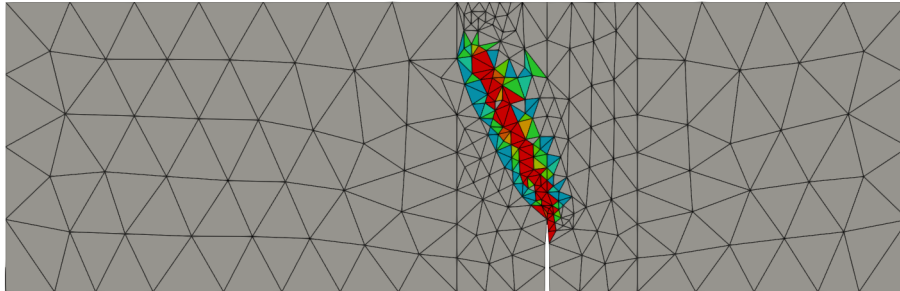


Figure 7.57: Load factor versus CMOD of the Gracia bending.

The Figs. 7.58 and 7.59 presented the crack and the final mesh of the analyses for cell-based and edge-based, respectively. The meshes of the phase-field models are more refined than the smeared crack model, which leads to a high computational cost. On the other hand, phase field models have the advantage of simulating complex cracks because the crack profile is more defined.

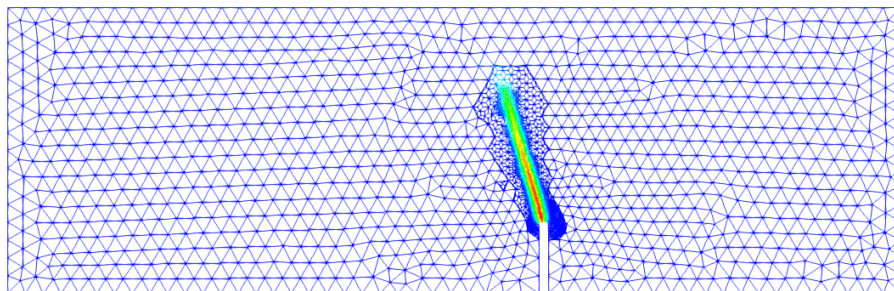


(a) Phase-Field

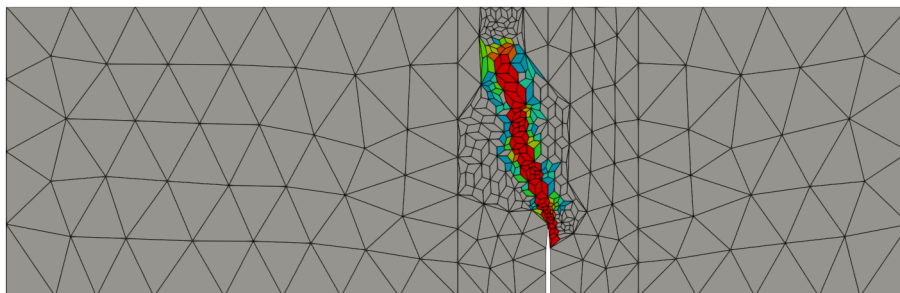


(b) Smearred crack

Figure 7.58: Crack and final mesh of the Gracia bending for cell-based.



(a) Phase-Field



(b) Smearred crack

Figure 7.59: Crack and final mesh of the Gracia bending for edge-based.

7.8 Notched rectangular specimen with a hole

The objective of this section is to investigate the adaptive strategy in specimen with hole. The model adopted was analysed by Shao et al. (2019) and is shown in Fig. 7.60. The material parameters are: Young's modulus $E = 5.98 \text{ kN/mm}^2$, Poisson's ratio $\nu = 0.22$, critical energy release rate $G_c = 2.28 \times 10^{-3} \text{ kN/mm}$, and length scale parameter $l_0 = 2.5 \text{ mm}$. The constitutive model of Miehe, Welschinger and Hofacker (2010) is applied with the energetic degradation function of Bourdin et al. (2000) and the geometric crack function with $\xi = 0$. The plane-strain state is adopted.

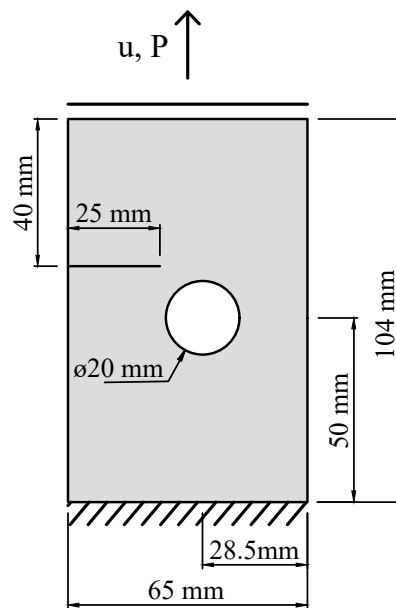


Figure 7.60: Geometry, loading and boundary conditions of the notched test.

The initial mesh is illustrated in Fig. 7.61.

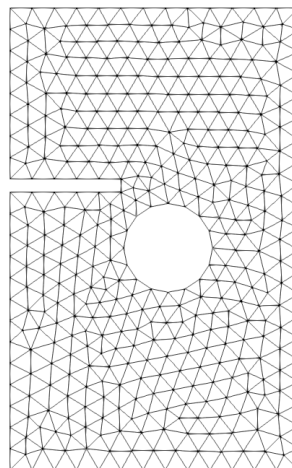


Figure 7.61: Initial mesh of the notched test.

The RPIMp shape functions and scaled exponential radial functions $c = 1$ were adopted for the meshfree region. The others parameters of the adaptive strategy are presented below:

- Smoothing domain - Cell-based T4 scheme
- Substitution criterion - Shao criterion
- Critical factor for substitution - $factor = 0.5$ and $PF_{critical} = 0.2$
- Scale of substitution - $scale = 2.0$
- Refinement criterion - phase-field criterion
- Level of refinement - $ref = 2$
- Critical factor for refinement - $factor = 0.7$
- Maximum number of refinements - $n = 10$
- Decay rate - $factorDecayRate = 0.1$

The displacement control method is applied with a increment of $\Delta u = 1 \times 10^{-3}$ mm on the top surface. The load-displacement curve is illustrated in Fig. 7.62. The jumps observed in the curves refer to the substitution and refinement of the steps 278 and 337. This behaviour is characteristic of the brittle fracture models.

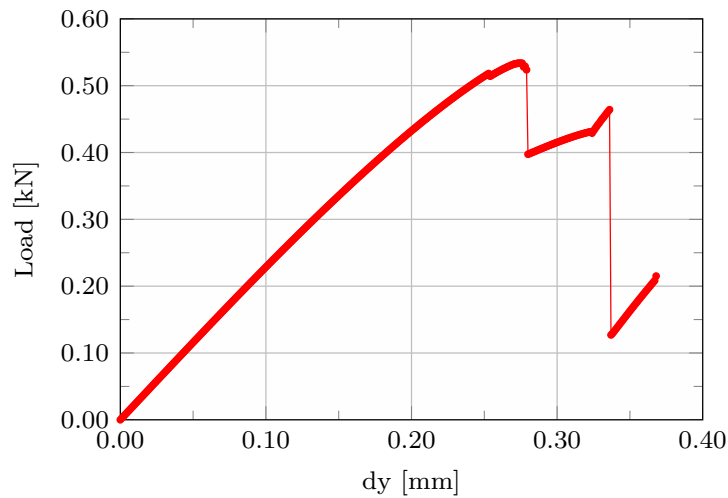


Figure 7.62: Load-displacement curve of the notched test.

The crack propagation with the adaptive refinement of the mesh is shown in Fig. 7.63 and the final crack of the Shao et al. (2019) is illustrated in Fig. 7.64. The two analyses presented similar profile of the phase-field.

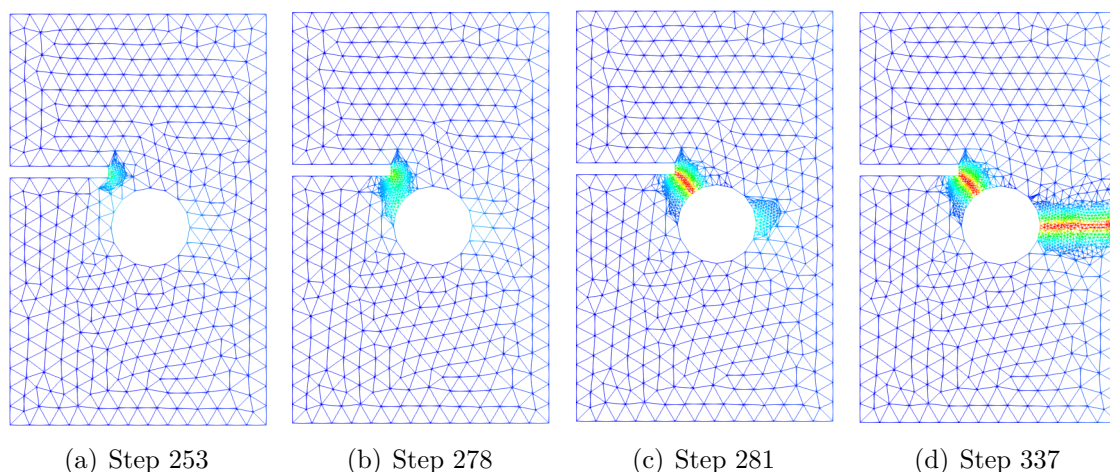


Figure 7.63: Crack propagation in different steps of the notched test.

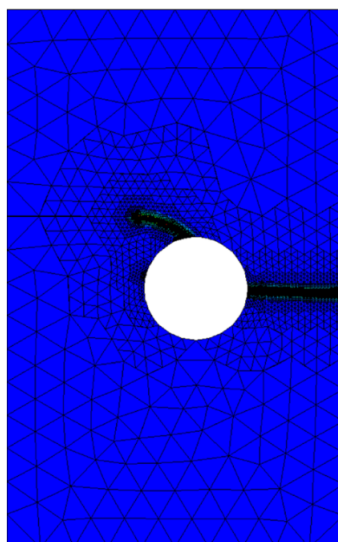


Figure 7.64: Final mesh of the Shao et al. (2019) for the notched test.

7.9 Two regions of substitution and refinement

The objective of this section is to verify a model that need of two regions of substitution. The example adopted is the asymmetric double notched tensile test studied by Molnar and Gravouil (2017). The geometry, loading and boundary conditions are depicted in Fig. 7.65. The following material properties are used: Young's modulus $E = 210 \text{ kN/mm}^2$, Poisson's ratio $\nu = 0.3$, critical energy release rate $G_c = 2.7 \times 10^{-3} \text{ kN/mm}$, and length scale parameter $l_0 = 0.2 \text{ mm}$. The constitutive model of Miehe, Welschinger and Hofacker (2010) is applied with the energetic degradation function of Bourdin et al. (2000) and the geometric crack function with $\xi = 0$. The plane-strain state is adopted.

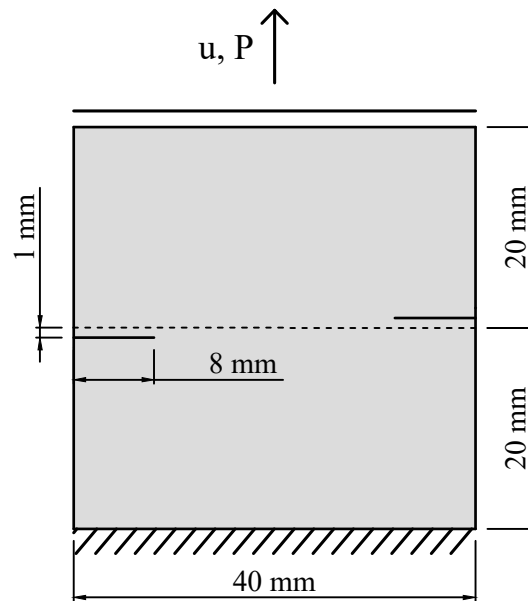


Figure 7.65: Geometry, loading and boundary conditions of the asymmetric tensile test.

The initial mesh is illustrated in Fig. 7.66.

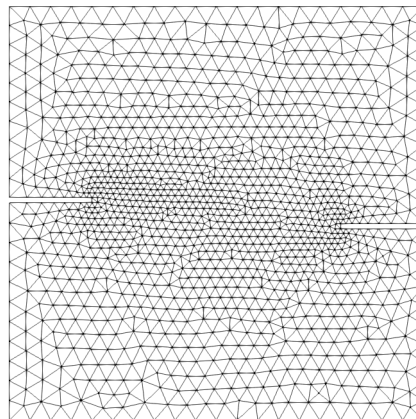


Figure 7.66: Initial mesh of the asymmetric tensile test.

The parameters of the adaptive strategy are shown:

- Smoothing domain - Edge-based T3
- Shape function - RPIMp Exponential $c = 1$
- Substitution criterion - Shao criterion
- Critical factor for substitution - $factor = 0.8$ and $PF_{critical} = 0.1$
- Scale of substitution - $scale = 3.0$
- Refinement method - phase-field method
- Level of refinement - $ref = 2$
- Critical factor for refinement - $factor = 0.6$
- Maximum number of refinements - $n = 100$
- Decay rate - $factorDecayRate = 0.0$

The non linear analysis is performed adopting the displacement control with increments of $\Delta u = 1 \times 10^{-3}$ mm for 35 steps and $\Delta u = 1 \times 10^{-4}$ mm for the rest of the simulation. The load-displacement curve is shown in Fig. 7.67 and the reference not present the load-displacement curve for comparison. The curve obtained is characteristic of brittle fracture.

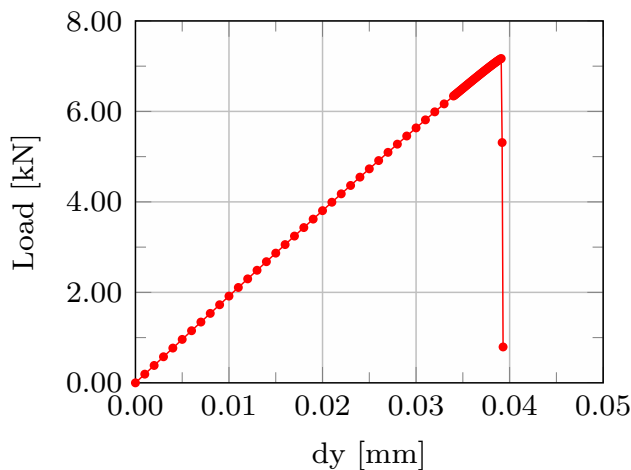
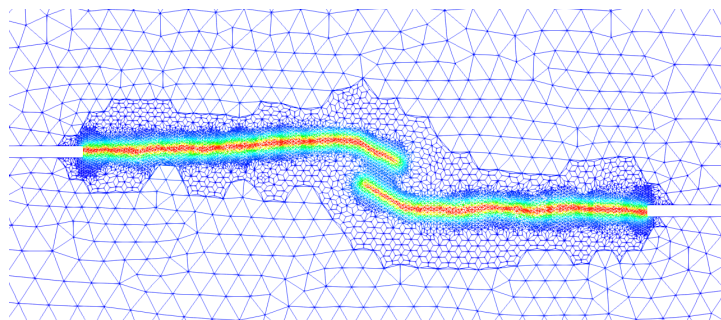
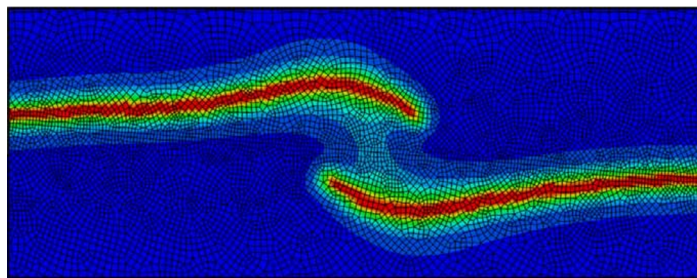


Figure 7.67: Load-displacement curve of the asymmetric tensile test.

The crack propagation and the adaptive mesh are presented in Fig. 7.69 for 3 different steps of load. The phase-field profile for the last step of the analysis is compared with the reference in Fig. 7.68. It is possible to observe that the adaptive strategy is able to correctly simulate the propagation of two cracks symmetrically.

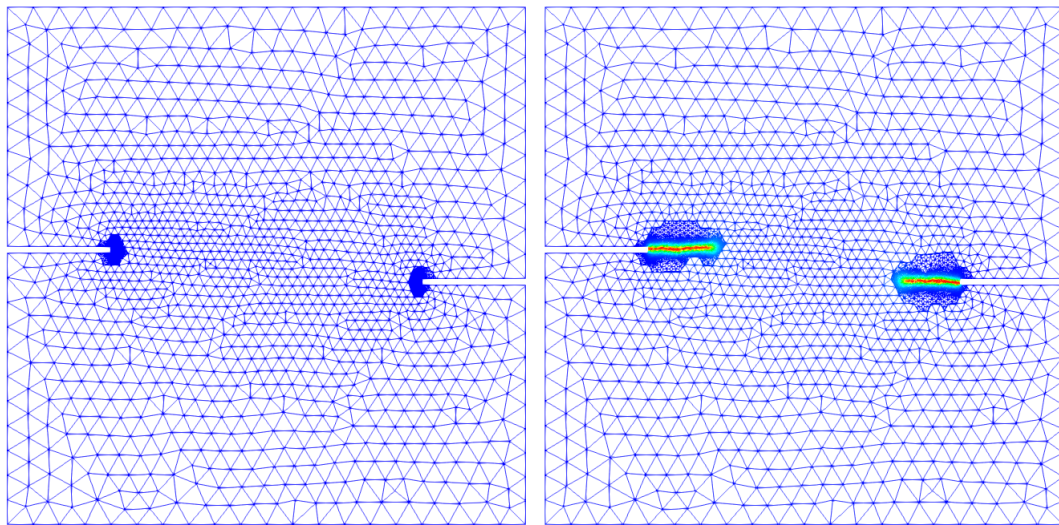


(a) Adaptive strategy



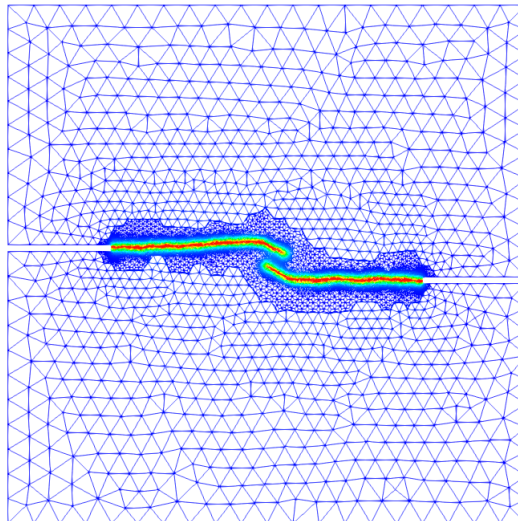
(b) Reference Molnar and Gravouil (2017)

Figure 7.68: Comparison of the crack profile with the reference.



(a) Step 1

(b) Step 86



(c) Step 87

Figure 7.69: Crack propagation in different steps of the asymmetric tensile test.

Chapter 8

Conclusions

The main aim of this thesis was to propose a novel strategy for the adaptive coupling between finite element method and smoothed point interpolation methods (SPIMs), applied to the phase-field modelling of fracture. SPIM are a family of meshfree methods that use the Point Interpolation Method (PIM) and Radial Point Interpolation Method (RPIM) for the construction of the shape functions and the smoothing operation to calculate the derivative of the shape functions. The phase-field is a model used for the representation of cracks, capable to detecting the nucleation, propagation and merging of cracks. While a large part of the literature focuses on FEM applications of phase-field modelling, with some contributions on meshfree methods, this work is, to the author knowledge, the first contribution on SPIMs combined with phase-field modelling of fracture.

The application of SPIM discretisations to the phase-field modelling of fracture required a new formulation of the smoothing operation which SPIMs are based on; this new formulation was necessary in order to take into account the presence of an additional field-variable, the phase-field value. Furthermore, a new trigonometric radial basis function was proposed, for a better representation of the phase-field geometric crack function $\alpha = 2\phi - \phi^2$. The study and implementation of the union of these two methods was performed in three stages: First, SPIM was adopted in the entire domain with a pre-refined mesh in the crack propagation region. In the second stage, a previously coupled FEM-SPIM was adopted with SPIM only in region of interest and the mesh pre-refined in this region. In the last stage, a adaptive coupling SPIM-FEM was proposed. In this adaptive strategy, the initial mesh is coarse and during the analysis it is automatically refined.

In all these strategies, it is possible to use the different smoothing domains cell-, edge- and node-based and T-schemes for nodes selection of the support domain. For the phase-field models, brittle fracture and quasi-brittle fracture can be used. The staggered solver with historical variable and the constrained optimization problem can be adopted.

In the following sections, the main aspects and contributions of each strategy are presented.

8.1 Full SPIM

The first study was to verify the stability and accuracy of using SPIM with phase-field modelling. For this, in the all domain, the meshfree method is adopted. This strategy can be used when region of crack propagation is known. In these regions, the mesh is previously refined.

Numerical simulations were performed using only SPIM and the results were compared with numerical FEM results and results of the literature. In general, the results shown a good agreement with the reference and the crack propagation as expected. The node-based did not presented good results. Analyses of computational time were performed and time of processing of the edge and cell-based were lower than FEM, but the SPIM presented a high pre-processing cost. The study of the influence of the parameter c used in exponential radial function shown that modifying this parameter does not influence the results. For these same simulations, a convergence test was performed. This test shown that the analysis performed with SPIM better approximated the peak of load compared to the FEM and this result was associated to shape functions adopted that better represent the phase field profile. With a mesh more coarse it was possible to obtain a good results. The results of this first step were published in Novelli, Gori and Pitangueira (2022).

8.2 Previously coupled FEM-SPIM

The second strategy was to verify the previously coupled FEM-SPIM model. In this case, the mesh is pre-refined in the crack propagation region. As the shape function used in the SPIM posses the Kronecker delta property, the coupling is done directly.

This strategy can be used when the path of crack propagation is known and the user want to use the SPIM to better approximate the crack region. In this case, the user must inform the region for substitution. The results obtained with this strategy presented a good agreement with reference and full FEM. The second step was published in Novelli, Saliba, Gori and Pitangueira (2022)

8.3 Adaptive SPIM-FEM coupling

The last strategy is the adaptive coupling SPIM-FEM model. This strategy is the major contribution of this work. The domain is initially discretised with a FEM coarse mesh. A criterion detects the region that need further refinement and this region is replaced by SPIM. This meshfree region goes through several refinements until the required level. It is interesting that the criterion detects the region in front of the crack, so that the crack propagates in the appropriated mesh.

All the process is automatic and the user must inform some parameters of the adaptive

strategy. These parameters are associated with the method for detecting the region of substitution, the size of this region, the criterion for detecting the faces of the meshfree region that will be refined and the level of refinement required. Among the criteria for detecting the region to be replaced are strain energy, equivalent strain, phase-field and a combined phase-field and the historical variable. This adaptive strategy is interesting when the path of crack propagation is not known.

Numerical simulations were performed to test the adaptive strategy. The examples analysed the influence of each parameter of the adaptive strategy. The results were compared with the experimental and numerical FEM. In general, the results presented a good agreement with the references. The criteria for substitution were able to correctly detect the region to be replaced, except the strain energy criterion when applied in models with compression regions. In relation to the factors used for substitution and refinement, factors with small values were more appropriate because the refinement region is larger. For phase-field models, it is important that the crack propagation region is refined. When using a smaller substitution factor, it is important to adopt a scale to increase the substitution region. Regarding the refinement criterion for the meshfree region, the phase-field presented the best results. Comparing the total number of nodes at the final of the analyses, this number was much lower than FEM with pre-refined mesh and same level of refinement. The adaptive strategy performed correctly for edge- and cell-based and for different phase-field constitutive models.

8.4 Future research topics

Based on the study presented in this work some future research topics are proposed.

- Adopt a constitutive model different of phase-field at the beginning of the analysis and during the analysis regions of the domain are detected and the phase-field is adopted. With this strategy, only some regions of the domain need of the additional phase-field variable.
- Implement different refinement methods of the mesh for the adaptive strategy. These different refinements aim to generate less distorted meshes.
- Apply the strategy to a broader class of problems. For example, hydraulic fracture, a topic with a number contributions about phase-field applications.

Bibliography

- Ahrens, J., Geveci, B. and Law, C. (2005), *Paraview: An end-User Tool for Large Data Visualization*, Visualization Handbook, Elsevier.
- Ambati, M., Gerasimov, T. and Lorenzis, L. (2015), ‘A review on phase-field models of brittle fracture and a new fast hybrid formulation’, *Computational Mechanics* vol. 55, 383–405.
- Amiri, F. (2019), ‘High-order phase-field model with the local and second-order maximum-entropy approximations’, *Frontiers of Structural and Civil Engineering* vol. 13, 406–416.
- Amiri, F., Millán, D., Arroyo, M., Silani, M. and Rabczuk, T. (2016), ‘Fourth order phase-field model for local max-ent approximations applied to crack propagation’, *Computer methods in applied mechanics and engineering* vol. 312, 254–275.
- Amiri, F., Millán, D., Shen, Y., Rabczuk, T. and Arroyo, M. (2014), ‘Phase-field modeling of fracture in linear thin shells’, *Theoretical and Applied Fracture Mechanics* vol. 69, 102–109.
- Amor, H., Marigo, J. and Maurini, C. (2009), ‘Regularized formulation of the variational brittle fracture with unilateral contact: Numerical experiments.’, *Journal of the Mechanics and Physics of Solids* vol. 57, 1209–1229.
- Areias, P., Rabczuk, T. and Msekhi, M. A. (2016), ‘Phase field analysis of finite-strain plates and shells including element subdivision’, *Computer Methods in Applied Mechanics and Engineering* vol. 312, 322–350.
- Arrea, M. and Ingraffea, A. (1982), Mixed mode crack propagation in mortar and concrete, PhD thesis, Department Of Structural Engineering, Cornell University, Ithaca, EUA.
- Arroyo, M. and Ortiz, M. (2006), ‘Local maximum-entropy approximation schemes: a seamless bridge between finite elements and meshfree methods’, *International Journal for Numerical Methods in Engineering* vol. 65, 2167–2202.
- Artina, M., Fornasier, M., Micheletti, S. and Perotto, S. (2015), ‘Anisotropic mesh adaptation for crack detection in brittle materials’, *SIAM Journal on Scientific Computing* vol. 37, B633–B659.

-
- Badnava, H., Msekh, M. A. and Rabczuk, E. E. T. (2017), ‘An h-adaptive thermo-mechanical phase field model for fracture’, *Finite Elements in Analysis and Design* vol. 138, 31–47.
- Balachandran, G. R., Rajagopal, A. and Sivakumar, S. M. (2008), ‘Meshfree galerkin method based on natural neighbors and conformal mapping’, *Computational Mechanics* vol. 42, 885–892.
- Bayao, R. G., Leão, H. M., Fortes, M. M., Gori, L. and Pitangueira, R. L. S. (2021), Implementation of a bound-constrained solver in phase-field modelling of fracture, in ‘Proceedings of the XLII Ibero-Latin-American Congress on Computational Methods in Engineering and III Pan-American Congress on Computational Mechanics’.
- Beletschko, T., Lu, Y. Y. and Gu, L. (1994), ‘Element-free galerkin methods’, *International Journal for Numerical Methods in Engineering* vol. 37, 229–256.
- Belytschko, T. and Organ, D. Krongauz, Y. (1995), ‘A coupled finite element elementfree galerkin method’, *Computational Mechanics* vol. 17, 186–195.
- Belytscho, T., Lu, Y. and Gu, L. (1994), ‘Element-free galerkin methods’, *International Journal Numerical Methods in Engineering* vol. 37, 229–256.
- Benson, S. J. and Munsun, T. S. (2006), ‘Flexible complementarity solvers for large-scale applications’, *Optimization Methods and Software* vol. 21, 155–168.
- Bhowmick, S. and Liu, G. R. (2018), ‘A phase field modeling for brittle fracture and crack propagation based on the cell-based smoothed finite element method’, *Engineering Fracture Mechanics* vol. 204, 369–387.
- Bordas, S. P. A., Duflo, M. and Le, P. (2008), ‘A simple error estimator for extended finite elements’, *Communications in Numerical Methods in Engineering* vol. 24, 961–971.
- Bourden, M. J., Hughes, T. J. R., Landis, C. M. and Verhoosel, C. V. (2014), ‘A higher-order phase field model for brittle fracture: Formulation and analysis within the isogeometric analysis framework’, *Computer Methods in Applied Mechanics and Engineering* vol. 273, 100–118.
- Bourdin, B., Francfort, G. A. and Marigo, J. J. (2000), ‘Numerical experiments in revisited brittle fracture’, *J Mech Phys Solids* vol. 48(4), 797–826.
- Burke, S., Ortner, C. and Suli, E. (2010), ‘An adaptive finite element approximation of a variational model of brittle fracture’, *SIAM Journal of Numerical Analysis* vol. 48, 980–1012.

-
- Chen, J. S., Pan, C., Wu, C. T. and Liu, W. K. (1996), ‘Reproducing kernel particle methods for large deformation analysis of non-linear structures’, *Computer Methods in Applied Mechanics and Engineering* vol. 139, 195–227.
- Chen, J., Yoon, S. and Wu, C. (2002), ‘Non-linear version of stabilized conforming nodal integration for galerkin mesh-free methods’, *International Journal for Numerical Methods in Engineering* vol. 53, 2587–615.
- Cottrell, J. A., Hughes, T. J. R. and Bazilevs, Y. (2009), *Isogeometric analysis: Toward integration of CAD and FEA*, John Wiley and Sons, Chichester.
- Cressie, N. (1990), ‘The origins of kriging’, *Mathematical Geology* vol. 22, 239–252.
- Duarte, C. A., Migliano, D. Q. and Becker, E. B. (2005), ‘A technique to combine meshfree- and finite element-based partition of unity approximations’, *Structural research series, Department of Civil and Environmental Engineering, University of Illinois at Urbana-Champaign*.
- Farrell, P. and Maurini, C. (2017), ‘Linear and nonlinear solvers for variational phase-field models of brittle fracture’, *International Journal for Numerical Methods in Engineering* vol. 109, 648–667.
- Fonseca, F. T. and Pitangueira, R. L. S. (2007), An object oriented class organization for dynamic geometrically nonlinear, in ‘Proceedings of the CMNE (Congress on Numerical Methods in Engineering)/ CILAMCE (Iberian-Latin-American Congress on Computational Methods in Engineering)’.
- Fortes, M. M. (2022), A bound-constrained solver for phase-field modeling of diffuse fracture, Master’s thesis, Universidade Federal de Minas Gerais, Belo Horizonte, MG, Brasil.
- Francfort, G. A. and Marigo, J. J. (1998), ‘Revisiting brittle fracture as an energy minimization problem’, *J Mech Phys Solids* vol. 46(8), 1319–1342.
- Galvez, J., Elices, M., Guinea, G. and Planas, J. (1998), ‘Mixed mode fracture of concrete under proportional and nonproportional loading’, *International Journal of Fracture* vol. 94, 267–284.
- Geuzaine, C. and Remacle, J. F. (2009), ‘Gmsh: a 3-d finite element mesh generator with built-in pre- and post-processing facilities’, *International Journal for Numerical Methods in Engineering* vol. 79, 1309–1331.
- Ghoneim, A. Y. (2020), ‘A smoothed particle hydrodynamics phase field method with radial basis functions and moving least squares for meshfree simulation of dendritic solidification’, *Applied Mathematical Modeling* vol. 77, 1704–1741.

- Gingold, R. A. and Monaghan, J. J. (1977), ‘Smooth particle hydrodynamics: Theory and applications to non-spherical stars’, *Monthly Notices of the Royal Astronomical Society* vol. 181, 375–389.
- Gori, L. (2018), Failure Analysis of Quasi-Brittle media using the Micropolar Continuum Theory, Elastic-Degrading Constitutive Models, and Smoothed Point Interpolation Methods, PhD thesis, Universidade Federal de Minas Gerais, Belo Horizonte, MG, Brasil.
- Gori, L., Penna, S. S. and Pitangueira, R. (2019), ‘G-space theory and weakened-weak form for micropolar media: Application to smoothed point interpolation methods’, *Engineering Analysis with Boundary Elements* vol. 101, 318–329.
- Goswami, S., Anitescu, C. and Rabczuk, T. (2020), ‘Adaptive fourth-order phase field analysis for brittle fracture’, *Computer Methods in Applied Mechanics and Engineering* vol. 361.
- Gracia-Álvarez, V. O., Gettu, R. and Carol, I. (2012), ‘Analysis of mixed-mode fracture in concrete using interface elements and a cohesive crack model’, *Sadhana* vol. 37, 187–205.
- Gu, Y. T., Wang, W., Zhang, L. C. and Feng, X. Q. (2011), ‘An enriched radial point interpolation method (e-rpim) for analysis of crack tip fields’, *Engineering Fracture Mechanics* vol. 78, 175–190.
- Heister, T., Wheeler, M. F. and Wick, T. (2015), ‘A primal-dual active set method and predictor-corrector mesh adaptivity for computing fracture propagation using a phase-field approach’, *Computer Methods in Applied Mechanics and Engineering* vol. 290, 466–495.
- Hirshikesh, C. J., Kannan, K., Annabattula, R. K. and Natarajan, S. (2019), ‘Adaptive phase field method for quasi-static brittle fracture using a recovery based error indicator and quadtree decomposition’, *Engineering Fracture Mechanics* vol. 220, 106599.
- Hirshikesh, H., Pramond, A. L. N., Waisman, H. and Natarajan, S. (2021), ‘Adaptive phase field method using novel physics based refinement criteria’, *Computer Methods in Applied Mechanics and Engineering* vol. 383.
- Hordijk, D. (1991), Local approach to fatigue of concrete, PhD thesis, Delft University of Technology, Delft, The Netherlands.
- Kamensky, D., Moutsanids, G. and Bazilevs, Y. (2018), ‘Hyperbolic phase field modeling of brittle fracture: Part i - theory and simulations’, *Journal of the Mechanics and Physics of Solids* vol. 121, 81–98.

-
- Karma, A., Kessler, D. A. and Levine, H. (2001), ‘Phase-field model of mode iii dynamic fracture’, *Physics Review Letter* vol. 87.
- Kasirajan, P., Bhattacharya, S., Arroyo, M., Rajagopal, A. and Reddy, J. N. (2020), ‘Phase field modeling of fracture in quasi-brittle materials using natural neighbor galerkin method’, *Computer methods in applied mechanics and engineering* vol. 366, 113019.
- Kastner, M., Henning, P., Linse, T. and Ulbricht, V. (2016), ‘Phase field modeling of damage and fracture - convergence and local mesh refinement’, *Advanced Methods of Continuum Mechanics for Materials and Structures* .
- Krysl, P. and Beletschko, T. (1997), ‘Element-free galerkin method: Convergence of the continuous and discontinuous shape functions’, *Computer Methods in Applied Mechanics and Engineering* vol. 148, 257–277.
- Kuhn, C., Schuter, A. and Muller, R. (2015), ‘On degradation functions in phase field fracture models’, *Material Science* vol. 108, 374–384.
- Lancioni, G. and Royer-Carfagni, G. (2009), ‘The variational approach to fracture mechanics. a practical application to the french panthéon in paris’, *Journal of Elasticity* vol. 95, 1–30.
- Leão, H. M. (2021), A critical study on phase-field modelling of fracture, Master’s thesis, Universidade Federal de Minas Gerais, Belo Horizonte, MG, Brasil.
- Li, B., Peco, C., Millán, D., Arias, I. and Arroyo, M. (2015), ‘Phase-field modeling and simulation of fracture in brittle materials with strongly anisotropic surface energy’, *International Journal for Numerical Methods in Engineering* vol. 102, 711–727.
- Li, S., Tian, L. and Cui, X. (2019), ‘Phase field crack model with diffuse description for fracture problem and implementation in engineering applications’, *Advances in Engineering Software* vol. 129, 44–56.
- Li, W., Nguyen-Thanh, N. and Zhou, K. (2020), ‘Phase-field modeling of brittle fracture in a 3d polycrystalline material via an adaptive isogeometric-meshfree approach’, *International Journal for Numerical Methods in Engineering* vol. 121, 5042–5065.
- Li, W., Nguyen-Thanh, N. and Zhou, K. (2022), ‘Phase-field modeling of interfacial debonding in multi-phase materials via an adaptive isogeometric-meshfree approach’, *Engineering Fracture Mechanics* vol. 269.
- Liu, G. (2009), *Meshfree Methods: Moving Beyond the Finite Element method*, CRC Press, New York.

- Liu, G., Dai, K. and Nguyen, T. (2007), ‘A smoothed finite element method for mechanics problems’, *Computational Mechanics* vol. 39, 859–877.
- Liu, G., Nguyen, T., Nguyen, H. and Lam, K. (2009), ‘A node-based smoothed finite element method (ns-fem) for upper bound solutions to solid mechanics problems’, *Computers and structures* vol. 87, 14–26.
- Liu, G. R. (2010), ‘A g space theory and a weakened weak form for a unified formulation of compatible and incompatible methods, part i: Theory and part ii: Applications to solid mechanics problems’, *International Journal for Numerical Methods in Engineering* vol. 81, 1093–1126.
- Liu, G. R. and Gu, Y. T. (2001), ‘A point interpolation method for two-dimensional solids’, *International Journal for Numerical Methods in Engineering* vol. 50, 937–951.
- Liu, G. R., Nguyen, T. T. and Lam, K. Y. (2009), ‘An edge-based smoothed finite element method (es-fem) for static, free and forced vibration analysis of solids’, *Journal of Sound and Vibration* vol. 320, 1100–1130.
- Liu, G. R. and Zhang, G. Y. (2008), ‘Edge-based smoothed point interpolation methods’, *International Journal of Computational Methods* vol. 5(4), 621–646.
- Liu, G. R. and Zhang, G. Y. (2009), ‘A normed g space and weakened weak (w2) formulation of a cellbased smoothed point interpolation method’, *International Journal of Computational Methods* vol. 6(1), 147–179.
- Liu, G. R., Zhang, G. Y., Dai, K. Y., Wang, Y. Y., Zhong, Z. H., Li, G. Y. and Han, X. (2005), ‘A linearly conforming point interpolation method (lc-pim) for 2d solid mechanics problems’, *International Journal of Computational Methods* vol. 2(4), 645–665.
- Liu, Z., Lu, M., Li, Q., Lv, Z., Chang, A., Pang, K. and Zhao, S. (2016), ‘A direct coupling method of meshless local petrov-galerkin (mlpg) and finite element method (fem)’, *International Journal of Applied Eledtromagnetics an Mechanics* vol. 51.
- Lucy, L. B. (1977), ‘A numerical approach to testing the fission hypothesis’, *The Astronomical Journal* vol. 82, 1013–1024.
- Mazars, J. (1984), Application de le M’ecanique de l’endommagement au comportement non lineaire et a la rupture du beton de Structure, PhD thesis, Université Pierre et Marie Curie - Laboratoire de Mécanique et Technologie, Paris, France.
- Miehe, C., Hofacker, M. and Welschinger, F. (2010), ‘A phase field model for rate-independent crack propagation: Robust algorithmic implementation based on operator splits’, *Computer Methods in Applied Mechanics and Engineering* vol. 199, 2765–2778.

-
- Miehe, C., Welschinger, F. and Hofacker, M. (2010), ‘Thermodynamically consistent phase-field models of fracture: Variational principles and multi-field fe implementations’, *International Journal for Numerical Methods in Engineering* vol. 83, 1273–1311.
- Molnar, G. and Gravouil, A. (2017), ‘2d and 3d abaqus implementation of a robust staggered phase-field solution for modeling brittle fracture’, *Finite Elements in Analysis and Design* vol. 130.
- Moutsanids, G., Kamensky, D., Chen, J. S. and Bazilevs, Y. (2018), ‘Hyperbolic phase field modeling of brittle fracture: Part ii-immersed iga-rkpm coupling for air-blast-structural’, *Journal of the Mechanics and Physics of Solids* vol. 121, 114–132.
- Nagarajara, S., Elhaddad, M., Ambati, M., Kollmannsberger, S., Lorenzis, L. and Rank, E. (2019), ‘Phase-field modeling of brittle fracture with multi-level hp-fem and the finite cell method’, *Computational Mechanics* vol. 63, 1283–1300.
- Nguyen, N., Nguyen, V. P., Wu, J., Le, T. and Ding, Y. (2019), ‘Mesh-based and mesh-free reduced order phase-field models for brittle fracture: One dimensional problems’, *Materials* vol. 12, 1858.
- Nguyen, T. T., Liu, G. R., Vu, H. D. and Nguyen, H. X. (2009), ‘A face-based smoothed finite element method (fs-fem) for visco-elastoplastic analyses of 3d solids using tetrahedral mesh’, *Computer Methods in Applied Mechanics and Engineering* vol. 198, 3479–3498.
- Nguyen-Thanh, N., Li, W., Huang, J. and Zhou, K. (2020), ‘Adaptive higher-order phase-field modeling of anisotropic brittle fracture in 3d polycrystalline materials’, *Computer Methods in Applied Mechanicals and Engineering* vol. 372, 113434.
- Novelli, L., Gori, L. and Pitangueira, R. L. S. (2021), Point interpolation methods for phase-field modelling of brittle fracture, in ‘XLII Ibero-Latin-American Congress on Computational Methods in Engineering and III Pan-American Congress on Computational Mechanics’, Rio de Janeiro, Brazil.
- Novelli, L., Gori, L. and Pitangueira, R. L. S. (2022), ‘Phase-field modelling of brittle fracture with smoothed radial point interpolation methods’, *Engineering Analysis with Boundary Elements* vol. 138, 219–234.
- Novelli, L., Saliba, S. S., Gori, L. and Pitangueira, R. L. S. (2022), A coupled finite element-meshfree smoothed point interpolation method for phase-field modelling, in ‘XLIII Ibero-Latin-American Congress on Computational Methods in Engineering’, Rio de Janeiro, Brazil.

-
- Novotny, A. A. and Fancello, E. A. (1998), ‘Um refinamento h, p e hp adaptativo na análise de flexão de placas semi-espessas’, *Revista internacional de métodos numéricos* vol. 14.
- Patil, R. U., Mishra, B. K. and Singh, I. V. (2017), ‘An adaptive multiscale phase field method for brittle fracture’, *Computer Methods in Applied Mechanics and Engineering* vol. 329, 254–288.
- Peng, F., Huang, W., Ma, Y., Zhang, Z. and Zhang, Y. (2020), ‘Phase field modeling of brittle fracture based on the cell-based smooth fem by considering spectral decomposition’, *International Journal of Computational Methods* vol. 18.
- Peng, F., Huang, W., Zhang, Z., Guo, T. and Ma, Y. (2020), ‘Phase field simulation for fracture behavior of hyperelastic material at large deformation based on edge-based smoothed finite element method’, *Engineering Fracture Mechanics* vol. 238.
- Penna, S. S. (2011), *Formulação Multipotencial para Modelos de Degradação Elástica - Unificação Teórica, Proposta de Novo Modelo, Implementação Computacional e Modelagem de Estruturas de Concreto*, PhD thesis, Universidade Federal de Minas Gerais, Belo Horizonte, MG, Brasil.
- Petersson, P. E. (1981), *Crack growth and development of fracture zones in plain concrete and similar materials*, PhD thesis, Division of Building Materials, Lund Institute of Technology, Lund, Suécia.
- Qiu, S., Duan, Q., Shao, Y., Chen, S. and Yao, W. (2022), ‘Adaptive finite element method for hybrid phase-field modeling of three-dimensional cracks’, *Engineering Fracture Mechanics* vol. 271.
- Rosolen, A., Millan, D. and Arroyo, M. (2013), ‘Second-order convex maximum entropy approximants with applications to high-order pde’, *International Journal for Numerical Methods in Engineering* vol. 94, 150–182.
- Saliba, S. S. (2022), *Acoplamento SPIM-FEM Adaptativo para Modelos de Degradação Elástica*, PhD thesis, Universidade Federal de Minas Gerais, Belo Horizonte, MG, Brasil.
- Saliba, S. S., Gori, L. and Pitangueira, R. L. S. (2021), ‘A coupled finite element-meshfree smoothed point interpolation method for nonlinear analysis’, *Engineering Analysis with Boundary Elements* vol. 128, 1–18.
- Sargado, J. M., Keilegavlen, E., Berre, I. and Nordbotten, J. M. (2021), ‘A combined finite element–finite volume framework for phase-field fracture’, *Computer Methods in Applied Mechanics and Engineering* vol. 373.

- Shao, Y., Duan, Q. and Qiu, S. (2019), ‘Adaptive consistent element-free galerkin method for phase-field model of brittle fracture’, *Computational Mechanics* vol. 64, 741–767.
- Shao, Y., Duan, Q. and Qiu, S. (2020), ‘Consistent element-free galerkin method for three-dimensional crack propagation based on a phase-field model’, *Computational Materials Science* vol. 179, 109694.
- Sousa, R. A. (2007), Adaptatividade geométrica e numérica na geração de malhas de elementos finitos em 2d e 3d, Master’s thesis, Pontifícia Universidade Católica do Rio de Janeiro, Rio de Janeiro, RJ, Brasil.
- Sun, Y., Liu, Z. and Tang, X. (2020), ‘A hybrid femm-phase field method for fluid - driven fracture propagation in three dimension’, *Engineering Analysis with Boundary Elements* vol. 113, 40–54.
- Tian, F., Tang, X., Xu, T. and Li, L. (2020), ‘An adaptive edge-based smoothed finite element method (es-fem) for phase-field modeling of fractures at large deformations’, *Computer Methods in Applied Mechanics and Engineering* vol. 372.
- Tian, F., Tang, X., Xu, T., Yang, J. and Li, L. (2019), ‘A hybrid adaptive finite element phase-field method quasi-static and dynamic brittle fracture’, *International Journal for Numerical Methods in Engineering* vol. 120, 1108–1125.
- Tootoonchi, A. and Khosghalb, A. (2016), A cell-based smoothed point interpolation method for flow-deformation analysis of saturated porous media, in ‘Proceedings of the VII European congress on computational methods in applied sciences and engineering’, Crete Island, Greece.
- Ullah, Z., Coombs, W. M. and Augarde, C. E. (2013), ‘An adaptive finite element meshless coupled method based on local maximum entropy shape functions for linear and nonlinear problems’, *Computer Methods in Applied Mechanics and Engineering* .
- Wang, D. and Wu, J. (2019), ‘An inherently consistent reproducing kernel gradient smoothing framework toward efficient galerkin meshfree formulation with explicit quadrature’, *Computer Methods in Applied Mechanicals and Engineering* vol. 349, 628–672.
- Wang, J. G. and Liu, G. R. (2000), A radial point interpolation method for elastoplastic problems, in ‘Fist International Conference on Structural Stability and Dynamics’, Taipei, Taiwan, pp. 703–708.
- Wang, J. G. and Liu, G. R. (2002), ‘A point interpolation meshless method based on radial basis functions’, *International Journal for Numerical Methods in Engineering* vol. 54, 1623–1648.

- Winkler, B. J. (2001), Traglastuntersuchungen von unbewehrten und bewehrten Betonstrukturen auf der Grundlage eines objektiven Werkstoffgesetzes für Beton, PhD thesis, Innsbruck University, Innsbruck.
- Wu, J., Nguyen, V., Nguyen, C., Sutula, D., Sinaie, S. and Bordas, S. (2020), ‘Phase-field modeling of fracture’, *Advances in Applied Mechanics* vol. 53, 1–183.
- Wu, J., Wang, D., Lin, Z. and Qi, D. (2019), ‘An efficient gradient smoothing meshfree formulation for the fourth-order phase field modeling of brittle fracture’, *Computation Particle Mechanics* vol. 7, 193–207.
- Wu, J. Y. (2017), ‘A unified phase field theory for the mechanics of damage and quasi-brittle failure’, *Journal of the Mechanics and Physics of Solids* vol. 103, 72–99.
- Wu, J. Y. (2018a), ‘A geometrically regularized gradient-damage model with energetic equivalence’, *Computer Methods in Applied Mechanics and Engineering* vol. 328, 612–637.
- Wu, J. Y. (2018b), ‘Robust numerical implementation of non-standard phase field damage models for failure in solids’, *Computer Methods in Applied Mechanics and Engineering* vol. 340, 767–797.
- Wu, Y., Magallanes, J. M., Choi, H. J. and Crawford, J. E. (2013), ‘An evolutionarily coupled finite element - meshfree formulation for modeling concrete behaviors under blast and impact loadings’, *Journal of Engineering Mechanics* vol. 139, 525–536.
- Yuan, H., Peng, C., Lin, Q. and Zhang, B. (2014), ‘Simulation of tensile cracking in earth structures with an adaptive rpim-fem coupled method’, *Journal of Civil Engineering* vol. 18, 2007–2018.
- Yue, Q., Zhou, W., Wang, Q., Feng, Y. T., Ma, G. and Chang, X. (2022), ‘An adaptive phase-field model based on bilinear elements for tensile-compressive-shear fracture’, *Computers and Mathematics with Applications* vol. 105, 112–135.
- Zander, N., Bog, T., Kollmannsberger, S., Schillinger, D. and Rank, E. (2015), ‘Multi-level hp-adaptivity: High-order mesh adaptivity without the difficulties of constraining hanging nodes’, *Computational Mechanics* vol. 55, 499–517.
- Zhang, F., Huang, W., Li, X. and Zhang, S. (2018), ‘Moving mesh finite element simulation for phase field of fracture and convergence of newton’s iteration’, *Journal of Computational Physics* vol. 356, 127–149.
- Zhang, P., Hu, X., Wang, X. and Yao, W. (2018), ‘An iteration scheme for phase field model for cohesive fracture and its implementation in abacus’, *Engineering Fracture Mechanics* vol. 204, 268–287.

- Zhou, S. and Zhuang, X. (2018), ‘Adaptive phase field simulation of quasi-static crack propagation in rocks’, *Underground Space* vol. 3, 190–205.

Appendices

Appendix A

Trigonometric radial function for linear elastic problem

This appendix present the influence of the application of the trigonometric radial function, proposed in the Section 4.2.3, in a linear elastic problem.

The example refers to square panel with a circular hole subjected to a unidirectional tensile load in the x-direction, as illustrated in Fig. A.1. The plane stress condition is considered. Due to symmetry, only the upper right quarter of the square panel is modelled. The parameters used are: Loading $p = 10$ N/m, Young's modulus $E = 1 \times 10^7$ N/m², Poisson's ratio $\nu = 0.3$, diameter of the hole $a = 1.0$ m and length of the panel $b = 5.0$ m.

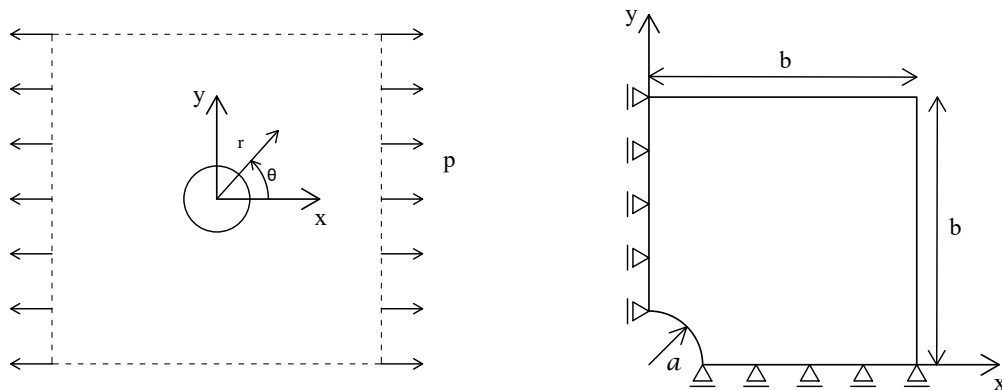


Figure A.1: Square panel with a hole subjected to a tensile load in the horizontal direction.

The analytical solution of the stress field in polar coordinates of (r, θ) are listed below. The normal stress in the x-direction:

$$\sigma_x(x, y) = p \left\{ 1 - \frac{a^2}{r^2} \left\{ \frac{3}{2} \cos 2\theta + \cos 4\theta \right\} + \frac{3a^4}{2r^4} \cos 4\theta \right\} \quad (\text{A.1})$$

The normal stress in the y-direction:

$$\sigma_y(x, y) = p \left\{ -\frac{a^2}{r^2} \left\{ \frac{1}{2} \cos 2\theta - \cos 4\theta \right\} + \frac{3a^4}{2r^4} \cos 4\theta \right\} \quad (\text{A.2})$$

The shear stress:

$$\sigma_{xy}(x, y) = p \left\{ -\frac{a^2}{r^2} \left\{ \frac{1}{2} \sin 2\theta + \sin 4\theta \right\} + \frac{3a^4}{2r^4} \sin 4\theta \right\} \quad (\text{A.3})$$

In the above equations, (r, θ) are the polar coordinates and θ is measured counter-clockwise from the positive x axis. The domain is discretised with four different meshes, as illustrated in Fig. A.2.

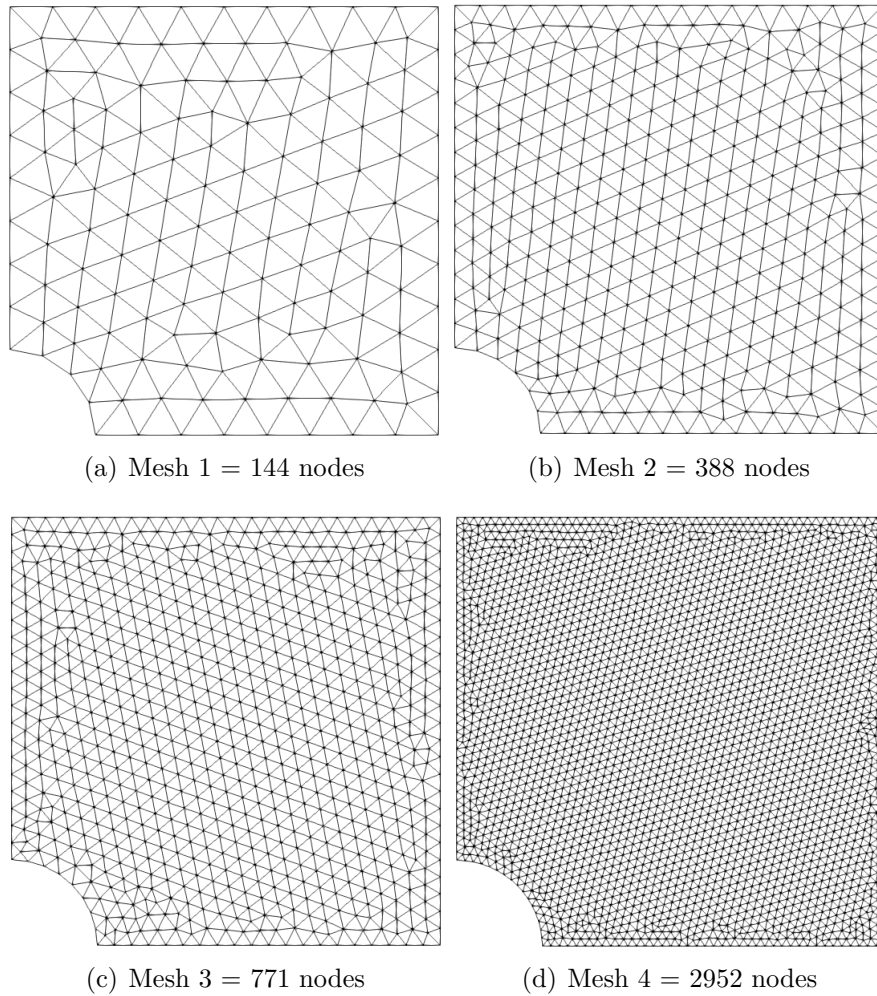


Figure A.2: Meshes of the square panel with a hole.

This example is performed with FEM, cell-based with exponential function, cell-based with trigonometric function and edge-based with trigonometric function. The convergence of σ_{xx} at $(x, y) = (0, 1)$ for the different methods is presented in Fig. A.3. The results are compared with the analytical solution. For this example, the edge-based with trigonometric function convergence faster than the other methods.

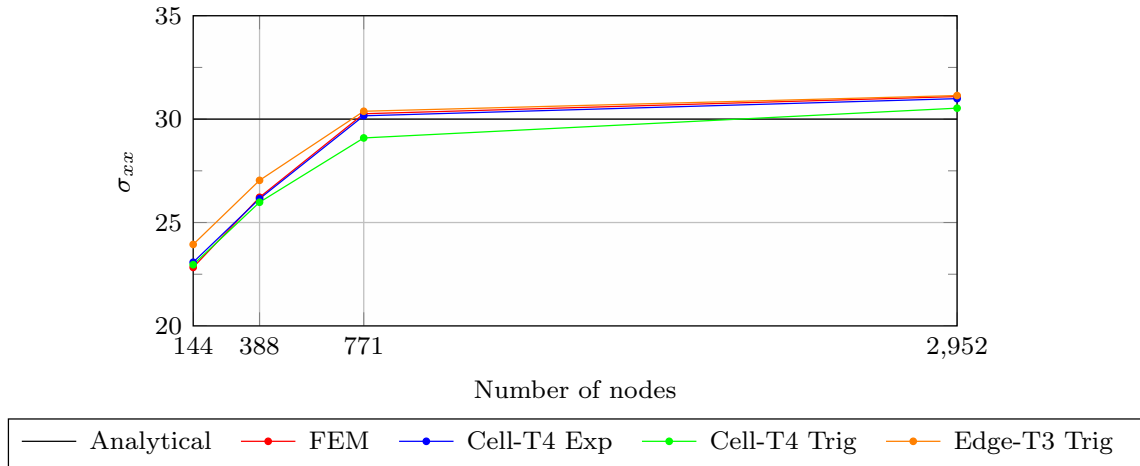


Figure A.3: Convergence of σ_{xx} at $(x, y) = (0, 1)$.

The stress components σ_{xx} of the smoothing domain in the boundary $x = 0$ are compared with the exact solution and FEM in Fig. A.4. The mesh 4 is adopted for FEM and cell-based with trigonometric radial function. It is possible to observe a good agreement of the cell-based with FEM and analytical solution.

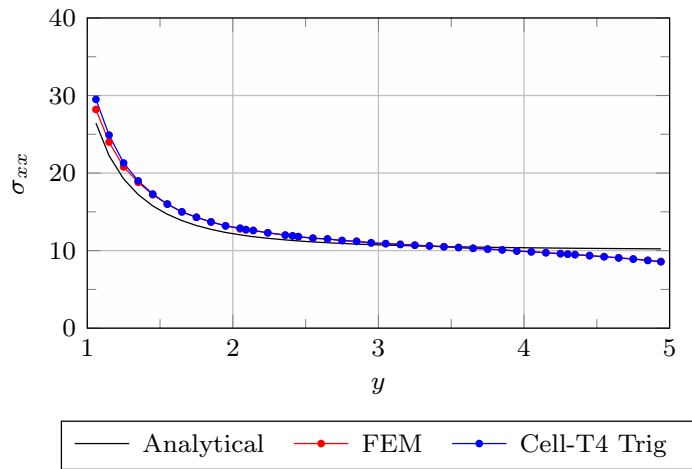


Figure A.4: Comparison between the exact solution, FEM and SPIM for σ_{xx} .

Appendix B

INSANE: INteractive Structural ANalysis Environment

This appendix aims to present the numerical core of the INSANE System. This system was developed by the Department of Structural Engineering (DEES) of the Federal University of Minas Gerais and was used for the implementation of this thesis.

INSANE is a free *software*, implemented in Java language according to the Object Oriented Programming (OOP) paradigm. The use of this language and the OOP allows the system to be segmented so that new researchers can work with each other, facilitating the maintenance and expansion of the code.

This system have the implementations of the phase-field models for brittle fracture (Leão (2021)) and quasi-brittle fracture (Bayao et al. (2021)), the meshfree methods (Gori (2018)) and coupled FEM-SPIM for damage models (Saliba (2022)).

The system can be divided into three main applications: preprocessor, processor and postprocessor. The pre and post processor represent the graphical interface of the system, with the pre-processor responsible for building the models and the post-processor responsible for viewing the results. The processor is the numerical core of the system and is responsible for solving the problem.

In this thesis, similar to realized in other works that study phase-field models Leão (2021), Fortes (2022), Bayao et al. (2021), additional software are used in the analyses. The background triangular cells are generated with GMSH Geuzaine and Remacle (2009). The boundary conditions, loads and material properties are inserted using the interface of the Insane. For viewing the results, the contour plots of the phase-field variable are generated using PARAVIEW Ahrens et al. (2005).

Next, the main structure of the numerical core of the system and the modifications are presented. The classes are shown in UML (*Unified Modelling Language*) diagrams. The modified classes are depicted in yellow, the new classes in green and the non modified classes in white, as illustrated in Fig. B.1.



Figure B.1: Classes representation in UML diagram.

B.1 Numerical core

The UML diagram that represents the numerical core of the system can be seen in Fig. B.2. It is structured from the abstract classes `Model` and `Solution` and the interfaces `Assembler` and `Persistence`.

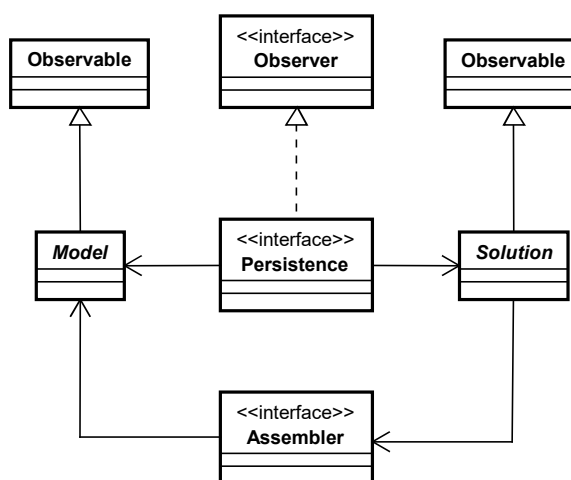


Figure B.2: Numerical core of the Insane.

The `Model` class contains the discrete model data such as nodes and elements. It provides to the `Assembler` class the necessary data for assembling the matricial system B.1. The `Solution` class is responsible for solving the system and finding, for example, the nodal displacements.

$$\mathbf{A} \cdot \ddot{\mathbf{x}} + \mathbf{B} \cdot \dot{\mathbf{x}} + \mathbf{C} \cdot \mathbf{x} = \mathbf{d} \quad (\text{B.1})$$

where \mathbf{x} is the vector of nodal dual parameters; $\dot{\mathbf{x}}$ and $\ddot{\mathbf{x}}$ are the vectors of the first and second time derivatives of the state variables; \mathbf{A} , \mathbf{B} and \mathbf{C} are the matrices of the system coefficients and \mathbf{d} is the vector of independent terms.

The `Model` and `Solution` classes communicate with the `Persistence` interface, which is responsible for processing input data and providing output data when changes are observed in the model. This communication between classes takes place through the *Observer-Observable* pattern. In this way, any change that occurs in the observed objects is passed on to the observing object.

B.2 Model

The abstract class `Model` (Fig. B.3) represents the discrete model. This class depends on the numeric method. `FemModel` represents the discrete model for the finite element method, `MeshfreeModel` represents the model for meshfree methods with standard Gauss integration, `SmoothedPimMeshfreeModel` corresponds to the model for the meshfree methods of the PIM family with smoothed shape functions and `CoupledSmoothedPimMeshfreeFemModel` represents the coupled model FEM-SPIM.

For the implementation of phase-field model discretised with SPIM and coupled FEM-SPIM, the following modifications needed to be made.

The computation of the shape functions in the center of the smoothing domain was inserted in the operation `computedShapeFunction()`. This value is necessary in the phase-field formulation.

The attributes `refinementMethod`, `levelofRefinement` and `factorDecayRate` were inserted in the class `CoupledSmoothedPimMeshfreeFemModel`. New criteria for substitution and refinements were inserted and different operations were modified for include the variables of the phase-field model. It is important to emphasize that the operation `updateCoupledSmoothedModel()` is responsible by verify if the model will be replaced or refined and realized this modification.

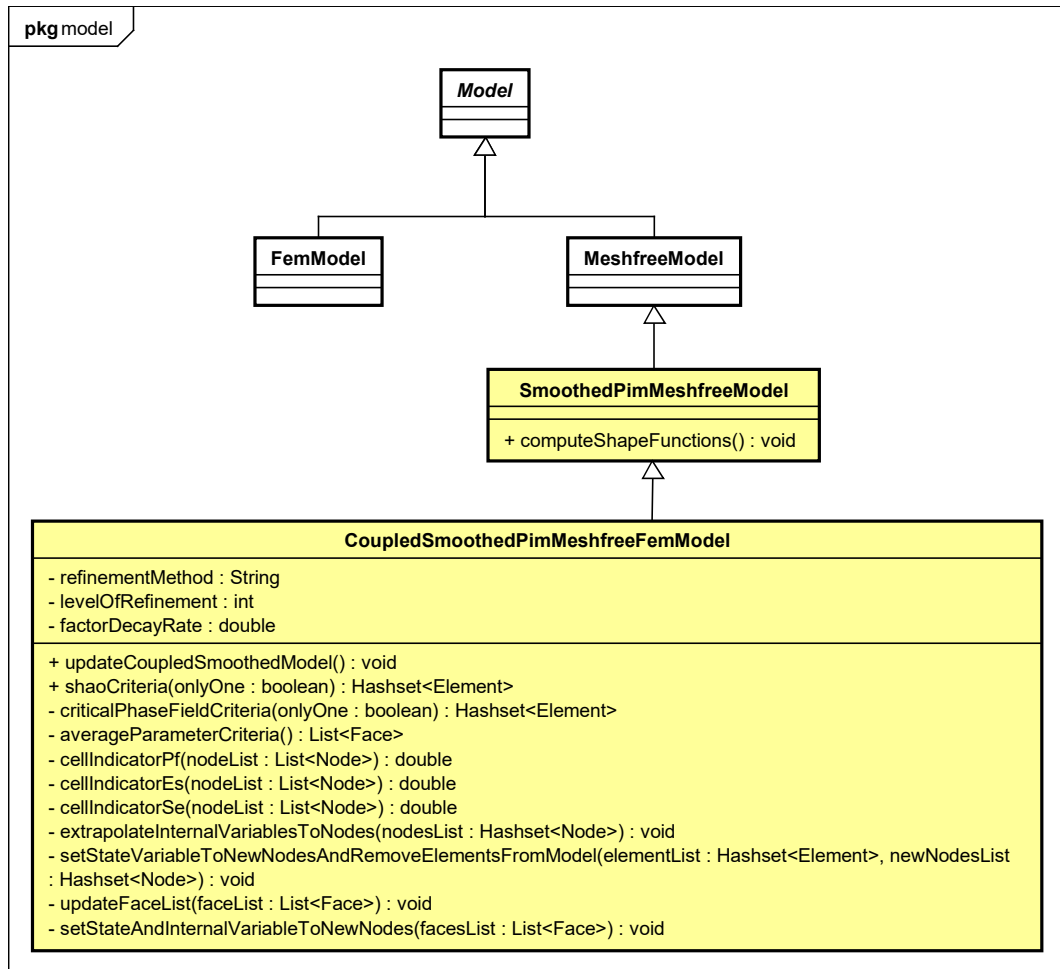


Figure B.3: Model class.

Other classes related to modification of the model in the adaptive strategy were also changed. The class `CoupledMeshfreeFemDataManager` illustrated in Fig. B.4 is responsible by realized the modification of the model. The operations are in the specific class which inherits from `CoupledMeshfreeFemDataManager`, `CoupledMeshfreeFemModification` and `CoupledMeshfreeFemRefinement`. In these classes, the modified methods are presented. The main modifications are associated to the phase-field variable present in the nodes and the level of refinement inserted in the vertex to control de number of refinements.

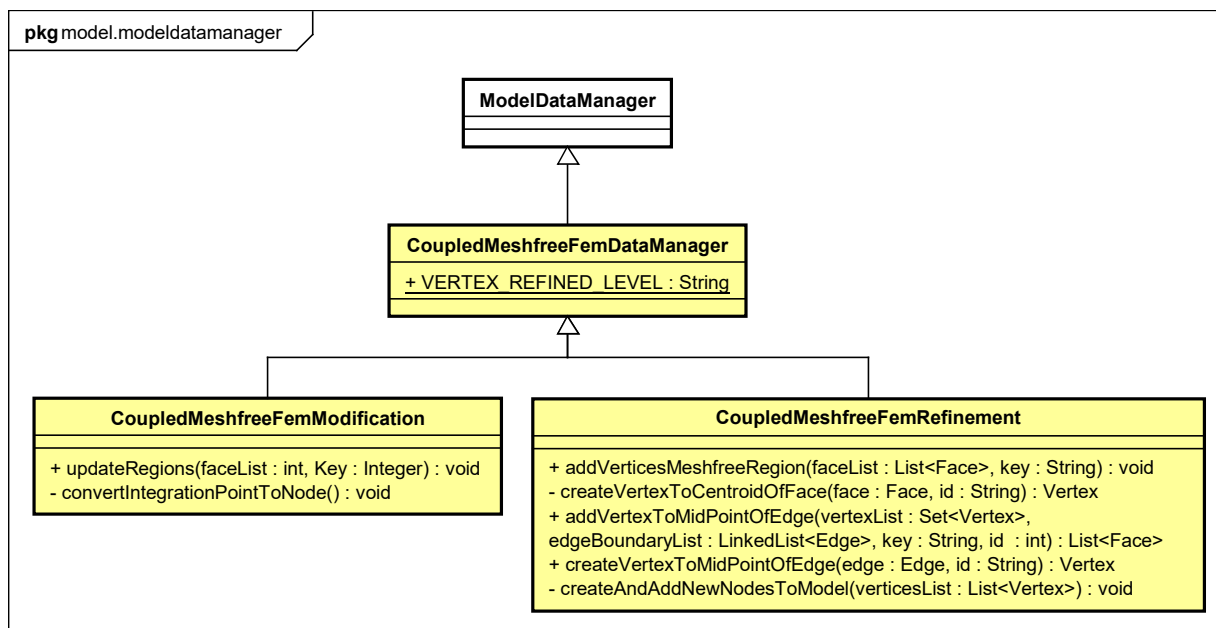


Figure B.4: DataManager class.

Other class changed was `PimModelGenerator`, where the degree of freedom of the phase-field was added in the new nodes created.

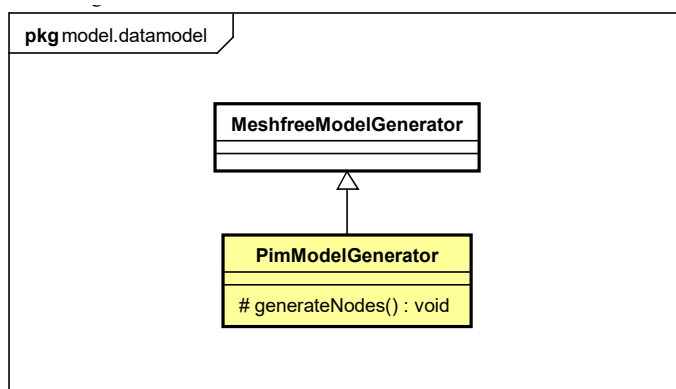


Figure B.5: DataModel class.

B.2.1 Problem Driver

The `Model` package also contains the abstract class `ProblemDriver`. This class is required by the `Assembler` for the numerical integration and assembly of the parts of the equation B.1 for a part of the problem domain. In the case of the finite element method, the inheriting classes `Parametric` and `PhysicallyNonLinear` are responsible for numerical integration for parametric finite elements, in linear and physically nonlinear elasticity problems, respectively. For the case of meshfree methods, there are the inheriting classes `MeshfreeSolidMech` and `PhysicallyNonlinearMeshfreeSolidMech` for standard Gaussian numeric integration and `SmoothedPim` and `PhysicallyNonlinearSmoothedPim` for

smoothed domain integration.

In this package, new classes were inserted, `PhaseFieldPhysicallyNonlinearMeshfree` and `PhaseFieldPhysicallyNonlinearSmoothedPim`. These classes contain methods to calculate the parts referring to the phase-field problem, stiffness matrix (`getPfIncrementalC()`) and vector of nodal forces equivalent to internal stresses (`getPff`).

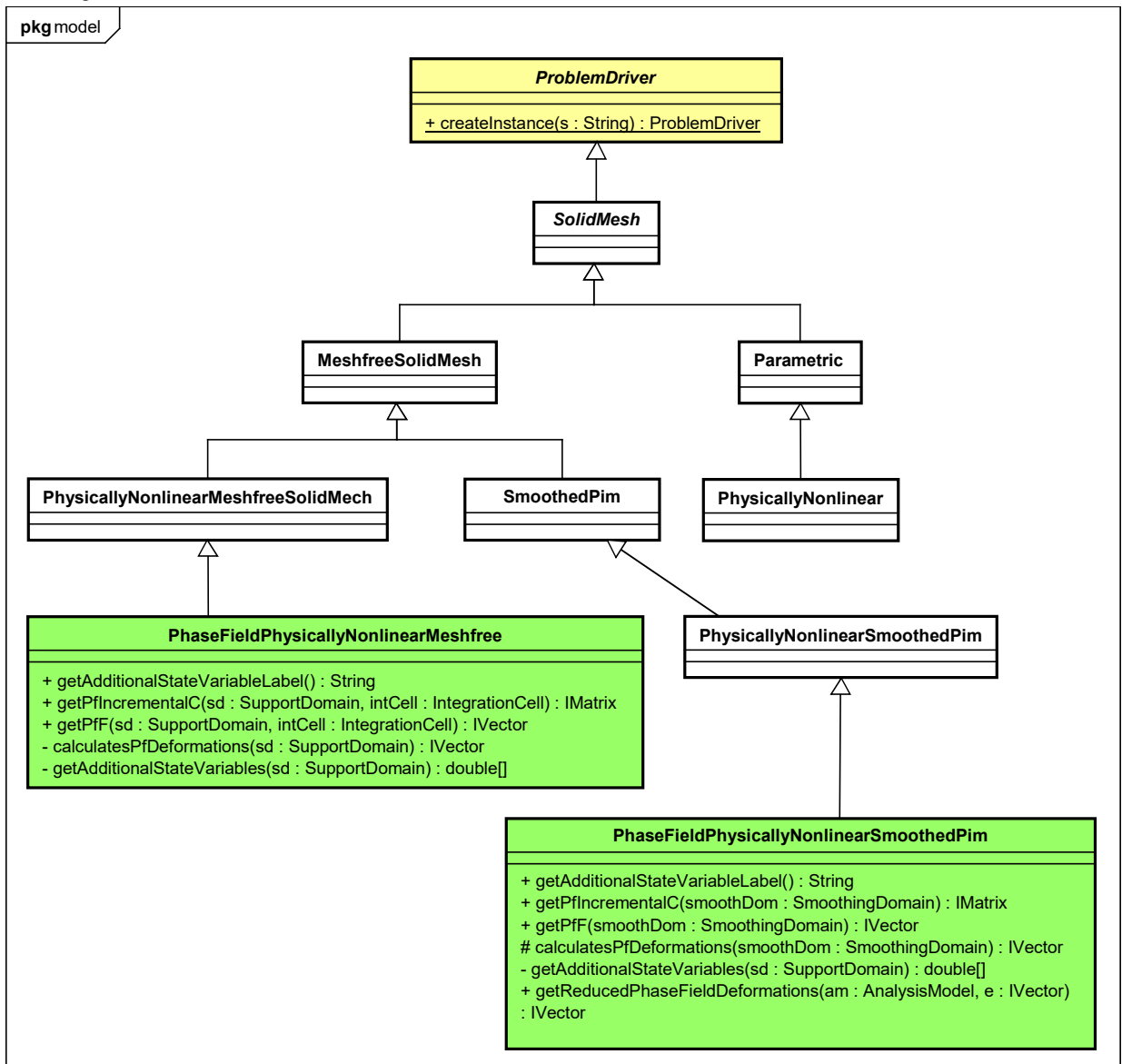


Figure B.6: ProblemDriver class.

B.2.2 Constitutive Model

The abstract class `ConstitutiveModel` is responsible for determining the constitutive operator matrix and the internal stress vector. Within the INSANE system, there is a unified framework of constitutive models developed in Penna (2011), which has damage models, distributed cracking models and plasticity models. In addition to this structure,

there are other implementations of constitutive models, such as the phase-field models illustrated in Fig. B.7. The constitutive model of phase-field for the staggered solver (`PhaseFieldStaggeredConstitutiveModel`) is a direct heir of the `ConstitutiveModel` class. This class has as heirs: the isotropic model class (`StgPfIsotropicConstModel`) and the anisotropic model classes (`StgPfLancioniConstModel`, `StgPfAmorConstModel` and `StgPfMieheConstModel`). The isotropic model has as heirs `StgPfWu2013ConstModel` and `StgPfWu2018ConstModel`.

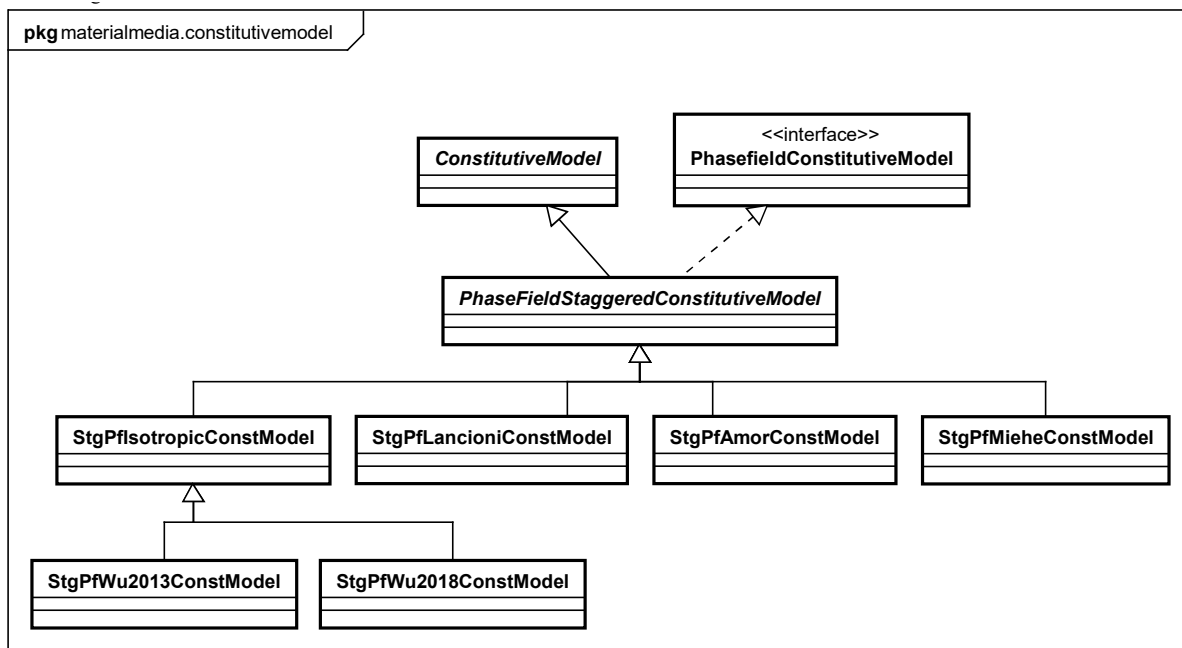


Figure B.7: ConstitutiveModel class.

B.2.3 Analysis Model

The abstract class `AnalysisModel` encompasses the different types of analysis of the INSANE system, whether for three-dimensional, plane or one-dimensional problems. These classes are responsible for informing the degrees of freedom and the operator of internal variables. In the case of plane problems, these are divided into three categories: plane stress state (EPT), plane strain state (EPD) and asymmetric.

`AnalysisModel` is responsible for assembling the matrices that contain the approximation functions and their derivatives. These matrices are required by the `ProblemDriver` class for calculating the stiffness matrices and internal force vectors. In the case of meshfree methods, the classes `PlaneStrainMeshfree` and `PlaneStressMeshfree` are direct heirs of `PlaneStrain` and `PlaneStress`, respectively.

In the `analysismodel` package, new classes for plane stress state and plane strain state were implemented (Fig. B.8), namely: `PlaneStressPhaseFieldStaggeredSolverMeshfree` and `PlaneStrainPhaseFieldStaggeredSolverMeshfree`, respectively. These classes con-

tain additional methods for assembling the matrices containing the shape functions and derivatives for the phase-field problem. These classes are the same for standard Gauss integration and smoothing domains, differing by the methods.

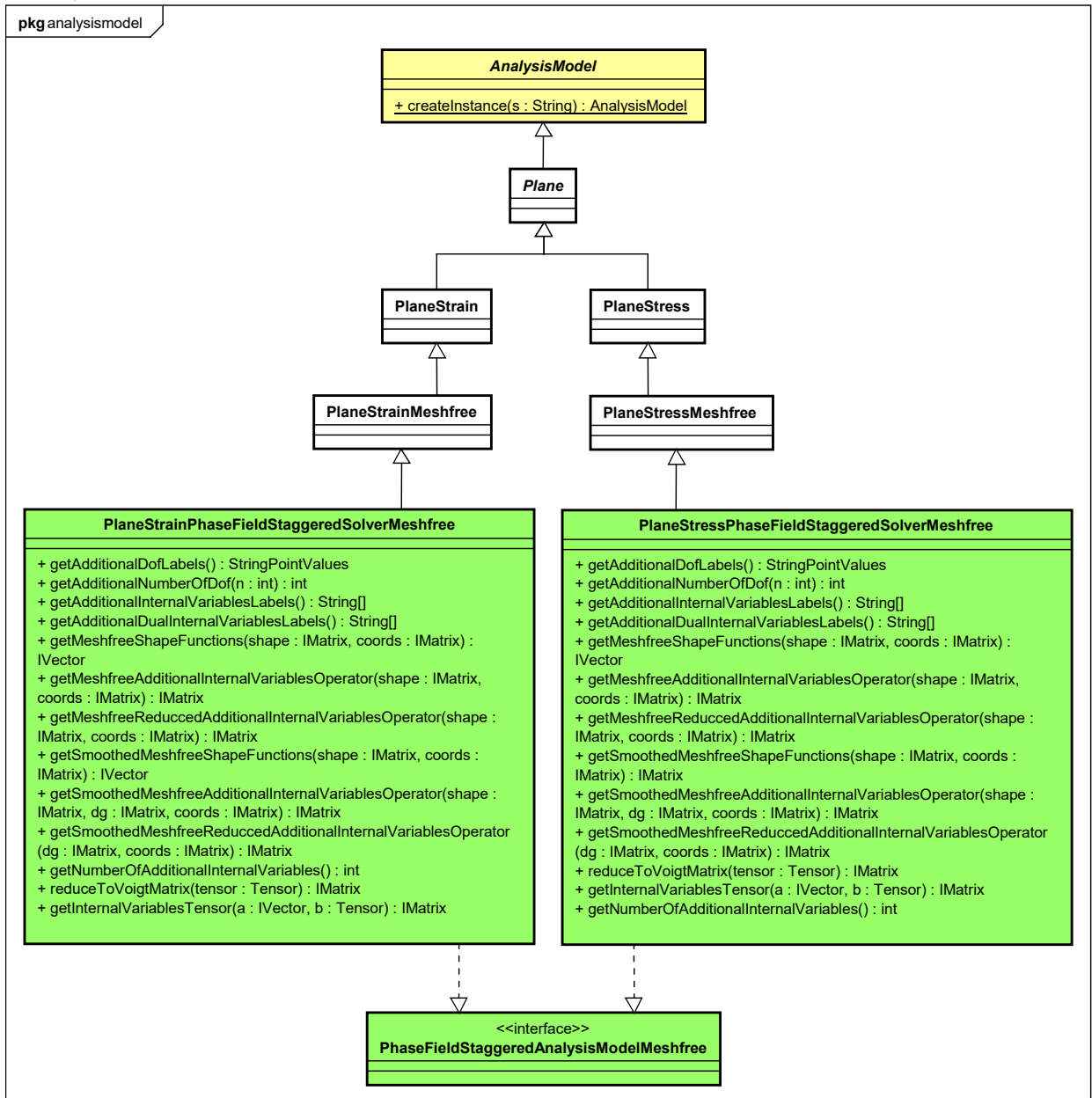


Figure B.8: AnalysisModel class.

B.3 Assembler

The `Assembler` interface (Fig. B.9) is responsible for assembling the global matrices and vectors needed to solve the problem. Like the `Model` class, the interface is individualized depending on the numerical method. For example, `FemAssembler` represents the finite element method, `MeshfreeAssembler` represents meshfree methods based on stan-

standard Gaussian integration, and `SmoothedMeshfreeAssembler` corresponds to meshfree methods with gradient smoothing.

In the `assembler` package six new classes have been implemented. These classes extend the meshfree method classes and contain new methods related to the phase-field problem, such as assembling new stiffness matrices and force vectors.

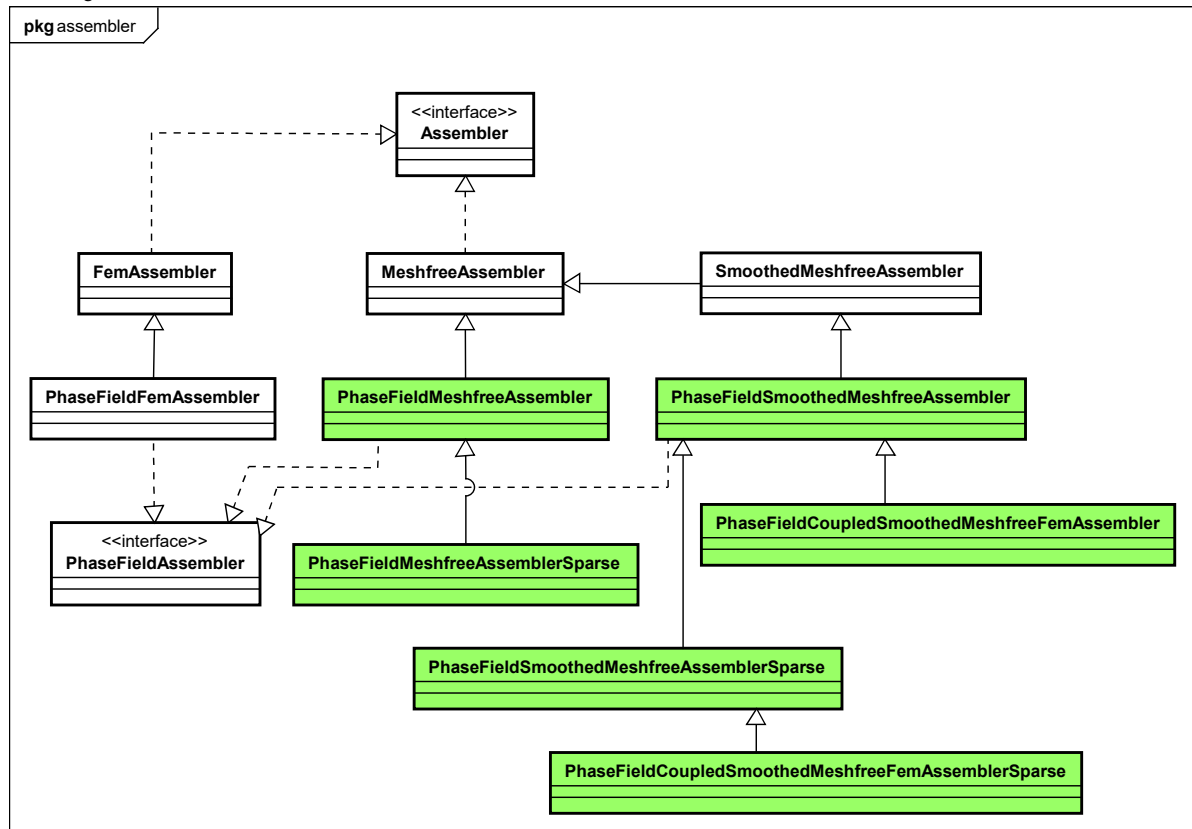


Figure B.9: Assembler class.

The Fig. B.10 shows the methods of the classes of phase-field and Fig. B.11 presents the methods of the classes of coupled model. The classes of coupled model possess the `femAssembler` as attribute. The methods of these classes access the methods of FEM assembler and meshfree assembler.

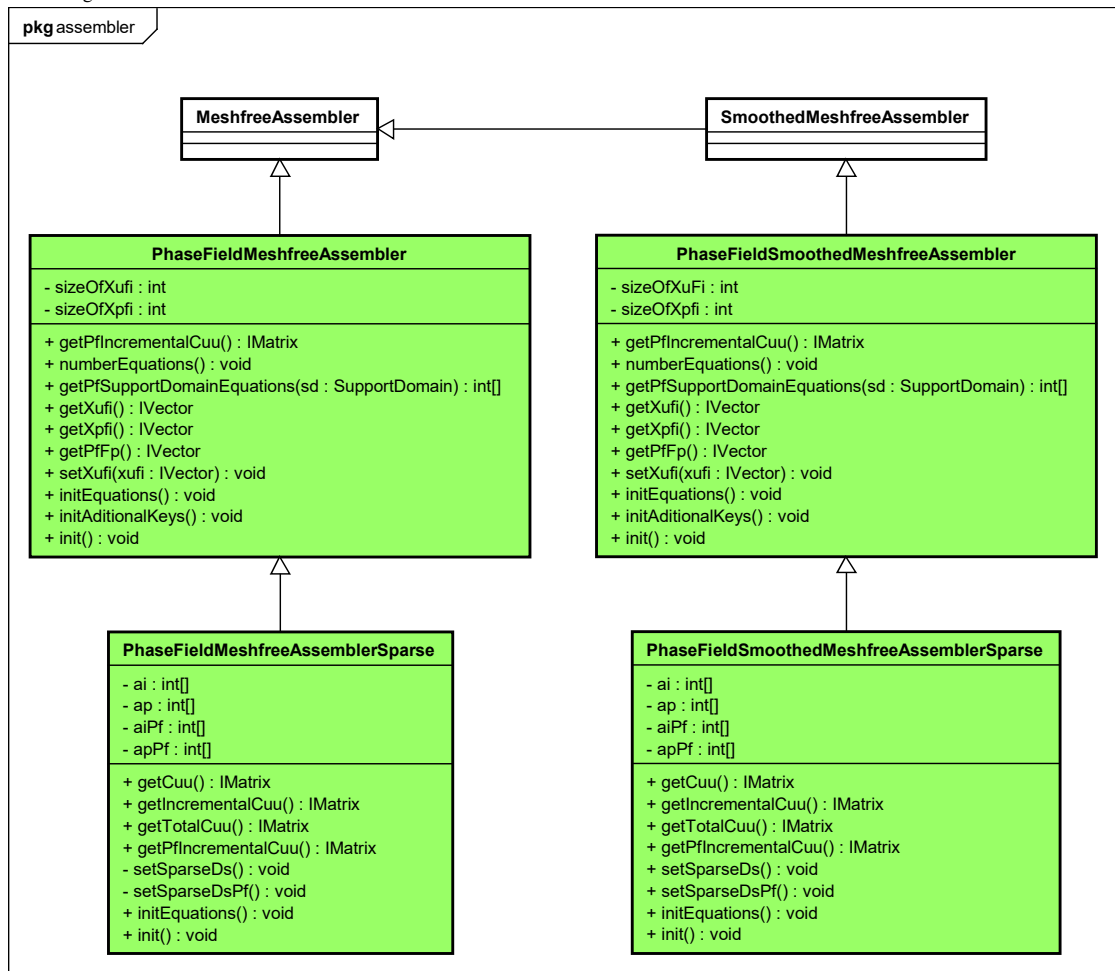


Figure B.10: Assembler phase-field class.

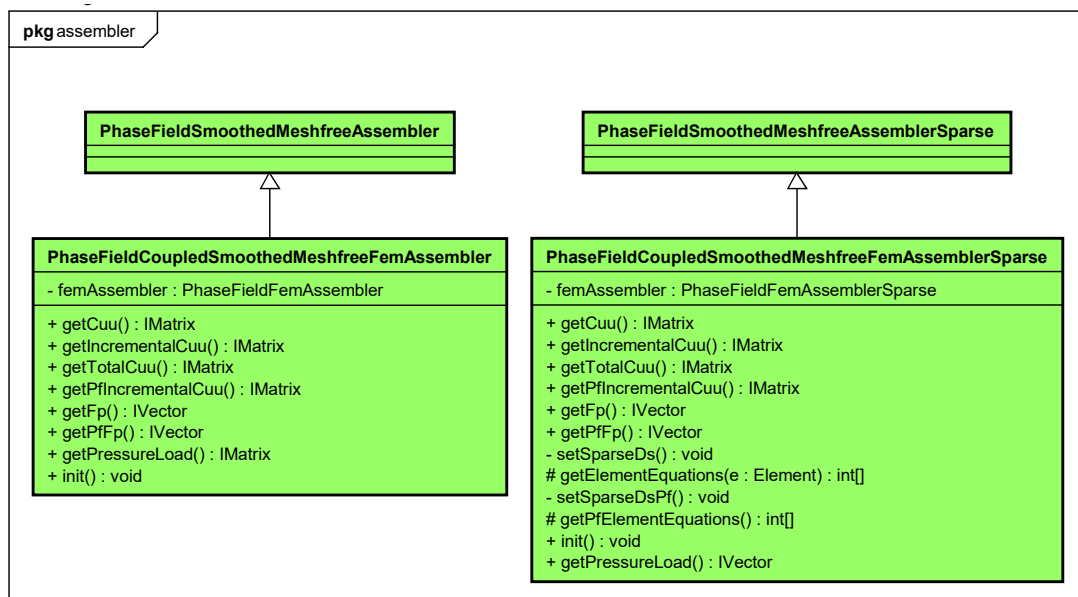


Figure B.11: Assembler coupled class.

B.4 Solution

The purpose of the abstract class `Solution` is to solve the system of the equation B.1. This class has different heirs, each one being responsible for solving a type of problem. Fig. B.12 presents the class diagram for solving static physically nonlinear problems. The class responsible for solving nonlinear problems is `StaticEquilibriumPath`. This class, in turn, has an instance of the `Step` class, which corresponds to the solution of one step of the analysis. In the case of the phase-field model and staggered solver, the solution of the step is divided in displacement problem and phase-field problem. As presented in 2.8, the staggered solver can be with historical variable or a constrained optimization problem. A specific step is implemented for each solver and the classes are depicted in Fig. B.13.

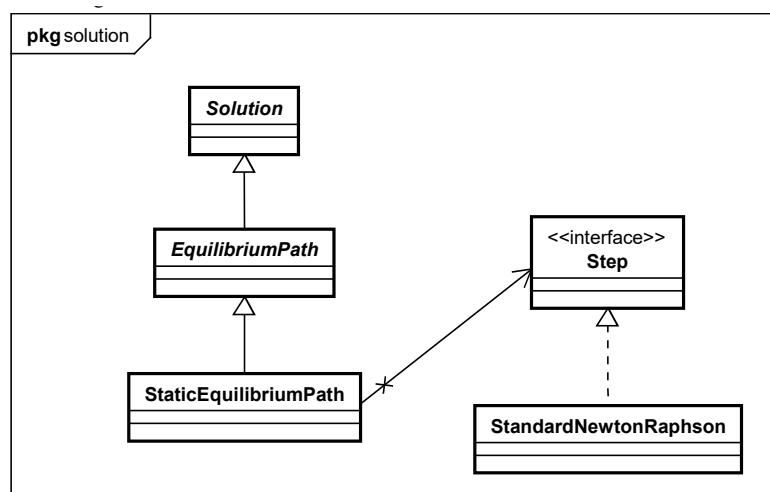


Figure B.12: Solution class.

In the adaptive strategy implemented, at the end of each converged step, it is verified if the model need be modified. A step converge when the global convergence is achieved. This convergence refers to both displacement and phase-field.

The analyse of the modification of the model is directed to the model. If the model have any modification, the new global iterations are performed until found the global convergence. This process can be performed many times in the same step and when the model don't have modifications the new step is performed.

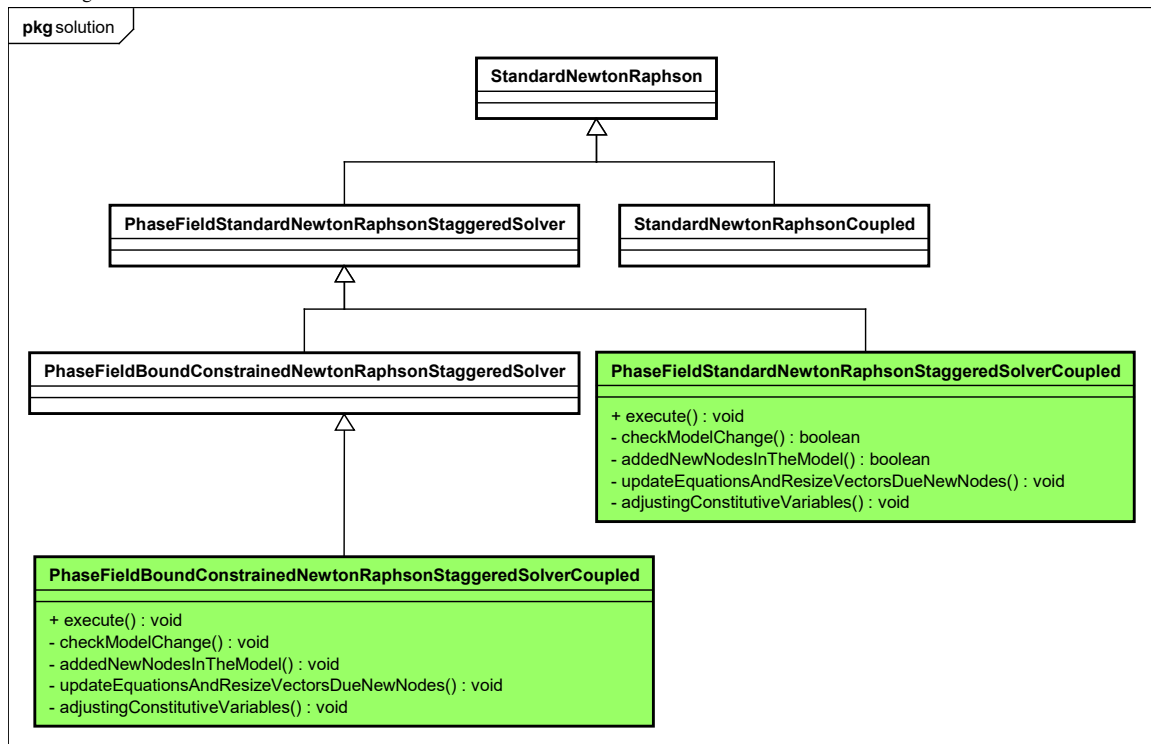


Figure B.13: Step class.

B.5 Persistence

As presented, the abstract class `Persistence` is responsible by reading the input file and create the output files. This class was modified for the phase-field models. The reading of the new steps, degenerations and materials were implemented in the class `Persistence`. In the class `DiscreteModelPersistenceAsXml` the variable of phase-field was inserted in the output files. The parameters of the adaptive strategy are reading in the class `CoupledMeshfreeFemModelPersistenceAsXml`.

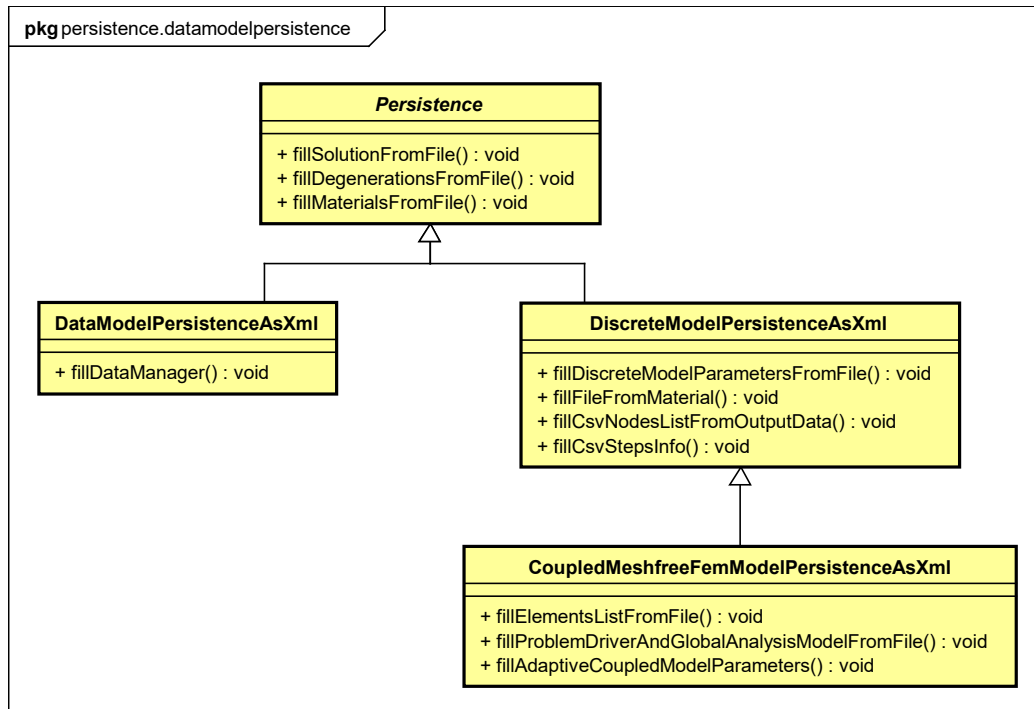


Figure B.14: Persistence class.

B.6 Radial Function

The new trigonometric radial function was implemented in the class `TrigonometricRf`. Two methods were inserted `getRadialFunction` and `getDerivedRadialFunction`. This class extends the `RadialFunction`, Similar to the `ExponentialRf` and `MultiquadricRf`.

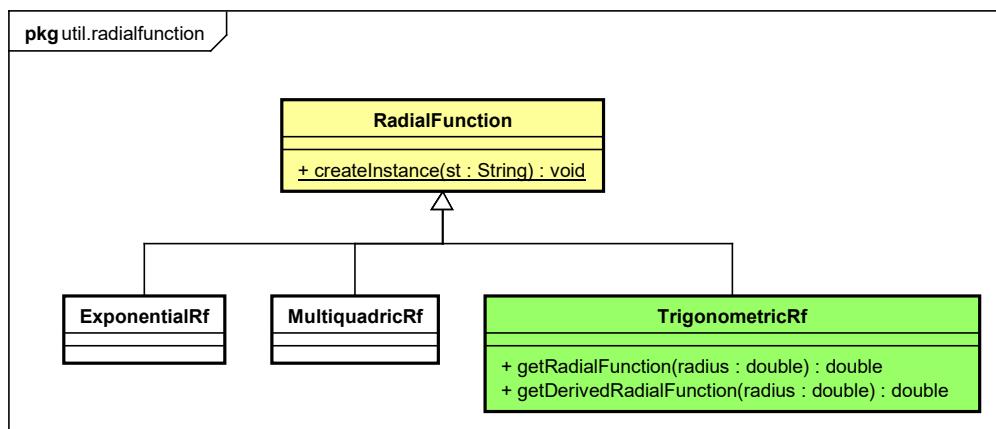


Figure B.15: Radial function class.

Appendix C

Input file model

This appendix will show the examples of input file for the analyses. As presented in the numerical simulations, the examples are divided in three categories: full SPIM, previously coupled FEM-SPIM and adaptive FEM-SPIM coupling.

Figure C.1 present the input file of the full SPIM model. The file is divide in `solution`, `geometric model` and `discrete model`. The `geometric model` (Fig.C.2) contains the vertex list, edge list and face list. The `discrete model` has the `shape function`, `support nodes strategy`, `problem drive`, `analisis model`, `material`, `degeneration`, `face attributes`, `nodes list`, `vertices list`, `integration domains list` and `loading`.

The example of `material` is illustrated in Fig. C.3. The material proprieties, the geometric crack function and the energetic degradation function are presented.

The degeneration is referent to the phase-field and is shown in Fig. C.4.

The file of the node is depicted in Fig. C.5. In phase-field models and the plane state, each node has three different variables referent to Dx , Dy , Pf .

The example of integration domain is illustrated in Fig. C.6. In the example, the edge-based is shown. In the file, all the integration cells in the boundary of the domain are presented.

The file of the previously coupled model is shown in Fig. C.7. This file has the substitution region. For the rectangular region, two nodes should be presented.

The discrete model parameters are depicted in Fig. C.8. The discretisation strategy should be indicated: cell-based, edge-based or node-based.

In the adaptive coupled models, the adaptive model parameters are presented (Fig. C.9). The substitution strategy has the type of criteria (`type`), value for substitution (`refvalue`) and boolean variable that indicate if the integration point will be converted in node (`convertIP`). The substitution area indicate the `shape` (circle or square) and the `scale`. The variable transfer strategy is only `average`. The refinement of the mesh-free region should inform the boolean variable `refine`, the `maxNumberOfRefinements`, the critical value for refinement (`factorCriticalValue`), the level of refinement of the mesh (`levelOfRefinement`), the `type` of criteria (PhaseField, StrainEnergy or Equiva-

lentStrain) and factorDecayRate.

```

1  <?xml version='1.1' encoding='UTF-8'?>
2  <Insane xmlns="http://www.dees.ufmg.br"
3  xmlns:xsi="http://www.w3.org/2001/XMLSchema-instance"
4  xsi:schemaLocation="http://www.dees.ufmg.br insane.xsd">
5    <Solution class="StaticEquilibriumPath">
6      <SolverType>200</SolverType>
7      <NumMaxSteps>150</NumMaxSteps>
8      <Step class="PhaseFieldStandardNewtonRaphsonStaggeredSolver">
9        </Step>
10     <IterativeStrategyList>
11     </IterativeStrategyList>
12     <StepNumber>0</StepNumber>
13     <FinalLoadFactor>0.0</FinalLoadFactor>
14   </Solution>
15   <!-- Geometric Model -->
16   <GeometricModel>
17   </GeometricModel>
18   <!-- Discret model -->
19   <DiscreteModel class="SmoothedPimMeshfreeModel">
20     <DiscreteModelParameters>
21       <ShapeFunctionsList>
22       </ShapeFunctionsList>
23       <SupportNodesStrategiesList>
24         <SupportNodesSelection type="T3Scheme" label="t3scheme"/>
25       </SupportNodesStrategiesList>
26       <ProblemDriver>PhaseFieldPhysicallyNonLinearSmoothedPim</ProblemDriver>
27
28       <GlobalAnalysisModel>PlaneStrainPhaseFieldStaggeredSolverMeshfree</GlobalAnalysisModel>
29
30       <MaterialList>
31       </MaterialList>
32
33       <DegenerationList>
34       </DegenerationList>
35
36       <AttributesMap>
37         <FaceAttributes>
38           <Face label="1">
39
40             <AnalysisModel>PlaneStrainPhaseFieldStaggeredSolverMeshfree</AnalysisModel>
41           </Face>
42         </FaceAttributes>
43       </AttributesMap>
44     </DiscreteModelParameters>
45
46     <NodeList>
47     </NodeList>
48
49     <!-- Vertices List -->
50     <IntegrationCellsVerticesList>
51       <Vertex label="1">
52         <Coord>0.0000000000000000E00 0.0000000000000000E00
53         0.0000000000000000E00</Coord>
54         <ContainingVertex>1</ContainingVertex>
55       </Vertex>
56     </IntegrationCellsVerticesList>
57
58     <IntegrationDomainsList>
59     </IntegrationDomainsList>
60
61     <LoadingList>
62     </LoadingList>
63   </DiscreteModel>
64 </Insane>

```

Figure C.1: Input file of the full SPIM model.

```

1 <GeometricModel>
2   <VertexList>
3     <Vertex label="1">
4       <Coord>0.000000000000000E00 0.000000000000000E00 0.000000000000000E00</Coord>
5     </Vertex>
6   </VertexList>
7   <EdgeList>
8     <Edge label="1">
9       <VertexIncidence>6 15</VertexIncidence>
10      <Shape>Edge</Shape>
11    </Edge>
12  </EdgeList>
13  <FaceList>
14    <Face label="1">
15      <EdgeIncidence>361 363 362</EdgeIncidence>
16    </Face>
17  </FaceList>
18 </GeometricModel>

```

Figure C.2: Input file of the geometric model.

```

1 <Material class="PhaseFieldMaterial" label="Material">
2   <Elasticity>38.0</Elasticity>
3   <Poisson>0.2</Poisson>
4   <LENGTH_SCALE>5.0</LENGTH_SCALE>
5   <GeometricCrackFunction>
6     <GCFCClass>WuXiCrackFunction</GCFCClass>
7     <XI>2.0</XI>
8   </GeometricCrackFunction>
9   <EnergeticDegradationFunction>
10    <EDFCClass>Wu2017CornelissensEnergeticFunction</EDFCClass>
11    <etal>3.0</etal>
12    <Ft>0.003</Ft>
13    <eta2>6.93</eta2>
14  </EnergeticDegradationFunction>
15  <FractureEnergy>1.25E-4</FractureEnergy>
16 </Material>

```

Figure C.3: Input file of the phase-field material.

```

1 <Degeneration class="PhaseFieldPrescribedDegeneration" label="Section">
2   <Height>1.000000</Height>
3   <CSMaterial>Material</CSMaterial>
4   <Thickness>1.000000</Thickness>
5 </Degeneration>

```

Figure C.4: Input file of the degeneration.

```

1 <Node label="1">
2   <Coord>0.000000 0.000000 0.000000</Coord>
3   <NodeValues>
4     <DOFLabels>Dx Dy PF</DOFLabels>
5     <Restraints>>false false false</Restraints>
6     <MasterDOFs>>false false false</MasterDOFs>
7     <Stiffness>0.00000E00 0.00000E00 0.00000E00</Stiffness>
8     <PreDisplacements>0.00000E00 0.00000E00 0.00000E00</PreDisplacements>
9   </NodeValues>
10 </Node>

```

Figure C.5: Input file of the nodes.

```

1  <IntegrationDomain type="EdgeBasedSmoothingDomain" label="SD-1">
2    <Edge>1</Edge>
3    <Degeneration>Section</Degeneration>
4    <AnalysisModel>PlaneStrainPhaseFieldStaggeredSolverMeshfree</AnalysisModel>
5    <ConstitutiveModel>StgPfmieheConstModel</ConstitutiveModel>
6    <IntegrationOrder>1 0 0 </IntegrationOrder>
7    <ShapeFunction>sh1</ShapeFunction>
8    <SupportNodesStrategy>t3scheme</SupportNodesStrategy>
9    <Values>
10     <SmoothingArea>1.204789120147856700E-04</SmoothingArea>
11   </Values>
12   <IntegrationCellsList>
13     <IntegrationCell label="IC-1">
14       <Cell>UnidimensionalIntCell</Cell>
15       <Incidence>6 9455</Incidence>
16       <CellValues>
17         <OutwardNormal>9.256129699891511000E-01 -3.784714385364669000E-01
18         </OutwardNormal>
19       </CellValues>
20       <Face>5006</Face>
21     </IntegrationCell>
22     <IntegrationCell label="IC-2">
23       <Cell>UnidimensionalIntCell</Cell>
24       <Incidence>9455 15</Incidence>
25       <CellValues>
26         <OutwardNormal>8.842121923778894000E-01 4.670854299272096400E-01
27         </OutwardNormal>
28       </CellValues>
29       <Face>5006</Face>
30     </IntegrationCell>
31     <IntegrationCell label="IC-3">
32       <Cell>UnidimensionalIntCell</Cell>
33       <Incidence>15 6</Incidence>
34       <CellValues>
35         <OutwardNormal>-1.0000000000000000E00 -0.0000000000000000E00
36         </OutwardNormal>
37       </CellValues>
38       <Face>5006</Face>
39     </IntegrationCell>
40   </IntegrationCellsList>
</IntegrationDomain>

```

Figure C.6: Input file of the integration domains.

```

1  <?xml version='1.1' encoding='UTF-8'?>
2  <Insane xmlns="http://www.dees.ufmg.br"
  xmlns:xsi="http://www.w3.org/2001/XMLSchema-instance"
  xsi:schemaLocation="http://www.dees.ufmg.br insane.xsd">
3    <!-- Solution -->
4    <Solution class="StaticEquilibriumPath">
5      <SolverType>200</SolverType>
6      <NumMaxSteps>200</NumMaxSteps>
7      <Step class="PhaseFieldBoundConstrainedNewtonRaphsonStaggeredSolverCoupled">
8        <NumMaxIterations>100</NumMaxIterations>
9        <Tolerance>1.0E-4</Tolerance>
10       <GlobalTolerance>0.001</GlobalTolerance>
11       <ConvergenceType>2</ConvergenceType>
12       <EquilibriumType>1</EquilibriumType>
13     </Step>
14     <IterativeStrategyList>
15       <IterativeStrategy class="DisplacementControl" LoadFactor="-0.0035">
16         <NodeControl>4</NodeControl>
17         <DirectionControl>y</DirectionControl>
18       </IterativeStrategy>
19     </IterativeStrategyList>
20     <StepNumber>0</StepNumber>
21     <FinalLoadFactor>0.0</FinalLoadFactor>
22   </Solution>
23
24   <!-- Substitution region -->
25   <RegionForReplacement>
26     <Vertex label="1"> <Coord>245.0 30.0 0.0</Coord> </Vertex>
27     <Vertex label="2"> <Coord>255.0 100.0 0.0</Coord> </Vertex>
28   </RegionForReplacement>
29
30   <!-- Informations of the discret model -->
31   <DiscreteModel class="CoupledSmoothedPimMeshfreeFemModel">
32     <AdaptiveAnalysis>false</AdaptiveAnalysis>
33
34     <DiscreteModelParameters class="CoupledSmoothedPimMeshfreeFemModel"
35       domain="2D">
36     </DiscreteModelParameters>
37
38     <!-- Nodes -->
39     <NodeList>
40     </NodeList>
41
42     <!-- Elements -->
43     <ElementList>
44     </ElementList>
45
46     <!-- Loading -->
47     <LoadingList>
48       <Loading label="Carregamento 1">
49     </Loading>
50   </LoadingList>
51   <ScalarFunctions>
52     <ScalarFunction type="ConstantFunction" label="Function-1.0">
53       <Amplitude>1.000E00</Amplitude>
54     </ScalarFunction>
55   </ScalarFunctions>
56   <LoadCombinations>
57     <LoadCombination label="LoadCombination1">
58       <LoadCase loading="Carregamento 1" inc="true" scalarFunction="Function-1.0"/>
59     </LoadCombination>
60   </LoadCombinations>
61 </DiscreteModel>
</Insane>

```

Figure C.7: Input file of the coupled model.

```

1  <DiscreteModelParameters class="CoupledSmoothedPimMeshfreeFemModel" domain="2D">
2
3  <!-- Meshfree model -->
4  <DiscreteModelGenerator>PimModelGenerator</DiscreteModelGenerator>
5
6  <!-- Faces Attributes -->
7  <FacesAttributes>
8    <Face>
9
10     <AnalysisModel>PlaneStressPhaseFieldStaggeredSolverMeshfree</AnalysisModel
11     >
12     <ConstitutiveModel>StgPfWu2013ConstModel</ConstitutiveModel>
13     <Degeneration>Section</Degeneration>
14     <ShapeFunction>sh1</ShapeFunction>
15     <SupportNodesSelection>t4scheme</SupportNodesSelection>
16   </Face>
17 </FacesAttributes>
18
19 <!-- Discretization Strategy -->
20 <DiscretizationStrategy>
21   <NodalDistributionStrategy
22     type="InformedDistribution"></NodalDistributionStrategy>
23   <IntegrationDomainsStrategy type="CsPimTriangular2dStrategy" intOrd="1"
24     cells="1"></IntegrationDomainsStrategy>
25 </DiscretizationStrategy>
26
27 <!-- Integration Order -->
28 <LoadingsTreatment>
29   <IntegrationOrder object="LL1" intOrd="14 0 0"></IntegrationOrder>
30 </LoadingsTreatment>
31
32 <!-- Shape Function -->
33 <ShapeFunctionsList>
34   <ShapeFunction type="RPimPolyReproductionShape" label="sh1">
35     <BasisFunctions type="ScaledRadialBasisFunctions2D">
36       <RadialFunction type="ExponentialRf">
37         <ShapeParameter>1</ShapeParameter>
38       </RadialFunction>
39     </BasisFunctions>
40     <PolynomialReproduction>
41       <PolynomialBasisFunction>Polynomial2D</PolynomialBasisFunction>
42       <NumberPolynomialTerms>3</NumberPolynomialTerms>
43     </PolynomialReproduction>
44   </ShapeFunction>
45 </ShapeFunctionsList>
46
47 <!-- Support Nodes Selection -->
48 <SupportNodesStrategiesList>
49   <SupportNodesSelection type="T4Scheme" label="t4scheme">
50     </SupportNodesSelection>
51 </SupportNodesStrategiesList>
52
53 <!-- Problem driver -->
54 <ProblemDriver>PhaseFieldPhysicallyNonLinearSmoothedPim</ProblemDriver>
55
56 <!-- Global analysis model -->
57 <GlobalAnalysisModel>PlaneStressPhaseFieldStaggeredSolverMeshfree</GlobalAnalysisM
58 odel>
59
60 <!-- Material -->
61 <MaterialList>
62 </MaterialList>
63
64 <!-- Degeneration -->
65 <DegenerationList>
66 </DegenerationList>
67
68 </DiscreteModelParameters>

```

Figure C.8: Input file of the discrete model parameters.

```

1  <?xml version='1.1' encoding='UTF-8'?>
2  <Insane xmlns="http://www.dees.ufmg.br"
  xmlns:xsi="http://www.w3.org/2001/XMLSchema-instance"
  xsi:schemaLocation="http://www.dees.ufmg.br insane.xsd">
3    <!-- Solution -->
4    <Solution class="StaticEquilibriumPath">
5      <SolverType>200</SolverType>
6      <NumMaxSteps>150</NumMaxSteps>
7      <Step class="PhaseFieldStandardNewtonRaphsonStaggeredSolverCoupled">
8        <NumMaxIterations>500</NumMaxIterations>
9        <Tolerance>0.001</Tolerance>
10       <GlobalTolerance>0.001</GlobalTolerance>
11       <ConvergenceType>2</ConvergenceType>
12       <EquilibriumType>1</EquilibriumType>
13     </Step>
14     <IterativeStrategyList>
15       <IterativeStrategy class="DisplacementControl" LoadFactor="1.0E-4">
16         <NodeControl>38</NodeControl>
17         <DirectionControl>x</DirectionControl>
18       </IterativeStrategy>
19     </IterativeStrategyList>
20     <StepNumber>0</StepNumber>
21     <FinalLoadFactor>0.0</FinalLoadFactor>
22   </Solution>
23
24   <!-- Informations of the discret model -->
25   <DiscreteModel class="CoupledSmoothedPimMeshfreeFemModel">
26     <AdaptiveAnalysis>true</AdaptiveAnalysis>
27
28     <DiscreteModelParameters class="CoupledSmoothedPimMeshfreeFemModel" domain="2D">
29
30       <!-- Adaptive parameters -->
31       <AdaptiveCoupledModelParameters>
32         <SubstitutionStrategy type="ShaoCriteria" refValue="0.3" refValuePf="0.2"
33           convertIP="true"></SubstitutionStrategy>
34         <SubstitutionArea shape="Circle" scale="2.0"></SubstitutionArea>
35         <VariableTransferStrategy type="Average"
36           numberOfMonomials="3"></VariableTransferStrategy>
37         <MeshfreeArea refine="true" maxNumberOfRefinements="15"
38           factorCriticalValue="0.9" levelOfRefinement="2"
39           type="PhaseField" factorDecayRate="0.1"></MeshfreeArea>
40       </AdaptiveCoupledModelParameters>
41     </DiscreteModelParameters>
42
43     <!-- Nodes -->
44     <NodeList>
45     </NodeList>
46
47     <!-- Elements -->
48     <ElementList>
49     </ElementList>
50
51     <!-- Loading -->
52     <LoadingList>
53       <Loading label="Carregamento 1">
54       </Loading>
55     </LoadingList>
56
57     <ScalarFunctions>
58       <ScalarFunction type="ConstantFunction" label="Function-1.0">
59         <Amplitude>1.000E00</Amplitude>
60       </ScalarFunction>
61     </ScalarFunctions>
62
63     <LoadCombinations>
64       <LoadCombination label="LoadCombination1">
65         <LoadCase loading="Carregamento 1" inc="true" scalarFunction="Function-1.0"/>
66       </LoadCombination>
67     </LoadCombinations>
68
69   </DiscreteModel>
70 </Insane>

```

Figure C.9: Input file of the adaptive model.